A Physio-chemical Predictive Model of Dynamic Thrombus Formation and Growth in Stenosed Vessels

Hamid Hosseinzadegan

Dissertation submitted to the faculty of the Virginia Polytechnic Institute and State University in partial fulfillment of the requirements for the degree of

Doctor of Philosophy
In
Mechanical Engineering

Danesh K. Tafti, Chair
Bahareh Behkam
John C. Chappell
John W. Grant
Rui Qiao
Anne E. Staples

Sep 28th 2017
Blacksburg, Virginia

Keywords: Numerical modeling, Atherosclerosis, Platelet adhesion, Platelet activation, Embolism

A Physio-chemical Predictive Model of Dynamic Thrombus Formation and Growth in Stenosed Vessels

Hamid Hosseinzadegan

ABSTRACT

According to the World Health Organization (WHO), Cardiovascular Disease (CVD) is the leading cause of death in the world. Biomechanics and fluid dynamics of blood flow play an important role in CVD mediation. Shear stress plays a major role in platelet-substrate interactions and thrombus formation and growth in blood flow, where under both pathological and physiological conditions platelet adhesion and accumulation occur. In this study, a three-dimensional dynamic model of platelet-rich thrombus growth in stenosed vessels using computational fluid dynamics (CFD) methods is introduced. Platelet adhesion, aggregation and activation kinetics are modeled by solving mass transport equations for blood components involved in thrombosis. The model was first verified under three different shear conditions and at two heparin levels. Three-dimensional simulations were then carried out to evaluate the performance of the model for severely damaged (stripped) aortas with mild and severe stenosis degrees. For these cases, linear shear-dependent functions were developed for platelet-surface and platelet-platelet adhesion rates. It was confirmed that the platelet adhesion rate is not only a function of Reynolds number (or wall shear rate) but also the stenosis severity of the vessel. General correlations for adhesion rates of platelets as functions of stenosis and Reynolds number were obtained based on these cases. The model was applied to different experimental systems and shown to agree well with measured platelet deposition. Then, the Arbitrary Lagrangian Eulerian (ALE) formulation was used to model dynamic growth by including geometry change in the simulation procedure. The wall boundaries were discretely moved based on the amount of

platelet deposition that occurs on the vessel wall. To emulate the dynamic behavior of platelet adhesion kinetics during thrombus growth, the validated model for platelet adhesion, which calculates platelet-surface adhesion rates as a function of stenosis severity and Reynolds number, was applied to the model. The model successfully predicts the nonlinear growth of thrombi in the stenosed area. These simulations provide a useful guide to understand the effect of growing thrombus on platelet deposition rate, platelet activation kinetics and occurrence of thromboembolism (TE) in highly stenosed arteries.

A Physio-chemical Predictive Model of Dynamic Thrombus Formation and Growth in Stenosed Vessels

Hamid Hosseinzadegan

GENERAL AUDIENCE ABSTRACT

Continuous platelet deposition in coronary arteries creates a narrow necking area at some susceptible regions such as bifurcations, stented arteries and ruptured vessel walls. These narrow regions, known as stenoses, are the number one cause of heart attacks. In this work, a predictive model of platelet deposition (i.e. thrombosis) is developed based on previous experimental and clinical data on human blood. Fluid shear stresses play a major role in platelet-substrate interactions and thrombus formation and growth in blood flow, where under both pathological and physiological conditions platelet adhesion and accumulation occur.

In addition to simulating the blood flow patterns in arteries with computational fluid dynamics (CFD), the model is able to reliably predict the amount of platelets deposited in injured areas, the severity of the blockage in the blood flow, and the time for occlusion. The results of our model are much more accurate than previous models and are validated by comparing them to clinical data for thrombus formation in stenosed arteries. Thus, the project contributes towards better diagnosis and treatment of vascular disease with implications on the monitoring and management of cardiovascular diseases and providing useful guidelines to design improved devices such as left ventricular assist devices, mechanical heart valves, stents, etc.

Dedicated to my parents

ACKNOWLEDGEMENTS

I would like to thank all the people who contributed in some way to the work described in this dissertation. First and foremost, I thank my academic advisor, Professor Danesh K. Tafti, who has provided me extensive support and professional guidance and taught me a great deal about both scientific research and life in general. Additionally, I would like to thank my committee members Professor John W. Grant, Professor Rui Qiao, Professor Anne Staples, Professor Bahareh Behkam, and Dr John Chappell for their interest in my work.

Every result described in this thesis was accomplished with the help and support of fellow lab-mates. I am grateful to all of those with whom I have had the pleasure to work during this project. Also, I would like to acknowledge the National Science Foundation for the financial support of this work.

Nobody has been more important to me in the pursuit of this project than the members of my family. I would like to thank my parents and grandparents, whose love and guidance are with me in whatever I pursue, and my beloved brothers for supporting me.

TABLE OF CONTENTS

LIST OF FIGURES

LIST OF TABLES

NOMENCLATURE

ADP	Adenosine Diphosphate
ALE	Arbitrary Lagrangian Eulerian
AN	Apical Aneurysm
$\mathrm{A_{ROI}}$	Region of interest area, $\mathrm{mm^2}$
ATIII	Antithrombin
$\mathrm{C_i}$	Concentration of species i ($\mathrm{PLT.mm^{-1}}$, μM, $\mathrm{U.ml^{-1}}$)
CDR	Convection Diffusion Reaction
CFL	Cell Free Layer
CVD	Cardiovascular Disease
$\mathrm{D_i}$	Total mass diffusivity of species i, $\mathrm{m^2.s^{-1}}$
$\mathrm{D_{b,i}}$	Brownian diffusivity of species i, $\mathrm{m^2.s^{-1}}$
$\mathrm{d_p}$	Particle diameter used to calculate Stk number, m
$\mathrm{d_{PLT}}$	Platelet diameter, m
$\mathrm{D_{s,i}}$	Enhanced diffusivity of species i, $\mathrm{m^2.s^{-1}}$
DCM	Dilated Cardiomyopathy
DNS	Direct Numerical Simulation
DVM	Deep Venous Thrombosis
FSI	Fluid Structure Interaction
GPIb	Cohesive integrin receptor
GPVI	Adhesive glycoprotein integrin receptor
[H]	Heparin concentration, $\mathrm{U.ml^{-1}}$
HF	Heart Failure
$\mathrm{k_{1,TxA_2}}$	Reaction rate constant for inhibition of $\mathrm{TxA_2}$, $\mathrm{s^{-1}}$
$\mathrm{k_{aa}}$	Activated platelet-platelet adhesion rate, $\mathrm{cm.s^{-1}}$
$\mathrm{k_{aa_0}}$	Activated platelet-platelet adhesion rate baseline parameter, $\mathrm{cm.s^{-1}}$

$\mathrm{k_{as}}$	Activated platelet-surface adhesion rate, $\mathrm{cm.\,s^{-1}}$
$\mathrm{k_{as_0}}$	Activated platelet-surface adhesion rate baseline parameter, $\mathrm{cm.\,s^{-1}}$
$\mathrm{k_{rs}}$	Resting platelet-surface adhesion rate, $\mathrm{cm.\,s^{-1}}$
$\mathrm{k_{rs_0}}$	Activated platelet-surface adhesion rate baseline parameter, $\mathrm{cm.\,s^{-1}}$
$\mathrm{k_{pa}}$	Platelet activation rate, $\mathrm{s^{-1}}$
L	Half width of the channel, tube radius, cm
$\mathrm{L_{mar}}$	Platelet margination length scale, m
$\mathrm{l_{ref}}$	Characteristic length used to calculate Stk number, m
LV	Left Ventricle
LVAD	Left Ventricular Assist Device
MHV	Mechanical Heart Valve
$\mathrm{M_{\infty}}$	Capacity of surface for first platelet layer, $\mathrm{PLT.\,cm^{-2}}$
$\mathrm{M_{as}}$	Surface coverage due to resting platelets, $\mathrm{PLT.\,cm^{-2}}$
$\mathrm{M_{as}}$	Surface coverage due to activated platelets, $\mathrm{PLT.\,cm^{-1}}$
$\mathrm{M_{at}}$	Deposition due to activated platelets, $\mathrm{PLT.\,cm^{-1}}$
$\mathrm{M_{rs}}$	Deposition due to resting platelets, $\mathrm{PLT.\,cm^{-1}}$
MMP	Metalloproteinases
N	Average near-wall platelet count, $\mathrm{PLT.\,mm^{-3}}$
PAS	Nondimensional Platelet Activation State parameter
$\mathrm{PAS^{p}}$	Nondimensional PAS value for particles (equal to PAS)
$\mathrm{PAS^{c}}$	Nondimensional PAS value in fluid cells
PRP	Platelet Rich Plasma
PT	Prothrombin
$\mathrm{Q_{intial}}$	Initial flow rate applied at the stenosed channel inlet, $\mathrm{mL.s^{-1}}$
$\mathrm{Q_{mean}}$	Mean flow rate averaged over total perfusion time, $\mathrm{mL.s^{-1}}$
R	Nondimensional vessel unstenosed radius
$\mathrm{R_{acc}}$	Number of accumulated platelets per unit time, $\mathrm{PLT.\,s^{-1}}$

R_{RBC}	Radius of red blood cell, m
Re	Reynolds number at inlet
Re_{apex}	Reynolds number at the apex
s_{p,TxA_2}	Rate of synthesis of TxA_2 by platelet, $nmol.PLT^{-1}.s^{-1}$
$S(x,t)$	Available free surface
s	Stenosis degree, %
Stk	Stokes number
t_{qss}	Simulation time corresponding to quasi-steady state, s
Th	Thrombin
TE	Thromboembolism
TxA_2	Thromboxane A_2
u_{ref}	Fluid Reference velocity used to calculate Stk number, $m.s^{-1}$
vWf	Von Willebrand factor
V_{acc}	Platelet accumulation rate in region of interest, $mm.s^{-1}$
V_{aorta}	Maximum flow velocity at the aortic valve outlet, $cm.s^{-1}$
V_{LVAD}	Maximum flow velocity at the LVAD outlet, $cm.s^{-1}$
V_{mitral}	Maximum flow velocity at the mitral valve inlet, $cm.s^{-1}$

Greek

$\alpha_2\beta_1$	Adhesive integrin receptor
$\alpha_{IIb}\beta_3$	Cohesive integrin receptor
β	Conversion factor to convert thrombin concentration from $U.ml^{-1}$ to μM ($nmol.U^{-1}$)
$\dot{\gamma}$	Local fluid shear rate, s^{-1}
$\dot{\gamma}_w$	Wall shear rate, s^{-1}
Γ	Griffith's template model for the kinetics of the heparin-catalyzed inactivation of thrombin by antithrombin
θ	Fraction of resting platelets that activate upon surface contact

λ	Shear enhancement factor, s
λ_{ADP}	Amount of ADP per activated platelet, $\mathrm{nmol.PLT^{-1}}$
μ	Blood viscosity, $\mathrm{Pa.s}$
μ_{f}	Fluid viscosity used to calculate Stk number, $\mathrm{Pa.s}$
ϕ_{rt}	Rate of thrombin generation from prothrombin at the surface of resting platelets, $\mathrm{U.PLT^{-1}.s^{-1}}$
ϕ_{at}	Rate of thrombin generation from prothrombin at the surface of activated platelets, $\mathrm{U.PLT^{-1}.s^{-1}}$
ρ	Blood density, $\mathrm{kg.m^{-3}}$
ρ_{p}	Particle density used to calculate Stk number, $\mathrm{kg.m^{-3}}$

1 Introduction

1.1 Motivation

According to the Centers for Disease Control and Prevention (CDC), Cardiovascular Disease (CVD) is the leading cause of death for both men and women in the United States. About 610,000 people die of heart disease in the U.S. every year – that's 1 in every 4 deaths. Arterial wall mechanics and fluid dynamics of blood flow play an important role in CVD mediation. Thrombosis is a pathological condition which develops in blood vessels subject to certain mechanical and chemical stimuli. Arterial thrombosis in the coronary arteries can restrict crucial blood flow to the heart muscles leading to a heart attack. In addition, thromboembolism (TE) has the potential of serious complications and even death. Understanding the etiology of thrombogenesis and embolism using experiments and computational modeling has been the subject of extensive research. Platelets, which are responsible for the primary hemostatic plug formation, adhere to the vessel wall, change in shape and get activated to form reversible aggregates. This research develops and utilizes a predictive dynamic geometry-dependent model of thrombus growth that can be applied to a wide range of blood flow rates and stenosis severities. This is an important step as the current study utilizes a first of its kind continuum-based model with variable thrombus geometry. Also, with the increasing incidence of heart failure, there is a renewed clinical interest in ventricular fluid dynamics and modeling of thrombus formation in assist devices such as left ventricular assist device (LVAD). Every year about 735,000 Americans have a heart attack according to CDC. Thus, the project contributes towards better diagnosis and treatment of vascular disease and will have broad ranging implications on the monitoring and management of cardiovascular diseases and providing useful guidelines to design improved devices such as LVADs, mechanical heart valves, stents, etc.

1.2 Objective

The main objective of this study was to develop a comprehensive model of thrombus formation and growth which is predictive and applicable to a wide range of flow characteristics and geometries. In the past decade, there has been a considerable work to study the platelet activation, adhesion and aggregation in various geometries under in-vitro conditions. However, developed continuum-based models in the literature are not predictive and need to be recalibrated using experimental observations every time they are applied to a new problem with different boundary conditions. To reproduce a realistic scenario on the thrombosis and related phenomena such as coagulation, platelet activation, and platelet margination in stenosed arteries, new functions were found based on clinical observations that relate platelet adhesion rates to the stenosis degree of the vessel and the flow Reynolds number at the stenosis apex. These functions are able to reasonably predict the platelet deposition in stenotic flows. This work would be very helpful for design improvement of heart assist devices such as mechanical/prosthetic heart valves, stents, LVADs, etc.

1.3 Contributions of this work

The major contribution of this research was implementation of a predictive physics-based model of thrombus formation and growth that can be applied to a variety of geometries under a wide range of physiological and pathological flow conditions. This is was done by including the major blood components, namely platelets and platelet stimulating proteins and validating the model based on various in-vitro and ex-vivo experimental data. To our knowledge, this is the first study of its kind that takes into account the dynamic geometry of mural thrombi and also includes both biological and mechanical factors that contribute to platelet activation and deposition. Furthermore, the model is predictive for stenosed arteries and does not need to be calibrated based on case-specific experimental conditions. The following journal and conference papers were written and published during this work:

- Hosseinzadegan, H. and Tafti, D.K., 2017. Mechanisms of platelet activation and aggregation. To be submitted.
- Hosseinzadegan, H. and Tafti, D.K., 2017. Predictive modeling of thrombus growth in stenosed vessels with dynamic geometries using Arbitrary Lagrangian Eulerian method. Submitted to PLoS ONE.
- Hosseinzadegan, Hamid, and Danesh K. Tafti. "Modeling thrombus formation and growth." Biotechnology and Bioengineering (2017). doi:10.1002/bit.26343.
- Hosseinzadegan, Hamid, and Danesh K. Tafti. "Prediction of Thrombus Growth: Effect of Stenosis and Reynolds Number." Cardiovascular Engineering and Technology 8.2 (2017): 164-181. doi:10.1007/s13239-0170304-3.
- Hosseinzadegan, Hamid, and Danesh K. Tafti. "Validation of a time dependent physio-chemical model for thrombus formation and growth." ASME 2016 Fluids Engineering Division Summer Meeting collocated with the ASME 2016 Heat Transfer Summer Conference and the ASME 2016 14th International Conference on Nanochannels, Microchannels, and Minichannels. American Society of Mechanical Engineers. 2016. doi:10.1115/FEDSM2016-7803.

1.4 Organization of dissertation

Thesis is organized as follows: Chapter 2 presents a comprehensive review of both experimental and numerical studies related to platelet activation, margination, adhesion and aggregation. Chapter 3 presents the development, calibration and validation of the model applied to stenosed vessels with stationary geometry. Chapter 4 presents the sensitivity analysis performed to investigate of effect of different blood components and flow pulsatility on platelet deposition. Chapter 5 presents results for thrombus growth in stenosed vessels with dynamic geometry using Arbitrary Lagrangian Eulerian (ALE) method. Chapter 6 presents the implementation of shear-induced platelet activation model and its results for stenosed vessels. Chapter 7 discusses the preliminary work with results for thrombus formation in left ventricular assist device (LVAD). Finally, Chapter 8 presents conclusions and the summary.

2 Literature Review

The chapter reviews the state-of-the-art in computational modeling of thrombus formation and growth and related phenomena including platelet margination, activation, adhesion, and embolization. Presently, there is a high degree of empiricism in the modeling of thrombus formation. Based on the experimentally observed physics, the review gives useful strategies for predicting thrombus formation and growth. These include determining blood components involved in atherosclerosis, effective blood viscosity, tissue properties, and methods proposed for boundary conditions. In addition to the guidelines, ongoing research on the effect of shear stress on platelet margination, activation and adhesion, and platelet-surface interactions are reviewed. Reviewed studies are categorized to three major groups and shown in Figure 2.1: 1) experimental studies that focus on observation of interplatelet and platelet-wall chemical interactions, effect of shear stress on thrombosis, hemodynamics in various locations of vascular system, etc.; 2) numerical studies that develop an/or utilize modeling techniques to quantify thrombus formation and growth and related phenomena; 3) review studies which summarize the previous and ongoing research in this area.

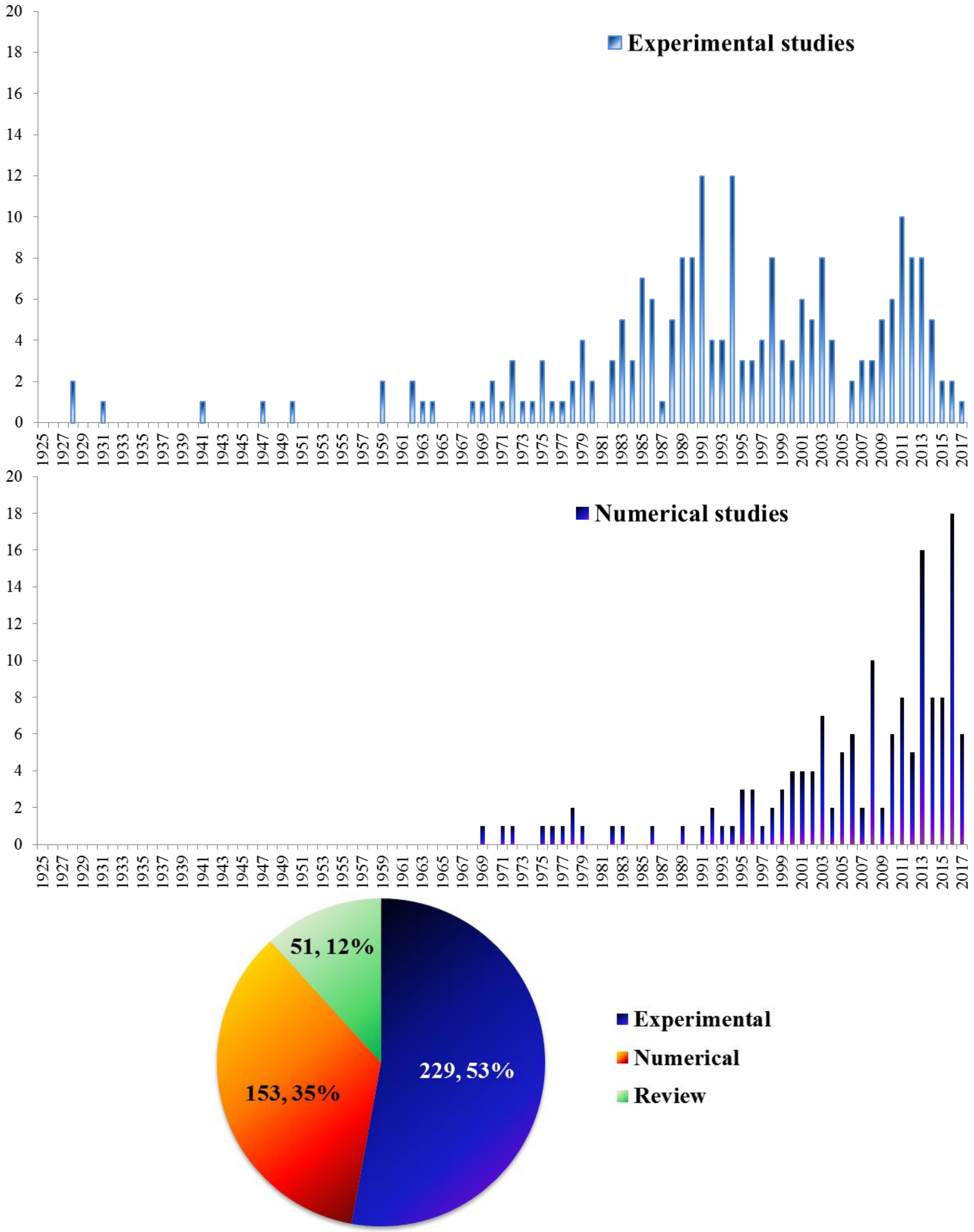

Figure 2.1 Number of reviewed experimental, numerical, and review studies with publication year from 1925 to 2017.

2.1 Introduction

Thrombosis is a pathological condition which develops in blood vessels subject to certain mechanical and chemical stimuli. Arterial thrombosis in the coronary arteries can restrict crucial blood flow to the heart muscles leading to a heart attack. Thrombus embolization has the potential of serious complications and even death. Understanding the etiology of thrombogenesis using experiments and computational modeling has been the subject of extensive research. Platelets, which are responsible for the primary hemostatic plug formation, adhere to the vessel wall, change shape and get activated to form reversible aggregates. This is followed by the formation of a fibrin network which fortifies and stabilizes the platelet aggregate [1], [2]. Additionally, red blood cells are involved in red clot formation (i.e. observed during deep venous thrombosis (DVT) and left ventricular thrombosis (LVT) [3]). Modeling thrombogenesis and growth is challenging because 1) together with platelet activation, many blood and tissue factors are involved in the process [4]–[7]; 2) chemical interactions between contributing constituents are complex and non-linear; 3) hemodynamics can significantly affect the formation and growth of thrombus as well as thromboembolism [8]–[10]; 4) because of the high degree of mechanical and biochemical complexity, mathematical models heavily rely on experiments for model parameterization. In spite of these challenges, much progress has been made in model development. This chapter surveys models developed for platelet deposition, activation, aggregation and modeling thromboembolism. Thrombosis modeling methods reviewed in this chapter are mostly relevant to white clot formation unless stated otherwise, since most models have primarily focused on thrombosis and thrombotic disorders in arterial flows. The strengths and weaknesses of the reviewed state-of-the-art are evaluated and recommendations are made for future research directions.

2.2 Mechanisms of platelet adhesion, activation and aggregation

2.2.1 Platelet adhesion to subendothelium

Of the most defining prerequisites for platelet adhesion to the subendothelium are the presence of specific receptors on platelets and vessel wall. Collagen is one of the major thrombogenic proteins on the vessel walls, available in the subendothelial matrix [11]. Integrin $\alpha_2\beta_1$ and the glycoprotein GPVI are the adhesion receptors of collagen [12], [13]. Glycoprotein GPVI is the common adhesion receptor between collagen and platelets. The von Willebrand (vWf) protein, synthesized in the platelet's internal cytoskeleton core (megakaryocytes) [14] and endothelial cells [15], is the other factor available in soluble state both on vessel walls and in plasma. The role of vWf in mediating platelet adhesion was first indicated by Tschopp et al. [6]; ~10 times longer bleeding time caused by impaired platelet adhesion to vessel wall has been shown for patients with von Willebrand's disease. The relationship between the levels of human vWf and platelet adhesion to cultured endothelial cells under *ex-vivo* and *in-vivo* conditions has been established in pig lung, porcine pulmonary artery and aorta [16]. In addition to von Willebrand factor, laminin, fibronectin, and thrombospondin on the vessel surface may play a role, although minor [17], in mediating platelet adhesion [4], [7], [18], [19].

2.2.2 Platelet activation and aggregation

Once platelets adhere to the vessel wall, specifically to the endothelium, they get activated, change dramatically in shape from a discoid ball to a sphere [20] to first increase the adhesion area and second, stimulate other platelets resting in plasma to become activated through biological mechanisms. These include signaling pathways [21] in the platelet extracellular membrane and secretion of soluble thrombogenic agonists to the plasma. Unlike the initiation of adhesion of platelets exposed to the subendothelium, the formation of platelet aggregates is based on platelet-platelet and platelet-stimuli interactions. Activated platelets in turn release their stored granules, including α granules and dense granules to the plasma, which leads to a sudden increase in the local concentration of agonists necessary for atherosclerosis [22].

Collagen, adenosine diphosphate (ADP), Thromboxane A_2 (TxA_2), thrombin, and fluid shear stress can alter processes leading to platelet activation. Therefore, platelet activation cannot be determined solely by any one of these factors. The role of ADP in platelet activation has been studied broadly to identify its contribution to the process [23]–[26]. Platelet activation propagation away from the wall is attributed to ADP proteins, which are released by dense α granules from activated platelets [7]. So, ADP makes activation possible for platelets without direct contact with the vessel wall. Thrombin is separated from prothrombin through proteolysis during platelet activation. The role of thrombin in activation has been quantified [27], [28] and compared to collagen-induced activation by Nieuwenhuis et al. [29]. Platelet activation also stimulates formation of another aggregation agent that contributes to thrombus formation, thromboxane A_2 (TxA_2) with platelet signaling via the arachidonic pathway [28], [30], [31]. TxA_2 along with thrombin and ADPs bind to their specific receptors on the platelet membrane and activate those receptors [19].

2.2.3 Dependence on wall/fluid local shear rate

The contribution of interactions between specific adhesive receptors and soluble stimuli to thrombogenesis can be dependent on the blood flow conditions. Although the sequence of events associated with platelet adhesion, aggregation and activation may remain the same, their occurrence and intensity, as well as the interaction of contributing factors with each other can be highly dependent on the local blood flow characteristics [32]. The highly shear-dependent role of von Willebrand factor, as one of the most important adhesive glycoproteins, has been explained well by Weiss [33]. Effects of shear stress on role of vWf in platelet activation and thrombogenesis are extensively reviewed by Fogelson and Neeves [34]. Similar effects of shear stress magnitude and shear gradients on platelet deposition or resistance to shear are documented well in the literature [35]–[41].

2.3 Modeling thrombus formation

Collagen fibers and the integrin vWf on the vessel wall, and the integrins vWf, GPIb, GPVI, $\alpha_2\beta_1$, and $\alpha_{IIb}\beta_3$ on the platelet surface along with the soluble fibrinogen in plasma, mediate platelet adhesion to the subendothelium (see Figure 2.2). Platelets are also activated in the presence of ADP, TxA_2, and thrombin in sufficient concentration. Prothrombin and its derivative, thrombin (i.e. generated form prothrombin via proteolysis), and antithrombin (ATIII), which inactivates the coagulation process, should be considered together if modeled.

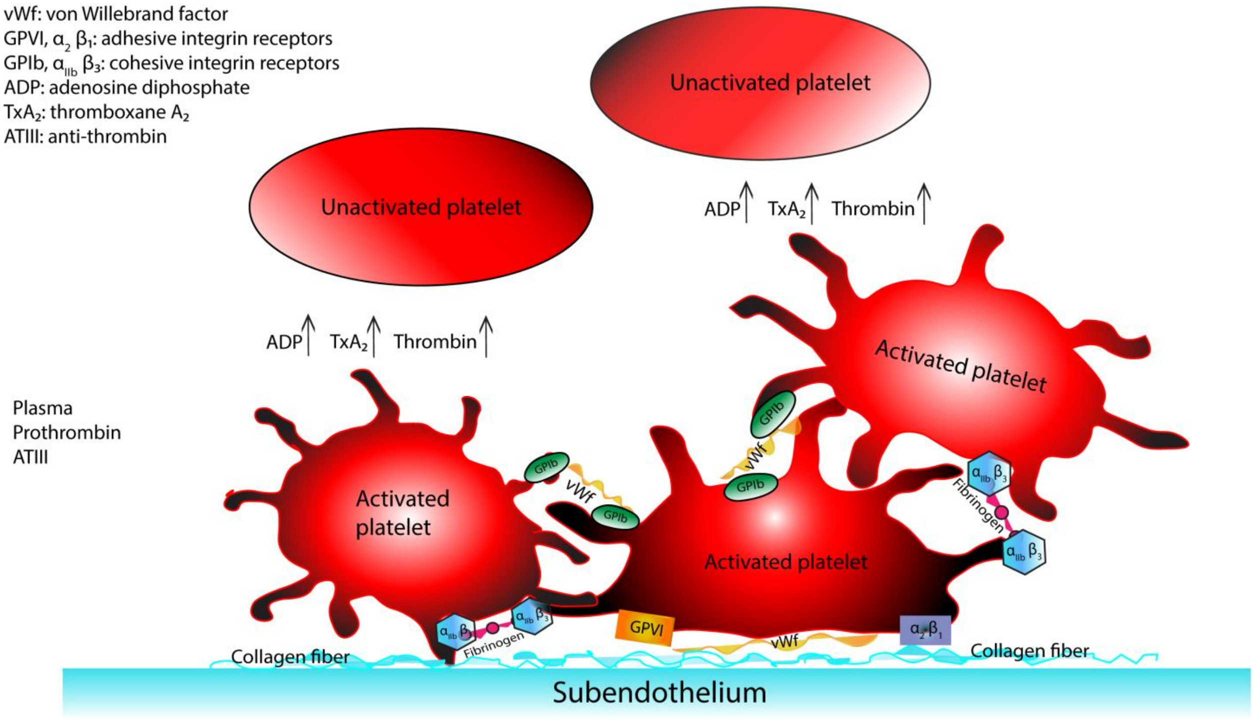

Figure 2.2 The platelet adhesion, activation, and aggregation mechanism. Unactivated platelets are discoid in shape whereas activated ones are spherical with sticky tethers. Unactivated platelets transform from low affinity to high affinity (activated) state upon contact with collagen fibers on subendothelium or if the concentrations of adenosine diphosphate (ADP), thrombin, or thromboxane A$_2$ are sufficiently high. ADP is secreted from platelets once activated, thrombin is generated from prothrombin through proteolysis, while antithrombin (existing in blood) inhibits the generation of thrombin. Platelet adhesion to collagen requires vWf, GPVI, and/or $\alpha_2\beta_1$ integrin receptors available on platelet membrane, whereas platelet-platelet cohesion occurs when the vWf multimer links two GPIb integrin receptors or fibrinogen links two $\alpha_{IIb}\beta_3$ receptors.

2.3.1 Blood components to be modeled

Amongst all blood components, the major elements that contribute to thrombus formation and growth include: resting platelets, activated platelets, fibrin (during red clot formation), von Willebrand factor (vWf), heparin, adenosine diphosphate (ADP) referred to as platelet-secreted agonist, thromboxane (TxA$_2$), prothrombin, thrombin, and antithrombin.

Platelet count in blood

When modeling platelets, depending on the animal from which the blood is collected, rates of platelet adhesion to vessel wall surface may be different not only due to difference in concentration of platelets in blood, but platelet type [42], [43].

Table 2.1 presents platelet count in the blood of different species. When simulating blood flow, these values are needed to impose the proper platelet concentration at the inlet boundary of the modeled domain. Dependence of platelet deposition on animal blood type was quantified for the first time by Grabowski et al. [44] using blood samples of human, pigs, dogs, and rabbit. The ratio of number of activated to resting platelets (i.e. level of background platelet activation) also could be different and has to be accounted for when modeling whole blood. This ratio can vary from 5% (1 activated platelet to 20 unactivated platelet) to 10% [45], [46].

Heparin

Heparin is a blood thinner agent and arrests blood clot formation after or before surgery. In many *in vitro* experiments the collected blood is heparinized to prevent clots before being circulated in the perfusion chamber. No significant change in platelet deposition results was reported with heparin levels lower than 1.4 $U.ml^{-1}$ [47].

Table 2.1 Platelet concentration and heparin levels used in experimental studies categorized by blood type

Blood type	Platelet count ($\times 10^6 \frac{PLT}{ml}$)	Heparin level	Whole blood/PRP	Ref.
Human	220 ± 7	1000-5000 IU	Whole blood	[48]
Human	364.15 ± 14.29	50 U/kg	Whole blood	[49]
Human	400	0	PRP*	[29]
Human	200	20 U/ml	PRP	[50]
Human	200	2 U/ml	Whole blood	[28]
Human	100-500	2.5 U/ml	PRP	[46]
Pig	324 ± 10-409 ± 14	1.37 U/ml	Whole blood	[47]
Pig	210 ± 74	3.5 IU/ml	Whole blood	[51]
Pig	200	0	PRP	[52]
Pig	291 ± 41-411 ± 58	1.26-1.78 U/ml	Whole blood	[53]
Pig	343.5 ± 82	0	Whole blood	[54]
Dog	300	0	PRP	[31]
Dog	193-430	0	Whole blood	[55]
Rabbit	204-338	100 U/kg	PRP	[56]
Rabbit	453 ± 101-479 ± 131	4 U/ml	Whole blood	[44]
Baboon	268 ± 28-301 ± 30	0	Whole blood	[9]
Baboon	246 ± 137-336 ± 35	4 U/ml	Whole blood	[44]

* PRP: Platelet-rich plasma

2.3.2 Platelet activation

Unactivated platelets in the plasma can transform to a high affinity (activated) state. This transformation takes place at a certain activation rate (k_{pa}). Biological and mechanical factors synergistically control the specific agonist secretion/synthesis pathways required for platelet activation. Computational methods for modeling of biological and flow-related factors are reviewed here. The highly shear-dependent role of von Willebrand factor, as one of the most important adhesive glycoproteins, has been shown and measured by Shankaran et al. [57], [58] and Westein et al. [59]. In flow conditions with shear rates lower than a critical threshold, adhesion of platelets takes place by mechanical pathways, such as diffusion, rather than chemical reaction kinetics [7], [60]. However, in high shear rates platelet adhesion to subendothelium is mediated by surface reactivity of platelets, which requires necessary amounts of vWf molecules [61]. Besides, the intensity of platelet adhesion to vWf-rich subendothelium is directly correlated with local shear rate. However, current computational models do not include vWf and are based on the assumption that the platelet activation occurs as a result of high concentrations of ADP, thromboxane A_2, and thrombin-related components or exposure to high shear stress.

2.3.2.1 Biological activation

Platelets can be stimulated by contact with molecules existing in plasma. Three major platelet activating agonists are ADPs, thrombin, and TxA_2. The critical concentration required for maximal platelet stimulation through biological pathways is 2 μM of ADP [62], 0.1-0.3 $U.ml^{-1}$ of thrombin [33], [63], [64], and 0.6 μM of TxA_2 [65]. TxA_2 is synthesized on platelet membrane as the platelet gets activated. Rate of synthesis of TxA_2 per platelet is $9.5 \times 10^{-12}\ nmol.s^{-1}$ [64]. Activated platelets also release a certain amount of the agonist adenosine diphosphate (ADP) from dense α granules during activation. This amount per platelet is $2.4 \times 10^{-8}\ nmol$ as reported by Adams and Feuerstein [66]. A continuum model that considered ADP as the sole stimulatory agonist was developed by Fogelson [67]. As an extension to Fogelson's model, platelet activation rate based on concentrations of the aforementioned agonists in plasma was defined by Sorensen et al. [68] as:

$$\begin{aligned} k_{pa} &= 0, && \Omega < 1 \\ k_{pa} &= \frac{\Omega}{t_{act}}, && \Omega \geq 1 \end{aligned} \tag{2.1}$$

where Ω is the activation function:

$$\Omega = \sum_{j=1}^{3} w_j \frac{[a_j]}{[a_{j,crit}]} \tag{2.2}$$

In Eqs. (2.1) and (2.2), t_{act} is the characteristic time constant for platelet activation; $[a_j]$ is the concentration of jth agonist; $[a_{j,crit}]$ is the threshold concentration of that agonist for platelet activation; and w_j is the agonist-specific weight to differentiate between weak and strong agonists. The glycoprotein IIb/IIIa signals platelet activation and incipient aggregation. According to [23], [62] and [69], expression of receptors of this glycoprotein takes place within 1-3 s. This duration roughly manifests the activation time t_{act}. A later study [70] showed that platelet shape change due to activation, adhesion and secretion starts within 1 s and is complete around 5s.

The inherent limitation of Sorensen's model (Eq. (2.2)) is the step function platelet activation assumption, which does not reflect the real behavior of platelets. Platelet activation is a gradual process and the time scale corresponding to 10-40% activation exposed to physiological shear conditions can be as high as 30 min [71]. Due to its discontinuous character, the application of Eq. (2.2) in numerical schemes can be difficult and stability issues associated with sudden increase/drop in platelets concentration can be introduced.

2.3.2.2 Shear-induced activation and exposure time

The other independent pathway for platelet activation is the shear-induced mechanism by which platelets experiencing high shear stress (>500 s^{-1}) for a certain exposure time get activated regardless of concentrations of platelet activating agonists [34], [72]. Several models are developed based on the underlying physics to predict the shear-induced platelet activation. Hemodynamic shear has been shown to stimulate platelets and endothelial cells and activate platelets [73]. Experimental studies suggest that lower shear rates (with platelet exposure times of 0.075-3.3.045 s) are not sufficient to activate platelets [74]. A shear rate magnitude of 5000 s^{-1}

and 3000 s^{-1} were used in [75] and [76] as a minimum threshold required for shear-induced platelet activation. However, more recent studies include residence/exposure time of platelets and differentiate between different components of shear rate. Purvis Jr and Giorgio [77] calculated the elongational rates of deformation in shear rates of 1390-4167 s^{-1}.

Shadden and Hendabadi [78] developed a model to predict the potential regions for platelet activation in stenosed vessels with peak inlet and throat Reynolds numbers of 142 and 340. The activation potential (AP) α for a platelet at position $x_0 = x(t_0)$ at time t_0 is defined as follows:

$$\alpha(x_0, t_0; t) = \int_{t_0}^{t} \parallel e(x(s), s) \parallel_F ds \tag{2.3}$$

where $x(s)$ is evaluated along the platelet trajectory and e denotes the deformation tensor. This model shows maximum activation potential near the apex of stenosis which explains why thrombus initially forms there (see Figure 2.3). In this method the principal rates of deformation, hence principal stresses, are integrated along the platelet trajectory with the platelet modeled as a fluid element. It is assumed that platelet activation occurs solely through fluid mechanics' pathways. Moreover, the equations of rigid particle motion from [79] have been used when implementing this model. Therefore, two limitations are associated with this model: its application is limited to laminar flow conditions; and it is valid only for dilute suspensions of platelets where they do not collide with each other and vessel walls.

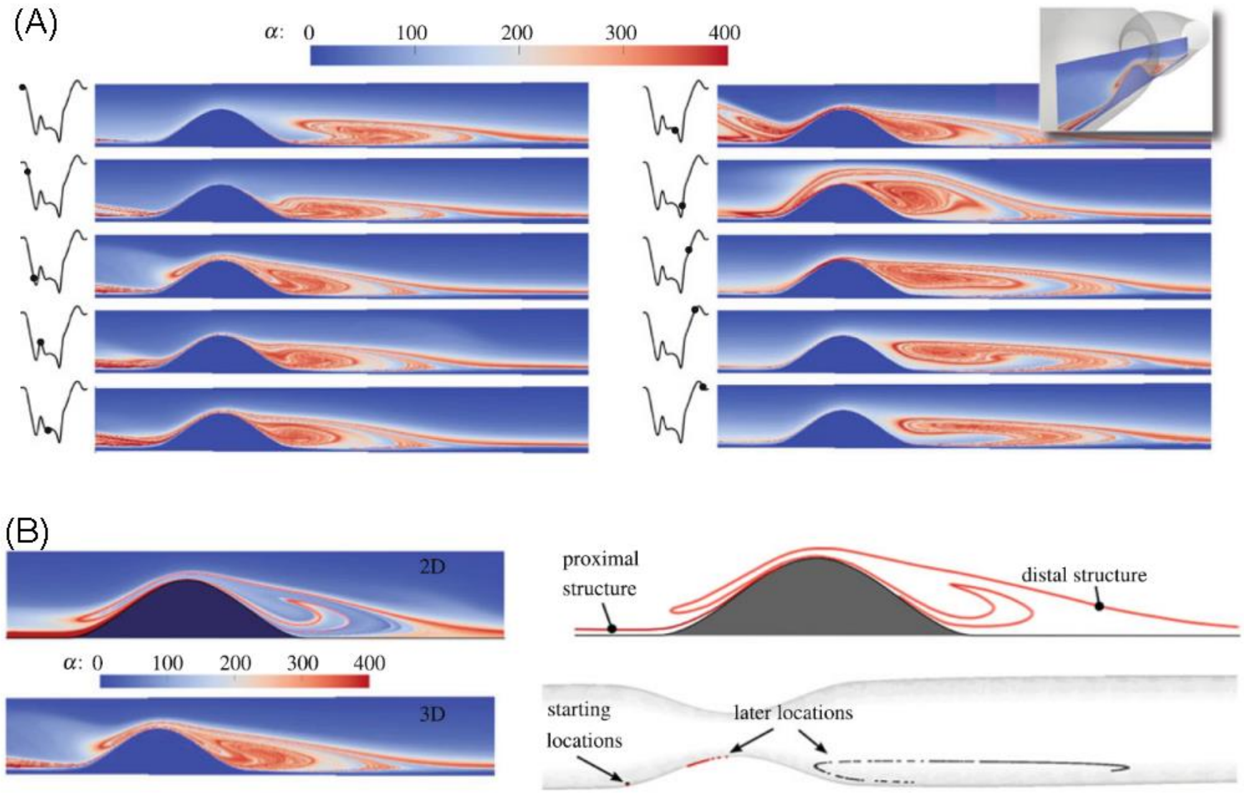

Figure 2.3 A) Instantaneous Activation Potential (AP) field near the stenosis in different phases of cardiac cycle; B) Comparison of AP field in 2D with 3D stenosed tube. The proximal structure is dominated by shear but also separates flow that accumulates near the apex, as shown for the 3D simulation in the bottom row. The starting locations of two groupings of particles (appearing as one point due to their proximity) are initially divided by the proximal structure in 3D AP field (bottom left). The later locations are plotted after 1 cardiac cycle of time had elapsed. Images are reprinted from Shadden and Hendabadi [78] and with permission from Springer.

Cao and Rittgers [80] measured the residence time of Amberlite particles (1.05 g.cm^{-3}, 400 µm, 80.ml^{-1}) representing platelets in stenosed regions of arteries (75% and 95%). The experiment was set up *in-vitro* with pulsatile inlet waveforms similar to those in the internal carotid artery (ICA) and the left anterior descending (LAD) coronary artery with peak inlet Reynolds number of Re = 94-734. A particle washout profile index (PWPI) was defined as the number of particles present in diastolic flow region at each cardiac cycle by the number of particles at the end of first cycle. PWPI measurements over 10 cycles were correlated with the cycle number with an exponential curve fit:

$$PWPI(T) = Ae^{-\beta T} \tag{2.4}$$

where T is the cycle number. Also the critical particle washout cycle (where PWPI<0.01) was determined for each experimental case.

Experimental measurements of serotonin release, as an indicator of platelet activation, show that a certain combination of shear stress and exposure time results in platelet activation [81]. An activation level of ~90 dyne$^{2.3}$s.mm$^{-4.6}$ for shear was used by Goodman et al. [82] based on the experimental data collected by Hellums [83]. The relationship reads as:

$$\tau^{2.3}t = \int_0^T \tau^{2.3}dt = \int_{s_1}^{s_2} \frac{\tau^{2.3}}{v} ds \tag{2.5}$$

where τ is the shear stress, and s is the distance from s_1 to s_2 along the streamline, and v is the velocity. An alternative threshold for platelet activation has been introduced in [84] for mural thrombosis modeling in arterial stenosis using the equation:

$$\dot{\gamma}t = \int_0^T \dot{\gamma}dt = \int_{s_1}^{s_2} \frac{\dot{\gamma}}{v} ds \tag{2.6}$$

where $\dot{\gamma}$ is the local fluid shear rate (s^{-1}). Tambasco and Steinman (2003) employed this model for the threshold level of activation (105 dyne.cm^{-2}). Figure 2.4 depicts the results for transit times of Lagrangian fluid elements (LFEs) over 8 cardiac cycles in 30% eccentric and concentric stenosed carotid bifurcations. A power-law equation was fit by Goodman et al. [82] to data from [83]. It was demonstrated that the time required for surface-adherent platelet activation as a function of shear stress was:

$$t = 4.0 \times 10^6 \tau^{-2.3} \tag{2.7}$$

where τ is the shear stress experienced by the platelet.

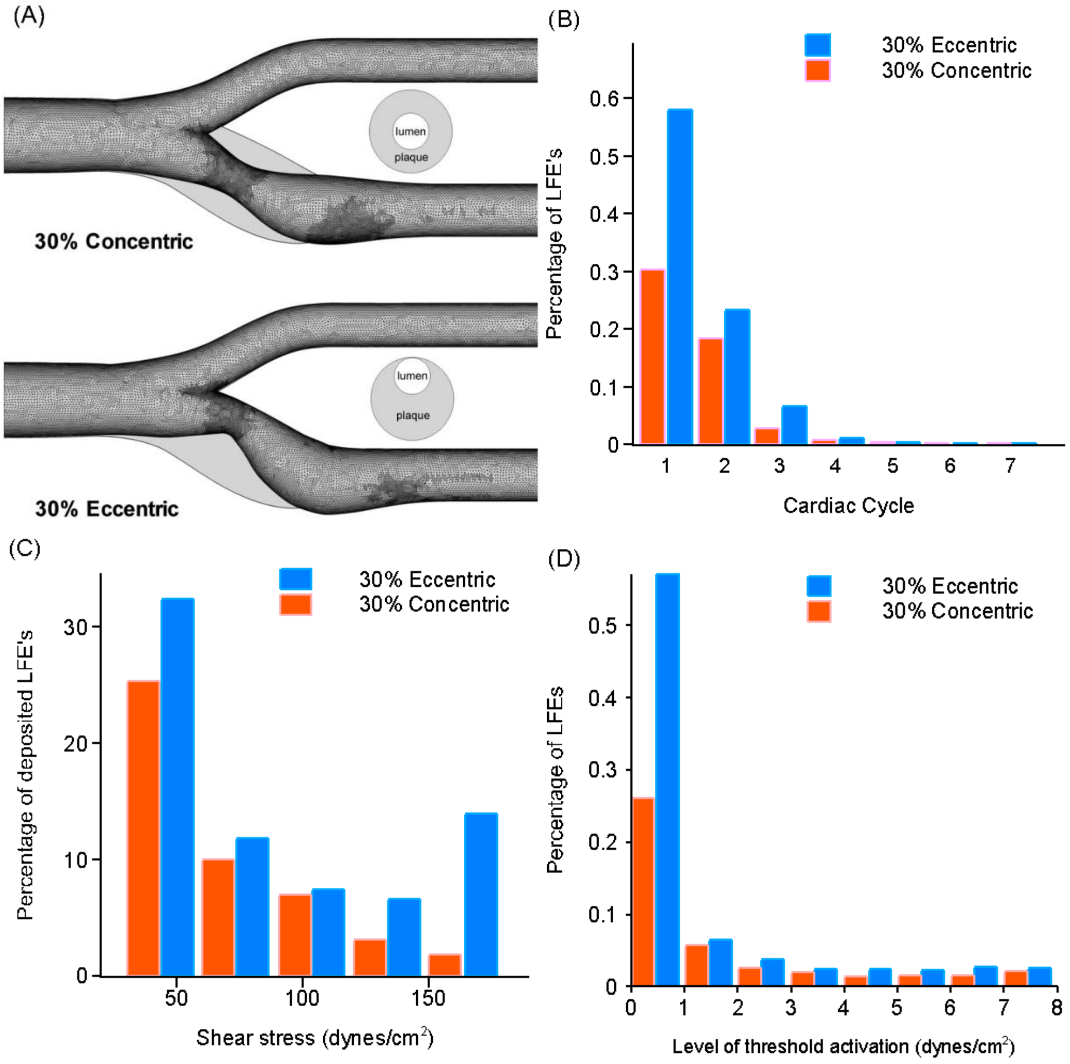

Figure 2.4 (A) Geometries of modeled eccentric and concentric stenoses. Image is reprinted from Tambasco [85] **and with permission from Springer; (B) Transit times for the subset of Lagrangian fluid elements (LFEs) exposed to a shear stress above 105 dyne.cm^{-2}. There are more shear-exposed particles in the eccentric compared to the concentric model; (C) Percentage of LFEs as a function of the maximum shear stress exposure they experienced along their trajectories. The percentages of LFEs exposed to maximum shear stresses above 30 dynes/cm^2 are higher for the eccentric model vs. concentric model; (D) Percentage of LFEs that experienced nonzero levels of threshold activation (LTA). The relative distributions of LTA are broadly consistent with those for the transit times of shear-exposed LFEs shown in Fig 2.4(B).**

These models give an estimation of shear-induced activation; however they are not able to capture the effects associated with shear gradient as well as shear history of platelets along their path. As a result, more complicated models are developed that account for dynamic conditions experienced by platelets.

Similar to the power-law based formulation of shear-induced hemolysis level [86], Soares et al. [87] proposed a novel model redefining the original power law equation:

$$PAS(\tau, t) = C\tau^{\alpha} t_{exp}^{\beta} \tag{2.8}$$

where $PAS(\tau, t)$ is the platelet activation state parameter, t_{exp} is the exposure time of platelet subjected to shear stress, and the constants C, α, and β were optimized for PAS by minimizing the discrepancy between experimental data and Eq. (2.8). Sheriff et al. [88] adapted the cumulative power law (CPL) model originally developed by Grigioni et al. [89], [90]. They expanded Eq. (2.8) to include the dynamic aspect of platelet activation:

$$PAS_{CPL}(\tau(t), t) = C_1 \int_{t_0}^{t_{total}} \beta\tau(t)^{\alpha} t^{\beta-1} dt + C_2 \int_{t_0}^{t_{total}} \alpha\tau(t)^{\alpha-1} t^{\beta} \frac{|d\tau(t)|}{dt} dt + PAS(t_0) \tag{2.9}$$

where C_1, C_2, α, and β were found based on experimental data obtained for both steady and pulsatile conditions (oscillating frequencies of 0.78-6.25 Hz). This model has been shown to describe activation well for exposure times of 0-4 min and shear stresses of 1-70 dyne.cm^{-2} and shear rate peaks of 188-1500 s^{-1} (over 4 min) for oscillating cases.

One of the shortcomings of methods based solely on shear rates is the complete neglect of biological factors involved in shear-induced platelet activation. Several studies suggest that ADP [91]–[94], vWf [36], [37], [95], and thrombin-related blood components [28], [64], [96]–[98] or combination of these elements have roles in shear-induced activation both in platelet-rich plasma (PRP) and whole blood.

2.3.3 Platelet margination

Flowing blood segregates to two regions which are different in their composition; RBC-depleted (or platelet-rich) area and near-center region where RBCs are concentrated [99], [100]. This phenomenon is referred to as platelet margination. The antimargination of RBCs in small vessels (10–500 μm) leads to reduced hematocrit and apparent viscosity [101]. Methods for computational modeling of platelet margination are reviewed here. A coarse-grained model of erythrocyte hydrodynamics in a Couette flow [102] suggests that the thickness h of the RBC depleted zone thickness scales as $h \sim \phi^{-1/2}$ (Figure 2.5), where ϕ is the hematocrit:

$$h \sim \left(\frac{S_{zz}}{\mu\dot{\gamma}a^2}\right)^{1/2} \phi^{-1/2} \tag{2.10}$$

In Eq. (2.10), S_{zz} is the particle stresslet (i.e. force dipole), μ is the external viscosity, a is the equivalent particle radius of RBC, and $\dot{\gamma}$ is the wall shear rate.

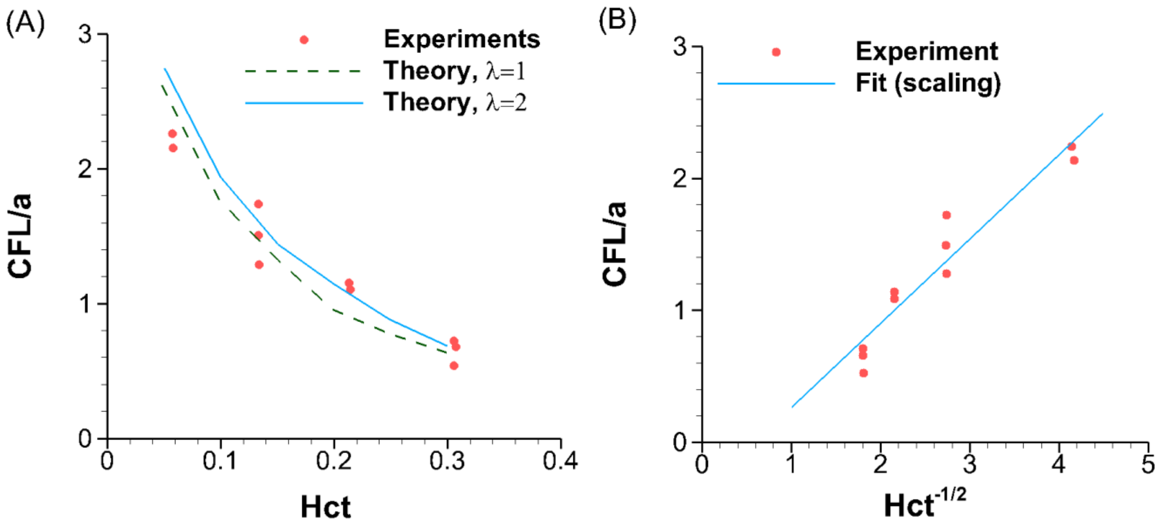

Figure 2.5 Comparison between experimental data (in-vitro) and the coarse-grained theory: cell free layer thickness (CFL) vs. Hematocrit (Hct). Two capillary numbers are introduced in the model based on the bending forces and the shear elasticity of the cell membranes: Ca_B, the ratio of the viscous shear stresses to bending forces; and Ca_s that is the ratio of viscous stresses to shear elastic forces (A) Comparison with Bugliarello et al. [103]. In experiments, the flow capillary number (Ca_s) varies from 0.4 to 1.6, and the channel height is H/a = 14.3. The plot from the theory is for Ca_s = 1, and channel height H/a = 14. λ is the viscosity ratio between the interior fluid and exterior fluid of the modeled red blood cell. (B) Comparison between experiments and Pries scaling relation CFL~Hct $^{-1/2}$ as predicted by theory [102]. **Fahraeus effect for human and rat blood was corrected by Narsimhan et al. [102], because the tube hematocrit is smaller than the feed hematocrit to satisfy the mass conservation.**

To model the near-wall platelet excess, induced by RBCs, a skewed inlet platelet concentration is used along with variable platelet diffusivity. A quadratic inlet profile for concentration of platelets is suggested by Wagner [104] as follows:

$$C_p(y) = \begin{matrix} C_0, & |H-y| \leq H - L_b \\ C_0\left(1 + A\dfrac{(|H-y| - H + L_b)^2}{L_b^2}\right) & \end{matrix} \tag{2.11}$$

where y is the normal distance from the wall, H is the channel half width, L_b is the excess-platelet boundary layer thickness, and C_0 is the concentration of platelets outside the boundary layer, and A is the augmentation constant. $A = 5.6$ is applied by Sorensen et al. [68] in channel flow simulations.

For platelets in platelet-rich plasma (PRP) it can be assumed that they diffuse in plasma solely due to their Brownian motion ($D_{b,PLT}$). However, in whole blood the diffusion coefficient of platelets can be dramatically augmented (up to 3 orders of magnitude) due to margination [105]. This effect, referred to as the shear-enhanced or the shear rate-dependent mass diffusivity of platelets [106], is formulated by [107] as follows:

$$D_s = 0.18.\, R_{RBC}^2.\, \dot{\gamma} \tag{2.12}$$

where R_{RBC} denotes the radius of the red blood cell and $\dot{\gamma}$ is the local fluid shear rate. The total diffusivity of the platelet is then given as:

$$D_{PLT} = D_{b,PLT} + D_s \tag{2.13}$$

Keller's model does not correlate diffusivity with hematocrit. However, platelet accumulation on subendothelium can be 57-fold higher in whole blood than in a suspension of platelets alone and increases with increasing hematocrit [108]. To account for effects of hematocrit on platelet diffusivity, a generalized correlation has been suggested by Antonini et al. [109] for application in an arbitrary-dimensional frame-invariant setting:

$$D_s = 0.18\, R_{RBC}^2\, \sqrt{tr\varepsilon^2} \tag{2.14}$$

where $tr\varepsilon^2$ is the second invariant of the rate of strain tensor. An alternative empirical formulation for enhanced diffusivity of platelets is proposed by [110] for the enhanced diffusivity of platelets in whole blood as follows:

$$D_s = 0.15 R_{RBC}^2.\, \dot{\gamma}.\, HCT(1 - HCT)^n \tag{2.15}$$

where HCT denotes the volume fraction of red blood cells in blood suspension (hematocrit), $\dot{\gamma}$ is the local shear rate, n is a constant at 0.8 ± 0.3, and R_{RBC} is the volume based equivalent spherical radius of a red blood cell. Figure 2.6 shows the results for axial distribution of platelet flux obtained using the Zydney and Colton model in stenosed tubes [111].

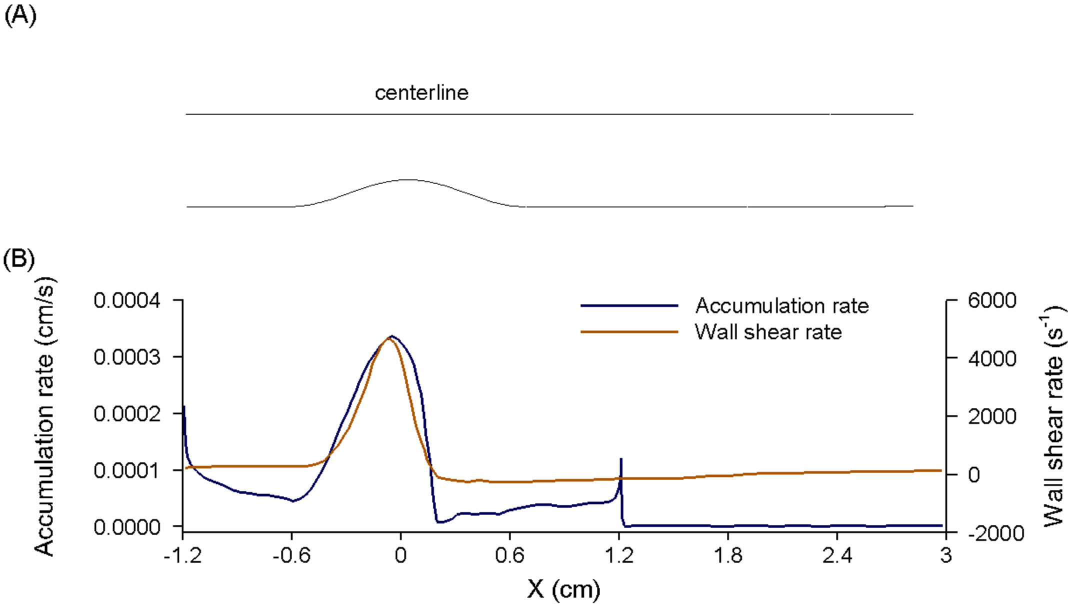

Figure 2.6 (A) Model geometry; (B) axial distributions of platelet accumulation rate and wall shear rate in stenosed (75% area reduction) collagen-coated tube. Platelet accumulation rate is not proportional to wall shear rate, but the location of highest accumulation rate was close to the location of maximum shear rate, and the minimum accumulation rate occurred near the separation point [111].

Another approach to model the whole blood as a continuum was introduced by Mehrabadi et al. [112]. They extracted effective diffusivity profile (see Figure 2.7) based upon their direct numerical simulation (DNS) solution and used it in their species transport equation as the coefficient of diffusion.

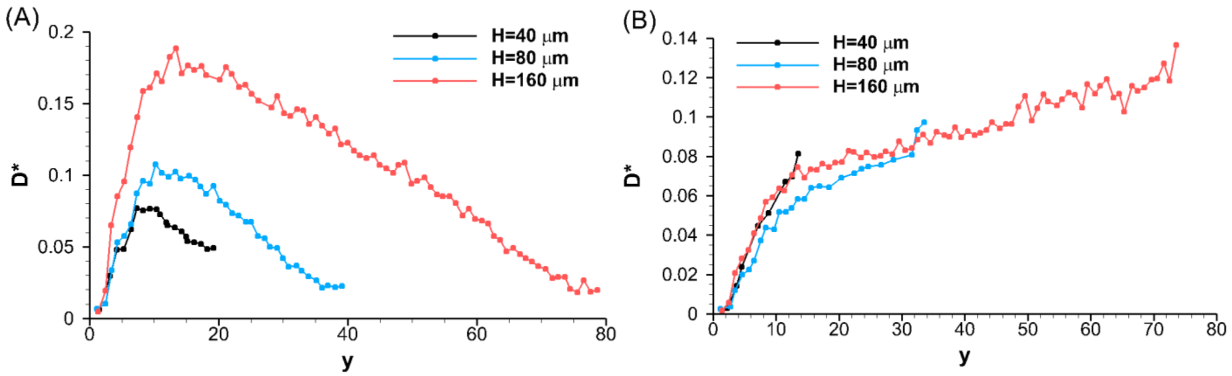

Figure 2.7 Cross-channel profiles of platelet effective diffusivity D_{yy} calculated from DNS platelet trajectories at various channel heights H. Effective diffusivity is normalized by (A) average shear rate $\dot{\gamma}_{ave}$ and (B) by $a^2 \times \dot{\gamma}(y)$ where a is platelet effective radius and $\dot{\gamma}(y)$ is local shear rate (Mehrabadi et al. [112]).

Another approach suggested by [113] uses the local fluid shear, Peclet number $Pe = a\dot{\gamma}/D_s$ based on the particle radius a, and the effective diffusivity of the solute in the stagnant suspension D_s to calculate the augmentation of the transport of extracellular solutes. Augmentation (%) is defined as:

$$A = \frac{D_e - D_s}{D_s} \times 100 \tag{2.16}$$

where D_e is the effective diffusivity. It was shown that the augmentation in suspensions of human and bovine erythrocytes increases with shear rate, hematocrit, cell size, and cell rigidity (see Figure 2.8). For normal cells at 40% hematocrit A can be calculated with Eq. (2.17).

$$A = 6.1\, Pe^{0.9} \tag{2.17}$$

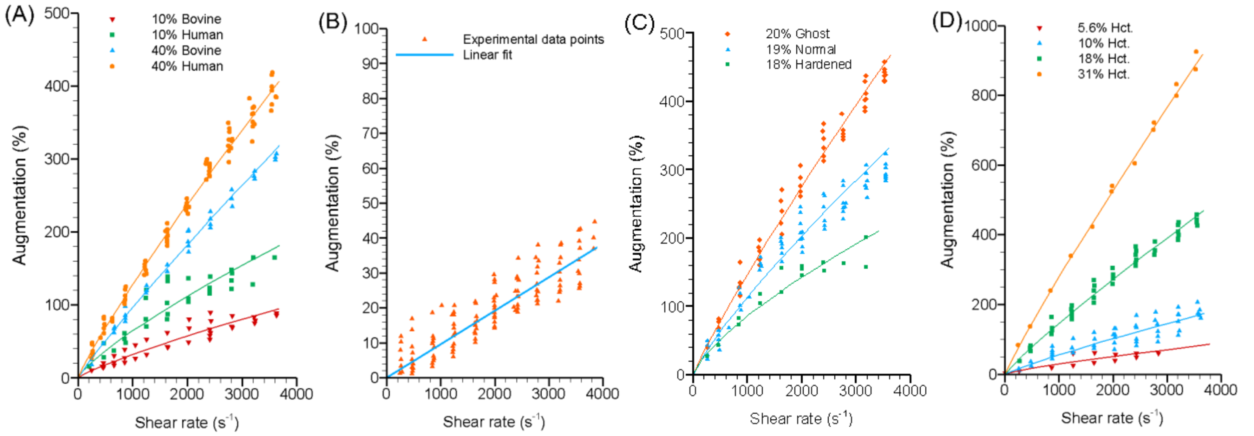

Figure 2.8 Results from Wang and Keller [113] demonstrate the effect of A) blood type and hematocrit, B) shear rate, C) cell rigidity, and D) hematocrit on platelet diffusivity augmentation.

2.3.4 Blood viscosity

Is blood a non-Newtonian shear-thinning fluid?

There are three distinct shear rate ranges for blood viscosity: low shear region where blood can be considered Newtonian, viscosity is constant and can be as high as 16-56 mPa.s [114], [115]; middle (shear-thinning) region where the apparent viscosity decreases with increasing shear rate [116]; high shear region where blood behaves Newtonian and viscosity values can be as low as 1-4.76 mPa.s [117], [118]. At shear rates around 50 s^{-1} changes in hematocrit can cause large variations in blood viscosity; but at higher shear rates, the whole blood is a Newtonian fluid and viscosity can be approximated by a constant rather than shear-proportional [119], [120]. The threshold shear rate above which the blood viscosity is constant is reported ~100-300 s^{-1} at hematocrit of 45% [116], [121], [122]. Several models are developed to model the non-linear behavior of blood viscosity under different conditions. Table 2.2 lists some of commonly used non-Newtonian viscosity models.

Table 2.2 Non-Newtonian viscosity models used in the literature to model blood flow

Model	Shear-dependent viscosity	Comments
Power Law	$\mu = p.(\dot{\gamma})^{n-1}$	Works well only for shear-thinning region [123]
$p = 14.67\ \mathrm{mPa.s^n}$ and $n = 0.7755$ [124]		
Carreau	$\mu = \mu_\infty + (\mu_0 + \mu_\infty).[1 + (\lambda\dot{\gamma})^2]^{(n-1)/2}$	Matches experimental observations for shear rates of 0.05-100 s^{-1} [125]
$\mu_\infty = 0.0345$ poise, $\mu_0 = 0.56$ poise, $\lambda = 3.313$ s, $n = 0.3568$ [126]		
Carreau-Yasuda	$\mu = \mu_\infty + (\mu_0 + \mu_\infty).[1 + (\lambda\dot{\gamma})^p]^{(n-1)/p}$	Includes two-phase properties of blood [127]–[129]
$\mu_\infty = 1\ \mathrm{mPa.s}$, $\mu_0 = 12\ \mathrm{mPa.s}$, $\lambda = 0.086$ s, $n = 0.681$, $p = 0.222$ [118]		
Ballyk (Generalized Power Law)	$\mu = \lambda(\dot{\gamma}).\dot{\gamma}^{n(\dot{\gamma})-1}$ $\lambda(\dot{\gamma}) = \mu_\infty + \Delta\mu.\exp[-(1 + \lvert\dot{\gamma}\rvert/p_1)\exp(-p_2/\lvert\dot{\gamma}\rvert)]$ $n(\dot{\gamma}) = n_\infty + \Delta n.\exp[-(1 + \lvert\dot{\gamma}\rvert/p_3)\exp(-p_4/\lvert\dot{\gamma}\rvert)]$	Predicts the distribution of wall shear stress better in low shear regions. It encompasses the Newtonian model at middle range and high strain (~200 s^{-1}), and the Power Law model for low strain. [126], [130]
$\mu_\infty = 0.0345$poise, $\Delta\mu = 0.25$ poise,$p_1 = 50$, $p_2 = 3$, $p_3 = 50$ and $p_4 = 4$ [126]		
Casson	$\mu = \left[(\eta^2.J_2)^{1/4} + 2^{-1/2}.\tau_y^{1/2}\right]^2.J_2^{-1/2}$ $\tau_y = 0.1(0.625\varepsilon_{RBC})^3$ $\eta = \mu_0(1 - \varepsilon_{RBC})^{-2.5}$	Predicts wall shear stress magnitudes better in oscillatory flows compared to Newtonian and Power Law models. (Casson, 1959; Neofytou and Tsangaris, 2006)
$J_2 = \frac{1}{2}\dot{\gamma}^2$, $\tau_y = 0.1(0.625\varepsilon_{RBC})^3$, $\eta = \mu_0(1 - \varepsilon_{RBC})^{-2.5}$, $\mu_0 = 0.012$ poise, $\varepsilon_{RBC} = 0.37$ [132]		
Herschel-Bulkley	$\mu = p.(\dot{\gamma})^{n-1} + \tau_y/\dot{\gamma}$	Demonstrates close agreement with experimental data for prediction of pulsatile flow in stenosed arteries (Picart et al., 1998; Herschel and Bulkley, 1926)
$p = 8.9721\ \mathrm{mPa.s^n}$, $n = 0.8601$, $\tau_y = 0.0175\ \mathrm{N/m^2}$ [134]		
Quemada	$\mu = \sqrt{\mu_\infty} + (\sqrt{\tau_y})/(\sqrt{\lambda} + \sqrt{\dot{\gamma}})$	Includes the yield stress τ_y in addition to fluid shear rate [120].
$\mu_\infty = 0.02982\ \mathrm{dyne.s/cm^2}$, $\tau_y = 0.2876\ \mathrm{dyne/cm^2}$, $\lambda = 4.02\ s^{-1}$ [135]		
Walburn-Schneck	$\mu = p_1.e^{p_2\varepsilon_{RBC}}.e^{p_4(TPMA/\varepsilon_{RBC}^2)}.(\dot{\gamma})^{-p_3\varepsilon_{RBC}}$	Includes TPMA (i.e. composed of fibrinogen and globulin) level in addition to cell concentration [136].
$p_1 = 50$, $p_2 = 3$, $p_3 = 50$ and $p_4 = 4\ g^{-1}$, $\varepsilon_{RBC} = 40\%$, $TPMA = 25.9\ g.l^{-1}$ [126]		

During a cardiac cycle the local fluid shear rate varies from zero to 1400 s^{-1} [137], [138]. Therefore, when simulating an unsteady/pulsatile flow under realistic conditions there are periods that the blood should be modeled as a non-Newtonian fluid (see Figure 2.9).

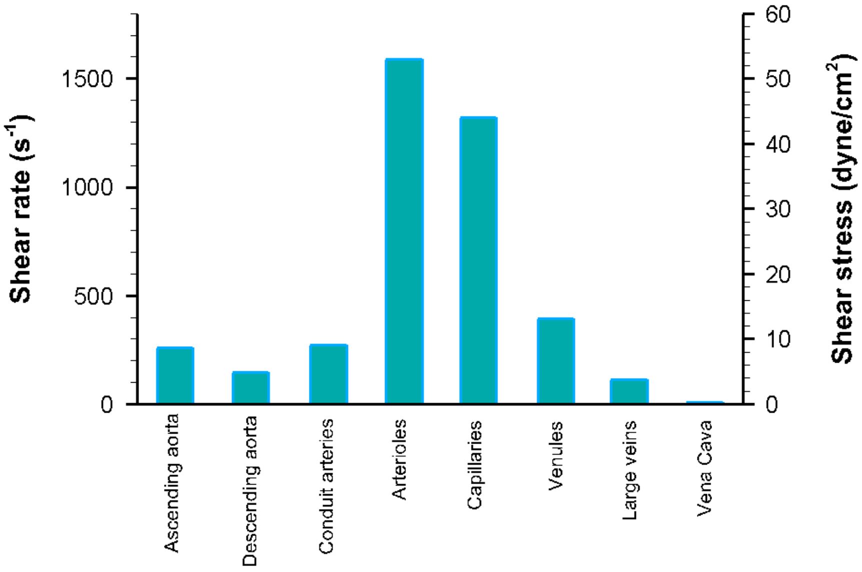

Figure 2.9 Shear rates and corresponding shear stress values in various vessels During a cardiac cycle the local fluid shear rate varies from zero to 260 s^{-1} in the ascending aorta, 148 s^{-1} in descending aorta, 274 s^{-1} in conduit arteries, 1591 s^{-1} in arterioles, 1322 s^{-1} in capillaries, 396 s^{-1} in venules, 113 s^{-1} in large veins, and 9 s^{-1} in vena cava [137], [138].

2.3.5 2.3.5. Surface specificity of platelet adhesion (flux terms)

In arterial thrombosis two factors at the wall boundary determine the extent of thrombus growth: geometry (or stenosis degree), and surface material properties of the thrombus [139].

2.3.5.1 Material

Collagen can activate platelets upon surface contact [140]. Rosing et al. (1985) determined the collagen concentration of 0.5 and 1.2 nmol.L^{-1} respectively for threshold and maximal effect of collagen required for activated platelet aggregation and release. Collagen proteins include several types; however five of them (types I, III, IV, V and VI) are present in the vessel tissues [7], [142]. Platelets can mainly adhere to collagen (types I, III, IV) or to von Willebrand molecules found in collagen. Table 2.3 gives the surface material, geometry and flow characteristics of experiments investigating thrombus formation and growth. Experimental results of these studies provide insightful data that can be used for validation of computational models of embolization, platelet adhesion, aggregation, and activation.

Table 2.3 Surface material, geometries, and flow characteristics of thrombosis models

Surface	Geometry	Model	Reynolds number	Wall shear rate (s^{-1})	Perfusion time (min)	Ref.
Collagen	Parallel plate	In vitro human	0.1-3	100-1500	1-5	[143], [144]
Collagen I	Tubes	Ex vivo baboon	150-300	265-2120	20-120	[145]
Collagen I	Stenoses	Ex vivo baboon	150	0-20000	20-120	[145]
Collagen I	Parallel plate	In vitro human	1	1000	1.25	[28]
Collagen III	Parallel plate, 2D stenosis	Ex vivo human	2-40	210-2600	5	[72]
Collagen III, Thermanox	Stenosed parallel plate	Ex vivo human	20	450-32000	5	[74], [146]
Collagen and Teflon	Expansion	Ex vivo human	66	0-750	60-120	[9]
Collagen I, III, IV, V, ECM	Parallel plate	In vitro human	-	300,1600	5	[50]
Collagen I	Stenosed tube	In-vitro human	160	265-22000	15	[111]
Collagen I	Stenosed tube	In-vitro pig	1.2-2.3	200-100000	280 seconds	[51]
Collagen	Stenosed tube	In-vitro pig	3.6-72	3800-16000	5	[147]
Collagen I	Stenosed tube	In-vitro pig	21	130-347000	10	[148]
Tunica media	Stenosed tubes	Ex vivo pig	30-180	212-33500	1-30	[47]
Tunica media	Stenosed tubes	Ex vivo pig	60	424-50000	10	[49]
Injured artery	Stenosis	In vivo dog	113-233	13000-82000	-	[55]
Injury artery	Stenosis	In vivo dog	80	300-53000	-	[149]
Human atheroma	U channel	Ex vivo pig	60	1690	5	[150]
ePTFE with ECs, collagen, fibronectin	Tubes	Ex vivo baboon	64	106	60	[151]

2.3.5.2 Effect of stenosis

Effect of stenosis, stent, and grafts is well documented in both laminar and turbulent flows. Effect of shear stress on platelet deposition in stenosed vessels has been investigated ex-vivo [47], in-vitro and in-vivo [53] to reveal the relationship between wall/local shear rate and distribution of platelet deposition on severely injured vessels. It has been shown that the apex of a stenosis is the most susceptible region for platelet deposition, hence thrombus formation. Platelet deposition in stenosed regions can be also enhanced by hydrodynamic interactions with red blood cells even with a hematocrit as low as 10% [152]. Most of the experimental and numerical investigations of platelet deposition in stenosed vessels suggest that the highest level of platelet accumulation occurs near the stenosis apex [41], [49], [51], [53], [55], [140], [145], [147], [153]–[158]. However, results from a few *in-vitro* studies showed highest deposition in regions distal and proximal to the throat and least deposition at the apex [59], [84], [112], [148], [159] due to embolization (i.e. detachment of platelet aggregates from apex). The higher deposition in these regions is attributed to high wall shear stresses and can be modeled by using a general shear-dependent equation for platelet-wall adhesion rate [160]:

$$Da = Da_0 + \alpha\tau \tag{2.18}$$

In Eq. (2.18), τ is the nondimensional shear stress at the wall, Sh_0 and α are arbitrary constants determined based on experimental data. The ratio of surface reactivity to platelet diffusivity is measured by the platelet Damkohler number (Da):

$$Da = \frac{kL}{D_{PLT}} \tag{2.19}$$

where k is the dimensional adhesion rate (in m.s^{-1}), and D_{PLT} denotes the platelet effective mass diffusivity (in m^{2}.s^{-1}), and L_{ref} is the characteristic length. Sorensen et al. [68] showed that increasing the platelet adhesion rates leads to a transition from an adhesion-limited regime (Da≈1) to a diffusion-limited regime (Da≈100). A common hypothesis is that utilizing a shear-dependent diffusion coefficient can yield augmented deposition in regions with high wall shear rates. A simplified model of platelet deposition in stenosed tubes was proposed by Wootton et al. [111]. Species transport equation was solved for platelets in which the mass diffusivity of platelets was assumed to be a function of wall shear rate based on Zydney and Colton's formulation (2.15). Based on Fick's second law, mass flux as a linear function of platelet concentration at the surface was defined as the boundary condition:

$$D_e \left.\frac{\partial c}{\partial n}\right|_{wall} = j(x) = k_t c_0(x) \tag{2.20}$$

where k_t is the adhesion rate constant ($\sim 5 \times 10^{-3}\ cm/s$) and c_0 is the concentration of platelets at the surface. An alternative analytical equation used by Bark and Ku [158] for platelet deposition flux is the Leveque model:

$$J_{PLT} = \frac{\bar{c}_{PLT}}{\dfrac{1}{k_t} + \dfrac{1.86}{\left(\dot{\gamma}\,\dfrac{D_{PLT}^2}{x}\right)^{1/3}}} \tag{2.21}$$

where k_t is the kinetic platelet binding rate, $\bar{c}_{PLT}$ is the average platelet volume fraction, x is the axial dimension along the stenosed length, $\dot{\gamma}$ is the local wall shear rate and D_{PLT} denotes the effective platelet diffusivity enhanced by the presence of RBCs. Eq. (2.21) does not take the non-uniform distribution of platelets or red blood cells into account. Therefore, a non-uniform platelet concentration should be imposed at the inlet along with the Leveque model to mimic the platelet margination.

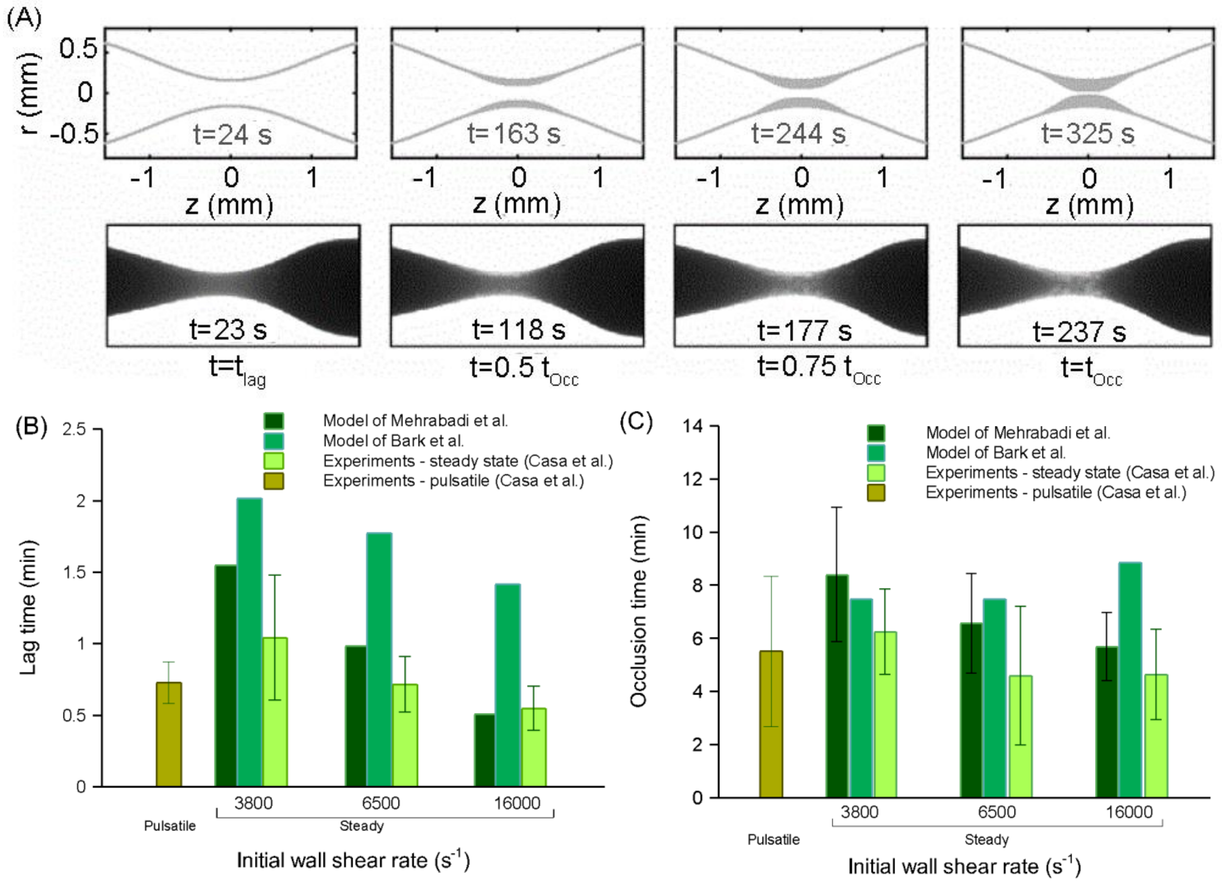

Figure 2.10 Modeling results in stenosed glass capillary from Mehrabadi et al. [148] and Casa and Ku [147]: (A) Modeling results of thrombus formation in stenosed region (top) and experimental SEM images (bottom) at initial wall shear rate of 16000 s^{-1} at lag time and 50, 75 and 100% of occlusion time (experimental images (bottom) are reprinted from Casa and Ku [147] with permission from Springer and numerical results (top) are reprinted from Mehrabadi et al. (2016) with permission from Elsevier); (B) predicted lag times for pulsatile and steady flows; (C) occlusion times in capillaries compared to experimental measurements in whole porcine blood flow.

A correlation proposed by Mehrabadi et al. [148] based on experimental measurements predicts the thrombus growth rate ($\dot{R}$) as a function of time and wall shear rate:

$$\dot{R}(t,\dot{\gamma}_w) = \begin{cases} 0 & \text{if } t < t_{lag}(\dot{\gamma}_w), \\ ae^{b\dot{\gamma}_w} + ce^{d\dot{\gamma}_w} & \text{if } t > t_{lag}(\dot{\gamma}_w) \end{cases} \tag{2.22}$$

where the constants a, b, c, and d are given by Mehrabadi et al. (2016), and $t_{lag}(\dot{\gamma}_w)$ is a power-law function fit to experimental data:

$$t_{lag}(\dot{\gamma}_w) = 1.69 \times 10^6 \dot{\gamma}_w^{-1.2} \quad (s) \tag{2.23}$$

Lag time is the time for thrombus volume to reach $\mathbf{10^6\ \mu m^3}$. Figure 2.10 demonstrates the corresponding results compared to experimental images of thrombus formation. Lag times obtained using this method matched with results from Bark and Ku [158] that used Eq. (2.24**)**.

$$t_{lag}(\dot{\gamma}_w) = 280\dot{\gamma}^{-0.2}\ (s) \tag{2.24}$$

2.3.6 Cardiovascular device-induced thrombosis and platelet activation

Thrombosis is a major issue for cardiovascular assist devices design and implementation. In aortic heart valves, platelet activation and aggregation can readily occur when wall shear rates reach 1500 dynes.cm^{-2}. Several attempts have been made to test computational models for thrombogenesis at shear levels associated with mechanical heart valves (MHVs) and left ventricular assist devices (LVADs). Seo et al. (2016) used a coupled chemo-fluidic computational model to predict thrombin and fibrin generation and platelet deposition in infarcted left ventricles (LVs). This high-fidelity model was tested for ventricles with large, medium and small apical aneurysms and was capable of predicting red clot formation under pulsatile flow conditions. The model included both biochemical reactions of coagulation and hemodynamics. Convection diffusion reaction (CDR) equations were solved to model the blood coagulation cascade. Implementation of this model enables in-depth studies of thrombosis in patient-derived infarcted LVs. It was quantitatively indicated that the weak flow strength in the apical region results in LV thrombus formation. Navitsky et al. [161] introduced a thrombus susceptibility potential (TSP) metric based on wall shear rates and exposure times to improve a

LVAD design under *in-vivo* conditions. Shear rates of 500 s^{-1} and 1000 s^{-1} were set as thresholds and cutoff values for initiation and inhibition of platelet deposition, respectively, based on data from [162]. A numerical study of platelet activation in a bileaflet MHV revealed that the shear stress history (level of activation) near the leaflet is ~10 fold higher in comparison with the core flow [163]. Because the platelets that flow near the leaflet get trapped in the wake's vortices, whereas other platelets easily leave the post-valve region. A similar effect in MHVs was shown by Alemu and Bluestein [164]. Post-procedure platelet activation in a MHV and a bioprosthetic heart valve (BHV) was compared by Hedayat et al. [165] using three different models; the linear activation model [84], the damage accumulation model [164], and Soares model [88]. It was shown that the activation in the MHV was several times higher than in the BHV for all tested cases. Also it was indicated that the damage accumulation model predicted the highest activation rate among the all models. Since the linear model did not account for the damage history and the transient nature of the flow, it underestimated the platelet activation in pulsatile flows. The damage accumulation model of Alemu and Bluestein needs empirical calibration each time, therefore, the Soares model seems to be the best approach for modeling platelet activation under both static and dynamic shear conditions.

2.3.7 Embolism and thrombus stability

Initiation of embolism due to detachment of platelet aggregates from thrombus is determined by the interplay between binding force of platelet-platelet bonds and shear forces at the surface exerted by the fluid. Platelet aggregates can form in the lumen area without needing to have contact with the vascular surface when resting platelets are subject to very high fluid shear rates (>5,000 s^{-1}) [166]. This is the second mechanism of free emboli formation, but no numerical model has been developed yet for capturing this phenomenon. Platelet adhesion to the extracellular matrix (ECM) can be floppy (at initial stage) or firm depending on the type of participating receptors. vWf mediates platelet tethering to subendothelium that leads to unstable adhesion [167]. Firm platelet adhesion on extracellular cell matrix (ECM) or collagen is mediated by GPVI together with G protein-coupled receptors (GPCRs) stimulated by local secretion of agonists [19]. Thrombus stability and factors regulating the hindered transport through thrombus is comprehensively reviewed in [34]. Firm adhesion does not necessarily require their activation [168] and takes place under high shear conditions.

Both discrete and macroscopic models capable of rapid parametric experimentation with three-dimensional flows have successfully simulated various embolic events. Additionally, the relation between thromboembolism and thrombi exposure to fluid shear forces is assessed using computational methods. Within the past decade, such techniques have made significant advances in understanding the complexity of the mechanics of embolization. However, there is no measured experimental data on shear stress distribution on thrombus/embolus due to difficulties associated with measuring temporal variations and the small scale of the problem. Thanks to increases in computing capabilities, the thrombus-plasma interaction problem has been tackled by using a variety of numerical techniques. These include fluid-structure interaction (FSI) and force coupling methods [169], [170], the cellular Potts method [171], [172], several particle methods [69], [173]–[176], the immersed boundary method [177], and the hybrid Monte Carlo-lattice Boltzmann method [178]. Fluid-structure interaction (FSI) is a coupling between laws that govern structural mechanics and fluid dynamics. This technique can realistically capture the multiphysics interaction between the blood flow and thrombus/embolus. Vahidi and Fatouraee [170] utilized a CFD-FSI model along with arbitrary Lagrangian Eulerian (ALE) method to simulate the transportation of a buoyant embolus in a pulsatile flow within a stenosed microvessel. In other studies, modeling the detachment of emboli from a forming thrombus has been attempted. The multiscale model of Fogelson and Guy [177] predicts platelet-wall and platelet-platelet bindings based on the formation of adhesive and cohesive ‘links’ between vascular wall and platelets, and between platelets. Although this model allows inclusion of detailed mechanisms of unbinding, emboli formation was not implemented due to some computational restrictions. However, a field of aggregation intensity was presented which provides an approximate estimation of the location at which embolization is likely to occur (Figure 2.11a).

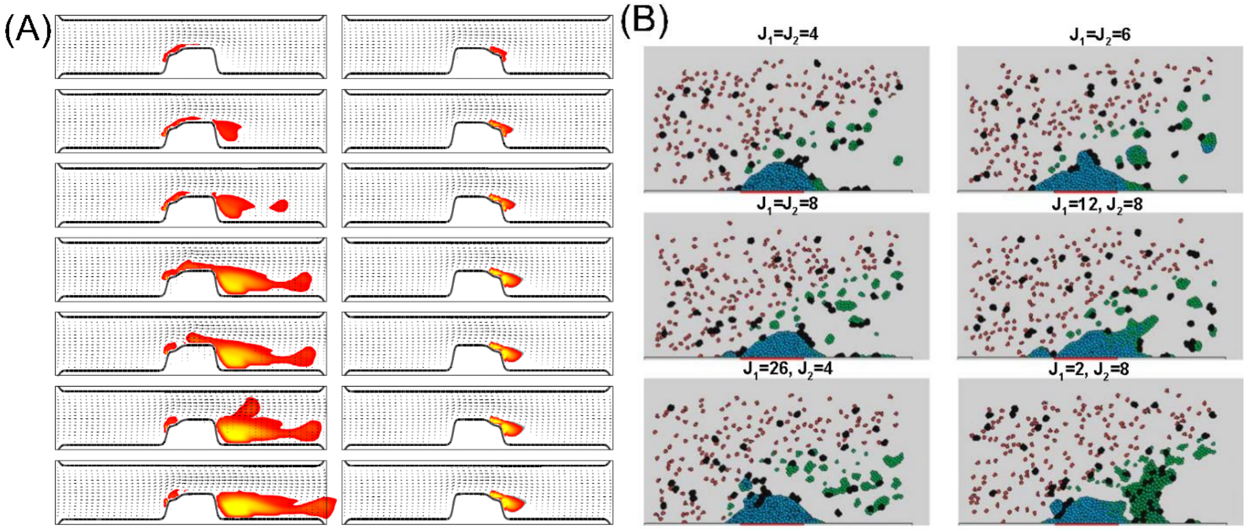

Figure 2.11 Embolization modeling; (A) Simulation results by Fogelson and Guy [177] show that embolization risk is dramatically higher when the rupture locates upstream of the stenosis; snapshots show instantaneous velocity field and the aggregation intensity distribution in the domain (dark: low intensity, light: high intensity). Left: Ruptured edge is located upstream and flow is accelerating. Right: Rupture is located downstream and flow is slowing. Images are reprinted with permission from Elsevier. (B) Simulation results of platelet aggregation after 24s demonstrate different volume of emboli for different energy constant values J_1 and J_2; J_1 is the adhesion constant of activated platelet-activated platelet interaction and J_2 is the adhesion energy constant of activated platelet with high fibrin-activated platelet with low fibrin [171]. Blood cells (black), quiescent platelets (red), activated platelets (green), and platelets with high fibrin (blue) are modeled as discrete particles in the model.

Xu et al. [171], [172] used a cell-based multiscale model of thrombus (red clot) formation with the cellular Potts method. Advantages of this comprehensive model includes modeling of 1) blood cells and ligands carried by them that can change the thrombus stability, 2) releasing of chemical agonists by adherent platelets, 3) thrombin generation by coagulation reactions, 4) fibrin production which provides a fibrin network adding to the structural integrity, and 5) embolus formation in the form of particles ensemble floating in the flow (Figure 2.11b). These make the model very useful for modeling venous or capillary flows. On the other hand, it has some shortcomings. First, it is costly because of integration of too many non-linear equations in the model. Second, it can be applied only to small domains (<100 μm) due to computational limits, hence is not appropriate to be used for modeling arterial flows. Goodman et al. [82] used the continuum model of Sorensen et al. [68] and built up the thrombus volume based on calculated platelet deposition cell by cell by setting the fluid viscosity to infinity (i.e. very large number). For modeling embolization they introduced the single-platelet 'embolization function' of shear stress based on experimental measurements. An exponential function was fit to the measured fraction of surface-adherent platelets that embolize, F_{emb}:

$$F_{emb} = e^{-0.0095\tau_{max}/t_{emb}} \tag{2.25}$$

where τ_{max} is the maximum local shear stress (dyne.cm^{-2}). t_{emb} is the characteristic embolization time (s) (i.e. the duration of the platelet free perfusion).

2.4 Summary

Several modeling techniques designated to simulate platelet margination, adhesion, activation, and aggregation, and/or embolization were reviewed in this chapter (see Table 2.4**).**

Table 2.4 Computational models of embolization, platelet margination, adhesion, aggregation, and activation

Reference	Model	Method	Validation	Shear rate (s^{-1})
Fogelson et al. [67]	Platelet activation and aggregation	Continuum, ADR equations	-	-
Sorensen et al. [68], [179]	Platelet adhesion, aggregation, and activation	Continuum, ADR equations	In-vitro	100-1000
Fogelson et al. [180]	Coagulation, platelet aggregation	Discrete, IBM	-	-
Goodman et al. [82]	Embolism, platelet adhesion, aggregation, and activation	Continuum, ADR equations	In-vitro	650-5800
Pivkin et al. [169]	Platelet adhesion, activation and aggregation	Discrete, force coupling	-	12-96
Filipovic et al. [69]	Platelet adhesion, activation and aggregation	Discrete, DPD model	In-vitro	500-1500
Fogelson and Guy [177]	Platelet activation and aggregation	Discrete and continuum (multiscale), IBM	-	0-1750
Mori et al. [175]	Platelet adhesion and aggregation	Discrete, Voigt model	In-vitro	5000
Alenitsyn et al. [181]	Platelet adhesion and aggregation	Continuum, Richardson’s theory	In-vivo	15-300
Bark and Ku [182], Mehrabadi et al. [148]	Platelet aggregation	Continuum, empirical correlation	In-vitro	20000-400000
Kamada et al. [173], [174]		MPS	In-vitro	4-12
Xu et al. [171], [172]	Embolism, platelet adhesion and aggregation	Discrete and continuum (multiscale), cellular Potts	-	4-30000
Crowl and Fogelson [183]	Platelet margination	Discrete and continuum (multiscale), LBM-IBM	In-vitro	400-1100
Flamm et al. [178]	Platelet adhesion and aggregation	Discrete, Hybrid Monte Carlo-Lattice Boltzmann	In-vitro	200-3000
Vahidi and Fatouraee [170]	Embolus-thrombus interaction	CFD-FSI, ALE	-	1400-23000
Bark and Ku [158]	Platelet aggregation	Continuum, Leveque model	In-vitro	100-100000
Chesnutt and Han [184], [185]	Embolism, platelet adhesion, aggregation, and activation	Discrete, Discrete Element Method (DEM)	In-vitro	0-3100
Narsimhan et al. [102]	Platelet margination	Discrete, Coarse-grained theory	In-vitro	200-2000
Reasor Jr et al. [10]	Platelet margination	Discrete, RBC membrane model, coarse-grained spectrin-link method, LBM	In-vitro	355-2500
Shadden and Hendabadi [78]	Platelet activation	Continuum, FTLE	-	0-1300
Sheriff et al. [88], Soares et al. [87]	Platelet activation	Particle tracking, LDH-based model	In-vitro	28-2000
Tosenberger et al. [176]	Embolism, platelet adhesion and aggregation	Discrete and continuum, DPD-PDE hybrid model	In-vivo	3000
Mehrabadi et al. [112]	Platelet margination	Continuum, DFEB	In-vitro	50-500
Mukherjee et al.[186]	Embolism	Discrete, one-way coupled DPM	-	1000-200,000

Approaches that model blood as a continuum include solving advection diffusion reaction (ADR) equations [67], [68], [82], the Leveque model [158], the Richardson's theory [181], Bark's correlation [43], [182], diffusion with free-escape boundary (DFEB) method [112], and finite time Lyapunov exponent (FTLE) measure [78]. Discrete and multiscale models include force coupling [169], coarse-grained theory [102], discrete element method (Chesnutt and Han, 2013; 2016), DPD and hybrid DPD-PDE [69], [176], fluid-structure interaction (FSI) [170], cellular Potts [171], [172], Lattice Boltzmann method (LBM) and hybrid Monte Carlo-Lattice Boltzmann [178], [183], immersed boundary method (IBM) and LBM-IBM [177], [180], [183], LDH-based models [87], [88], moving particle semi-implicit (MPS) [173], [174], RBC membrane model [10], and Voigt model [175]. Most of these models are validated using in-vitro data, whereas many *in-vivo* observations are not reflected under *in-vitro* conditions. Albeit numerous aspects of coagulation, platelet deposition and aggregation, and embolization are addressed with these models, to the best of our knowledge, there is no validated patient-specific model capable of predicting thrombus formation and embolism under *in-vivo* conditions. Moreover the gap between microscopic processes (e.g. coagulation) and large scale phenomena such as margination can be linked with multiscale and mesoscopic models. The next research challenge is to integrate available features into more comprehensive predictive models.

3 Development, calibration and validation of the thrombosis model for stenosed vessels with stationary geometry

Shear stresses play a major role in platelet-substrate interactions and thrombus formation and growth in blood flow, where under both pathological and physiological conditions platelet adhesion and accumulation occur. In this chapter, a shear-dependent continuum model for platelet activation, adhesion and aggregation is presented. The model was first verified under three different shear conditions and at two heparin levels. Three-dimensional simulations were then carried out to evaluate the performance of the model for severely damaged (stripped) aortas with mild and severe stenosis degrees in laminar flow regime. For these cases, linear shear-dependent functions were developed for platelet-surface and platelet-platelet adhesion rates. It was confirmed that the platelet adhesion rate is not only a function of Reynolds number (or wall shear rate) but also the stenosis severity of the vessel. General correlations for adhesion rates of platelets as functions of stenosis and Reynolds number were obtained based on these cases. Finally using the new platelet adhesion rates, the model was applied to different experimental systems and shown to agree well with measured platelet deposition.

3.1 Introduction

Cardiovascular diseases (CVD) are the number one causes of death in the world. According to the world health organization (WHO), cardiovascular disease represents 30 % of all global deaths. Thus, there is a critical need to address existing and emerging challenges and develop novel tools to diagnose, monitor, and treat cardiovascular diseases. According to Virchow's triad [187] changes in blood components, vessel wall surface or flow characteristics can lead to thrombosis. In terms of components, platelets whether suspended in the blood stream or attached to the vessel wall are known to be one of the major components involved in thrombosis. They can bind together and have three forms depending on the flow conditions: grouping of platelets in hemostasis called plugs, free emboli that can be carried by blood flow, and pathological extension of hemostasis (i.e. thrombosis). Hemostasis is a natural mechanism, which arrests hemorrhaging; however the other two forms occur only under abnormal conditions. Experimental and numerical investigations of such pathological situations in various vasculatures have been carried out to explain the role of potential mechanical and biological elements at play [188]. The effects of these factors are evaluated from both fluid dynamics and chemical standpoints.

Once adhered to the vessel wall, specifically to the endothelium, platelets get activated, change dramatically in shape and spread on the surface to take on a pancake-like shape [20], [189] to first increase the adhesion area and second, stimulate other platelets resting in plasma to become activated through biological mechanisms. These mechanisms are different from general adhesion mechanisms and include signaling pathways [21] in the platelet extracellular membrane and secretion of soluble thrombogenic agonists to the plasma. Unlike the initiation of adhesion of platelets exposed to the subendothelium, the formation of platelet aggregates is based on the platelet-platelet and platelet-stimuli interactions. Activated platelets in turn release their stored granules, which leads to sudden increase in local concentration of agonists necessary for platelet plug formation.

Collagen, adenosine diphosphate (ADP), thromboxane A_2 (TxA_2), prothrombin, thrombin, antithrombin, heparin, and shear stress as the major contributors and serotonin, epinephrine, and matrix metalloproteinases (MMP) as weak platelet agonists can alter processes leading to platelet activation [23], [27], [30], [34], [190]. One should note that the contribution of interactions between specific adhesive receptors and soluble stimuli to thrombogenesis can be dependent on the blood flow conditions. Although the sequence of events associated with platelet adhesion, aggregation and activation may remain the same, their occurrence and intensity as well as the interaction of contributing components with each other can be highly dependent on the local blood flow characteristics.

Platelet adhesion and aggregation take place under a wide range of physiological flow shear rates (20-1800 s^{-1}) as well as at pathological shear rates as high as 20,000 s^{-1} [34]. The effect of flow shear rate on platelet adhesion rate was first investigated by Turitto and Baumgartner [60]. The in-vitro study was performed on platelet adhesion to subendothelium in rabbit aorta, and the initial rate of platelet adhesion was shown to increase with increasing vessel wall shear rate, up to shear conditions as high as 2,600 s^{-1}. After 2,600 s^{-1}, the rate of adhesion decreased with increasing wall shear rate and finally it was inhibited at a shear rate of 10,000 s^{-1}. Besides general correlations of platelet adhesion as a function of shear rate, the shear dependent role of thrombin has been studied as one of the major contributing factors for thrombus formation [48]. It has been indicated that thrombin contributes to thrombus formation at very low (50 s^{-1}) and intermediate shear rates (650 s^{-1}).

Several studies have been performed to reveal the potential relationship between local wall shear stress in blood flow and restenosis [182], [191], [192] or unfavorable platelet aggregation and adhesion in various vascular systems [193]–[195]. Mehrabadi et al. [43] and Bark et al. [51] correlated their experimentally observed results for thrombus growth rate as a function of local wall shear rate in highly stenosed collagen-coated tubes. Mehrabadi et al. [43] used a mathematical time- and wall shear-dependent relation with empirical parameter values from Colace and Diamond [196] to predict the occlusion time in stenosed tubes. Their results demonstrate maximum thrombus growth rate at wall shear rate of 10000 s^{-1}. Bark et al. [51] fitted two correlations with experimental data having shown that peak values of growth rate correspond to wall shear rate of ~6000 s^{-1}. Similar effect of shear stress on platelet deposition in stenosed vessels has been investigated ex-vivo [47], in-vitro [51] and in-vivo [53] to reveal the relationship between wall/local shear rate and distribution of platelet deposition on severely injured vessels. It has been shown that the apex of a stenosis is the most susceptible region for platelet deposition, hence thrombus formation.

Previous studies exclude the presence of important biological components such as ADP, thrombin, antithrombin and heparin involved in atherosclerosis or ignore the effect of shear stress on platelet-platelet and platelet-surface binding kinetics. They have not considered the effect of flow characteristics along with stenosis on the rate of platelet adhesion to vessel wall. Employing the constant platelet adhesion rates do not account for the shear- or flow-dependent mechanisms observed for platelet deposition. In this chapter we analyze platelet deposition in channel flow as well as in stenosed damaged vessels, with mild and severe stenosis (29-80%), within a wide range of pathological shear rates (>100 s^{-1}). In contrast to previous numerical studies using CFD, we include shear effects (mechanical factor) as well as all seven major blood components/agonists that contribute to platelet accumulation and thrombus formation (biological factors). Previous numerical models including those proposed by David et al. [160], Sorensen et al. [179], Goodman et al. [82], and Bark et al. [158] need to be recalibrated every time they are applied to a new experimental setup with different flow conditions. Goodman et al. have used Sorensen’s model for tubular expansion problem and used 2.5×10^{-6} $m.s^{-1}$ and 3.5×10^{-5} $m.s^{-1}$ for adhesion rates of resting platelet to surface, and activated platelets to surface, respectively, whereas these values were found to be 3.7×10^{-5} $m.s^{-1}$ and 4.6×10^{-5} $m.s^{-1}$ in the original model

[82]. Wootton et al. used Leveque's model but with new constants after recalibration of parameter values for stenosed tubes through trial and error [111]. Taylor et al. applied the same model to a rotating disc system [197]. They have used a parameter value of 5×10^{-9} $m.s^{-1}$ (as the best-fit value) for the adhesion rate of activated platelets to surface, whereas this value was 4.6×10^{-5} $m.s^{-1}$ in the original model. In another study, they remodified the model to be able to predict the deposition in asymmetric expansion problem [198]. In this chapter a useful general function is presented and validated for platelet adhesion rate as a function of stenosis severity and local Reynolds number at the stenosis apex. This allows us to predict the platelet deposition in stenosed vessels with different flow and geometry (stenosis) characteristics rather than refitting the results to experimental data. The continuum model estimates are compared with available experimental results for platelet deposition in stenosed tubes in the range of 29-80% stenosis and apex Reynolds number range of 46 to 900.

3.2 Methods

3.2.1 Computational Model

In the past decade, direct simulations of flowing blood cell suspensions have become possible. A recent review article provides details on simulation methods and challenges [34]. These simulations provide insight into the physical mechanisms that drive platelet deposition at the cell scale. However, modeling all cells as discrete entities is still computationally expensive and challenging for large domains such as coronary arteries. Simulation of platelets and red blood cells in a typical artery with a 2 mm diameter requires injecting at least 800 million particles into the domain with the correct associated physics of deformation, margination, etc., which is not feasible yet for anything other than a one-of-a-kind calculation. In our quest to maintain as much realism in our system as possible, we choose a continuum approach and following Sorensen's approach [68], solve the mass conservation and Navier Stokes equations, as well as mass transport equations in the present chapter. The first equation governing the fluid (i.e. plasma) is the continuity equation:

$$\frac{\partial \rho}{\partial t} + \vec{\nabla}.(\rho \vec{u}) = 0 \tag{3.1}$$

where ρ is the fluid density and $\vec{u}$ denotes the velocity vector field. The governing momentum equation solved reads as:

$$\frac{\partial}{\partial t}(\rho \vec{u}) + \vec{\nabla}.(\rho \vec{u}\vec{u}) = -\vec{\nabla} p + \mu \vec{\nabla}.\left(\vec{\nabla}\vec{u}\right) \tag{3.2}$$

Since the wall shear rate magnitudes are above 100 s^{-1} for all test cases, blood is considered as a Newtonian fluid with a constant viscosity of 0.0035 Pa.s [121], [122]. This range of shear rate (0-100 s^{-1}) occurs in a very small portion (< 1%) of the tested domains near the reattachment point (see Figure 3.10). Therefore, we believe that non-Newtonian effects are negligible in the simulation. Energy equation is not solved, because the role of the thermal transport during platelet adhesion is absolutely insignificant [111].

The GenIDLEST numerical code is used to solve the governing equations [105], [199]. A finite volume formulation with a semi-implicit algorithm is used to discretize the momentum and mass transport equations. A grid independence study over grids varying from 16000 elements to 201,000 elements was done to make sure that the results are independent of the grid size (see Table 3.1).

Table 3.1 Grid independence analysis for case 1; effect of grid size on platelet deposition and mass fraction of platelets and ADP at x=25 μm and y=0, t=3.6e-3 s. The grid with 192,000 elements was used for this case.

Number of cells	Deposition ($\mathrm{PLT.cm^{-2}}$)	ADP mass fraction (g/g)	Resting platelets mass fraction (g/g)
16,000	2795 (7.4%)*	3.28×10^{-4} (15.9%)	2.08×10^{-3} (5.6%)
37,000	2735 (5.1%)	3.18×10^{-4} (18.4%)	2.04×10^{-3} (3.6%)
80,000	2734 (5.0%)	3.99×10^{-4} (2.3%)	2.04×10^{-3} (3.5%)
192,000	2625 (1.0%)	3.93×10^{-4} (0.7%)	1.98×10^{-3} (0.5%)
201,000	2602	3.9×10^{-4}	1.97×10^{-3}

* Percentages represent the difference between deposition/mass fraction values with those of the finest grid. The finest grid was used as the baseline grid to investigate the effect of mesh size on variation of the deposition/mass fraction.

3.2.2 Mass Transport Equations

Platelet activation and adhesion is a complex process. There are a number of continuum models which have been used to describe platelet activation and adhesion [67], [82], [87], [111], [160]. The major role of adenosine diphosphate (ADP), platelet-phospholipid-dependent thrombin generation, and thromboxane A_2 (TxA_2) synthesis on platelet membrane in platelet activation and aggregation are experimentally observed in [62], [63], [65] and their quantified contribution to platelet deposition is discussed in detail in [200]. In spite of experimental evidence, most models do not take the effect of thrombin and thromboxane on thrombosis into account and include ADP as the only platelet-activating agonist, while some studies assume platelet activation and adhesion at the same rate and do not include TxA_2, ADP, or thrombin-related agonists. In such models, mass transport equations are solved only for platelets with no differentiation between activated platelets and non-activated platelets. In order to have a physically relevant representation of the complex interactions, all seven mass transport equations introduced by Sorensen et al. [179] are included in the present model: 1) resting platelets (RP), 2) activated platelets (AP), 3) ADP, 4) TxA_2, 5) prothrombin (PT), 6) thrombin (Th), 7) antithrombin (ATIII). For all of them the mass transport equation is solved:

$$\frac{\partial C_i}{\partial t} + div(u.C_i) = div\big(D_i.grad(C_i)\big) + S_i \qquad\qquad i = 1,2,\ldots,7 \tag{3.3}$$

where C_i is the concentration of species i, D_i is the mass diffusion coefficient of species i, and S_i is the generation/consumption term for species i to model platelet-platelet, platelet-agonist, and agonist-agonist interactions in the lumen area. The original form of generation/consumption terms and wall deposition/consumption terms proposed by Sorensen et al. [179] was used as the starting point.

3.2.3 Mass Diffusivities

In whole blood the diffusion coefficient of platelets and thrombin-related species (i.e. thrombin, prothrombin and antithrombin) can be dramatically augmented by the presence of red blood cells (by up to 3 orders of magnitude) compared to the case where there are no red blood cells in plasma. This effect, referred to as the shear-enhanced or the shear rate-dependent mass diffusivity, is formulated by Keller [107] as follows:

$$D_s = 0.18R_{RBC}^2\dot{\gamma} \tag{3.4}$$

where R_{RBC} denotes the radius of the red blood cell (~2.75 μm) and $\dot{\gamma}$ is the local fluid shear rate (s^{-1}). Thus the total diffusivity of the platelets and thrombin-related species is given as:

$$D_i = D_{b,i} + D_s \tag{3.5}$$

In Sorensen's work in channel flow, however, the shear-enhanced mass diffusivity of species i, D_i is assumed to be constant for all species, because instead of the local fluid shear rate, they used the fully-developed shear rate value at the wall ($\dot{\gamma}_w$) for calculating the effective mass diffusivities. Mass diffusivities have a large impact on the needed grid resolution and define the grid size near the wall. The first cell size in the grids was estimated based on an approximate boundary layer thickness proposed by Leveque, $\delta(\mathrm{z}) \sim (\mathrm{z}/\mathrm{PeL})^{1/3}$, where δ is the non-dimensional mass transfer boundary layer thickness, z is the axial distance from inlet, Pe denotes the Peclet number and L is characteristic length respectively [201]. Peclet number is defined as $\mathrm{Pe} = \mathrm{uL}/\mathrm{D}$ where u is the average velocity, L is the characteristic length, and the smallest mass diffusivity in the model is assumed for D. Platelets have the smallest Brownian mass diffusivities ($1.58 \times 10^{-13}\ m^2.s^{-1}$). Considering the enhancement factor of $1.36 \times 10^{-12}\ m^2$, the smallest effective diffusivity corresponds to the cases 12-14 (see Table 3.2) where the inlet wall shear rate is 265 s^{-1}. The thinnest boundary layer thickness in these cases is ~19 μm. In light of this, the radial grid was heavily skewed toward the wall to capture the mass transport in the boundary layer. The first cell height was 0.2-12 μm in the used grids (see Table 3.1). The cell height at the wall can be very different from case to case because the first cell height depends on the mass boundary layer thickness, which in turn is approximated by Leveque equation [201]. As mentioned earlier in 3.2.3, the first cell heights were calculated using the Leveque approximation first and then a grid independence study has been performed. Boundary layer thickness can be very different for each case depending on the magnitude of the Peclet number. Higher Peclet number and locations nearer the leading edge or inlet will result in thinner mass boundary layer thickness. Table 3.1 shows the grid study performed for case 1 as a sample case. The grid with 192,000 elements was used for this case as the deposition values as well as mass fractions of different species were independent of the grid size (with less than 1% variation with respect to the finest grid values). Also, the ratio of Leveque's approximated mass transport layer thickness to the first cell height used in the simulation was ~49 for this case. A similar ratio was used to set the first cell height and spacing near the wall for other cases.

3.2.4 Source Terms

Resting platelets in the plasma can transform to a high affinity (activated) state. This transformation takes place at a certain rate k_{pa}, known as the platelet activation rate, and results in transformation of resting platelets. On the other hand based upon activation, activated platelets are generated at the same rate (Eq. (**3.7**). Meanwhile, activated platelets release a certain amount of adenosine diphosphate (ADP) agonists during activation. ADP makes activation possible for platelets without their direct contact with the collagen fibers on vessel walls (Eq. (3.8)). Thrombin, the other activator protein, can form through proteolysis process and transformation of factor II (prothrombin) to IIa during platelet activation (Eq. (3.10) and (3.11)). Proteolysis occurs on the platelet membrane with the rates of ϕ_{rt} and ϕ_{at} to the membrane of resting and activated platelets, respectively. Platelet activation also stimulates formation of another aggregation agent, thromboxane A_2 (Eq. (3.9)). TxA_2 along with thrombin and ADP binds to their specific receptors on platelet membrane and activate them [19].

$$S_{RP} = -k_{pa}.C_{RP} \tag{3.6}$$

$$S_{AP} = +k_{pa}.C_{AP} \tag{3.7}$$

$$S_{ADP} = +\lambda_{ADP}.k_{pa}.C_{RP} \tag{3.8}$$

$$S_{TxA_2} = +s_{p,TxA_2}.C_{AP} - k_{1,TxA_2}.C_{TxA_2} \tag{3.9}$$

$$S_{PT} = -\beta.C_{PT}.(\phi_{at}.C_{AP} + \phi_{rt}.C_{RP}) \tag{3.10}$$

$$S_{Th} = +C_{PT}.(\phi_{at}.C_{AP} + \phi_{rt}.C_{RP}) - \Gamma.C_{Th} \tag{3.11}$$

$$S_{ATIII} = -\Gamma.\beta.C_{Th} \tag{3.12}$$

where λ_{ADP} denotes the amount of ADP released by newly activated platelets, and Γ is the Griffith's template model for the kinetics of the heparin-catalyzed inactivation of thrombin by antithrombin [202].

3.2.5 Reactive Walls

Platelet deposition on the surface is modeled by using mass flux terms for interacting species as shown in Eqs. 3.13-18 below. It is assumed that the resting platelets stick to the surface at constant rate k_{rs}. As they adhere to the wall, with the decreasing free surface available the number of platelets adhering to the surface decreases. Activated platelets can adhere to other activated platelets in addition to the surface. Therefore two first order adhesion rates are considered for activated platelets: k_{as} and k_{aa}. Once the resting platelets deposit on the free surface available at the wall, a fraction of them (θ) transform to high affinity state and release ADP's. Here, θ is assumed to be equal to 1, based on [179]. This makes $M_r(x,t)$ zero, as all deposited platelets on the wall would be activated platelets. Presence of activated platelets on the surface, in turn, results in generation of platelet-synthesized agonist TxA$_2$ with a synthesis rate of s_{p,TxA_2}.

$$J_{RP} = -S(x,t).k_{rs}.C_{RP} \tag{3.13}$$

$$J_{AP} = -\left(S(x,t).k_{as} + \left(\frac{M_{as}(x,t)}{M_\infty}\right).k_{aa}\right).C_{AP} \tag{3.14}$$

$$J_{ADP} = \lambda_{ADP}.\left(\theta.S(x,t).k_{rs}.C_{RP} + k_{pa}.M_r(x,t)\right) \tag{3.15}$$

$$J_{TxA_2} = M_{at}(x,t).s_{p,TxA_2} \tag{3.16}$$

$$J_{PT}(x,t) = -\beta.(M_{at}(x,t).\phi_{at} + M_r(x,t).\phi_{rt}).C_{PT} \tag{3.17}$$

$$J_{Th}(x,t) = (M_{at}(x,t).\phi_{at} + M_r(x,t).\phi_{rt}).C_{PT} \tag{3.18}$$

Here, a positive term represents generation at the wall and a negative term indicates consumption/deposition of species i. All parameter values used in the model are given in Table 3.3.

Table 3.2 Test cases for verification and calibration with corresponding flow characteristics.

Case	Geometry	Channel width /tube diameter (mm)	Stenosis (%)	Re	Shear rate at inlet (s^{-1})	Flow rate (mL/min)	Ref.
1	2D channel (in-vitro)	0.2	0	2.1	1000	396	54
2	2D channel (in-vitro)	0.2	0	1.05	500	198	25
3	2D channel (in-vitro)	0.2	0	0.21	100	39.6	52
4	3D stenosed vessel (in-vitro)	2	35	30	212	10	24
5	3D stenosed vessel (in-vitro)	2	35	120	853	40	24
6	3D stenosed vessel (in-vitro)	2	35	180	1280	60	24
7	3D stenosed vessel (in-vitro)	2	55	30	212	10	24
8	3D stenosed vessel (in-vitro)	2	80	30	212	10	24
9	3D stenosed vessel (in-vitro)	2	80	120	853	40	24
10	3D stenosed vessel (in-vitro)	2	80	180	1280	60	24
11	3D stenosed vessel (ex-vivo)	2	80	60	415	20	62
12	3D stenosed tube (in-vitro)	4	29.3	160	265	99.5	30
13	3D stenosed tube (in-vitro)	4	50	160	265	99.5	30
14	3D stenosed tube (in-vitro)	4	68.4	160	265	99.5	30
15	3D stenosed tube (in-vitro)	1.5	78	3.6	18	0.7	64
16	3D stenosed tube (in-vitro)	1.5	78	6.2	30	1.2	64
17	3D stenosed tube (in-vitro)	1.5	78	16.5	74	3	64
18	3D asymmetric stenosed channel	0.75	66.7	8	1267	0.78	65
19	3D asymmetric stenosed channel	0.75	66.7	10.5	1334	1.02	65
20	3D asymmetric stenosed channel	0.75	66.7	16.7	1958	1.62	65
21	3D asymmetric stenosed channel	0.75	66.7	21.4	3059	2.34	65

3.2.6 Calculation of Platelet Deposition

Time integration of platelet fluxes over perfusion time gives the accumulated platelet deposition $M_{at}(x,t)$ which denotes the total number of deposited platelets per unit vessel area:

$$M_{at}(x,t) = \int_0^t \left[S(x,t).\,k_{rs}.\,C_{RP} + \left(S(x,t).\,k_{as} + \left(\frac{M_{as}(x,t)}{M_\infty} \right).\,k_{aa} \right).\,C_{AP} \right].\,dt \qquad (3.19)$$

Note that total deposition is equal to deposited activated platelets because we have already assumed that resting platelets get activated upon surface contact to be consistent with [68], [179].

3.2.7 Test cases

3.2.7.1 2D Channel Flow

Using the model developed by Sorensen et al. [179] results from three sets of simulations performed in channel flows are compared to experimental results in the literature. These cases are set up for model verification here. First one, studied by Wagner and Hubbell [28] is a 2D channel with a collagen-coated surface. The other two cases are set up based on Hubbell and McIntire's work [143] (cases 2 and 3). For these cases, to account for the presence of red blood cells in the flow and mimic the platelet margination effect, similar to previous studies [68], [179] a platelet-excess boundary layer was considered for platelets at the inlet:

$$C(y) = \begin{cases} C_0, & |H-y| \le H - L_b \\ C_0\left(1 + 5.6\,\frac{(|H-y| - H + L_b)^2}{L_b^2}\right), & |H-y| \ge H - L_b \end{cases} \qquad (3.20)$$

where y is the vertical distance from the channel wall (in cm), H is the half width of the channel (in cm), L_b is the excess-platelet boundary layer thickness, which is assumed to be 35% of the channel half width, C_0 is the uniform concentration of platelets outside the boundary layer, which is 60% of the average inlet concentration.

3.2.7.2 Flow in 3D Stenosed Vessels under In-Vitro Condition

To determine the applicability of the current model under different pathological conditions in non-parallel flow domains with higher shear rates, one set of in-vitro experiments by Badimon and Badimon [47] were picked from the literature. This study has been performed on stenosed sections cut from pig aorta with different stenosis severities and flow rates. The volumetric flow data and vessel diameter/length are based on Badimon's experiments. Figure 3.1b demonstrates the corresponding experimental setup. In the experiments heparinized porcine whole blood was perfused for 1-30 minutes over tunica media of pig aorta at three flow rates of 10, 40, and 60 ml/min and heparin level of 1.37 U.ml^{-1}. Table 3.2 lists the corresponding flow characteristics and geometric parameters. Experimental data in [47] are given for a single Re for the 55% stenosis case and no data was provided for cases with flow rates of 40 and 60 ml.min^{-1} to compare the numerical results with.

Table 3.3 Species-specific and additional parameter values used in the model

Parameter	Value	Units	Ref.
$\mathbf{D_{b,PLT}}$	$\mathbf{1.58 \times 10^{-13}}$	$\mathbf{m^2.s^{-1}}$	[203]
$\mathbf{D_{b,ADP}}$	$\mathbf{2.57 \times 10^{-10}}$	$\mathbf{m^2.s^{-1}}$	[64]
$\mathbf{D_{b,TxA_2}}$	$\mathbf{2.14 \times 10^{-10}}$	$\mathbf{m^2.s^{-1}}$	[64]
$\mathbf{D_{b,PT}}$	$\mathbf{3.32 \times 10^{-11}}$	$\mathbf{m^2.s^{-1}}$	[64]
$\mathbf{D_{b,T}}$	$\mathbf{4.16 \times 10^{-11}}$	$\mathbf{m^2.s^{-1}}$	[64]
$\mathbf{D_{b,ATIII}}$	$\mathbf{3.49 \times 10^{-11}}$	$\mathbf{m^2.s^{-1}}$	[64]
$\boldsymbol{\beta}$	$\mathbf{9.11 \times 10^{-3}}$	$\mathbf{nmol.U^{-1}}$	[68]
$\mathbf{M_\infty}$	$\mathbf{7 \times 10^{6}}$	$\mathbf{PLT.cm^{-2}}$	[68]
$\boldsymbol{\phi_{at}}$	$\mathbf{3.69 \times 10^{-9}}$	$\mathbf{U.PLT^{-1}.s^{-1}}$	[204]
$\boldsymbol{\phi_{rt}}$	$\mathbf{6.5 \times 10^{-10}}$	$\mathbf{U.PLT^{-1}.s^{-1}}$	[204]
$\boldsymbol{\mu}$	$\mathbf{0.0035}$	$\mathbf{Pa.s}$	[68]
$\boldsymbol{\rho}$	$\mathbf{1106.4}$	$\mathbf{kg.m^{-3}}$	[68]
$\boldsymbol{\lambda_{ADP}}$	$\mathbf{2.4 \times 10^{-8}}$	$\mathbf{nmol.PLT^{-1}}$	[66]
$\mathbf{s_{p,TxA_2}}$	$\mathbf{9.5 \times 10^{-12}}$	$\mathbf{nmol.PLT^{-1}.s^{-1}}$	[64]
$\mathbf{k_{1,TxA_2}}$	$\mathbf{1.61 \times 10^{-2}}$	$\mathbf{s^{-1}}$	[143]

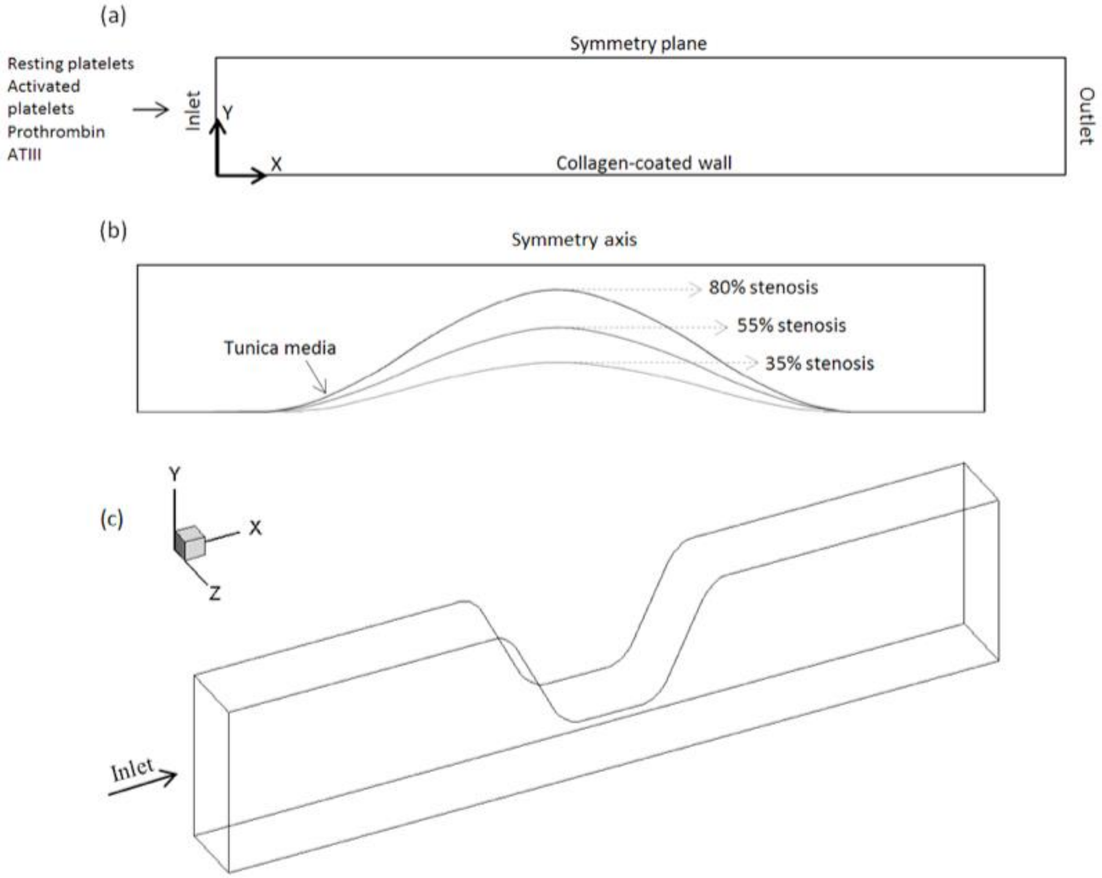

Figure 3.1 Schematic representation of test cases in (a) 2D channel, (b) cross section of stenosed region of 3D vessel, (c) 3D channel of Li et al. [205] **with 67% asymmetric stenosis.**

Platelet margination occurs over a wide range of vessel diameter (d > 15 μm) [53] under both physiological and pathological conditions. However, for a developing parallel flow it can take at least 3~4 seconds to yield the near wall RBC-free layer with high platelet concentration [53]. In the experimental setup of Badimon et al., stripped aorta vessels were cut and located in a perfusion chamber, which results in flow disturbance at the inlet of stenosed region. The length of the cut vessels (~7 mm) is not enough under the given flow conditions for blood cells to redistribute and push the platelets toward the skimming layer (time scale=R^2/D_{platelet}). An approximate margination length scale can be calculated using the formula proposed by Mehrabadi et al. ($L_{\text{mar}} = \frac{H}{12K.R_{RBC}^2}$) [206]. Assuming K=0.18 based on Keller's enhanced diffusivity for platelets [68] gives $L_{mar} \approx 450\, m$ which reveals that margination does not occur for this setup. The requirement for a long tube length for platelet margination is also confirmed by Mehrabadi et al. for a 3mm diameter tube [112]. Therefore, no wall-skewed inlet boundary condition due to platelet margination has been assumed for the 3D stenotic flow simulations.

3.3 Results and discussion

3.3.1 2D Channel Flow

For the 2D channel cases, platelet deposition distribution (number of platelets per unit area) along the channel is the final parameter of interest in our model. Figure 3.2a compares our numerical results for total platelet deposition with experimental data after 75 seconds. As it is illustrated, the trend of our prediction matches well with the experimental results. However, there is some discrepancy between our results and those from [28].

Results for platelet deposition as a function of axial position along the channel wall, reproduced for the cases 2 and 3, are presented at t=120 s. For the case with higher shear flow condition ($\dot{\gamma}_w$=500 s^{-1}), platelet deposition results are compared to experimental data points. Figure 3.2b shows that the model slightly overpredicts the experimental measurements of [143]. For case 3 with low wall shear rate ($\dot{\gamma}_w$=100 s^{-1}), our results match well with the experimental results, especially for x>5 mm (Figure 3.2c). These cases were run to validate our implementation. Therefore, parameter values that we used are taken from Sorensen's study which were calibrated to the experiments. In their study, the near wall grid was ~20-40 times coarser and time step sizes were ~1-6 s, which is very large compared to ours (~5-20 μs). As a result, our grid captures the near-wall phenomena more precisely. Therefore, if an attempt was made to find the best combination of parameter values that match our results with experimental data for channel flows, different values will be obtained. This was not pursued because our focus was not deposition between parallel plates but in stenosed flows.

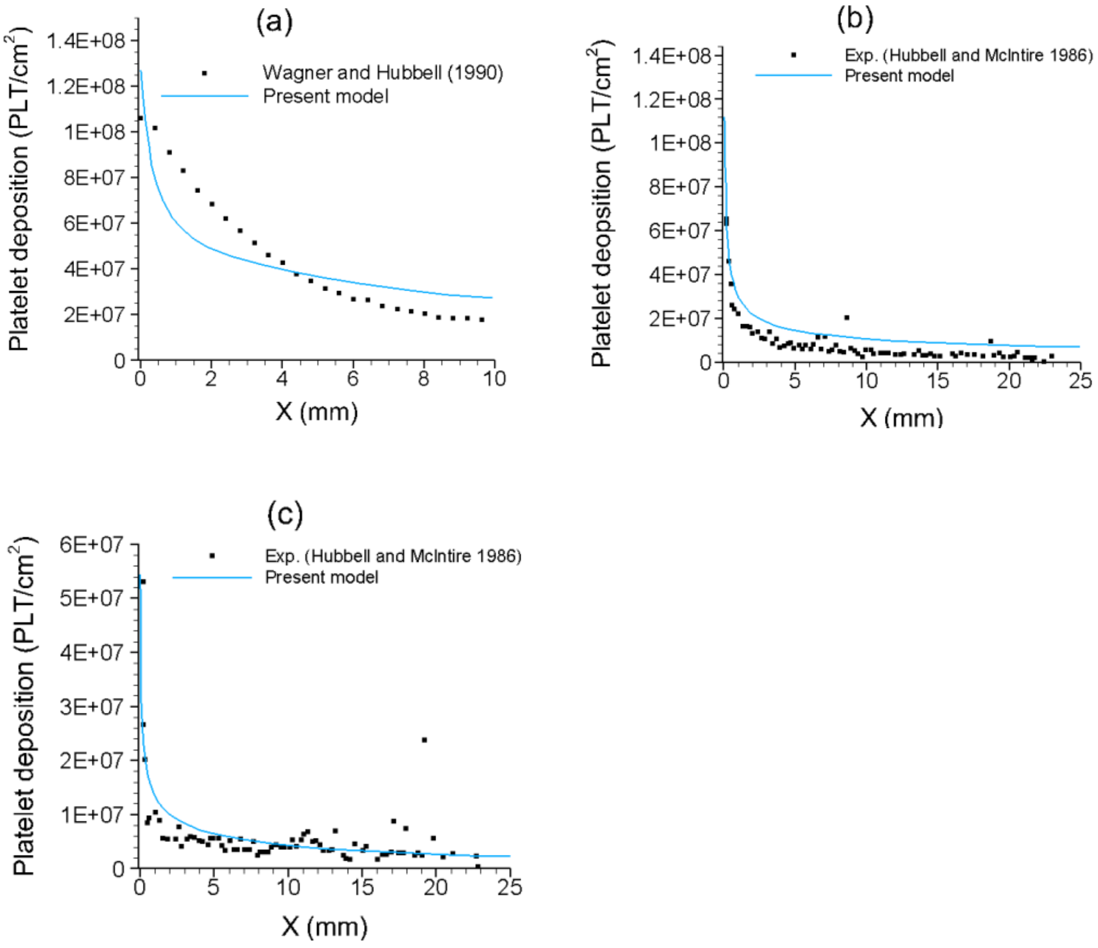

Figure 3.2 Comparison of axial distribution of platelet deposition on collagen predicted by the model with experimental results for a) case 1: t = 75 s, [H] =2 units, $\dot{\gamma}_w$=1000 s^{-1} [28]; b) case 2: t = 120 s, [H] =2 units, $\dot{\gamma}_w$=500 s^{-1} [143]; c) case 3: t = 120 s, [H] =10 units, $\dot{\gamma}_w$=100 s^{-1} [143].

3.3.2 3D Stenosed Vessels

In this section, numerical results for distribution of platelet deposition as well as time evolution of total deposition in the stenosed region are compared to experimental data. Results are categorized based on the Reynolds number and stenosis severity. The ratio of surface reactivity to platelet diffusivity is measured by the platelet Damkohler number (Da= $k.L/D_{PLT}$). Sorensen et al. [179] showed that increasing the platelet adhesion rates leads to a transition from an adhesion-limited regime (Da≈1) to a diffusion-limited regime (Da≈100). Using the constant values for platelet adhesion rates ($k_{rs} = 3.7 \times 10^{-5}\, m.s^{-1}$, $k_{as} = k_{aa} = 4.6 \times 10^{-5}\, m.s^{-1}$) and variable Keller diffusivity [107] for platelets in our simulations yields very low Sh numbers. The local Sh numbers at the apex (with high wall shear rate values) are as low as ~0.1-0.51 for 80% stenosis, ~9.48 for 55% stenosis, and ~4.74-28.46 for 35% stenosis cases. As a result, adhesion-limited deposition was expected and observed in our predictions of Badimon's cases [47] especially for highly stenosed vessels. This was in contrast to their experimental finding that showed much higher deposition values at the stenosis apex. Therefore, to compensate for this effect, augmented adhesion rates for platelets were employed in our model to make the platelet-wall reaction mechanism dominant near the apex. Previous experimental work has shown that platelet adhesion rates are not only functions of local shear rate. Based on the results from [51] and [43] thrombus growth rate is a function of flow rate and stenosis degree, and the deposition rate can be dramatically different for the same wall shear rate (see Figure 3.3). Thus it is necessary that any model development effort take this factor into consideration.

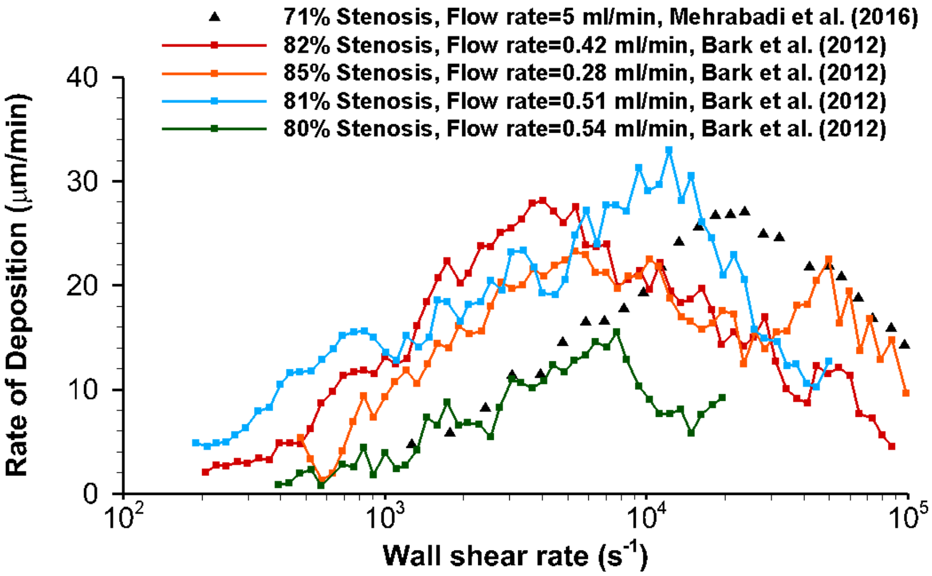

Figure 3.3 Comparison of thrombus growth rate as a function of wall shear rate. Depending on the vessel stenosis degree and inlet flow rate, the thrombus growth rate can be dramatically different for the same wall shear rate. Data are plotted based on the experimental results from Bark et al. [51] and Mehrabadi et al. [148].

Following an approach similar to that of David et al. [160] the new adhesion rates of platelets k_i (i.e. k_{rs}, k_{as}, and k_{aa}) are defined as linear functions of local wall shear rate based on the binding kinetics of platelets [7]. We define the enhanced adhesion rate as:

$$k_i(x) = k_{i_0}.\left(1 + \lambda.\dot{\gamma}_w(x)\right) \tag{3.21}$$

where $\dot{\gamma}_w(x)$ is the local wall shear rate, λ is the shear enhancement factor, and k_{i_0} is the baseline value. The enhancement factor is defined to account for the effect of wall shear rate. A similar approach was used by David et al. [160] in stagnation point flow to augment the adhesion rate in high shear regions.

In line with experimental observations, the model is calibrated using Reynolds number and degree of stenosis in two steps. First, the calibrated values are obtained for λ to match the axial distribution of deposition; in the second step, k_{i_0} is adjusted in order to reach the experimental values of total deposition in the stenosis.

3.3.3 Distribution of Platelet Deposition: Effects of Stenosis Degree and Flow Rate

In the experiments by Badimon [47] the stenosed section of the vessels is divided into 5 equal segments (0.9 mm each) in each of which the deposited platelets are counted. The different values of deposition in these segments is due to local change in wall shear rate. The shear enhancement factor λ in Eq. (3.21) augments the effect of shear rate on platelet-surface and platelet-platelet adhesion. λ is an arbitrary value and has to be defined through calibration. During the calibration of platelet distribution, the values of adhesion rate constants used by Sorensen et al. [68], [179] are used for k_{i_0}. Considering the fact that the highly stenosed region is pathologically of the utmost importance, we assumed the platelet deposition percentage at the apex region (i.e. segment 4) as our target parameter and tried to match our numerical predictions with the experimental results by altering the enhancement factor, λ in Eq. (3.21). Note that the errors associated with experimental measurements are as high as ~15% [47]. Figure 3.4a-g demonstrate the numerical results for distribution of platelet deposition using the obtained values of λ at quasi-steady state ($t=t_{qss}$). For Re=30 to 180 and stenosis degrees of 35%, 55%, and 80%, the simulations are run until a constant rate of deposition and a steady state for flow field is achieved, which means for $t>t_{qss}$ the distribution of platelets does not change substantially (less than 1%) in all segments.

A 5th order polynomial surface (see Fig. B.1 in Appendix B) was fit on the λ values in MATLAB® (MATLAB 8.4, The Mathworks Inc., Natick, MA, 2014). This was done using two input variables: stenosis degree, and the Re_{apex} calculated based on the vessel diameter and mean fluid velocity at the apex (see Eq. B.1. in Appendix B). It was observed that for Re<150, λ increases with stenosis percentage. This trend implies that for low Re flow, augmentation of platelet adhesion terms due to high shear near the apex is needed to reflect higher deposition values in this region. In other words, the platelet-surface reaction mechanism is predominant in low Reynolds number flow.

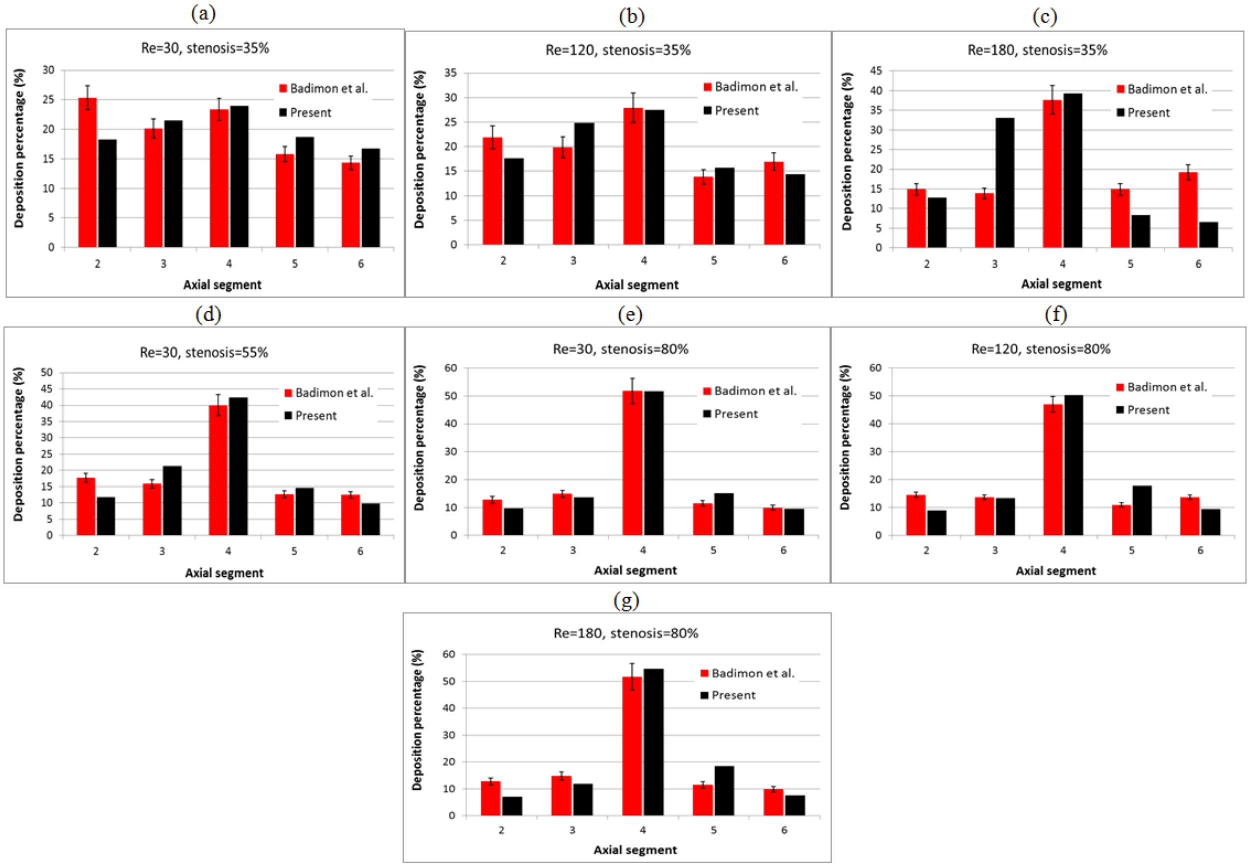

Figure 3.4 Comparison of 3D simulation results (black bars) with experimental data (red columns along with corresponding error bars) from Badimon and Badimon [47] for distribution of platelet deposition as a function of axial position (segments) in stenosed region of pig aorta.

3.3.4 Total Deposition: Temporal Evolution

Next, the base adhesion rates k_{rs_0}, k_{as_0}, and k_{aa_0} are calibrated with the absolute temporal values of platelet deposition observed in the experiments of Badimon and Badimon [47]. To do this, for each case with specific stenosis degree and blood flow rate the corresponding λ value (obtained in section 3.3.3) has been used to obtain k_{i_0} values. In the experiments by Badimon [47] the total perfusion times over which the platelet deposition in the stenosed area is measured are as long as 30 minutes which is not easy to reach in simulations due to computational limits. However we do not need to run our model for such long times because the rate of platelet deposition converges to constant values (Figure 3.5b). Figure 3.5a shows the time evolution of the mean value of total deposition in stenosed region for an exemplary case (Re=30, St=55%). A similar linear trend for platelet deposition was obtained for other cases. This linear behavior of the equations is also supported by Wagner and Hubbell [28], Govindarajan et al. [207] and Colace et al. [208]. Consequently, once convergence is achieved for platelet deposition rate, we can extrapolate our results linearly to larger times. In order to have a similar measure (i.e. line slope) for experimental data to compare the numerical results with, linear curve fits are obtained for Badimon's data. Figure 3.5c-i shows the results for time evolution of mean values of total platelet deposition in stenosed region.

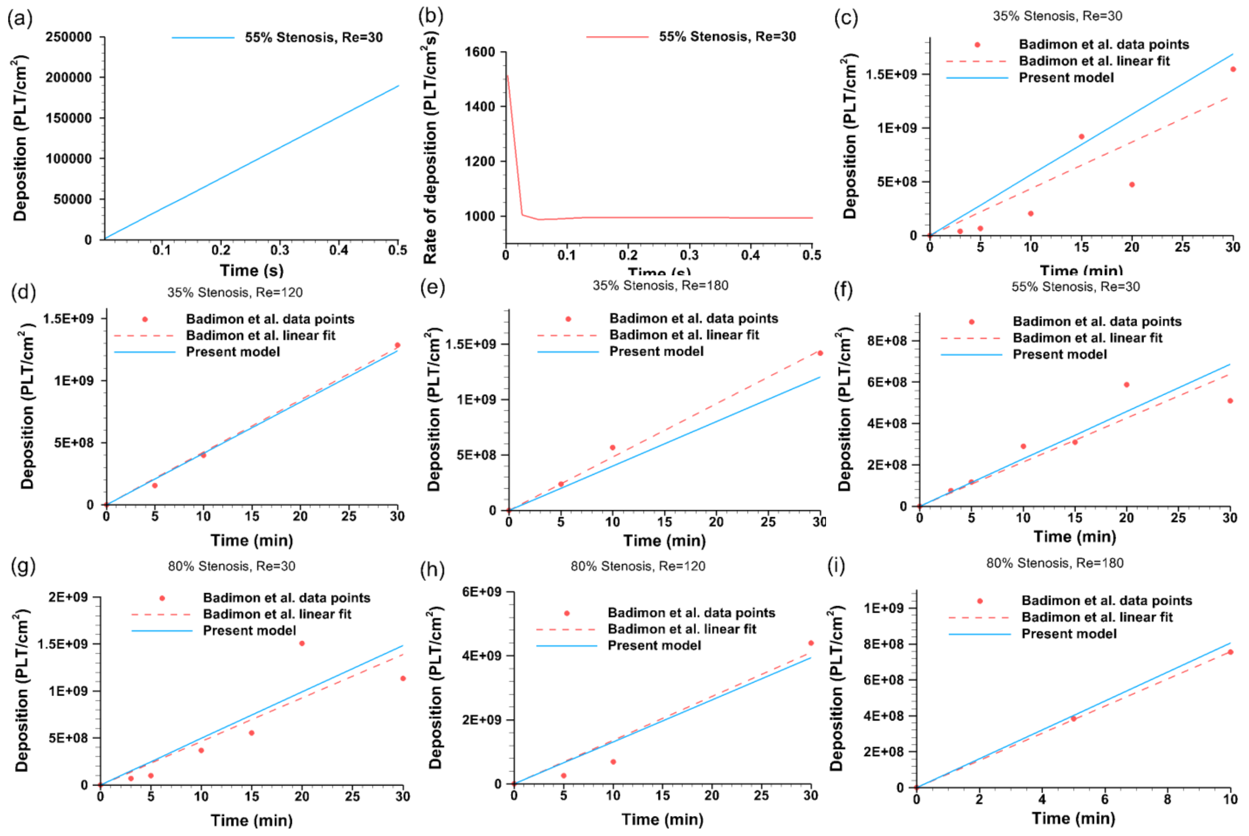

Figure 3.5 a) Mean value of deposition vs perfusion time in stenosed region (exemplary case: Re=30, 55% stenosis); b) rate of deposition vs perfusion time in stenosed region (exemplary case: Re=30, 55%); c-i) comparison of predicted values and experimental data from Badimon and Badimon [47] for time.

We fit surfaces to the obtained values of k_{rs_0}, k_{as_0}, and k_{aa_0} (in m.s^{-1}) to obtain a general function of stenosis degree and local Re at the apex of the stenosis (see Eq. B.2 in Appendix B).

3.3.5 Model Validation

3.3.5.1 Ex-vivo study case

To validate the model we apply it to a new system studied by Mailhac et al. [49] and employ the adhesion rates calculated using Eqs. B.1 and B.2 (see Appendix B). They measured platelet deposition in three different segments (i.e. prestenosis, apex, poststenosis) of 80% stenosed aorta at Re_{apex}=300 with a peak shear rate of 128,800 s^{-1} at the apex. The inlet platelet concentration is set to 252,000 $PLT.mm^{-3}$ to be consistent with the experiments.

Figure 3.6 compares the predictions using the calculated values of λ and k_{i_0} from Eqs. B.1. and B.2 (Appendix B). Measurements given for three intervals by Mailhac et al. [49] are quasi-linear, whereas the numerical values are linearly extrapolated based on a constant value of rate of deposition for short times. For the apex region the model overpredicts the deposition after considering the uncertainty in experiments. However, the predicted deposition values for prestenosis and poststenosis segments match well with the experimental data.

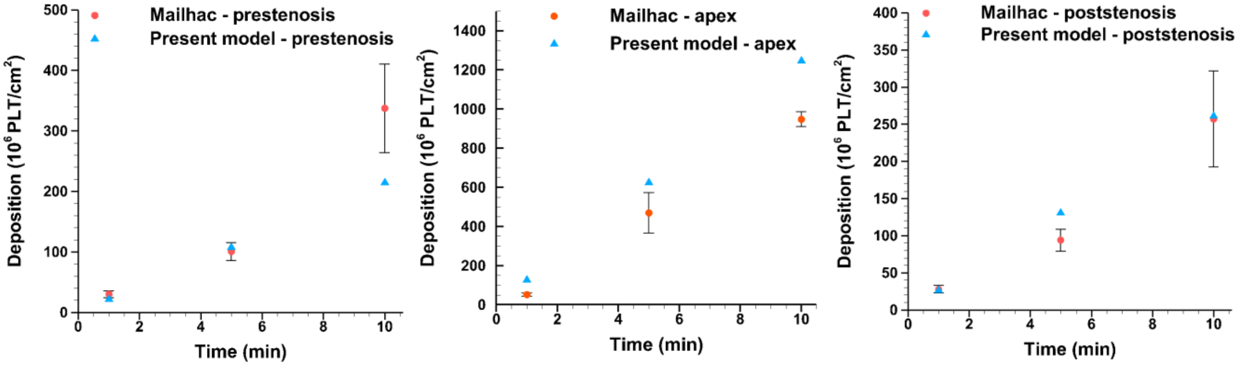

Figure 3.6 Predicted values vs experimental data from Mailhac et al. (62) for platelet deposition at prestenosis, apex and poststenosis regions; Re=60, 80% stenosis.

3.3.5.2 In-vitro study cases

The second validation case is set up based on the in-vitro experimental study of Wootton et al. [111]. Non-heparinized blood was perfused into the stenosed collagen-coated glass tubes and platelet accumulation was measured over the stenosis. Heparin level was set to zero for this set of simulations and an inlet concentration of 252,000 $PLT.mm^{-3}$ was imposed for platelets. For other species, the normal concentration levels were injected based on the given blood preparation methods in [111]. Also the shear-dependent diffusivity (see Eq. 3.5) was applied for platelets to account for the presence of red blood cells.

Platelet deposition was measured in 5 regions of interest (ROI) as explained by Wootton et al. [111] and the values for platelet accumulation rate at each ROI were reported for three stenosis degrees of 29.3%, 50%, and 68.4%. According to [111], the accumulation rate was calculated using the expression:

$$V_{acc} = \frac{R_{acc}}{N.A_{ROI}} \tag{3.22}$$

where V_{acc} is the accumulation rate ($\mathrm{mm.s^{-1}}$), R_{acc} is the number of platelets in ROI per unit time ($\mathrm{PLT.s^{-1}}$), N is the average near-wall platelet count in ROI ($\mathrm{PLT.mm^{-3}}$), and A_{ROI} is the ROI area ($\mathrm{mm^2}$). The average near-wall platelet count in our simulations was found to be $\sim 252{,}000\ \mathrm{PLT.mm^{-3}}$. Figure 3.7 shows the predicted values by our model compared to experimental results for different stenosis severities.

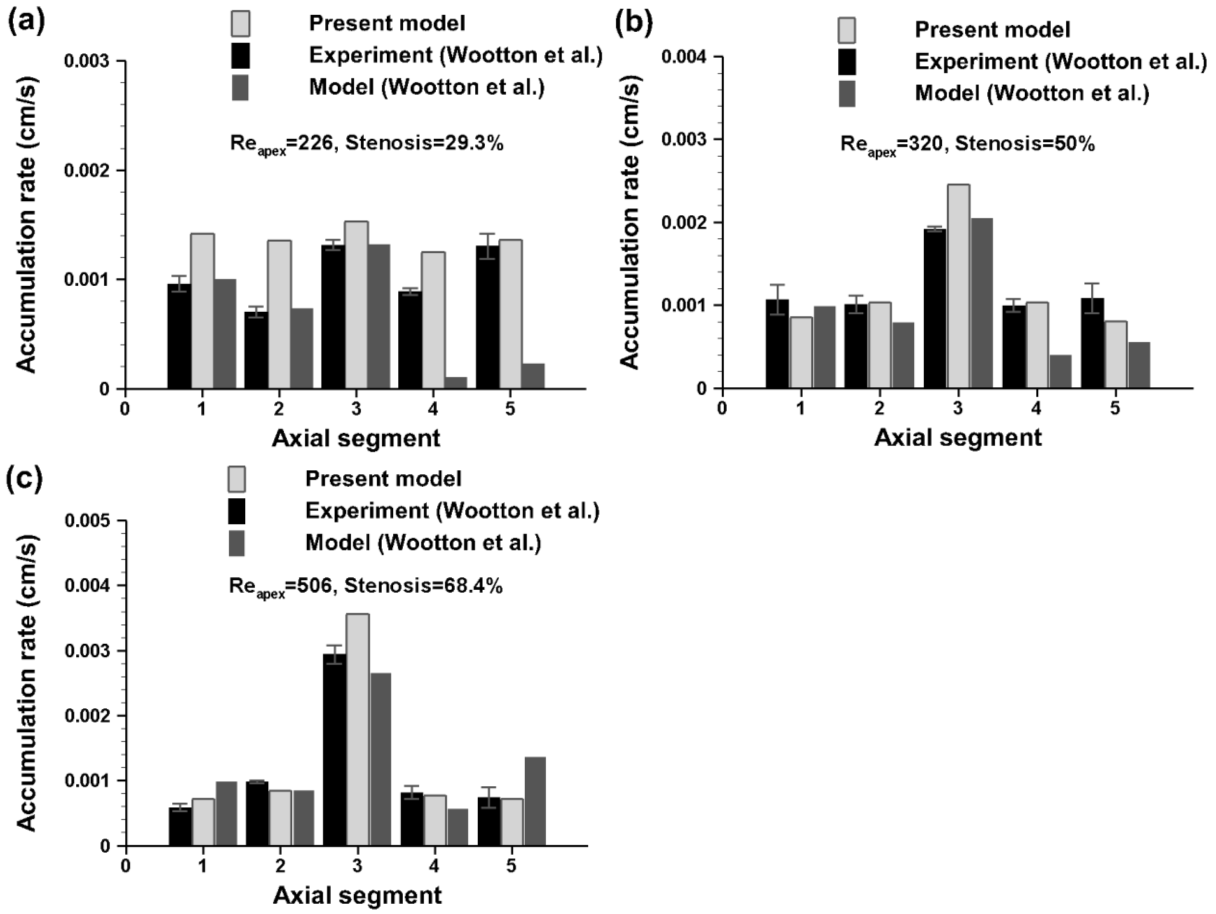

Figure 3.7 Comparison of predicted platelet accumulation rates by present model with experimental (mean±standard error) and numerical results from Wootton et al. (30). a) Re=160, 29.3% stenosis, b) Re=160, 50% stenosis, c) Re=160, 68.4% stenosis.

The current model matches experimental measurements well in the upstream, throat, and downstream sections of all three stenoses, whereas Wootton's model under predicts the deposition in segments 4 and 5 of 29.3% and 50% stenoses. The discrepancy of their model in the 29.3% stenosis case is more than one order of magnitude. However, the results from the present model agree well with the experimental data, especially for the 50% and 68.4% stenoses. Predicted occlusion times are 12, 31, and 77 min respectively for 68.4%, 50%, and 29.3% stenoses. Wootton's model predicted occlusion times (including lag times) of 15, 27, and 64 min for these cases. However, experimental measurements of Markou et al. [145] showed that no occlusion occurs for the 29.3% stenosis. Occlusion times in our study were calculated based on the peak accumulation rate in the stenosis throat and the distance between the apex and tube centerline. In order to do this, we divided the values of deposition per unit area by substrate capacity (M_∞); this gives the number of platelet monolayers. The number of layers was multiplied by the effective platelet diameter. An effective platelet diameter of $4.5\ \mu m$ was obtained using the occlusion time and the number of platelets deposited in segment 3 of 29.3% stenosed tube reported in [111].

The model was also applied to another set of validation cases based on experiments of Casa and Ku [147]. Whole porcine blood with a platelet count of 480,000 PLT.mm^{-3} was perfused at steady state into the test section of stenosed glass tubes coated with collagen. The blood was heparinized at 3.5 USP units.mL^{-1}, as described in [147]. Stenosis level, based on the diameter reduction, was ~78% and steady experiments were performed at apex wall shear rates of 3800, 6500, and 16000 s^{-1}. The corresponding inlet velocities are 0.66, 1.13, and 2.9 cm.s^{-1} respectively. Also the shear-dependent diffusivity (see Eq. 3.5) was applied for platelets to account for the presence of red blood cells. Figure 3.8a-c show the predicted results using the current model versus experimental SEM images for four instances corresponding to $0.25t_{occ}$, $0.5t_{occ}$, $0.75t_{occ}$ and complete occlusion time, t_{occ}. Occlusion time reported in [147] are the whole perfusion times, including lag times. The current model predicts the acute accumulation phase during which a distinguishable amount of deposition occurs. Most deposition takes place in this phase and the time that should be discarded is called the lag time (when the thrombus volume reaches $10^6\ \mu m^3$). Lag times are 60, 40, and 25 s for the 3800 s^{-1}, 6500 s^{-1}, and 16000 s^{-1} cases respectively. Occlusion times obtained using the present model are 5.2, 2, and 3.75 min compared to experimental times of 6.2 ± 1.7, 4.6 ± 2.7, and 4.6 ± 1.75 min respectively corresponding to cases with wall shear rates of 3800, 6500, and 16000 s^{-1}. All predicted occlusion times using our model are within the uncertainty limit of experiments, whereas results predicted using models of Mehrabadi et al. [43] and Bark et al. [51] do not fall in the experimental uncertainty range for cases with peak wall shear rates of 3800 s^{-1} and 16000 s^{-1} (Figure 3.8d). Also our predicted occlusion times agree better with experimental measurements trend wise; the case with wall shear rate of 6500 s^{-1} has the shortest blockage time compared to the other cases, whereas occlusion times predicted by other models are monotonic decreasing (Mehrabadi's model) and increasing (Bark's model) functions of wall shear rate.

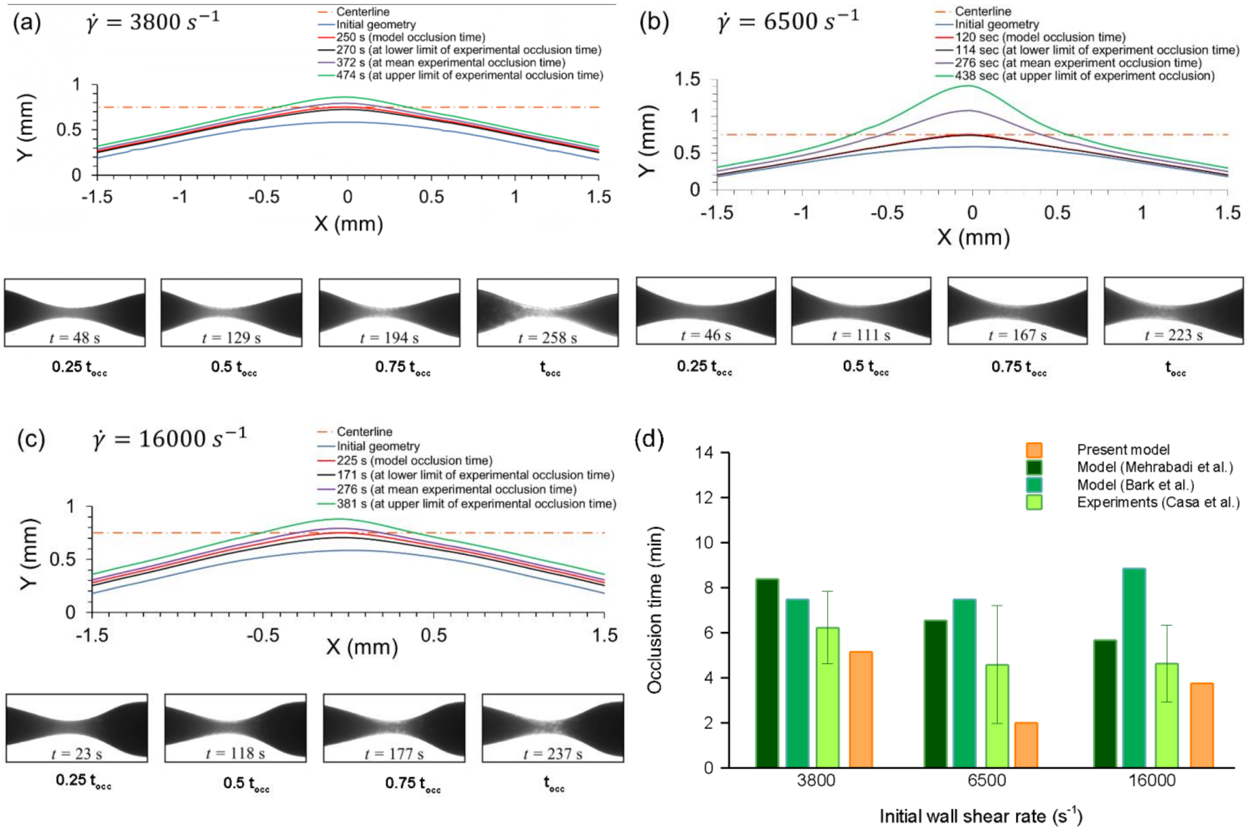

Figure 3.8 Comparison of predicted axial distribution of platelet deposition with experimental measurements of Casa and Ku [147] along with model predictions at lower limit, mean, and upper limit (mean±standard deviation) of experimental occlusion time: a) low shear case $\dot{\gamma}_w$=3800 s^{-1}; b) intermediate shear case $\dot{\gamma}_w$=6500 s^{-1}; c) high shear case $\dot{\gamma}_w$=16000 s^{-1}; d) predicted occlusion times by present model compared to predictions of Mehrabadi [148] and Bark [51] models as well as experimental data by Casa and Ku [147]. Experimental images are reprinted from Casa and Ku [147] with permission from Springer.

Finally, the model was applied to a 3D asymmetrically stenosed rectangular channel with test section of 300 $\mu m \times 750 \mu m \times 3000 \mu m$ studied in-vitro by Li et al. [205]. Numerical results of using the current model are compared for four cases with Li's experimental data. Stenosis degree is 66.7% for all cases and four different flow rates are imposed at the inlet which yield shear rate magnitudes of 4000, 7000, 10000, and 13000 s^{-1} at the apex. The stenosed side (bottom wall) was coated with collagen, and a platelet concentration of 248,000 PLT.mm^{-3} was set at the inlet section of the channel. Experimental results provided the full occlusion times and occlusion volumes. The occlusion volume is the integrated volume flow rate over perfusion time and was calculated by multiplying the occlusion time by inlet volume flow rate. The comparison between numerical and in-vitro experimental results are illustrated in Figure 3.9.

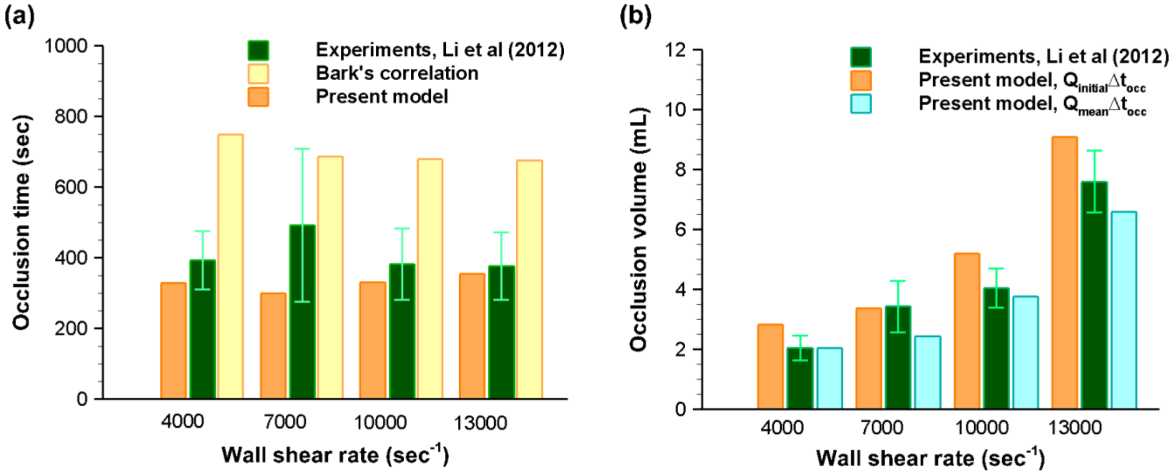

Figure 3.9 Predicted occlusion times and occlusion volumes compared to experimental results [205] in stenosed channel with 66.7% asymmetric stenosis at maximum wall shear rates of 4000, 7000, 10000, and 13000 sec^{-1}. a) Experimental data with standard deviation of Li et al. [205], results predicted by Bark's model [51], and results of the current model for channel occlusion time. b) Perfused blood volumes until full occlusion. Two flow rates were used to calculate the occlusion volume: 1) the initial flow rate which remains constant during the simulations ($Q_{initial}$), and 2) the mean flow rate which is calculated based on experimental data of Li et al. for $Q(t)$ versus perfusion time; averaging flow rate over perfusion time yields $Q_{mean} \approx 0.72Q_{initial}$ and Δt_{occ} values are occlusion times given in Fig. 3.9(a).

Occlusion times are calculated using mean platelet deposition (averaged in z direction) at the apex where lumen area in narrowest. As Figure 3.9a shows, using our model, we predict a normal closure time range of 300-354 s. All predicted occlusion times are in agreement with the experimental values from Li et al. [205]. Bark et al. [51] obtained an empirical correlation for thrombus growth rate as a function of shear rate. Using their correlations, the occlusion times are over predicted except for the case with maximum wall shear rate of 7000 s^{-1}. Whereas, predicted closure times using our model fall within the uncertainty limits of experimental results for all cases. Two sets of numerical results for occlusion volumes are compared with experimental data in Figure 3.9b depending on the flow rate value used. The first set was obtained by multiplying the occlusion time with the initial flow rate $Q_{initial}$ which remains constant during the simulations. For the second set of results, the mean flow rate (averaged over perfusion time) was used. The mean flow rate, based on the experimental observation of Li et al. [205], Q_{mean} is decreased to ~$0.72Q_{initial}$. This decrease is due to an increase in pressure drop caused by the gradual change of stenosis shape which is not included in our simulations by assuming a stationary (top) wall. The occlusion volume values of 2-6.6 mL are reasonably well predicted and lie within the experimental range of 1.6-6.6 mL.

3.3.6 Limitations

Wall shear-gradient effects in the recirculation zone distal to the apex (see Figure 3.10b and c), shear rates as high as 2300 s^{-1} and vortex shedding in stenotic blood flows can lead to embolization [163], [186], [208], [209]. Detachment of platelet aggregates from thrombi formed on the stenosis can occur followed by convection of emboli downstream [170]. Such free emboli formation depends on exposure time of thrombus to high shear, properties of formed thrombus and wall shear rate values. Given the experimental results from Badimon [47], we can notice a considerable drop in platelet deposition values after 15 minutes of perfusion (see Figure 3.5c, f, and g for drop in deposition and Figure 3.10b and c for streamlines in recirculation zone). However, by fitting a linear curve on experimental data points and using the linear extrapolation of simulation results for platelet deposition, we assume no free emboli formation takes place. According to Wootton et al., tubes with 75% and 90% stenoses were completely occluded as blood was perfused into the stenosis, whereas no occlusion occurred for the 50% stenosis case [111]. This is attributed to embolization after a certain change in throat geometry, whereas our model does not include the modeling of embolization. Our model predicts an occlusion time of 77 min for the 50% stenosis case. Experimentally measured occlusion times for 75% and 90% stenoses are not provided in Wootton’s study.

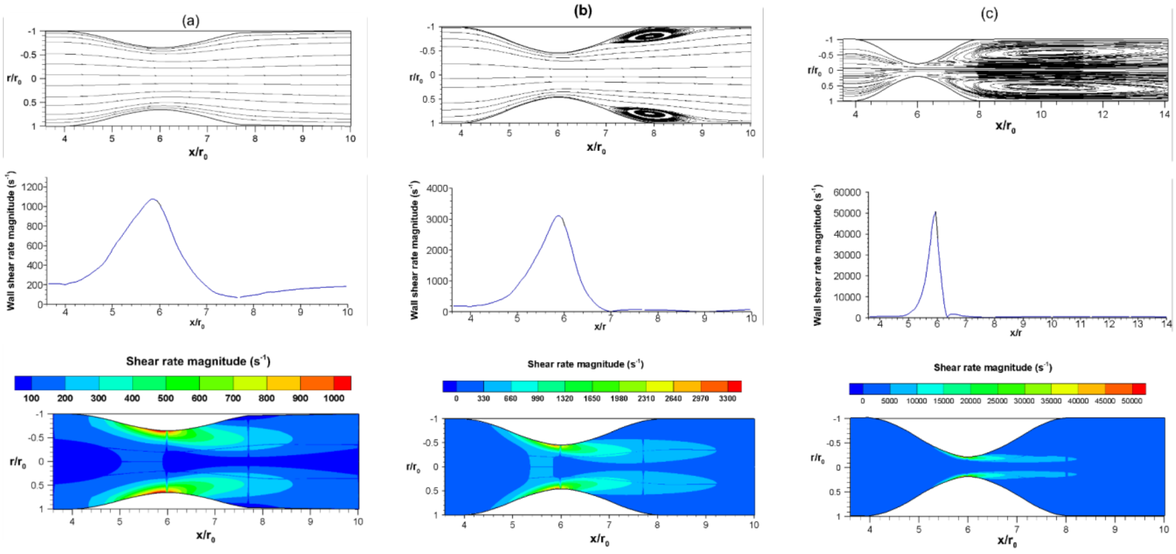

Figure 3.10 Streamlines, shear rate magnitude contours, and arterial wall shear rate magnitude as a function of axial position (normalized with respect to unstenosed tube radius) corresponding to Badimon’s cases [47]: a) case4: Re=30, 35% stenosis; b) case7: Re=30, 55% stenosis; c) case 8: Re=30, 80% stenosis. Higher stenosis degree (i.e. 55% and 80%) results in a recirculation zone distal to the apex, which in turn can lead to embolization.

In addition to embolization, fibrin deposition on the apex can affect the rate of deposition at high wall shear rates. Experimental observations by Barstad et al. [146] show that fibrin acts as a cap on the collagen-anchored platelet aggregates. This, results in lower platelet deposition in high shear regions. Deposition of fibrin (polymerized from fibrinogen existing in whole blood) is not measured by Badimon [47] and Mailhac et al. [49]. Therefore the thrombus is assumed to be made of platelet masses only. Thus our model does not explicitly model fibrin deposition.

The other fact which is not considered by making a linear thrombus growth assumption is that the vessel wall geometry does not change in shape. Assuming a diameter of 1-5 μm for deposited platelets, the mean values of thrombus height in stenosed region can reach values as high as ~100 μm, which is large enough to affect the flow patterns and evolution of thrombus growth. The model can be improved if the wall boundary is adjusted accordingly based on local deposition values to reflect the mural change in thrombus geometry.

All validation cases in the present work were studied under steady flow conditions. Effects of pulsatility on platelet deposition are studied by Casa and Ku [147] and Taylor et al. [197] in stenosed tube and rotating disc system. Modeling viscosity as a variable blood property (as a function of local shear rate) is required in unsteady/pulsatile flow conditions because of non-Newtonian behavior of blood in shear rates below 100 s^{-1}. Validation of the model under pulsatile flow conditions can be conducted as future work. Additionally, as the vessel nears occlusion, the viscosity becomes a function of the tube diameter (due to Fahreus-Lindquist effect). In the current model, this phenomenon was assumed to have negligible effect on platelet deposition, since the geometry does not change during the simulation.

3.4 Summary and Conclusion

In this chapter, a physics-rich predictive time- and shear-dependent physiochemical model was presented. The deposition results of the model have been shown to agree well with the experimental measurements. First, our predictions of axial platelet deposition for three channel flows were compared to experimental results to validate our model. Simulation results agreed well with corresponding experimental data. The model was then applied to the stenosed region of aortas with mild to high stenosis degrees under different flow conditions measured experimentally by Badimon and Badimon et al. [47]. Shear-dependent platelet adhesion rates were used and calibrated to find the value of shear enhancement factor as a function of stenosis severity and Reynolds number at apex. Finally, the calibrated model was applied to a new system with different flow characteristics [49]. Using the general functions for shear enhancement factor λ and reaction rate constant k_{i_0}, the values of these parameters were calculated based on the stenosis and local Re at the apex and acceptable agreement was achieved using the calibrated λ and k_{i_0}. As a concluding remark, our results reveal that the platelet adhesion in stenotic flow is a function of stenosis severity and Reynolds number at the stenosis apex and cannot be defined solely by shear rate values at the vessel wall. To the best of our knowledge, this is the first model that attempts to generalize predictions to more than one experimental observation.

Continuous platelet deposition in coronary arteries creates a narrow necking area at some potential regions such as bifurcations and ruptured vessel walls. These narrow regions are the number one cause of heart attacks. Thus, modeling time-dependent thrombus formation and growth can be beneficial for medical diagnosis and treatment. The presented simulations provide useful guidelines to design improved tools such as artificial valves, stents, etc.

4 Effect of platelet activating agonists and flow pulsatility on thrombus formation

4.1 Introduction

The effect of platelet activating agonists (i.e. adenosine diphosphate (ADP) molecules, thromboxane A_2 (TxA_2), and thrombin) on thrombus formation has not been studied extensively in the literature. Also, changes in thrombus growth rate due to pulsatility under physiological conditions are not well known yet. In this chapter we investigate the sensitivity of thrombus growth rate to flow pulsatility and to the presence of activating factors (i.e. ADP, TxA_2, and thrombin) in blood flow. The model introduced in chapter 3 was used for investigating these effects.

4.2 Investigation of effect of agonists on thrombus growth

4.2.1 Studied cases

Two experimental cases were chosen to study the effect of different agonists on thrombus growth. One of them is the experimental study of Mehrabadi et al. [148] (case 1) and the other one is from Wootton et al. [111] (case 2). Both experiments were performed with whole blood, which includes all platelet activating agonists, perfused in collagen-coated tubes. Flow characteristics and geometric parameters of the two cases are given in Table 4.1. To perform the sensitivity analysis, each of the platelet activating agonist was individually eliminated from the model to quantify its effect on platelet activation and deposition. Platelet activation is known as a precursor of thrombus formation and high levels of these agonists in blood can be defining in the evolution of thrombosis. It is calculated by summing the concentrations of ADP, TxA_2, and thrombin (Eq. 4.1) normalized by their critical values $C_{ADP_{crit}} = 2$ μM, $C_{TxA2_{crit}} = 0.6$ μM, $C_{T_{crit}} = 0.1$ U.ml^{-1} over the activation time ($t_{act} = 1s$). By performing the sensitivity analysis we investigate the potential relationship between coagulation proteins and platelet deposition.

$$k_{pa} = \frac{1}{t_{act}}\left(\frac{C_{ADP}}{C_{ADP_{crit}}} + \frac{C_{TxA_2}}{C_{TxA_{2}{}_{crit}}} + \frac{C_T}{C_{T_{crit}}}\right) \tag{4.1}$$

Table 4.1 Flow characteristics and geometric parameters of cases tested for sensitivity analysis

Studied case	Stenosis (%)	Re_{apex}	Blood type	Ref.
Case 1	71	74	Whole blood	Mehrabadi et al. [148]
Case 2	68.4	602	Whole blood	Wootton et al. [111]

4.2.2 Results

Results for platelet deposition, platelet activation as well as concentration of platelets are compared here between the full model (including all agonists) and the model with excluded agonists. Elimination of ADP, TxA_2, and thrombin can affect platelet activation and deposition depending on the flow conditions and inlet concentration of platelets and agonists. Mehrabadi's case has a stenosis degree of 71% and $Re_{apex} = 74$, whereas for Wootton's case, the stenosis degree is 68.4% and $Re_{apex} = 602$. Concentration of platelets at inlet was 250,000 PLT.mm^{-3} in Mehrabadi's experiments. Similarly in Wootton's experiments blood was perfused with a platelet count of 252,000 PLT.mm^{-3} at the inlet. All simulations (for both cases) were run with steady flows at the inlet.

Table 4.2 compares the results obtained for platelet deposition, and platelet activation rate for the full model (that includes all platelet activating agonists) and models with eliminated agonists (i.e.

ADP, TxA_2, and thrombin) at $t=t_{qss}$ when the simulations reach a quasi-steady state. As mentioned in Chapter 3, quasi-steady state ($t=t_{qss}$) is said to occur when the thrombus growth rate (platelet deposition rate) converges to a constant value. Note that both prothrombin and antithrombin are also excluded from the model when eliminating the thrombin from the model because the presence of prothrombin will lead to generation of thrombin in blood. Also, antithrombin will not affect the formation of thrombus in the absence of thrombin; therefore, all thrombin-related proteins were excluded when eliminating the thrombin from the model.

In both cases platelet activation occurs only due to high concentration of ADP with other agonists contribute less than 1% to activation. Deposition values are not affected by activating agonists in case1 where less than 1.2% difference was observed, whereas for case 2 although thromboxane A_2 and thrombin do not affect the deposition, the model without ADP predicts less deposition (~9%). This is due to ADP contribution to platelet activation; once platelets get activated they deposit faster at the vessel wall because adhesion rates of activated platelets are always larger than that of resting platelets ($k_{as} = k_{aa} = 1.24k_{rs}$). ADP did not affect the deposition in case 1 because platelet activation did not contribute more than 1.2% to platelet deposition.

The insignificant effect of thromboxane A_2 and thrombin on deposition is due to their direct relationship with deposition values M_{at}. According to Eqs. (3.16) and (3.18), generation of TxA2 and thrombin depend on deposition, therefore in short perfusion times (~0.3s for sensitivity cases) their effect is negligible due to smaller number of platelets deposited on the wall. Note that these agonists are generated at the surface of platelets.

Table 4.2 Effect of ADP, TxA_2, and thrombin on platelet activation and deposition. Deposition and platelet activation rates at the stenosis apex are compared at t=0.3s when a quasi-steady state is reached. Percentages in parentheses are the difference between full model results and results using the model without an agonist.

Case	Model	Platelet activation rate (s^{-1})	Deposition ($PLT.cm^{-2}$)
1	Full model	1.816	73641
1	Model w/o ADP	0 (100%)	72785 (1.16%)
1	Model w/o TxA_2	1.81 (0.3%)	73640 (<0.1%)
1	Model w/o thrombin	1.8 (0.88%)	73639 (<0.1%)
2	Full model	7.267	1.00242×10^6
2	Model w/o ADP	0 (100%)	9.11×10^5 (9.12%)
2	Model w/o TxA_2	7.268 (<0.1%)	1.00382×10^6 (0.14%)
2	Model w/o thrombin	7.002 (<0.1%)	1.00175×10^6 (<0.1%)

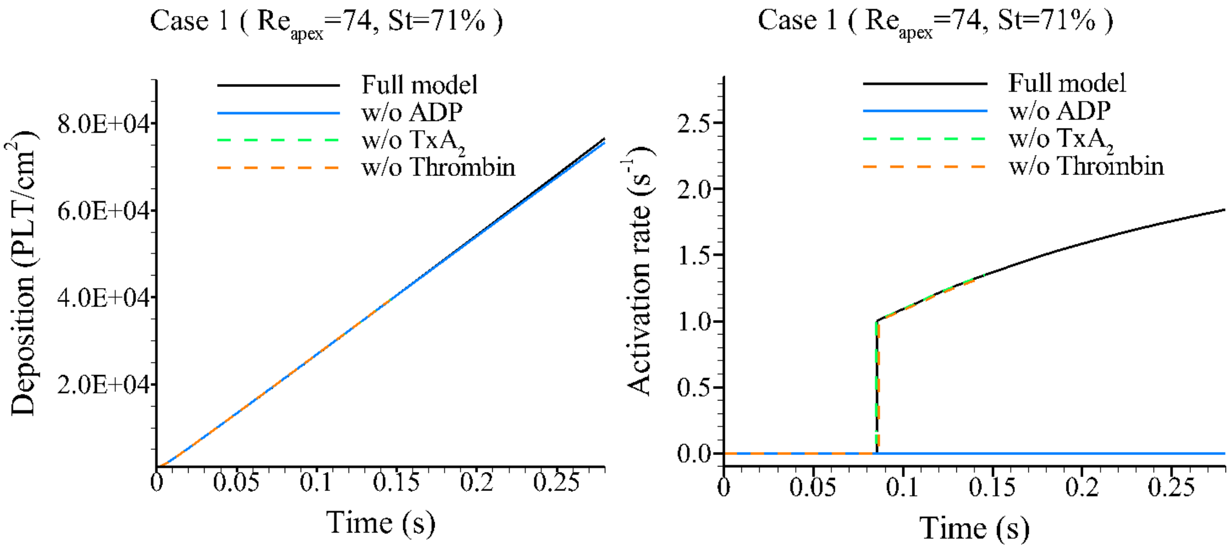

Figure 4.1 Effect of different agonists on platelet deposition, activation, and concentration of platelets for Mehrabadi's case [148]: case 1 with St=71% and Re_{apex}=74.

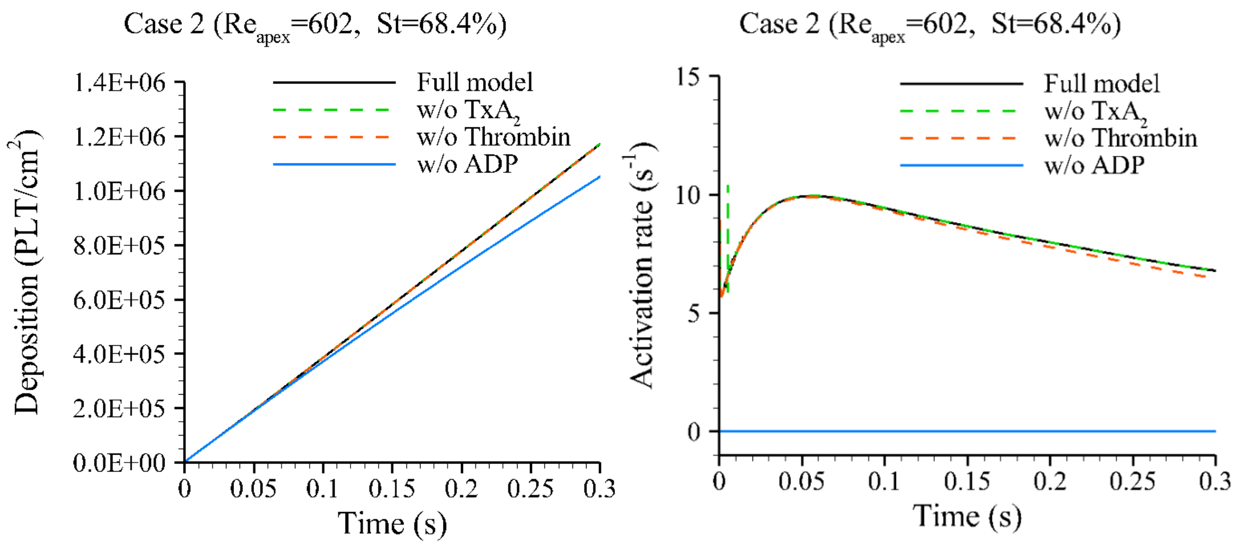

Figure 4.2 Effect of different agonists on platelet deposition, activation, and concentration of platelets for Wootton's case [111]: case 2 with St=68.4% and Re_{apex}=602.

4.3 Effect of pulsatility on thrombus growth rate

4.3.1 Studied case

There is only one experimental study in the literature that has studied the effect of pulsatility on thrombus growth and the time taken for occlusion of lumen area in stenosed vessels. Casa and Ku [147] perfused blood through a stenosed glass tube coated with collagen, under both steady and pulsatile conditions. For both cases, whole porcine blood with a platelet count of 480,000 PLT.mm^{-3} was perfused at steady state into the test section of stenosed glass tubes coated with collagen. The blood was heparinized at 3.5 USP units.mL^{-1}, as described in [147]. Stenosis level, based on the diameter reduction, was ~78% and steady experiments were performed at apex wall shear rates of 3800, 6500, and 16000 s^{-1}. The corresponding inlet velocities are 0.66, 1.13, and 2.9 cm.s^{-1} respectively. Also the shear-dependent diffusivity (see Eq. 3.5) was applied for platelets to account for the presence of red blood cells. In the steady case the maximum wall shear rate, which occurs at the apex, was 3800 s^{-1}. In the pulsatile case, the mean wall shear rate within a cycle was 3800 s^{-1} to be consistent with the steady case. 62 beats occur per minute and each cycle is 1.02 second (T=1.02s). Therefore, the frequency of pulsatility was 0.97 Hz and the blood perfusion continued for 4 min. Figure 4.3 shows the pulsatile profile imposed by Casa and Ku [147] at the inlet. Due to slight differences in different cycles in the experiments and also in order to have a periodic profile as a function of time to use in our calculations, a curve was fitted to the experimental data. A curve fit was done using a sum-of-sine profile in MATLAB® (MATLAB 8.4, The Mathworks Inc., Natick, MA, 2014) for 0-1 s. The velocity profile function obtained in MATLAB is given in Appendix C (Eq. C.1.).

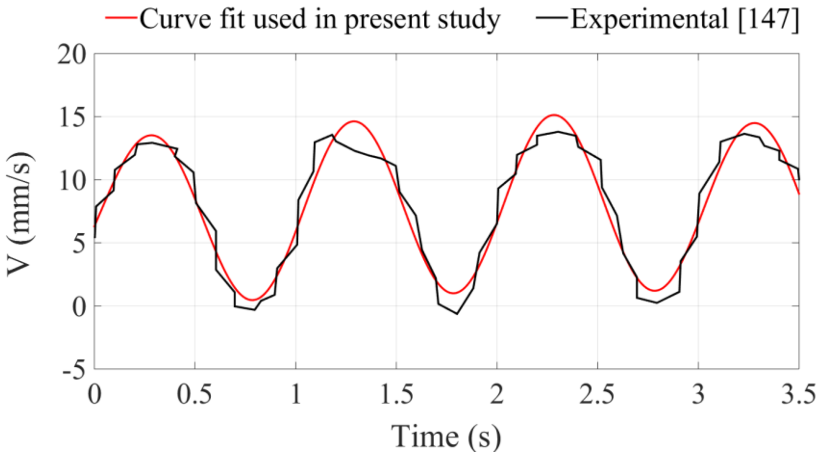

Figure 4.3 Comparison of experimental pulsatile blood flow profile (black) used in [147] and the fitted curve used in present study (red). The mean velocity averaged over a cycle is 6.6 mm.s^{-1} and each cycle is 1.02s (62 bpm).

4.3.2 Results

Both steady and pulsatile simulations were run for a time period equal to 5 cycles of pulsatile flow and thrombus growth rate was compared during this period. Three probes were put in the prestenosis, stenosis, and poststenosis regions of the test section to monitor the rate of thrombus growth rate. Figure 4.4 shows the locations of these probes. Figure 4.5 compares the instantaneous (black curve) and running time-averaged (orange curve) thrombus growth rate in the prestenosis region for the pulsatile case and the constant thrombus growth rate for the steady case. The orange curve corresponds to the averaged growth rate values over perfusion time: at a given time of t, the instantaneous growth rates from 0 to t are summed and divided by time t to calculate the time averaged value at t. As Figure 4.5 shows, for the case with steady flow thrombus growth rate converges to a constant value, whereas for the case with pulsatile blood flow, the growth rate fluctuates during each cycle in a pseudo-periodic manner.

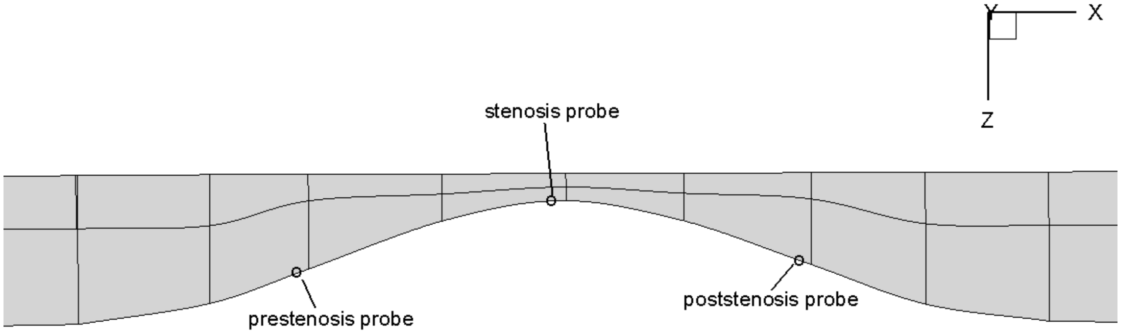

Figure 4.4 Probe locations in prestenosis, stenosis, and poststenosis regions of the stenosed test section.

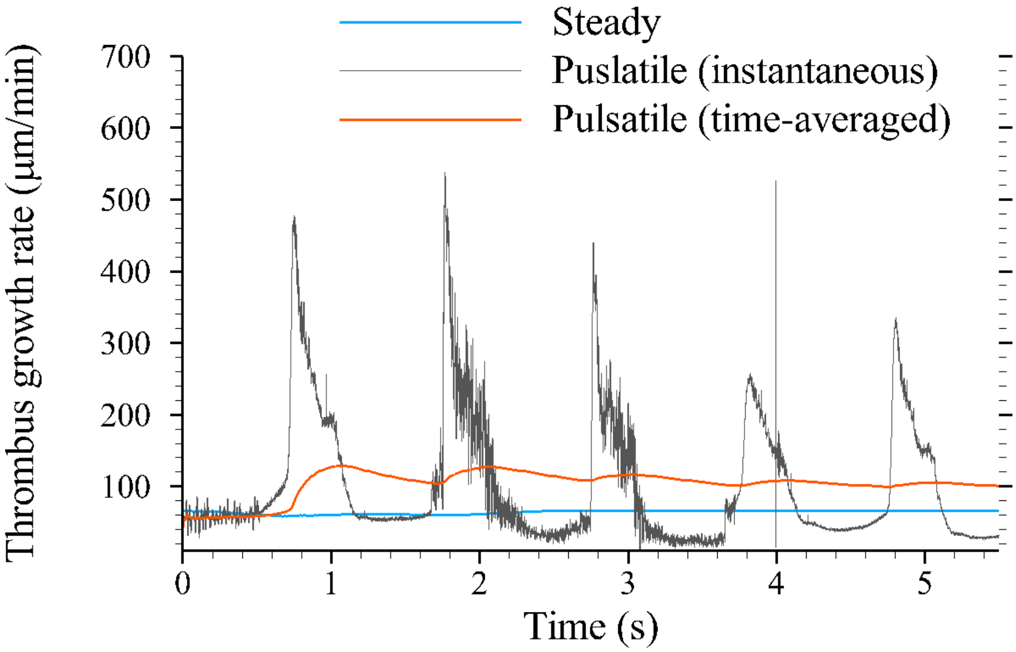

Figure 4.5 Comparison of thrombus growth rate in prestenosis region for Casa's cases [147] with steady and pulsatile inlet velocity profiles after 5 cycles of pulsatile flow. 62 beats occur per minute and each cycle is 1.02 second (62 bpm). Blue curve shows the variation of thrombus growth rate for the steady case. Black curve shows the instantaneous change of thrombus growth rate with time for pulsatile case. The orange curve corresponds to a running time-averaged growth rate over perfusion time: at a given time of t, the instantaneous growth rates from 0 to t are summed and divided by time t to calculate the running time averaged value at t.

As seen in Figure 4.7 and Figure 4.7 the trend of temporal variation of thrombus growth rate is different in prestenosis, stenosis, and poststenosis regions. In the prestenosis area, the thrombus growth rate increases slowly until the flow rate reaches it maximum value (t=0.274 s). With flow deceleration the growth rate starts to increase substantially and rapidly increases to its peak value when the flow rate is close to zero (t=0.777 s). We attribute this to the flow deceleration in this region because of the presence of stenosis, leading to larger residence times of platelets and higher deposition (see Figure 4.6 for the reverse flow and the recirculation zone around the apex from t=0.611s to t=0.893s). Note that platelets adhering to the wall through diffusion become a dominant mechanism when flow rate is close to zero (t=0.777 s). In the poststenosis region, variation of thrombus growth rate follows a trend opposite to the prestenosis area. Thrombus grows faster when flow acceleration is maximum and slower when the flow rate drops to its minimum value. Platelet adhesion rates depend on local wall shear rate according to Eq. (3.21). Thus, adhesion rates will increase when the flow rate (or wall shear rate) increases. Note that in this region thrombus formation is driven by both diffusion and adhesion mechanisms since the flow rate is not zero. In the middle (i.e. stenosis apex) region, the peak values of thrombus growth rate occur at some time between those of prestenosis and poststenosis regions. However, the peak values at the stenosis apex are highest (higher than prestenosis and poststenosis areas) within a cycle simply because the maximum wall shear rate occurs at the apex.

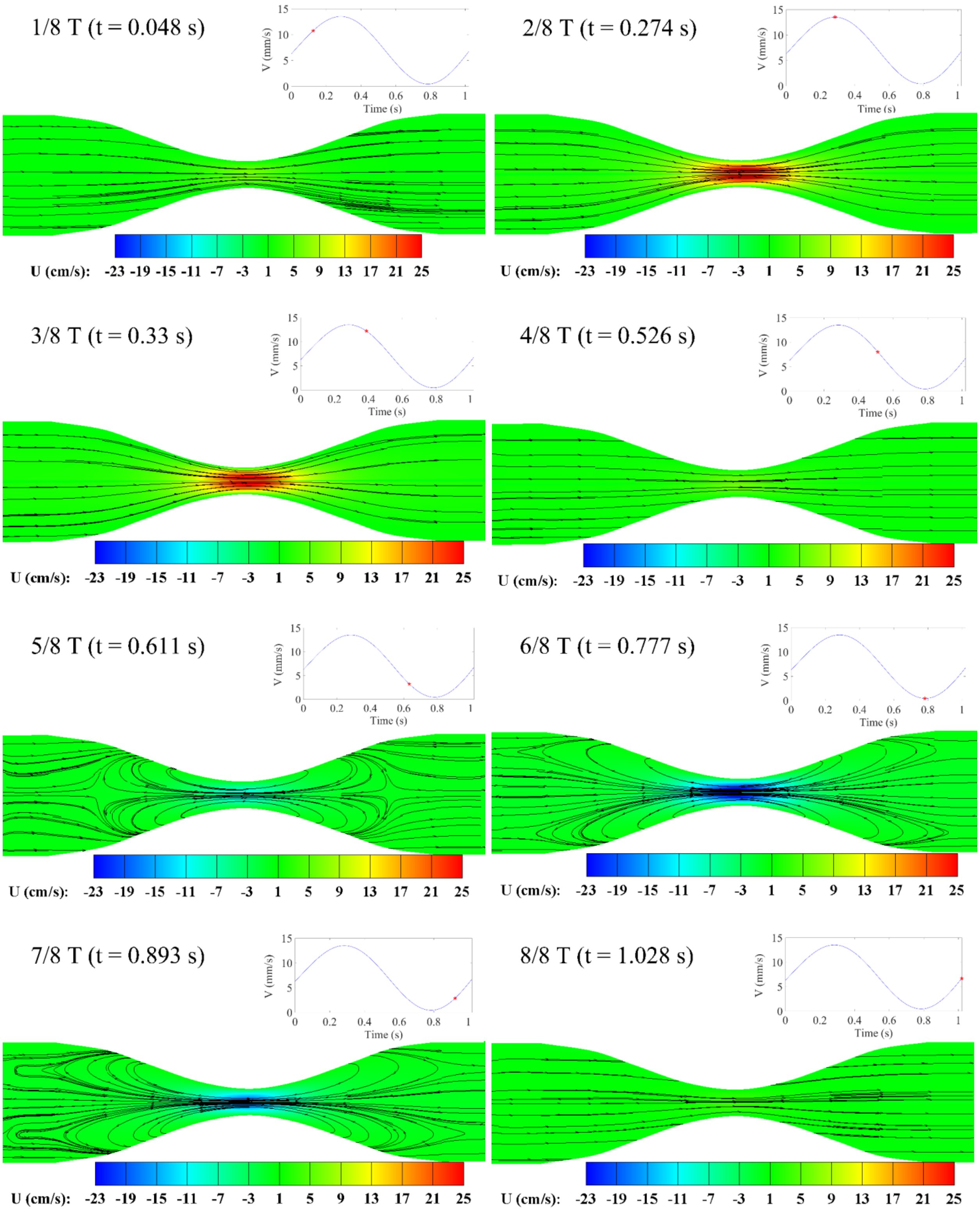

Figure 4.6 Velocity contours and streamlines at the stenosed area of the vessel at eight time values: t=0.125T, 0.25T, 0.375T, 0.5T, 0.625T, 0.75T, 0.875T, and T where T=1.02s.

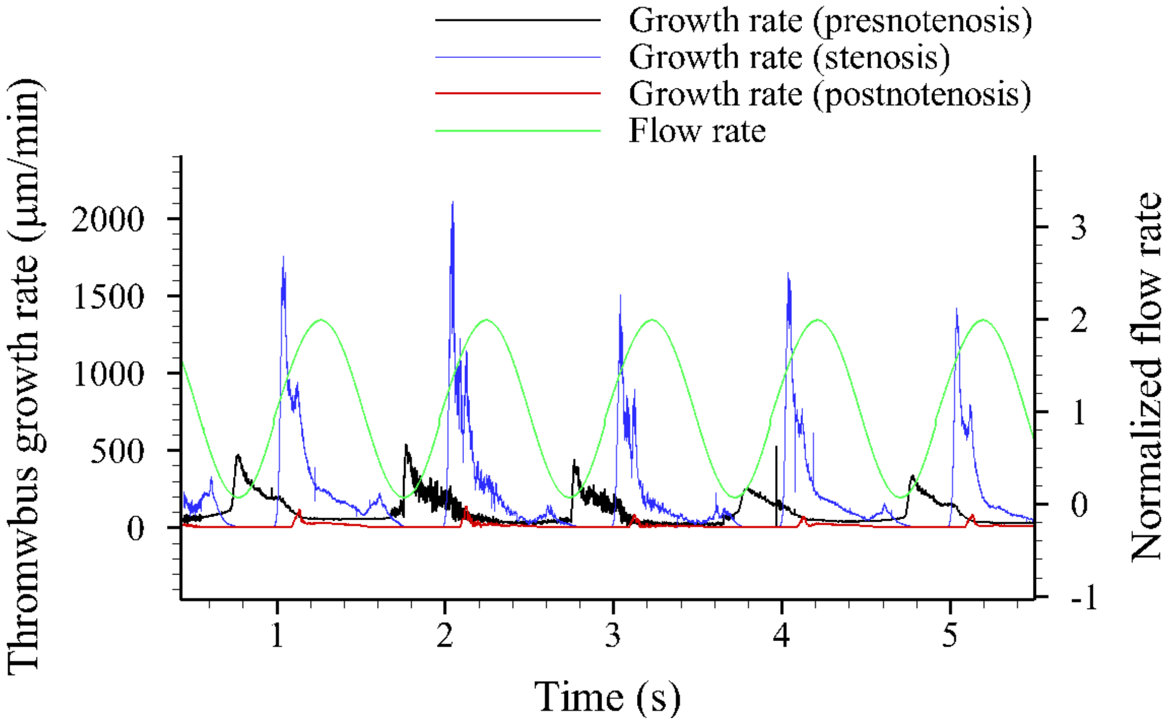

Figure 4.7 Comparison of thrombus growth rates in different regions of stenosed section under pulsatile flow conditions. Flow rate values (green curve) are normalized with respect to the mean flow rate.

Casa and Ku [147] reported occlusion times of 5.44±2.9 min for the pulsatile case and 6.2±1.6 min for the case with steady flow rate. Predicted occlusion times using our model are 3.35 min for the pulsatile case and 5.2 min for the steady case. Thus we can confirm that the predicted results for the pulsatile case follows the correct experimental trend and is in quantitative agreement with experiments within the given experimental uncertainty.

4.4 Summary and Conclusion

Effects of platelet activating agonists as well as flow pulsatility on thrombus formation were investigated in this chapter. First, it was shown that ADP contributes substantially to platelet deposition and activation (~9% difference in deposition and 100% difference in activation were observed for case 2), whereas effects of thromboxane A_2 and thrombin on both deposition and activation were negligible for both cases 1 and 2. Second, it was shown that pulsatility can have considerable effect on thrombus formation, namely on the thrombus growth rate. The time-averaged rate of thrombus growth over 5 cycles for the pulsatile flow was shown to be approximately 1.5 times higher than the steady flow case. Our results confirm that pulsatility can lead to faster deposition and occlusion of stenosed vessels. This conclusion is in agreement with experimental findings of Casa and Ku who measured shorter occlusion times due to the blood flow pulsatility [147].

5 Predictive modeling of thrombus growth in stenosed vessels with dynamic geometry using the Arbitrary Lagrangian Eulerian (ALE) method

5.1 Introduction

This chapter introduces a three-dimensional dynamic model of platelet-rich thrombus growth in stenosed vessels using computational fluid dynamics (CFD) methods. Platelet adhesion, aggregation and activation kinetics are modeled by solving mass transport equations for blood components involved in thrombosis. Arbitrary Lagrangian Eulerian (ALE) formulation is used to model the growing thrombi with variable geometry. The wall boundaries are discretely moved based on the amount of platelet deposition that occurs on vessel wall. To emulate the dynamic behavior of platelet adhesion kinetics during thrombus growth, a validated model for platelet adhesion, which calculates platelet-surface adhesion rates as a function of stenosis severity and Reynolds number, is applied to the model. Results of the present model for vessel occlusion times and platelet deposition in stenosed region are compared to ex-vivo and in-vitro experimental data.

The method used in this chapter benefits from a predictive dynamic geometry-dependent model of thrombus growth that can be applied to a wide range of blood flow rates and stenosis severities. This is an important step as the current study utilizes a first of its kind continuum-based model with variable thrombus geometry. Moreover, the significance of this model can be seen in the quantification of effects of changes in mural thrombus geometry on platelet transport, activation and deposition kinetics. Previous models are not capable of simulating nonlinear growth of thrombus within large time frames (>1 min) without excluding biological factors such as thrombin, ADP, and TxA_2. Furthermore, in contrast to methodologies such as ones used in [181], [182] and [148] that are not capable of predicting embolism in highly stenosed vessels, the current model can reasonably capture thromboembolic events that frequently occur in the stenotic arterial flows.

5.2 Methods

As discussed in Chapter 3, using the present model along with stationary wall boundaries the rate platelet deposition converges to a constant value for short periods of perfusion time (< 1 min) [210]. In other words deposition increases linearly with perfusion time. This linear growth is also experimentally observed in [207], [208]. For longer perfusion times the stationary geometry assumption is not valid anymore because growing thrombi can considerably change the flow patterns, flow rate, wall shear stress distribution, and platelet transport kinetics. This leads to a temporally nonlinear thrombus growth.

5.2.1 Arbitrary Lagrangian Eulerian (ALE) method

A key ingredient of the algorithm to account for moving boundaries is the implementation of a dynamic mesh that responds to structural movement at the boundaries due to platelet deposition. In present study, arbitrary Lagrangian Eulerian (ALE) formulation [211] is used to dynamically move the grid based on the prescribed motion at the wall boundaries. The algorithm decouples the grid movement from the application of fluid conservation laws. The steps involved in the calculation of unsteady flow in the dynamic grid system are as follows:

1) The initial grid is read and the values of dependent variables are initialized.

2) The nodes on moving boundaries are displaced based on the measured platelet deposition.

3) The boundary movement is then transmitted to the interior of the domain in the rezoning phase. The transmittal of boundary motion to volume grid motion is done in a hierarchy of steps.

a) First the corner displacements of each computational block are computed using the spring analogy.

b) Second, the corner displacement of each block is transmitted to the nodal distribution in block edges, block faces, and block volumes, respectively, by using a modified transfinite interpolation (TFI) procedure. This step completes the rezone phase.

5.2.2 Thrombus growth modeling using ALE method

Thrombus growth can substantially affect the flow patterns in the poststenosis region especially in highly stenosed vessels. Additionally, if the blood flow is a pressure-driven flow, the growing thrombi can decrease the blood flow rate as pressure drop increases in the neck area. As they aggregate on the wall, platelets continuously form layers with certain thickness and narrow the stenosed section. Calculated number of platelets per unit area $M_{at}(x,t)$ represents a platelet layer with a known thickness distribution. Therefore, wall boundaries are moved based on the calculated platelet deposition. The evolution of vessel wall geometry is depicted in Figure 5.1.

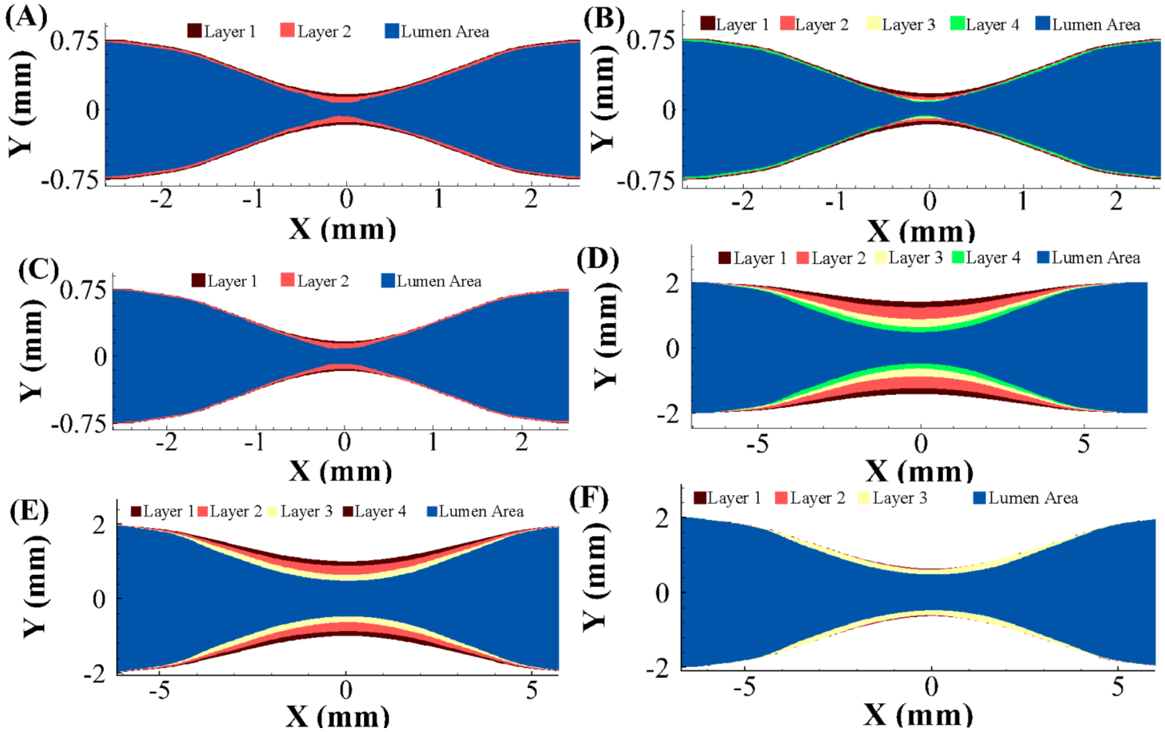

Figure 5.1 Time evolution of predicted mural thrombus with deposited layers for (A) case 1, (B) case 2, (C) case 3, (D) case 4, (E) case 5, (F) case 6.

The ALE method is used to dynamically move the boundaries and the mesh inside the domain as platelets deposit on the vessel wall. In order to do this, mass transport equations are solved using the initial geometry until the thrombus growth rate converges to a constant value (see Fig. 2). Figure 2 shows the variation of thrombus growth rate versus blood perfusion time at different probe locations in the vessel for Casa's case with initial maximum wall shear rate of 6500 s^{-1} (case 2) as a representative case. For the initial geometry, before the first wall movement, deposition rates converge to constant values at t=0.4s. Before this, deposition increases nonlinearly with time, whereas at this time the platelet deposition starts increasing linearly with time. The flow field reaches a steady state with a constant deposition rate, but since the deposition keeps increasing, we call this state the quasi-steady state. Once each quasi-steady state simulation has completed, the ALE method is applied to move the vessel wall boundaries based on the calculated deposition on the wall. After moving the wall boundaries, only the Navier-Stokes equations are solved to obtain the new flow field. Once the flow reaches steady state, given the new geometry (hence stenosis degree) and the new flow rate, new values of platelet adhesion rate are calculated using the adhesion rate functions (Eqs. (**5.1**, (**5.2**, (**5.3**). Then, mass transport equations are solved with the new adhesion rates until the thrombus growth rate converges to a new constant value. The wall boundaries are moved again based on the number of platelets deposited during the time period between the first movement and the second one. This procedure is repeated until occlusion occurs. The algorithm used for modeling thrombus with variable geometry is given in Figure 5.4.

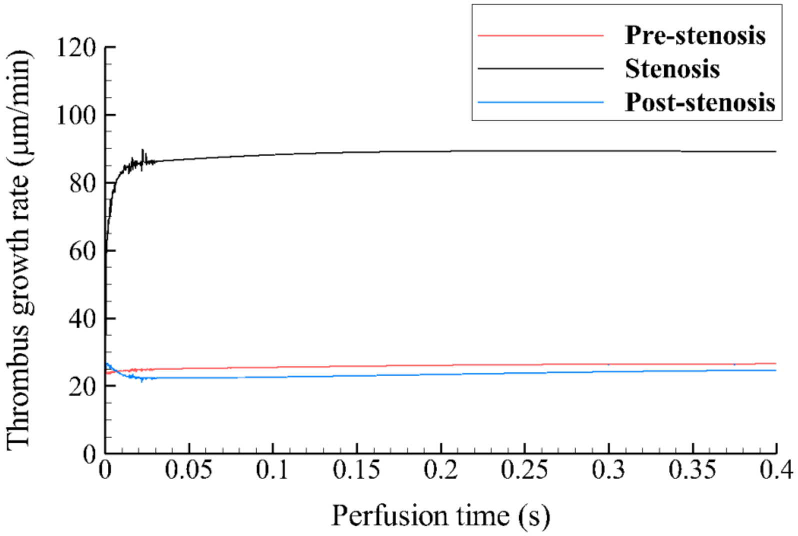

Figure 5.2 Temporal variation of deposition rate at different locations; movements are applied after thrombus growth rate reaches steady state.

Augmented adhesion rates for platelets were employed in our model to make the platelet-wall reaction mechanism dominant near the apex. Previous experimental work has shown that platelet adhesion rates are not only functions of local shear rate. Based on the results from [51] and [43] thrombus growth rate is a function of flow rate and stenosis degree, and the deposition rate can be dramatically different for the same wall shear rate. Thus it is necessary that any model development effort take this factor into consideration. Following an approach similar to that of David et al. [160], adhesion rates of platelets k_i (i.e. k_{rs}, k_{as}, and k_{aa}) are defined as linear functions of local wall shear rate based on the binding kinetics of platelets [7]. We define the adhesion rate as:

$$k_i(x) = k_{i_0}.\left(1 + \lambda.\dot{\gamma}_w(x)\right) \tag{5.1}$$

$$k_{i_0}(r,s) = c_1 r^2 s^3 + c_2 r^3 s^2 + c_3 r^4 s + c_4 r^5 + c_5 r s^3 + c_6 r^2 s^2 + c_7 r^3 s + c_8 r^4 + c_9 s^3 + c_{10} r s^2 + c_{11} r^2 s + c_{12} r^3 + c_{13} s^2 + c_{14} r s + c_{15} r^2 + c_{16} s + c_{17} r + c_{18} \tag{5.2}$$

$$\lambda(r,s) = c_1 r^2 s^3 + c_2 r^3 s^2 + c_3 r^4 s + c_4 r^5 + c_5 r s^3 + c_6 r^2 s^2 + c_7 r^3 s + c_8 r^4 + c_9 s^3$$
$$+ c_{10} r s^2 + c_{11} r^2 s + c_{12} r^3 + c_{13} s^2 + c_{14} r s + c_{15} r^2 + c_{16} s + c_{17} r + c_{18} \quad (5.3)$$

where $\dot{\gamma}_w(x)$ is the local wall shear rate, λ is the shear enhancement factor and augments the effect of shear rate on platelet-surface and platelet-platelet adhesion, and k_{i_0}(i.e. k_{rs_0}, k_{as_0}, and k_{aa_0}) is the baseline value. Constant coefficients $c_1 - c_{18}$ are given in [210], r is the Reynolds number based on the diameter and mean velocity at stenosis apex and s is the stenosis degree (%) (see Figure 5.3).

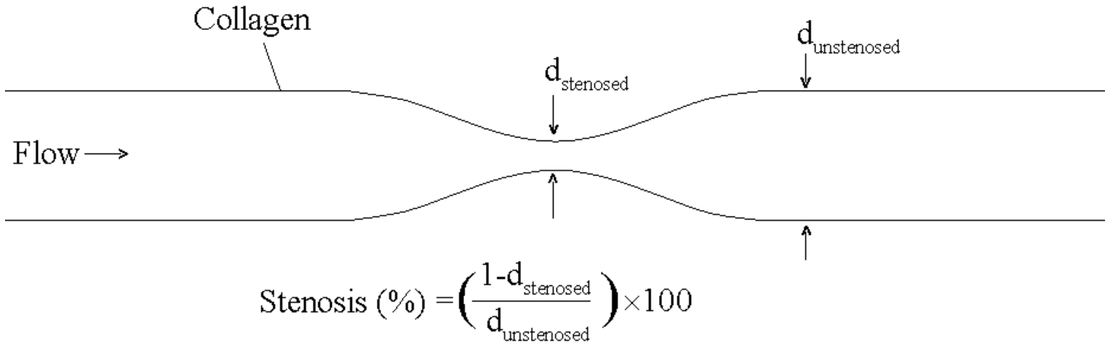

Figure 5.3 Schematic representation of cross section of the stenosed region of tested tubes. Stenosis degree is defined as the reduction in vessel diameter.

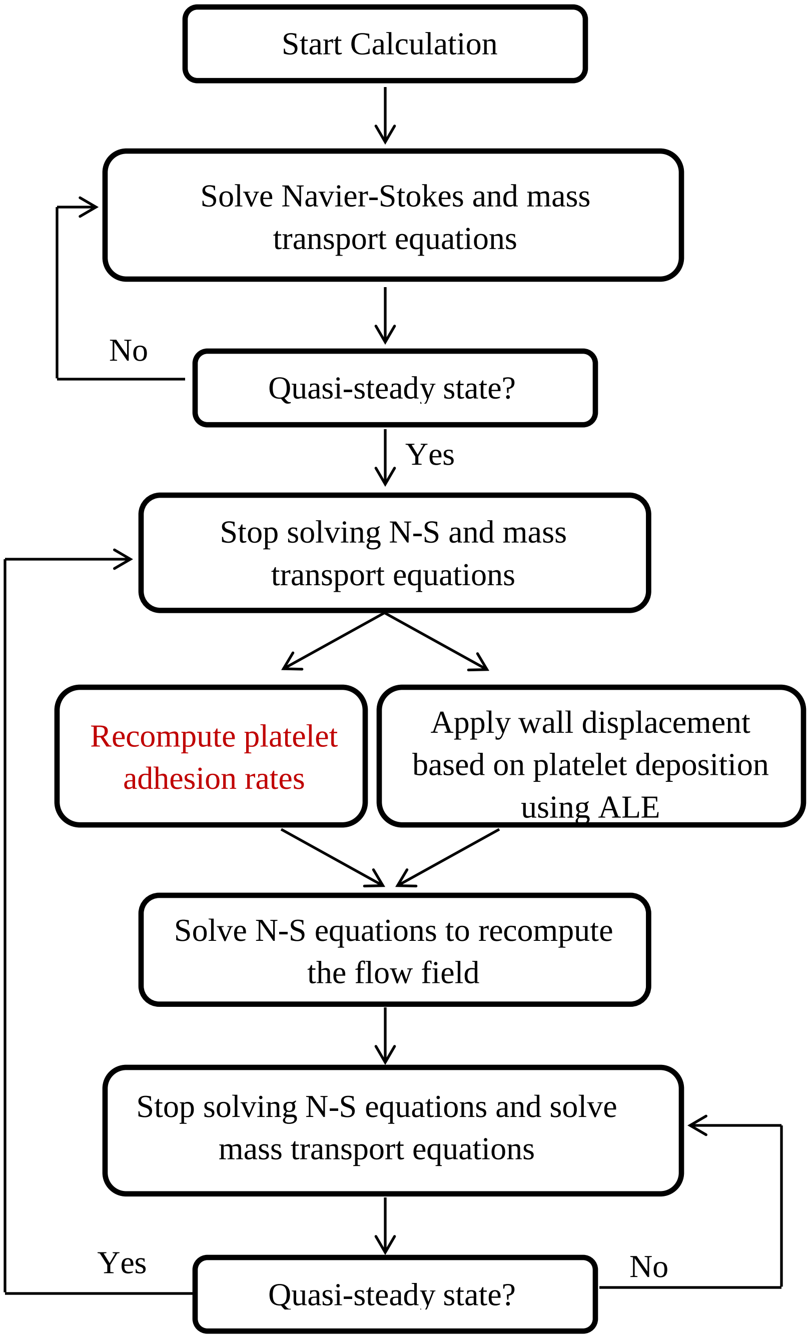

Figure 5.4 Algorithm used to model dynamic thrombus growth

5.2.3 Spatial smoothing of deposition

As discussed earlier, calculated platelet deposition values are used to move the wall boundaries. To ensure that a physically reasonable and smooth profile for wall boundary displacement is imposed, the following low pass spatial filter was used for smoothing the platelet deposition distribution:

$$\begin{aligned} M_{at}^{f}(i,j,k) = \frac{1}{256}\big(&M_{at}(i-3,j,k) - 18M_{at}(i-2,j,k) + 63M_{at}(i-1,j,k) \\ &+ 164M_{at}(i,j,k) + 63M_{at}(i+1,j,k) - 18M_{at}(i+2,j,k) \\ &+ M_{at}(i+3,j,k)\big) \end{aligned} \tag{5.4}$$

The filter uses the values at 8 neighbor cells and weighted deposition value at the center cell to calculate the filtered deposition. Figure 5.5 illustrates the geometry and the mesh before and after applying the filter for a sample case.

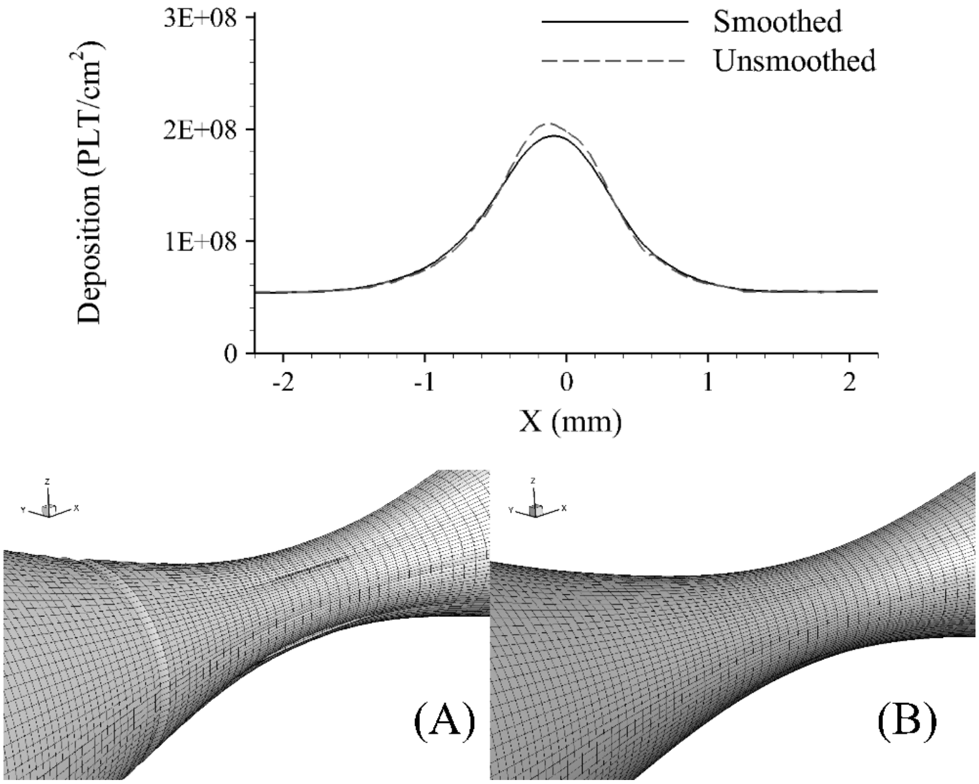

Figure 5.5 Distribution of platelet deposition versus nondimensional axial position and surface grids (A) before and (B) after applying the spatial filter for a representative case (case 2).

5.2.4 In vitro study cases

Simulations are based on two ex-vivo and in-vitro studies. In the first study by Casa and Ku [147] flow is driven by a constant pressure head, therefore, as thrombus forms and narrows the cross-sectional area in the stenosed area, flow rate decreases due to pressure drop in the throat. Whereas, in the second study by Wootton et al. [111] blood was perfused at constant flow rates. Table 5.1 shows the tested cases with corresponding flow characteristics and geometric parameters.

Table 5.1 Test cases with corresponding flow characteristics and geometric parameters.

Case	Tube diameter (mm)	Stenosis (%)	Re_{inlet}	Shear rate at inlet (s^{-1})	Flow rate (ml/min)	Ref.
1	1.5	78	3.6	18	0.7	[147]
2	1.5	78	6.2	30	1.2	[147]
3	1.5	78	16.5	74	3	[147]
4	4	29.3	160	265	99.5	[111]
5	4	50	160	265	99.5	[111]
6	4	68.4	160	265	99.5	[111]

5.2.4.1 Constant pressure head cases

To model thrombus formation in stenosed vessels under the experimental conditions of Casa and Ku [147], we perfused whole blood in the domain with a platelet count of 480,000 $\mathrm{PLT.mm^{-3}}$ at the inlet. In the experiments, blood was heparinized at 3.5 USP units.ml^{-1}, as described in [147]. Stenosis level, based on the diameter reduction, was 78% and steady experiments were performed at apex wall shear rates of 3800, 6500, and 16000 s^{-1}, corresponding to inlet velocities of 0.66, 1.13, and 2.9 cm.s^{-1} respectively. Also the shear-dependent diffusivity (see Eq. (3.5) was applied for platelets to account for the presence of red blood cells. Occlusion times were also reported for these cases. Time to occlusion, t_{occ}, was defined as the time at which the platelet mass no longer changed and flow rate becomes zero. This time is the whole perfusion time, including the lag time. The time that should be discarded is called the lag time (when the thrombus volume reaches $10^6\ \mu m^3$). Lag times are 60, 40, and 25 s for cases 1, 2, and 3 respectively.

5.2.4.2 Constant flow rate cases

Non-heparinized blood was perfused into the stenosed collagen-coated glass tubes (Fig. (**5.3**) and platelet accumulation was measured over the stenosis. Blood flow rate at the inlet is regulated at a constant value of 100 ml.min^{-1}. Heparin level was set to zero for this set of simulations and an inlet concentration of 252,000 PLT.mm^{-3} was imposed for platelets. For other blood components, the normal concentration levels were injected based on the given blood preparation methods in [111]. Also the shear-dependent diffusivity was applied for platelets to account for the presence of red blood cells.

Platelet deposition was measured in 5 regions of interest (ROI) as explained by Wootton et al. [111] and the values for platelet accumulation rate at each ROI were reported for three initial stenosis degrees of 29.3%, 50%, and 68.4%.

5.3 Results and discussion

Here we discuss different aspects of the predicted results for thrombus growth. First, we analyze the variation of platelet adhesion rates (k_{rs}, k_{as}, and k_{aa}) with stenosis degree s (%), and Reynolds number at the stenosis apex Re_{apex}.

Second, we discuss the variation of thrombus growth rate in relation to the wall concentration of platelets and agonists to understand the different physics underlying thrombus growth during the initial stages and near-occlusion stages of evolution of this process.

Third, we discuss the role of ADP, TxA_2, and thrombin in platelet activation. Platelet activation is known as a precursor to thrombus formation and high levels of these agonists in blood can be defining in the evolution of thrombosis. We also investigate the relationship between platelet activation and thrombus growth rate.

Another key aspect of our model is the capability to predict the occurrence of embolism in stenosed arteries under high shear conditions. We discuss our results for embolism that happens in high shear cases of Wootton et al. [111] and prevents vessel occlusion.

Finally, we present the relationship between thrombus growth rate and wall shear rate for all cases. Our results are compared to experimental data and the different behavior of thrombus growth in different shear rate ranges are discuss to delineate the effect of wall shear rate on platelet transport during thrombosis.

5.3.1 Variation of platelet adhesion rates and occurrence of embolism at high shear rates

Equation ((**5.1**) was used to apply variable platelet adhesion rates in the simulations. Platelet adhesion rate is a function of vessel stenosis degree, s (%) and Reynolds number at the apex, Re_{apex}. Initially, the adhesion rate is calculated based on the initial geometry used in the experiments. As platelets deposit on the wall, the lumen area gets narrower, thereby increasing stenosis degree. For Wootton's cases [111], since the flow rate at the inlet is regulated at a constant value in the experiments, Reynolds number at the stenosis apex keeps increasing with deposition. Variation of platelet adhesion rates baseline values (k_{i_0}) and shear enhancement factor (λ) versus stenosis degree of vessels are plotted in Figure 5.6. For Wootton's cases three simulations with different initial stenosis severities (29.3%, 50%, and 69%) were run using variable adhesion rates. Geometry change was applied in a discrete manner. Depending on change in adhesion rate baseline values and shear enhancement factor with increasing stenosis degree, steps with different durations were taken to reach complete occlusion. For the case with initial stenosis degree of 29.3%, vessel wall boundaries were moved at stenosis degrees of 29%, 38%, 56%, 68%, and 73%. For the 50% stenosis case, movements were applied at 50%, 56%, 69%, and 73%, and for the 69% stenosis case, boundaries were moved at 69%, 71%, and 73%.

For constant pressure head cases of Casa and Ku [147] three simulations with initial stenosis degree of 78% and initial peak wall shear rates of 3800, 6500, and 16000 s^{-1} were run. Similar to

Wootton's cases variable adhesion rates (Eqs. (**5.2**) and (**5.3**)) were used to account for the change in mural geometry of thrombus.

Table 5.2 shows the steps taken with Reynolds numbers at the apex Re_{apex}, associated stenosis degrees, s (%), shear enhancement factor λ (s) and adhesion rates baseline values k_{rs_0}, k_{as_0}, k_{aa_0} (m.s^{-1}) for all cases.

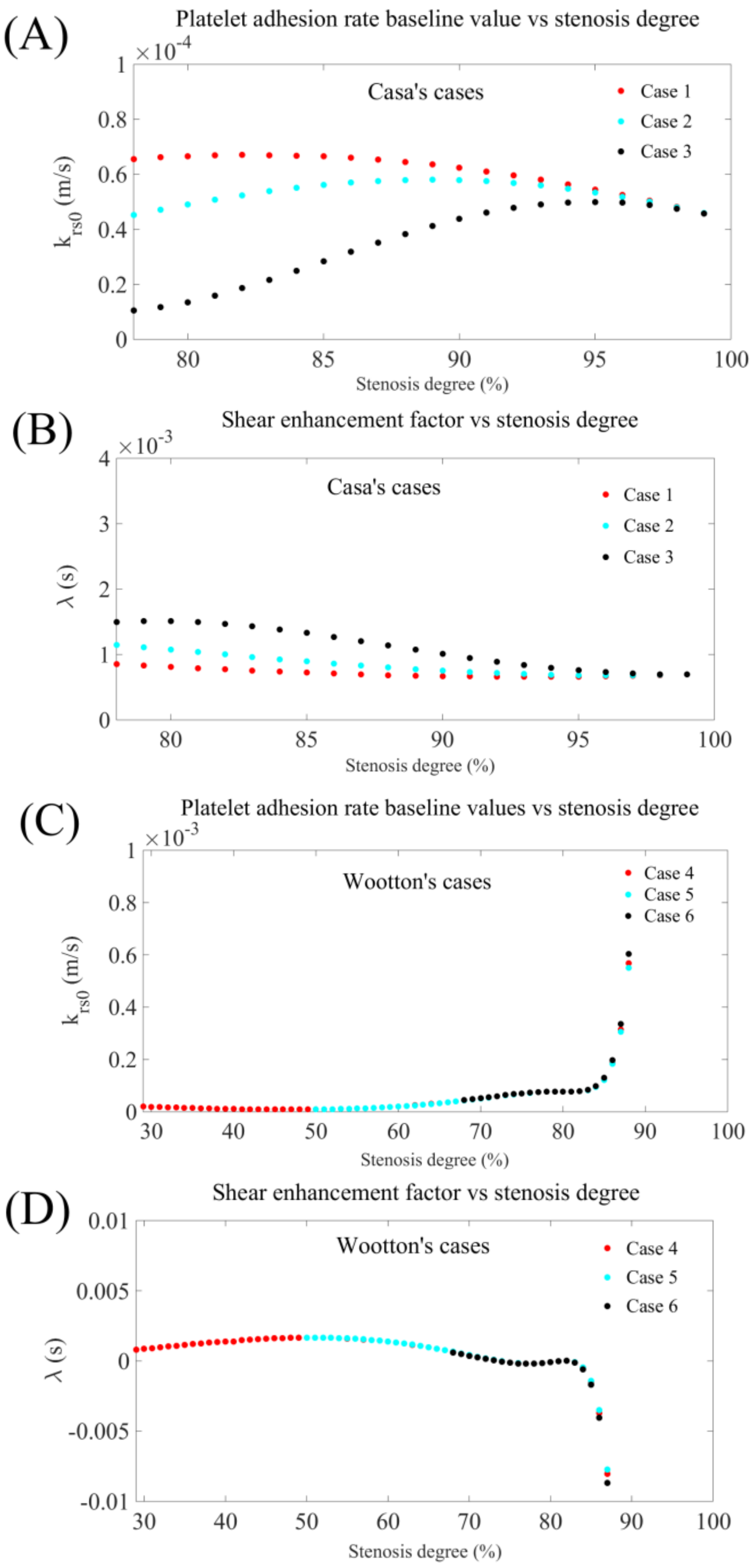

Figure 5.6 Variation of (A), (C) platelet adhesion rates baseline values (k_{i_0}) and (B), (D) shear enhancement factor (λ) versus stenosis degree of vessels.

Table 5.2 Variation of stenosis degree, local Reynolds number at the apex and platelet adhesion rates with deposition for all cases.

Case	Re_{apex}	Stenosis (%)	$k_{rs_0}\ (m.s^{-1})$	$k_{as_0}, k_{aa_0}\ (m.s^{-1})$	$\lambda\ (s)$
Casa’s cases					
Case 1					
Initial geometry	13.7	78	6.56×10^{-5}	8.16×10^{-5}	8.55×10^{-4}
Layer 1	11.4	80	6.64×10^{-5}	8.24×10^{-5}	8.14×10^{-4}
Layer 2	7.7	84.5	6.47×10^{-5}	8.04×10^{-5}	7.62×10^{-4}
Layer 3	3.4	92.2	5.59×10^{-5}	6.95×10^{-5}	7.28×10^{-4}
Occlusion		100			
Case 2					
Initial geometry	24.1	78	4.5×10^{-5}	5.6×10^{-5}	1.1×10^{-3}
Layer 1	14.	83	5.45×10^{-5}	6.78×10^{-5}	9.54×10^{-4}
Layer 2	10.1	87	5.41×10^{-5}	6.73×10^{-5}	8.9×10^{-4}
Layer 3	7.7	89	5.25×10^{-5}	6.53×10^{-5}	8.5×10^{-4}
Layer 4	10.7	93.5	4.08×10^{-5}	5.07×10^{-5}	9.96×10^{-4}
Occlusion		100			
Case 3					
Initial geometry	60	78	1.05×10^{-5}	1.31×10^{-5}	1.5×10^{-3}
Layer 1	49.6	81	1.26×10^{-5}	1.56×10^{-5}	1.5×10^{-3}
Layer 2	18.7	88.7	3.58×10^{-5}	4.45×10^{-5}	1.2×10^{-3}
Occlusion 3		100			
Wootton’s cases					
Case 4					
Initial geometry	225	29.3	4.56×10^{-5}	5.67×10^{-5}	8.05×10^{-4}
Layer 1	257.4	38	1.94×10^{-5}	2.41×10^{-5}	1.3×10^{-3}
Layer 2	363	56	1.37×10^{-5}	1.7×10^{-5}	1.58×10^{-3}
Layer 3	498.7	68	4.4×10^{-5}	5.47×10^{-5}	6.08×10^{-4}
Layer 4	664.9	76	7.22×10^{-5}	8.98×10^{-5}	-1.75×10^{-4}
Case 5					
Initial geometry	320	50	9.42×10^{-6}	1.17×10^{-5}	1.17×10^{-3}
Layer 1	665	56	1.37×10^{-5}	1.7×10^{-5}	1.58×10^{-3}
Layer 2	732	69	8.4×10^{-5}	1.04×10^{-4}	4.89×10^{-4}
Layer 3	665	76	7.22×10^{-5}	8.98×10^{-5}	-1.75×10^{-4}
Case 6					
Initial geometry	506	68.4	4.4×10^{-5}	5.47×10^{-5}	6.13×10^{-4}
Layer 1	533	69.2	5.1×10^{-5}	6.34×10^{-5}	4.16×10^{-4}
Layer 2	700.4	69.9	5.69×10^{-5}	7.07×10^{-5}	2.53×10^{-4}
Layer 3	665	76	7.22×10^{-5}	8.98×10^{-5}	-1.75×10^{-4}

For Casa's cases, wall shear rate $\dot{\gamma_w}$ throughout the simulations decreases as the growing thrombus increases the resistance and decreases the flow rate under a constant pressure head. This leads to an overall decrease in wall shear rate resulting in lower adhesion rates based on Eq. (5.1). As it can be seen in , for cases 1, 2, and 3, for which a constant pressure head is applied, Reynolds number at the apex Re_{apex} keeps decreasing with stenosis degree due to decreasing flow rate at the inlet. The only increase in Re_{apex} occurs when depositing layer 4 in case 2. This happens because of large increase in stenosis degree (increasing from 89% to 93.5%) that results in so large increase in velocity at the stenosis apex that Re_{apex} increases in spite of decreasing flow rate at the inlet.

Thus, platelet transport and adhesion behavior for constant flow rate cases is different from cases with constant pressure head due to the variable geometries and changes in flow characteristics. For cases of Casa and Ku [147] with constant pressure head applied at the inlet, the flow rate drops with thrombus growth. This leads to decreased velocity and wall shear rates at the apex. On the other hand, increase in the stenosis degree will narrow the neck area which results in increased velocities at the stenosis apex. The interplay of these two effects will define whether the Reynolds number decreases or not. However, for Wootton's cases (with regulated flow rate at the inlet) velocities at the apex increase with thrombus growth (or increasing the stenosis degree). This increase in velocity, hence wall shear rates, at some point leads to negative values of shear enhancement factor and negative platelet adhesion rates (see Table 5.2 and Figure 5.6D for k_{rs_0} and λ values). Note that $k_{as_0} = k_{aa_0} = \frac{4.6}{3.7} k_{rs_0}$ as found by Sorensen et al. [179]. Negative adhesion rates for platelets will result in influx (injection) of platelets at the wall, which physically represents detachment of platelet aggregates (or embolization) due to high shear rate values. This finding matches with Wootton's reports on frequent occurrence of embolism under high shear conditions [111]. The set of model equations (Eqs. (**5.1**(**5.3**) are deigned to capture these effects [210].

5.3.2 Temporal variation of thrombus growth rate and wall concentration of platelets and agonists

Thrombus growth rate profile was monitored in the simulations. For this purpose, monitoring probes were put at three different axial locations. Figure 5.7 depicts the location of probes in the domain.

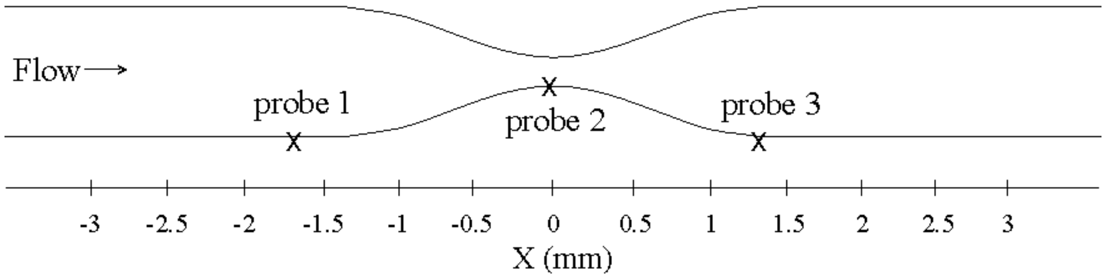

Figure 5.7 Location of monitoring probes put in the pre-stenosis (probe 1), stenosis (probe 2), and post-stenosis (probe 3) regions.

Figure 5.8A-F show variations of thrombus growth rate and wall concentration of different agonists and platelets versus different stenosis degrees for case 2 (6500 s^{-1}) at different locations in the vessel. As seen in Figure 5.8A, at all stenosis degrees, deposition rate (thrombus growth rates) is highest at the stenosis region (near the apex) compared to pre-stenosis and post-stenosis regions. This is due to high shear rates at the apex. On the other hand, maximum platelet activation occurs in the post-stenosis region because of lower adhesion rates and longer residence time of platelets. Due to lower adhesion of resting platelets at pre-stenosis and post-stenosis regions they are more likely to get activated and secrete activating agonists. Generation of ADP at the post-stenosis region is nearly twice as much as other regions (Figure 5.8D) mainly because it is directly related to activation rate (which is highest in the post-stenosis region).

However, for TxA_2 and thrombin, the highest rate of synthesis and generation occur in the stenosis region because their influx terms are proportionate with deposition (M_{at}) values (see Figure 5.8E and F). Therefore, since highest thrombus growth rate happens at the stenosis, generation of these two proteins is highest at the stenosis apex.

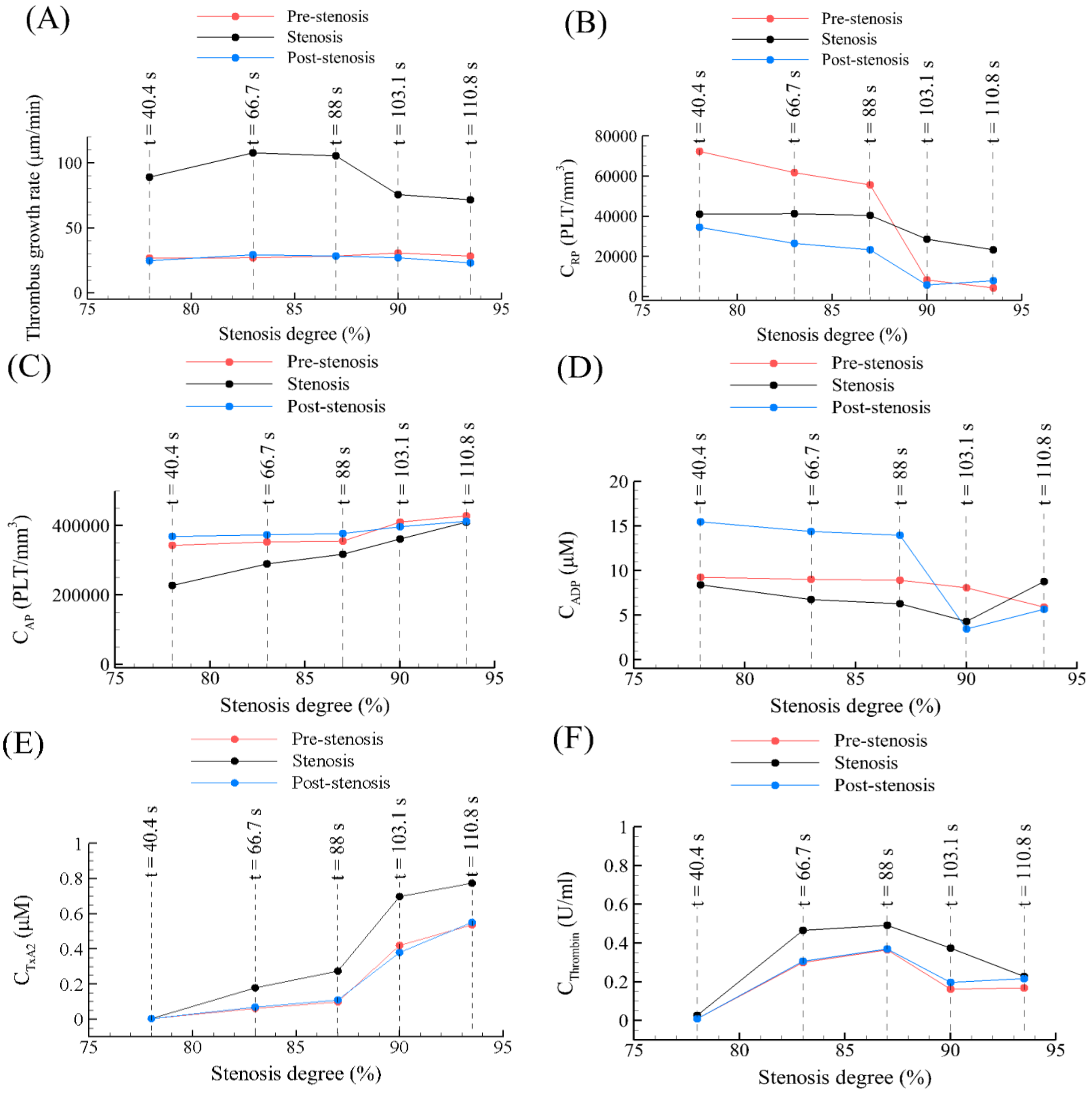

Figure 5.8 Variation of (A) thrombus growth rate and concentration of (B) resting platelets, (C) activated platelets, (D) adenosine diphosphates (ADP), (E) thromboxane A_2, and (F) thrombin with stenosis degree at different locations (pre-stenosis, stenosis and post-stenosis) for case 2.

The thrombus growth rate (Figure 5.8A) follows a trend similar to that of adhesion rate baseline values k_{rs_0} and shear enhancement factor λ (Figure 5.6). The only difference is that for Casa's case at wall shear rate of 6500 s^{-1} (case 2), in spite of an increase in adhesion rates, the rate of thrombus growth decreases when stenosis increases from 87% to 90% (see Figure 5.8A). This is due to two reasons. First, a significant increase in resistance at the necking area leads to a considerable drop in flow rate (at constant pressure head) when thrombus grows from 87% to 90%. Second, Eq. (5.1) predicts smaller values of adhesion rates for stenosis degree of 90% (with Re_{apex}=7.7) compared to 87% (with Re_{apex}=10.1). This results in a decrease in platelet deposition (90% stenosis).

Table 5.3 Maximum values of thrombin concentration and platelet activation rate at the wall with associated perfusion times

Case	Stenosis (%)	Max concentration of thrombin (U.ml^{-1})	Max platelet activation rate (s^{-1})	Perfusion time (s)
1	92.2	0.59	9.9	157.5
2	90	0.66	11	103
3	88.7	0.57	9.7	70.7
4	68	1.04	9.2	347.6
5	69	1.16	9.5	335.3
6	69.9	1.21	16.4	328.1

For case 2 as a representative case, it was observed that the wall concentration of thrombin increases with stenosis until 88 s; reaching a peak value (0.5 U.ml^{-1}), after which it starts to decrease (see Figure 5.8F). Peak values and associated perfusion times are given in Table 5.3. This happens because of the interplay between volumetric generation and generation of thrombin at the wall by deposited platelets. The surface generation of thrombin (see Eqs. (3.17(3.18) depends on platelet deposition, concentration of platelets, and concentration of prothrombin. In general, a large increase in platelet deposition results in considerable increase in wall concentration of thrombin. But at the same time, thrombin generation directly depends on wall concentrations of prothrombin. Therefore, because of the substantial decrease in concentration of prothrombin near the vessel wall, thrombin levels drop.

On the other hand, a continuous increase with stenosis degree is observed for thromboxane A_2 (see Figure 5.8E) since the synthesis rate of TxA_2 (s_{p,TxA_2}) in Eq. (3.16) is directly proportional to platelet deposition at the wall. Note that the volumetric generation of TxA_2 is directly proportional to the concentration of activated platelets only (and not resting platelets) near the wall. Therefore, an increase in concentration of activated platelets near the wall leads to an increase in the generation rate of TxA_2.

Wall concentrations of ADP in all regions of the stenosed area is nearly constant until stenosis degree reaches 87%; at this point due to a decrease in wall concentration of thrombin, platelet activation rate decreases, which in turn decreases the generation of ADP at the wall. However, the platelet activation rate at stenosis degree of 90% increases mainly because the wall concentration of TxA_2 exceeds its critical value (0.6 μM) and increases platelet activation, producing more ADP.

5.3.3 Role of thrombin, TxA_2, and ADP in platelet activation

Platelet activation rate is calculated by summing the concentrations of ADP, TxA_2, and thrombin (Eq. (5.5)) normalized by their critical values $C_{ADP_{crit}} = 2$ μM, $C_{TxA2_{crit}} = 0.6$ μM, $C_{T_{crit}} = 0.1\ \mathrm{U.ml^{-1}}$ over the activation time (t_{act}=1s). Roles of thrombin, TxA_2, and ADP in platelet activation are depicted in Figure 5.9, and Figure 5.10. In Figure 5.9A-C platelet activation rates at the wall are plotted versus concentration of platelet activating agonist normalized by its critical value (i.e. platelet activation threshold). Each distribution of points is obtained from one layer of deposited platelets added during the movement of the vessel wall. Data were collected after simulations reached quasi-steady state with constant rates of platelet deposition.

$$k_{pa} = \frac{1}{t_{act}}\left(\frac{C_{ADP}}{C_{ADP}{}_{crit}} + \frac{C_{TxA_2}}{C_{TxA_2}{}_{crit}} + \frac{C_T}{C_T{}_{crit}}\right) \tag{5.5}$$

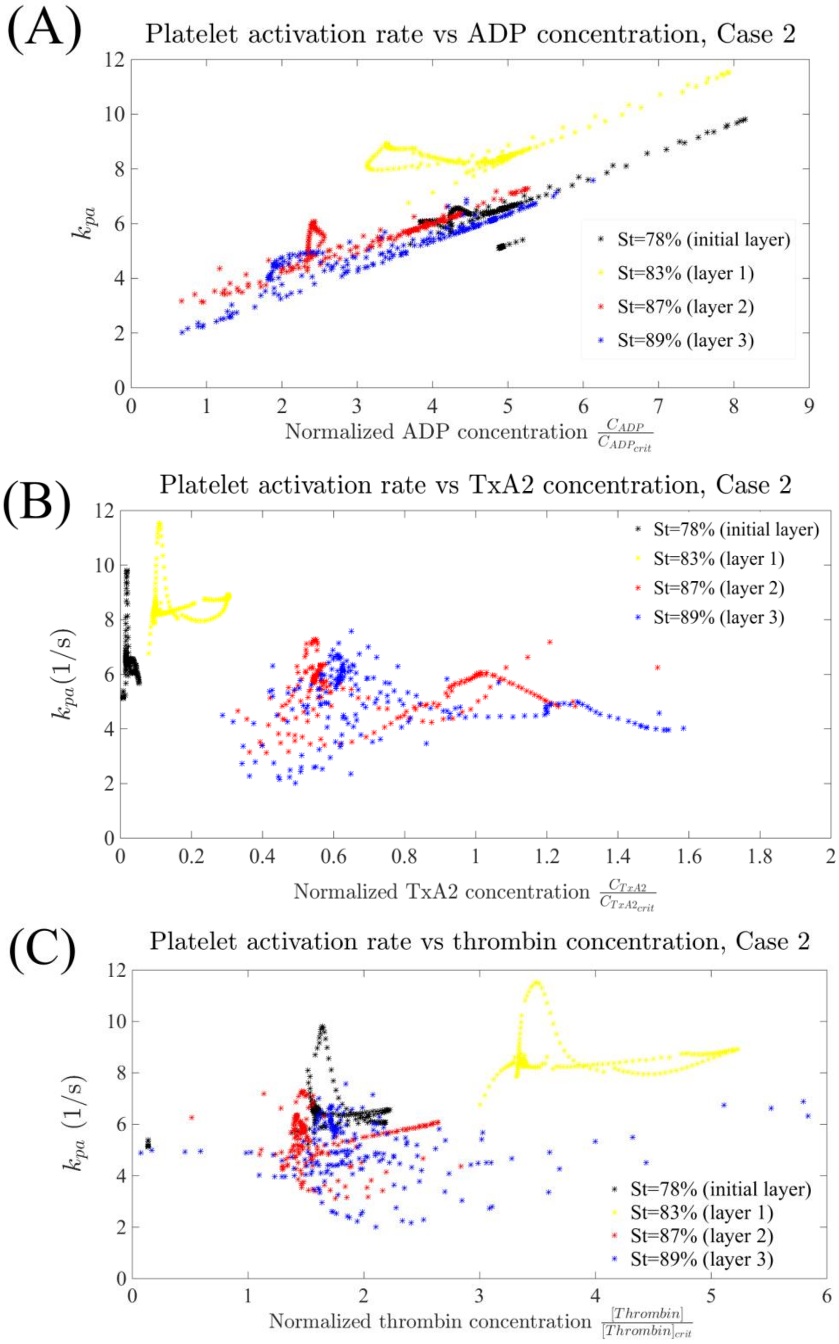

Figure 5.9 Role of thrombin, TxA_2, and ADP in platelet activation; platelet activation rates at the wall are plotted versus wall concentration of platelet activating agonist normalized by its critical value (i.e. platelet activation threshold). Each distribution of points is obtained from one layer of deposited platelets added during the movement of the vessel wall. Data were collected after simulations reached quasi-steady state with constant rates of platelet deposition.

Figure 5.10A-C illustrate percentage contribution of each activating agonist to platelet activation at different layers.

Comparing the plots in Figure 5.9 and Figure 5.10 reveals that a considerable portion of activation rate at the wall is due to high concentrations of ADP. The activation rate of platelets, k_{pa} increases with ADP levels especially during the formation of initial thrombus layers. In other words, ADP initiates the platelet activation in stenosed vessels; hence, the role of ADP in platelet activation is significant. However, its contribution decreases gradually for subsequent thrombus layers because of increasing concentrations of TxA_2 and thrombin. TxA_2 initially does not affect platelet activation but becomes more significant at later perfusion times (layer 2 for Casa's case with 6500 s^{-1}).

The effect of thrombin on platelet activation is more complex. Initially, thrombin concentration increases up to 5 times the critical level (layer 1 for Casa's case with 6500 s^{-1}) due to increased values of deposition (M_{at} in Eq. (3.18) but then starts to decrease because much less prothrombin is available near the wall due to its high consumption during deposition of multiple layers. In other words, deposition of platelet layers increases the generation rate of thrombin. Conversely, the large amount of platelet deposition results in lower concentration of prothrombin at the wall, which tends to decrease the production of thrombin. This complex behavior of thrombin matches with experimental observations of Olivier et al. [212] and Monroe et al. [213] in a tissue factor-initiated system. Peak values of platelet activation are given in Table 5.3. Note that platelet activation rate at the wall reaches its maximum values when highest thrombin concentrations occur, which reveals the important role of thrombin in platelet activation.

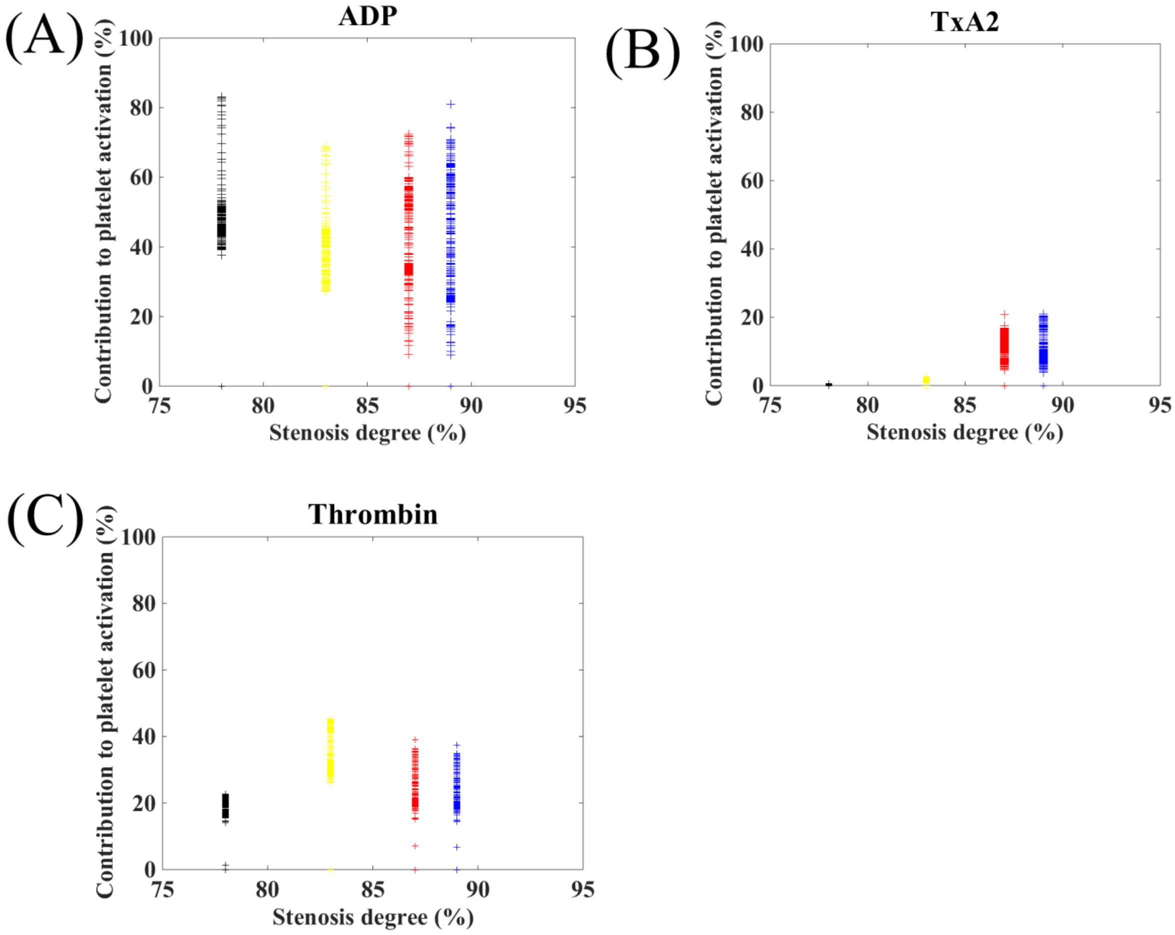

Figure 5.10 Percentage contribution of activating agonists at the wall, (A) adenosine diphosphate, (B) thromboxane A_2, and (C) thrombin to platelet activation at different layers for the case of Casa and Ku [147] with initial maximum wall shear rate of 6500 s^{-1} (case 2).

5.3.4 Thrombus growth rate versus wall shear rate and local Damkohler number (Da)

Using the time-dependent data from all cases, thrombus growth rate is plotted in Figure 5.12A-F against the vessel wall's local shear rate. Numerical results are compared to empirical correlations of Mehrabadi et al. [148] and Bark et al. [51] for thrombus growth rate in stenosed geometries. During both aforementioned experimental studies, the height of the mural thrombus was measured in **μm** and divided by the total perfusion time to calculate the rate. The growth rate was then correlated to the corresponding wall shear rate at the point where the deposition was measured. Here, we report the calculated thrombus growth rate values following a similar approach. At a given perfusion time, the amount deposited is used to obtain the growth rate. The local growth rate is associated with the wall shear rate at that location. Figure 5.11 presents our predicted results for Mehrabadi's case for variation of thrombus growth rate with wall shear rate versus experimental data of Mehrabadi et al. [43] and Bark et al. [51]. Our results match reasonably well with experimental data for shear rates of 0-10,000 s^{-1}, however, the negative correlation between thrombus growth rate and shear rate under higher shear rates (>10-20,000 s^{-1}) is not captured in our model. Mehrabadi et al. [148] explain that the elongation of von Willebrand factor (vWf) multimer in high shear rates results in explosive thrombus growth on collagen. However, they do not explain what causes the negative correlation. We attribute this decrease in the growth rate to occurrence of embolization at high shear rates. Figure 5.12A-F present our results for cases 1-6. These figures are plotted using all data points during the simulations. The shaded region represents the calculated thrombus growth rate for each layer starting from the initial geometry to the final geometry. Note that each step in our procedure yields a thrombus growth rate at different wall shear rates along the stenosed region.

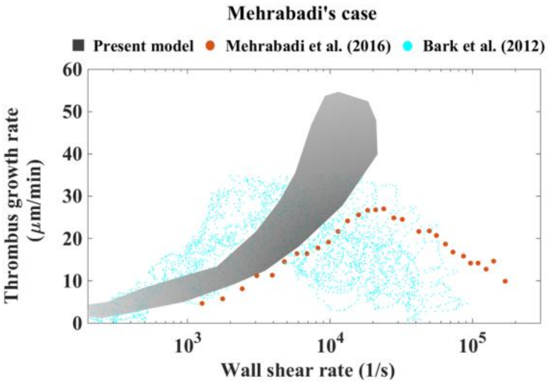

Figure 5.11 Comparison of predicted thrombus growth rate vs. wall shear rate using the current model with experimental data of Mehrabadi et al. [43] and Bark et al. [51]. The dark shaded regions represent our predicted results (data points) based on the data cloud obtained from our simulations at different perfusion times. Regions with lighter shades correspond to earlier perfusion times at initial mural thrombus and darker regions are associated with deposition layers at later perfusion times.

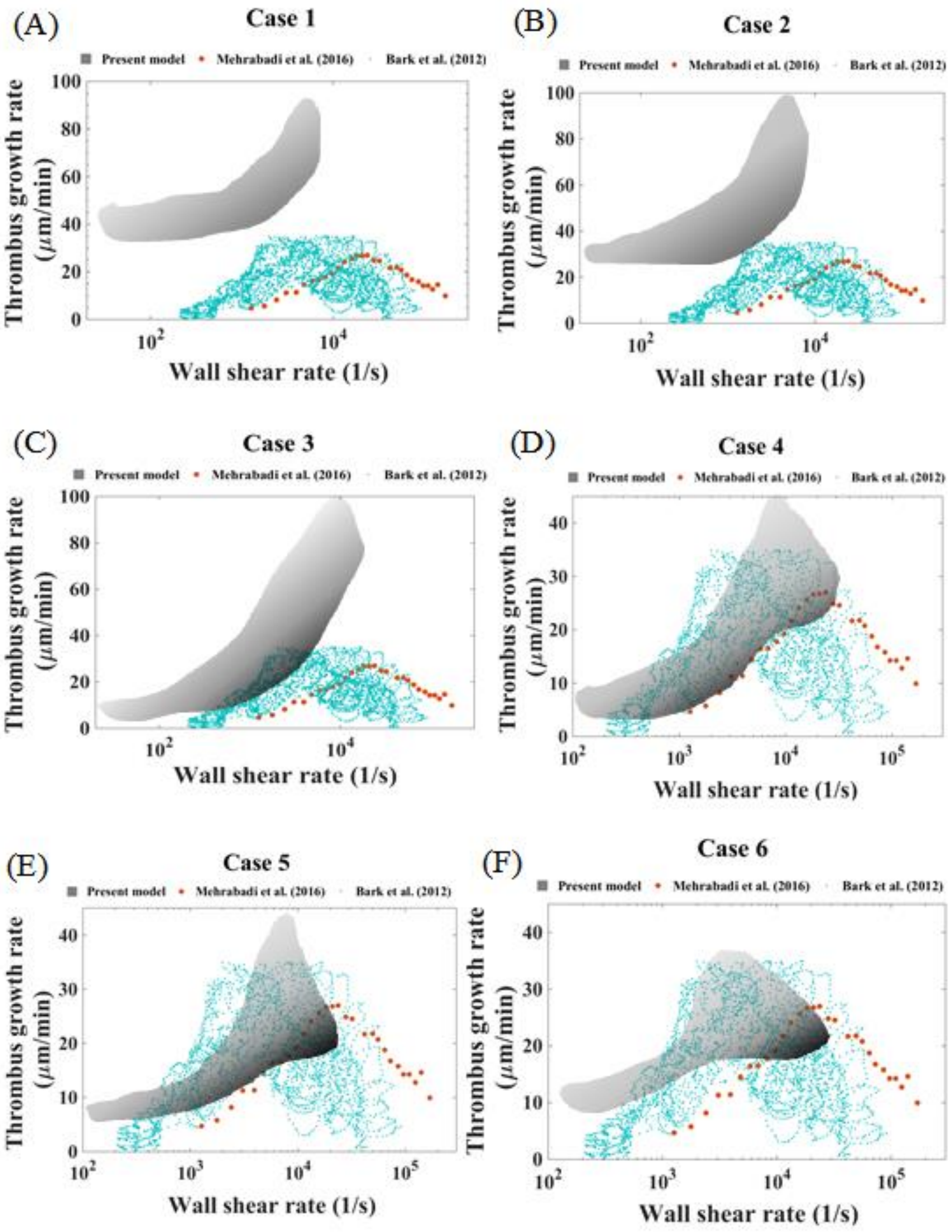
(A)
Case 1
Present model
Mehrabadi et al. (2016)
Bark et al. (2012)
Thrombus growth rate (μm/min)
Wall shear rate (1/s)
(B)
Case 2
(C)
Case 3
(D)
Case 4
(E)
Case 5
(F)
Case 6
0
10
20
30
40
60
80
100
10^2
10^3
10^4
10^5

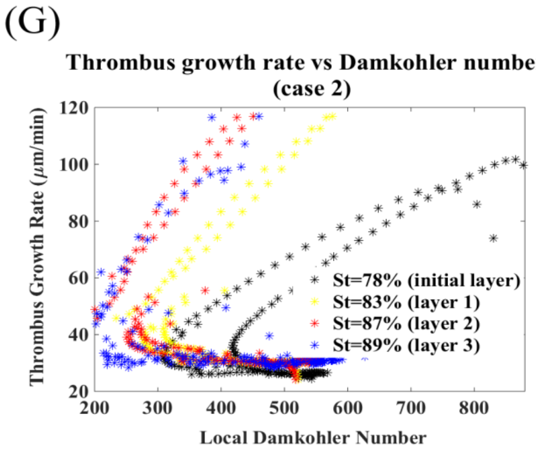

Figure 5.12 (A-F) Platelet deposition rate versus the vessel wall's local shear rate for different cases; the dark shaded regions represent our predicted results (data points) based on the data cloud obtained from our simulations at different perfusion times. Regions with lighter shades correspond to earlier perfusion times at initial mural thrombus and darker regions are associated with deposition layers at later perfusion times; (G) thrombus growth rate versus local Damkohler number for different deposited layers of case 2.

The ratio of surface reactivity to platelet diffusivity is measured by the platelet Damkohler number (Da= $k.L/D_{PLT}$). Thrombus growth rate versus local Damkohler number for different deposited layers of case 2 are plotted in Figure 5.12G. Sorensen et al. [179] showed that increase in Da will increase the thrombus growth rate. Our results match with Sorensen's finding; for larger Da thrombus growth occurs at a higher rate for all layers.

Figure 5.12 presents the thrombus growth rate variation with local wall shear rates for all cases. The dark shaded regions represent our predicted results (data points) based on the data cloud obtained from our simulations at different perfusion times. Regions with lighter shades correspond to earlier perfusion times at initial mural thrombus and darker regions are associated with deposition layers at later perfusion times. As seen in Figure 5.12, the thrombus growth rates associated with high shear cases (cases 3-6) are shifted to the right compared to low shear cases (cases 1-2). In other words, maximum deposition rate occurs at a higher wall shear rate for these cases. Therefore, while the experimental data of Mehrabadi et al. [43] and Bark et al. [51] has been characterized solely by the variation in wall shear rate, we believe that the thrombus growth rate is also a function of the degree of stenosis. That is, given the same wall shear rate, thrombus growth rate will vary depending on the degree of stenosis. Mehrabadi et al. and Bark et al. measured the thrombus growth rate for tubes with initial stenosis degrees of 71% and 80-85% respectively. This reveals the importance of using variable case-specific platelet adhesion rates using equations (5.2) and (5.3). In the aforementioned studies the flow Reynolds number varies from 2 to 12 and stenosis degrees of the initial geometries are within a range of 71-85%. Thus, the experimental results are valid only for a specific range, whereas in the current study, a wide range of Reynolds number (3-600) and stenosis degree (29-96%) are chosen to clearly demonstrate the effect of geometry or change in stenosis degree.

In the experiments of Bark et al. [51] whole blood perfusion in stenosed tubes with stenosis degrees of 80-85% yielded maximum thrombus growth rate of 35 $\mu m.min^{-1}$ at a wall shear rate of 6000 s^{-1}. They reported multiple occurrence of embolism in their experiments. Mehrabadi et al. [148] reported maximum growth rate of 26.8 ± 5.8 $\mu m.min^{-1}$ at a wall shear rate of $25{,}000 \pm 8400$ s^{-1} with occurrence of embolization. Our results for thrombus growth rate in cases with embolization indicate maximum thrombus growth rates of 44.53, 44.7, and 36.7 $\mu m.min^{-1}$ at wall shear rates of 7004, 6031, and 3400 s^{-1} respectively for cases 4, 5, and 6 (see Figure 5.12D-F).

Maximum growth rates were 91.51, 99, and 99.7 $\mu m.min^{-1}$ for cases 1, 2, and 3 respectively. For these cases, no negative correlation between thrombus growth rate and wall shear rate is observed in our results as growth rates keep increasing after wall shear rates of 5000-7000 s^{-1}. We attribute the lack of embolization in Casa's cases to the constant pressure head and the decrease in flow rate with increase in stenosis degree. It should be mentioned that Casa and Ku [147] also did not report any thromboembolic events in their study.

Effect of embolization on thrombus growth rate

Caution should be exercised when explaining the functional relationship between thrombus growth rate and vessel wall shear rate. As illustrated in Figure 5.12 high shear stenosis experience lower deposition rates compared to low shear cases as is illustrated in cases 1 and 2. Although platelet adhesion rates are correlated with local wall shear rate, decreased rates of deposition, for Wootton’s cases for instance, are caused by high shear-induced embolization.

Embolization was not observed for cases of Casa and Ku [147] due to lower shear rates compared to Wootton’s cases with high shear rates. Maximum wall shear rates for Casa’s cases did not exceed 12,000 s^{-1}, whereas this value was around 32,000 s^{-1} for Wootton’s cases. These combined results indicate that embolization occurs in supraphysiological wall shear rates (>20,000 s^{-1}). This finding matches with experimental observations of Mehrabadi et al. [148] for stenosed tubes with stenosis degree of 71%. They report that for wall shear rates higher than 25,000 s^{-1} associated with long perfusion times, thrombus growth rate is negatively correlated with wall shear rate. Bark et al. [51] also explain that effects of enhanced shear activation and platelet aggregation is balanced by increased embolization due to higher drag forces exerted on platelet aggregates at high shear rates.

5.3.5 Thrombus growth rate versus platelet activation

As seen in Figure 5.13, peak value of thrombus growth rate occurs at locations different than those of peak platelet activation rate. This is due to the large adhesion of resting platelets in the pre-stenosis and stenosed area at the apex. Thus, few platelets are available downstream of the apex for activation till platelets from the middle of the vessel diffuse towards the vessel wall.

This results in an increase in activation rate which reaches a peak value 1.06 mm downstream of the apex. Summation of normalized concentrations of activating agonists reaches its maximum value at this location. Figure 5.13 clearly shows the different locations of maximum deposition and maximum platelet activation rate for the geometry of Casa and Ku [147] with maximum wall shear rate of 6500 s^{-1} (case 2).

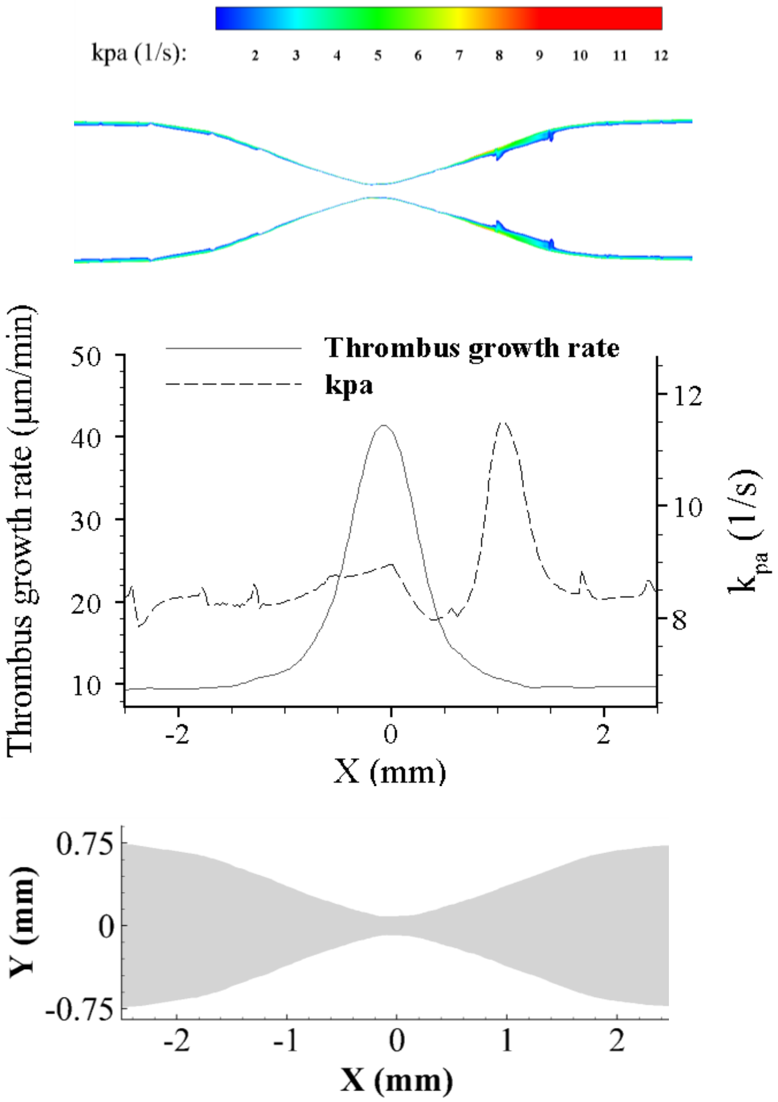

Figure 5.13 (Top) Platelet activation contours colorized by k_{pa} values. The contour lines with values below 1 are cut off since no activation occurs for $k_{pa} < 1\ s^{-1}$. Note that $k_{pa} = 1\ s^{-1}$ is the minimum activation threshold for platelets. (Middle) Different locations of maximum deposition and maximum platelet activation rate for the case of Casa and Ku [147] **with maximum wall shear rate of 6500 s^{-1} (case 2). (Bottom) Geometry of the stenosis area.**

5.3.6 Prediction of occlusion and embolism

Predicted occlusion times are compared with experimental observations of Casa and Ku [147] in Figure 5.14. For Casa’s cases where blood flow rate continuously decreases with thrombus growth, occlusion occurs for all cases (cases 1-3). However, for Wootton's cases with constant flow rate, in our simulations occlusion does not occur due to high wall shear rates.

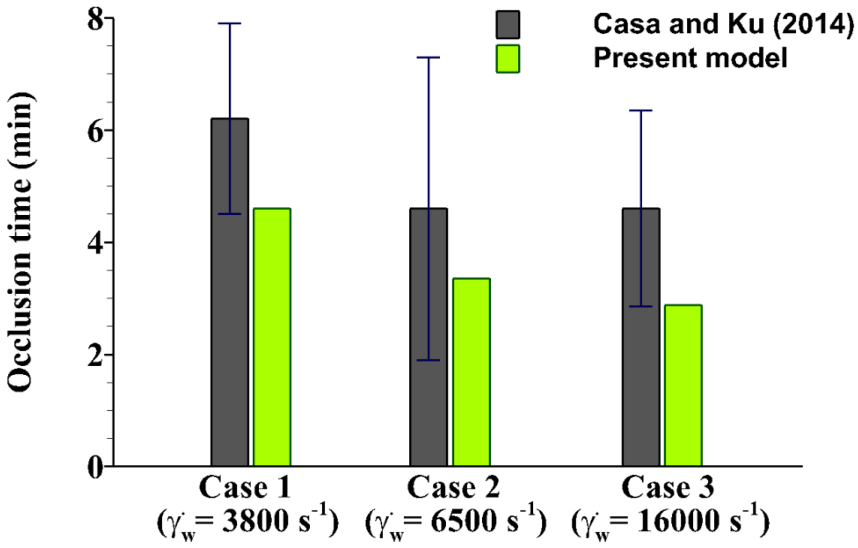

Figure 5.14 Comparison of predicted occlusion times with experimental data of Casa and Ku [147]. Occlusion does not occur for Wootton's [111] cases due to occurrence of embolism.

As Figure 5.14 shows, occlusion times obtained by the present model fall within the confidence limit of experimental data from Casa and Ku [147]. Predicted times are 276.2 s, 201.4 s, 173.1 s respectively for cases 1-3 and the corresponding experimental values report by Casa and Ku are 372±102 s, 276±162 s, and 276±105 s. For Wootton's cases (cases 4-6) occlusion does not occur in our simulations due to negative adhesion rates at the stenosis degree of 76%. Once the thrombus height (in radial direction) reaches 1.52 mm (~76%), negative λ results in negative k_{rs}, k_{as}, and k_{aa}. Thus, a transient decrease in platelet deposition occurs, suggesting that detachment predominates deposition and masses of platelets are dislodged from the surface. In the present modeling framework, the stenosis degree keeps oscillating between 70 to 76%. $M_{at}(x,t)$ when extrapolated to lower values (because of negative adhesion rates) lowers the stenosis degree to

~70%. A repeat of the procedure will extrapolate the stenosis degree back to 76% and so on. This embolism and regrowth phenomena, therefore, prevents complete occlusion of the vessel in our model. This matches perfectly with observations of Wootton et al. [111] and Markou et al. [145].

5.4 Summary and Conclusion

Continuous thrombus formation in stenosed vessels leads to substantial change in geometric shape of the wall. This process cannot be accurately modeled by using constant platelet-surface adhesion rates. In this chapter, an adaptive model of thrombosis was introduced that can predict evolving thrombus growth in stenosed vessels. Simulations were run under both constant flow rate and constant pressure head conditions to test two different scenarios. The significance of this model can be seen in the quantification of effects of changes in mural thrombus geometry on platelet transport, activation and deposition kinetics. Previous models are not capable of simulating nonlinear growth of thrombus within large time frames (>1 min) without excluding biological factors such as thrombin, ADP, and TxA_2. However, results using the current model demonstrate good agreement with experimental observations of nonlinear growth of thrombus, whereas constant values for platelet adhesion rates cannot capture the geometry-dependent platelet transport during thrombosis. Predicted occlusion times using the current numerical model were shown to be in better agreement with experimental observations using variable stenosis geometry and platelet adhesion rates. This is an important step as the model introduced in this chapter utilizes a first of its kind continuum model with variable thrombus geometry.

6 Implementation of shear-induced platelet activation model: Results for stenosed vessels

6.1 Introduction

Platelet activation is known as a precursor of thrombus formation under pathological conditions and can occur through biological or/and mechanical pathways. Biological mechanism is already implemented and validated in our model; and the effect of shear stress is taken into account in the model by using shear-dependent platelet adhesion rates and shear-dependent mass diffusivities for platelets and thrombin-related factors. But the shear-mediated platelet activation was not modeled. In this chapter, we implement a shear-induced platelet activation model to improve the model capability for predicting mechanically induced activation. As platelets navigate through the vascular system, they are stretched, sheared, and compressed by the local gradients in the flow. Many studies have shown mechanically induced platelet activation. Ramstack et al. [214] showed that platelet activation occurs for platelets exposed to flows with elevated shear rates for a long time. Hellums [83] found the locus of platelet activation threshold in a shear-time plot. Bluestein et al. [215] reported rates of platelet activation caused by high shear flow in different left ventricular assist device configurations. In another study, they introduced a parameter for level of platelet activation by integrating the spatial average of shear rate over platelet exposure time in a subset of a vessel [84]. Similarly, other researchers have developed some useful path-dependent, trajectory-based activation models [73], [78], [85], [164].

6.2 Methods

A recent method introduced by Soares et al. [87] and Sheriff et al. [88] provides a strong mathematical tool for quantifying shear-induced platelet activation. This model was successfully validated using experimental data obtained in-vitro under various conditions with static and dynamic (variable) shear rates.

Following a path-dependent approach of Blackshear et al. [216] to associate red blood cell damage (hemolysis) with shear stress and exposure time, the platelet activation state parameter, PAS is defined as:

$$PAS(\tau, t) = C\tau^{\alpha} t_{exp}^{\beta} \tag{6.1}$$

where τ is the local fluid shear stress (dyne.cm^{-2}), t_{exp} is the exposure time of platelet (s), and C, α and β are model constants that have to be found after on calibration of the model based on experimental data. In the experiments of Sheriff et al. [88], platelets were exposed to dynamic and constant shear stresses to emulate shear conditions found in blood-circulating devices. Tested shear profiles in [88] are given in Figure 6.1.

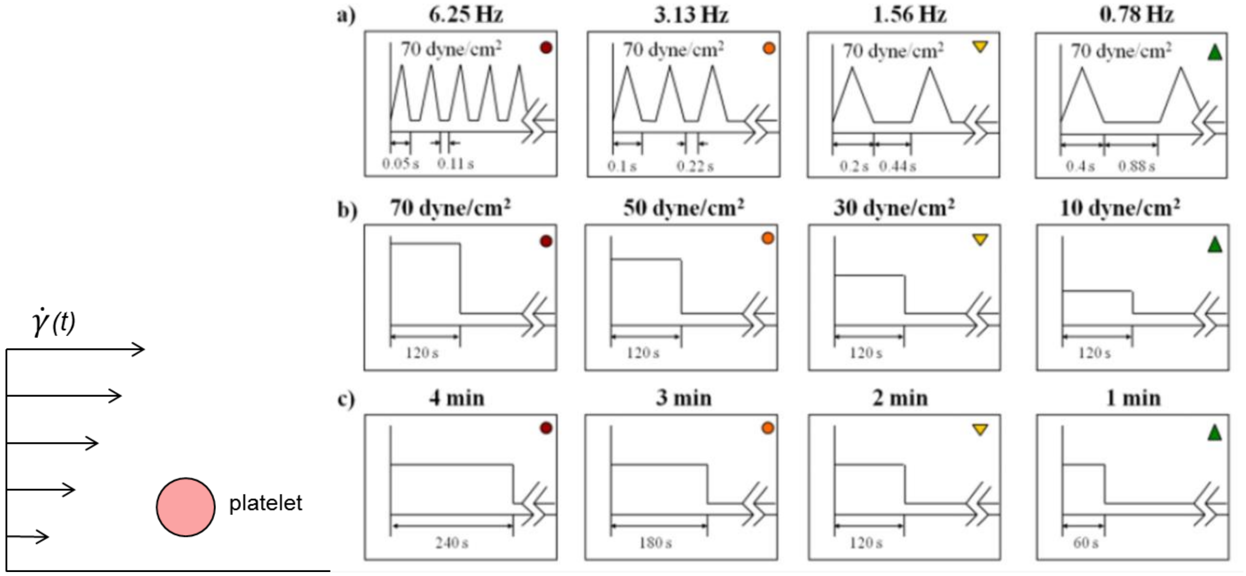

Figure 6.1 Shear stress functions used by Sheriff et al. [88] for calibration of shear-induced platelet activation model. Different profiles with a) variable frequency cases, b) variable shear magnitude, and c) variable durations were tested. Figure used from Springer with permission of Sheriff et al.

Expanding the Eq. (6.1) to account for dynamic conditions yields a cumulative power law (CPL) derivation of the initial PAS equation:

$$PAS_{CPL}(\tau,t) = C_1\beta \int_{t_0}^{t_{total}} \beta\tau(t)^{\alpha}t^{\beta-1}dt + C_2 \int_{t_0}^{t_{total}} \alpha\tau(t)^{\alpha-1}t^{\beta}\frac{|d\tau(t)|}{dt}dt + PAS(t_0) \qquad (6.2)$$

where $PAS(t_0)$ is the platelet activation state at the start of the experiment. Equation (6.2) will have a discretized form as follows:

$$PAS_{CPL}(\tau,t) = C_1\beta\sum_{i=1}^{n} t_i^{\beta-1}\tau_i^{\alpha}\Delta t_i + C_2\alpha\sum_{i=1}^{n}\tau_i^{\alpha-1}t_i^{\beta}|\tau_i-\tau_{i-1}| + PAS(t_0) \qquad (6.3)$$

Note that α, β, C_1 and C_2 are found after calibrating the model based on experimental data and are given in Table 6.1.

Table 6.1 PAS model constants found by Sheriff et al. [88] for constant and dynamic shear stress experiments.

Model	α	β	C_1	C_2
Constant shear	0.824	0.762	5.35×10^{-5}	0
Dynamic shear	1.0293	0.7249	1.3×10^{-4}	0

The PAS model was coded in MATLAB® (MATLAB 8.4, The Mathworks Inc., Natick, MA, 2014) using the constants (given in Table 6.1) to validate the implementation first. Time integration was done using the Euler explicit method. Then, the model was implemented in the main code as discussed later. The MATLAB code is given in Appendix D.

Implementation of the PAS model using particle tracking method

Since platelet activation state (PAS) is a path-dependent variable, it should be calculated for an individual platelet (Lagrangian viewpoint). Therefore, a particle tracking method was used to calculate the PAS values. In order to do this, representative particles were injected from the inlet into the domain. Generally, fluid forces exerted on particles in a flow can be important. However, due to the low Stokes number (Stk) of platelets in blood flow we assume that the representative particles follow the trajectory of the fluid flow (i.e. streamlines) and do not affect the flow. In other words, no force is exerted on fluid material by a representative particle. Stokes number is a nondimensional number that characterizes the behavior of particles in a fluid flow and is defined as the ratio of the characteristic time of a particle to the characteristic time of the flow:

$$Stk = \frac{\rho_p d_p^2 u_f}{18 \mu_f l_{ref}} \tag{6.4}$$

where ρ_p is the density of the particle, d_p is the particle diameter, u_f is the flow velocity, μ_f is the fluid viscosity, and l_{ref} is the characteristic length. Density of the particles ρ_p was assumed to be 1050 kg.m^{-3}, size of particles was assumed to be same as that of platelets ($d_{PLT} = 2.5$ µm), l_{ref} is the vessel radius (l_{ref}=0.75 mm) and the blood viscosity μ_f was assumed to be 3.5 mPa.s [68]. Maximum Stokes number of platelets in our simulations was around $1 \times 10^{-6} - 2 \times 10^{-6}$ which is a very low Stk number. This small value suggests that a platelet-sized particle does not affect the flow and is transported along the material point trajectory only.

The particle-specific platelet activation state, PAS^p is calculated for all particles. The parameter with which PAS^p can be combined and already exists in our framework is the platelet activation rate, k_{pa}. k_{pa} characterizes the biological activation and describes the extent of platelet activation due to concentration of thrombogenic agonists ADP, TxA$_2$, and thrombin.

Since k_{pa} is calculated at the fluid cell center, particle PAS values (PAS^p) should be eventually transferred from particles to cell centers to be used in the main thrombus formation model. In order to do this, the mean value of PAS (denoted as cell PAS, PAS^c) is calculated by using the particles located in neighbor cells. Particles within two neighbor cell layers are identified, and counted, and then PAS^p values are summed and divided by the number of particles. Figure 6.2 shows a schematic representation of particles distributed in the domain. For example, PAS^c for the target fluid cell number 2 and 17 are calculated as follows:

$$PAS_2^c = \frac{1}{5}(PAS_1^p + PAS_2^p + PAS_3^p + PAS_4^p + PAS_9^p) \tag{6.5}$$

$$PAS_{17}^c = \frac{1}{10}(PAS_1^p + PAS_2^p + PAS_3^p + PAS_4^p + PAS_6^p + PAS_7^p + PAS_8^p + PAS_9^p + PAS_{10}^p + PAS_{12}^p) \tag{6.6}$$

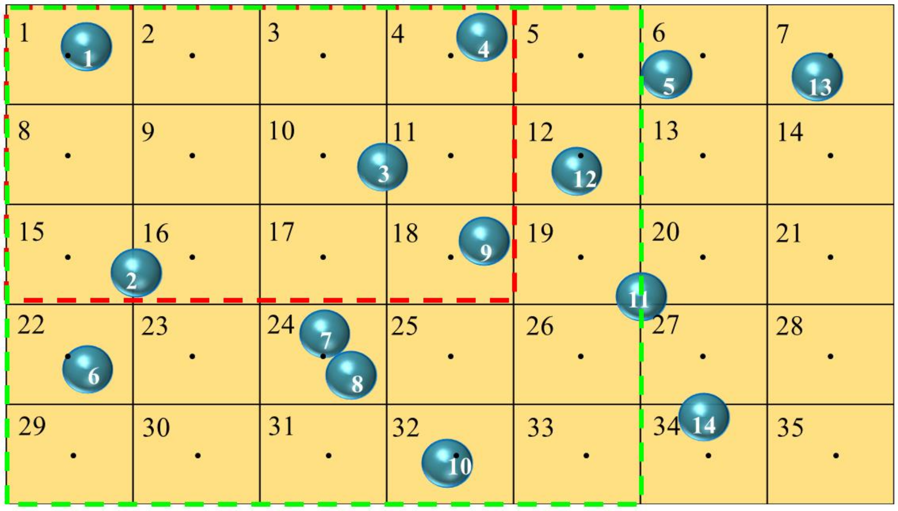

Figure 6.2 Calculation of platelet activation state (PAS) in a target fluid cell; particle PAS values are mapped from particles (blue) to fluid cell centers (yellow). The particle PAS values are averaged using the particles located within 2 cell layers around the target cell. The obtained mean value is assigned to the fluid cell center. 14 particles are distributed in 7x5 fluid grid (with total 35 fluid cells). Region with red dash lines shows the cells used to calculate PAS at cell 2. Region with green dash lines shows the cells used to calculate PAS at cell 17.

Two highly stenosed cases were examined for shear-induced platelet activation: Casa's cases with stenosis degree of 78% and maximum wall shear rates of 6500 s^{-1} (Re=5.3) and 16000 s^{-1} (Re=13.24).

6.3 Results

First, the implementation of the PAS model (in MATLAB®) is validated using the experimental data of Sheriff et al. [88]. Then, results for platelet activation state, PAS are presented in exemplary simulations that were run in stenosed tubes using the particle tracking method.

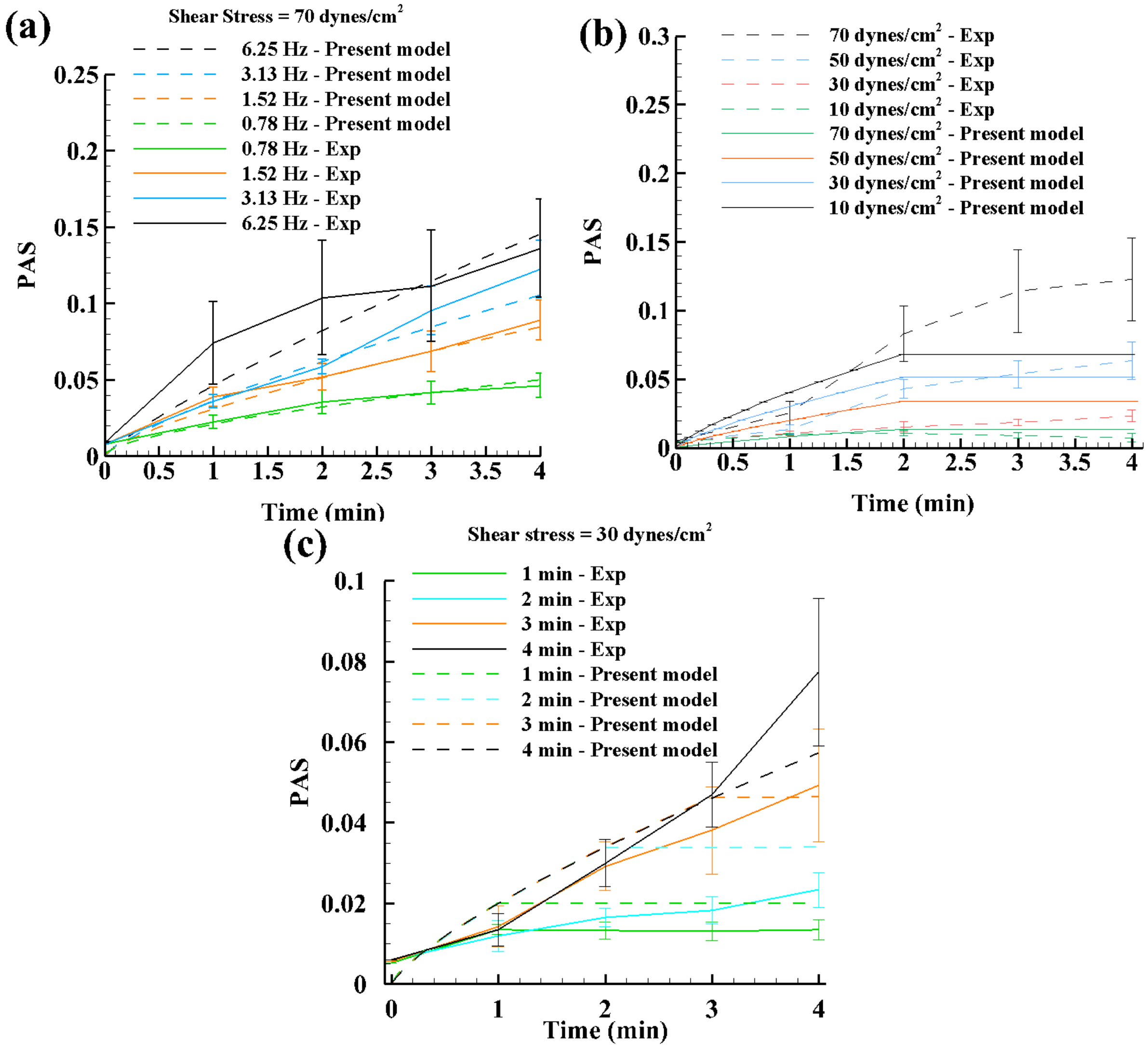

Figure 6.3 Comparison of our results for variation of platelet activation state PAS with time (using the implemented code in MATLAB®) with experimental results of Sheriff et al. [88] for (a) shear stress of 70 dynes.cm^{-2} with loading frequencies of 0.78 Hz, 1.52 Hz, 3.13 Hz, and 6.25 Hz; (b) different shear stress magnitudes of 10 dynes.cm^{-2}, 30 dynes.cm^{-2}, 50 dynes.cm^{-2}, and 70 dynes.cm^{-2}; (c) shear stress of 30 dynes.cm^{-2} with loading durations of 1 min, 2 min, 3 min, and 4 min.

Figure 6.3 compares our results for platelet activation state with experimental measurements of Sheriff et al. [88]. Although, our results are in good agreement with experimental results for all simulations, the effect of time step size on PAS is also investigated to make sure our results are independent of time step size Δt.

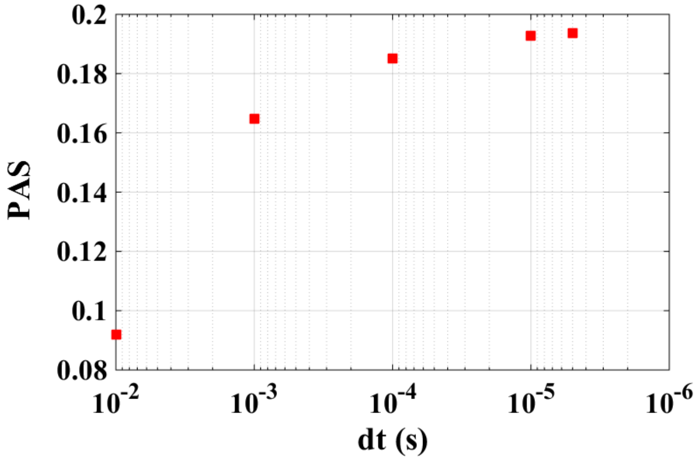

Figure 6.4 Dependence of integration time interval size on platelet activation state, PAS for dynamic case with shear stress of 70 dyne.cm^{-2} and frequency of 6.25 Hz at t=240s.

As Figure 6.4 shows, the nondimensional PAS value converges to a constant value for $\Delta t < 1 \times 10^{-5}$ s. All step sizes used in future stenosed tube simulations are smaller than this value, therefore, independence of PAS results on time step size is ensured.

For both simulations 7700 particles (d_p=2.5 μm) that represent unactivated platelets were seeded at the inlet with initial PAS values of zero. Enough particles were injected to make sure that they cover the cross sectional area of the vessel. The distribution of seeded particles at inlet boundary are illustrated in Figure 6.5.

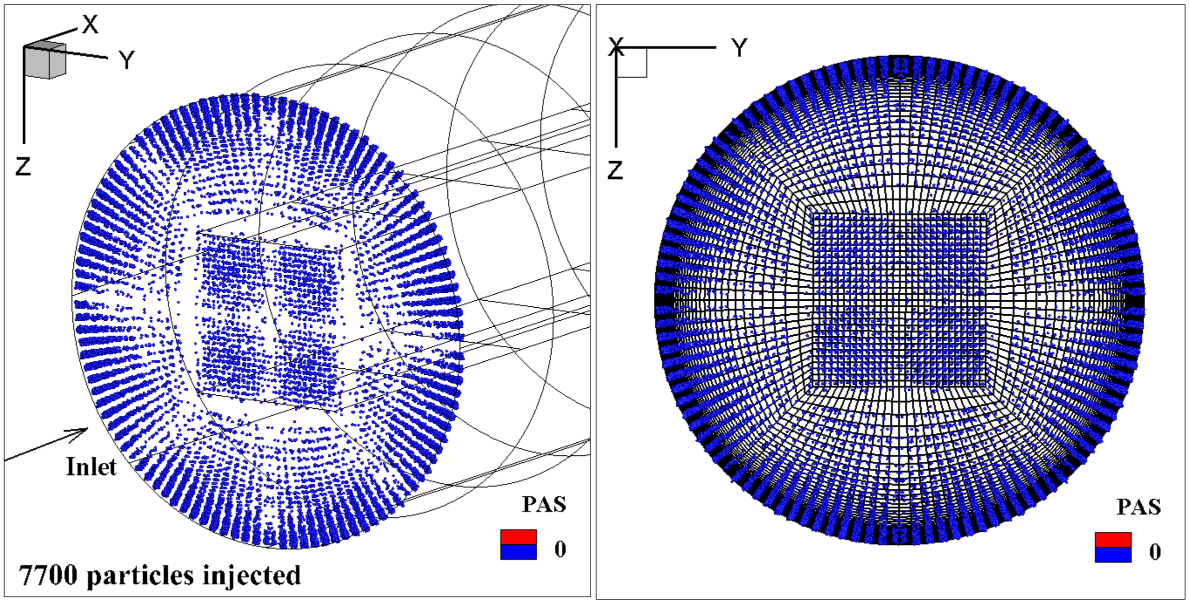

Figure 6.5 (Left) Isometric view of distribution of 7700 injected particles at the inlet boundary of computational domain. (Right) Front view of seeded particles and the fluid grid at the inlet. Initial PAS values were set to zero (i.e. no shear-induced platelet activation).

Results for platelet activation state in Casa's case (Re=5.3, $\dot{\gamma_w} = 6500\ s^{-1}$*)*

Particles colored by PAS contours are illustrated in Figure 6.6 and Figure 6.7 respectively for Casa's case with maximum shear rates of 6500 s^{-1} (mild shear, Re=5.3) and 16000 s^{-1}(high shear, Re=13.24). For the mild shear case, highest PAS values occur for particles in poststenosis area after they go through the neck area near the stenosis apex (see Figure 6.6). Since this region is associated with highest wall shear stresses in the vessel, one can conclude that activation happens at higher rate in the poststenosis region under mild shear conditions (Re=5.3 and ~6500 s^{-1}). Peak value of PAS, however, does not exceed 0.001 which means platelets hardly reach 0.1% shear-induced activation in short perfusion times (shorter than 5 s) and mild shear rates (6500 s^{-1}).

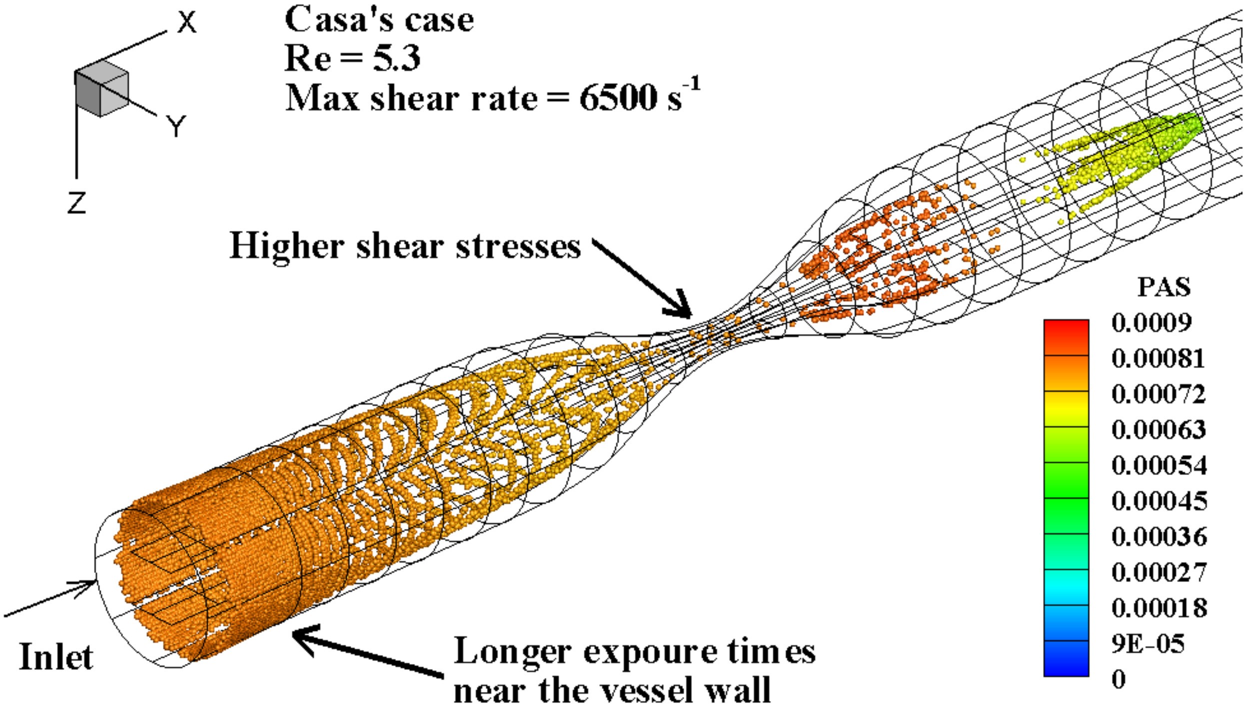

Figure 6.6 Injected particles colored by PAS for Casa's case with maximum shear rate of 6500 s^{-1} at the stenosis apex (Re=5.3).

Results for platelet activation state in Casa's case (Re=13.24, $\dot{\gamma}_w = 16000\ s^{-1}$*)*

Particles with PAS contour plots are illustrated in Figure 6.7. For the high shear case (16000 s^{-1}), PAS values are maximum in the vicinity of the vessel wall where velocities are close to zero (see the region near inlet in Figure 6.7) Since the particle velocity is equal to the flow velocity, particles near the wall stay in the lumen area for longer times. In other words, since PAS values are highest (~0.006) near the inlet boundary in the vicinity of vessel wall, platelet exposure time predominates the shear stress effect in the high shear case with maximum wall shear rate of 16000 s^{-1}.

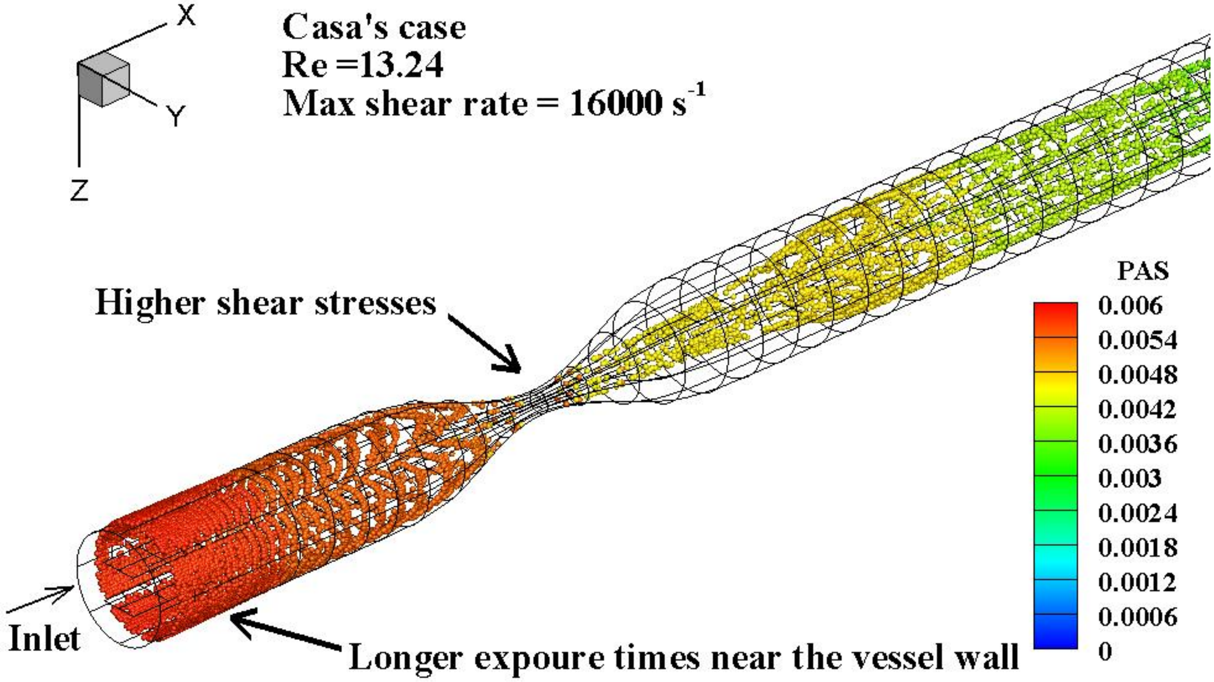

Figure 6.7 Injected particles colored by PAS for Casa's case with maximum shear rate of 16000 s^{-1} at the stenosis apex (Re=13.24).

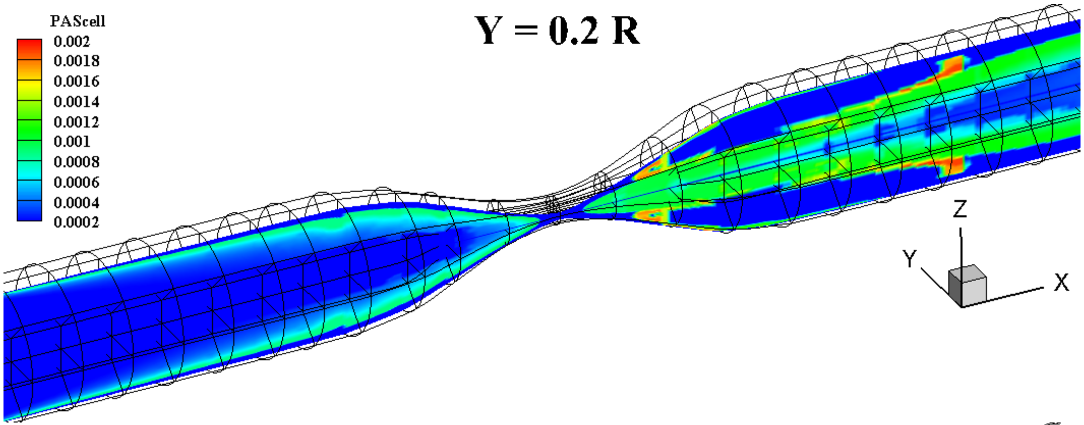
Y = 0.2 R
PAScell
0.002
0.0018
0.0016
0.0014
0.0012
0.001
0.0008
0.0006
0.0004
0.0002
Z
Y
X

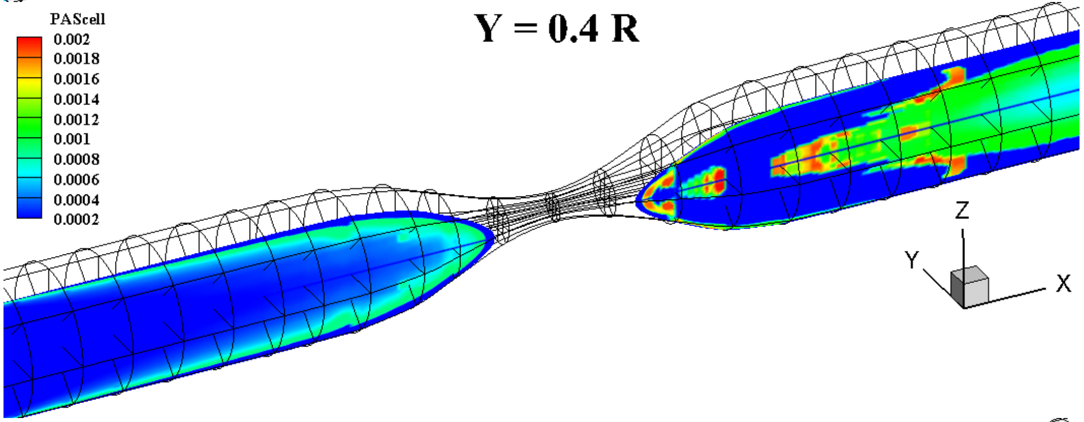
Y = 0.4 R
PAScell
0.002
0.0018
0.0016
0.0014
0.0012
0.001
0.0008
0.0006
0.0004
0.0002
Z
Y
X

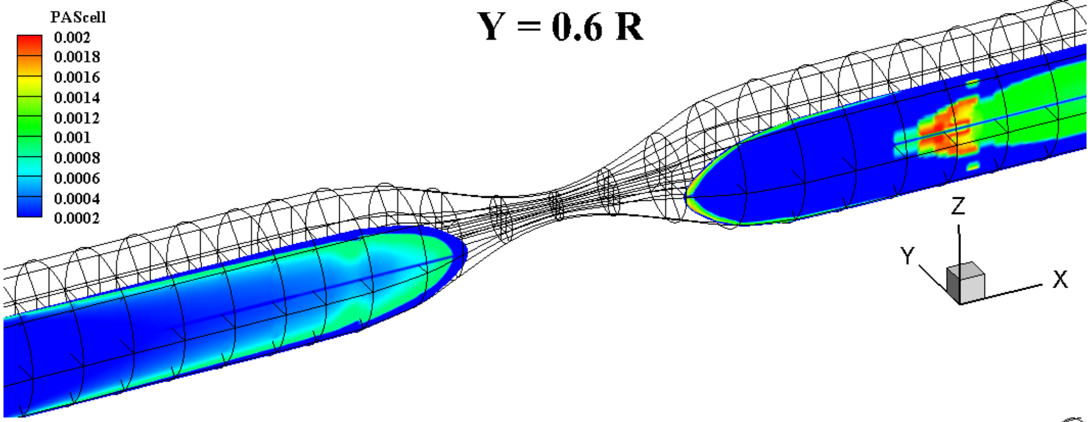
Y = 0.6 R
PAScell
0.002
0.0018
0.0016
0.0014
0.0012
0.001
0.0008
0.0006
0.0004
0.0002
Z
Y
X

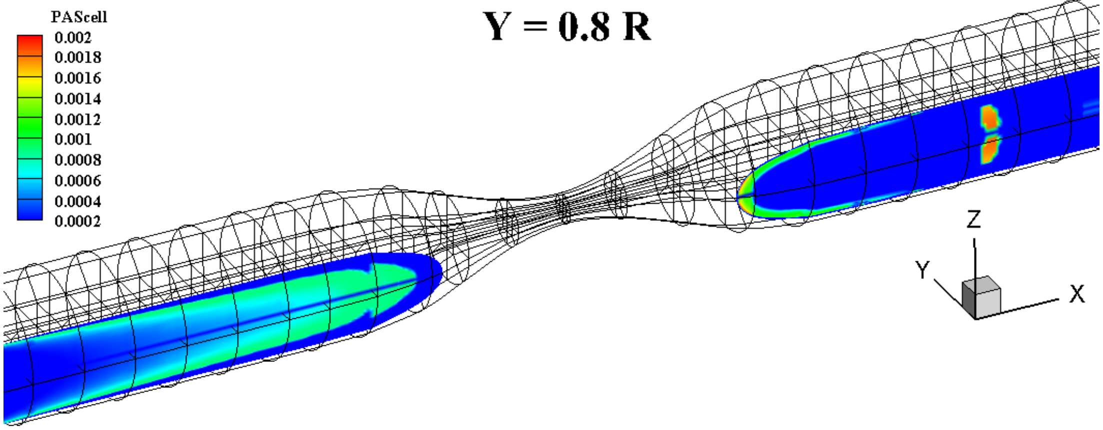
Y = 0.8 R
PAScell
0.002
0.0018
0.0016
0.0014
0.0012
0.001
0.0008
0.0006
0.0004
0.0002
Z
Y
X

Figure 6.8 Distribution of platelet activation state (PAS) at different locations in lateral direction: Y=0, 0.2R, 0.4R, 0.6R, and 0.8R where R is the unstenosed vessel radius. PAS^c values do not exceed 0.002 in the computational domain.

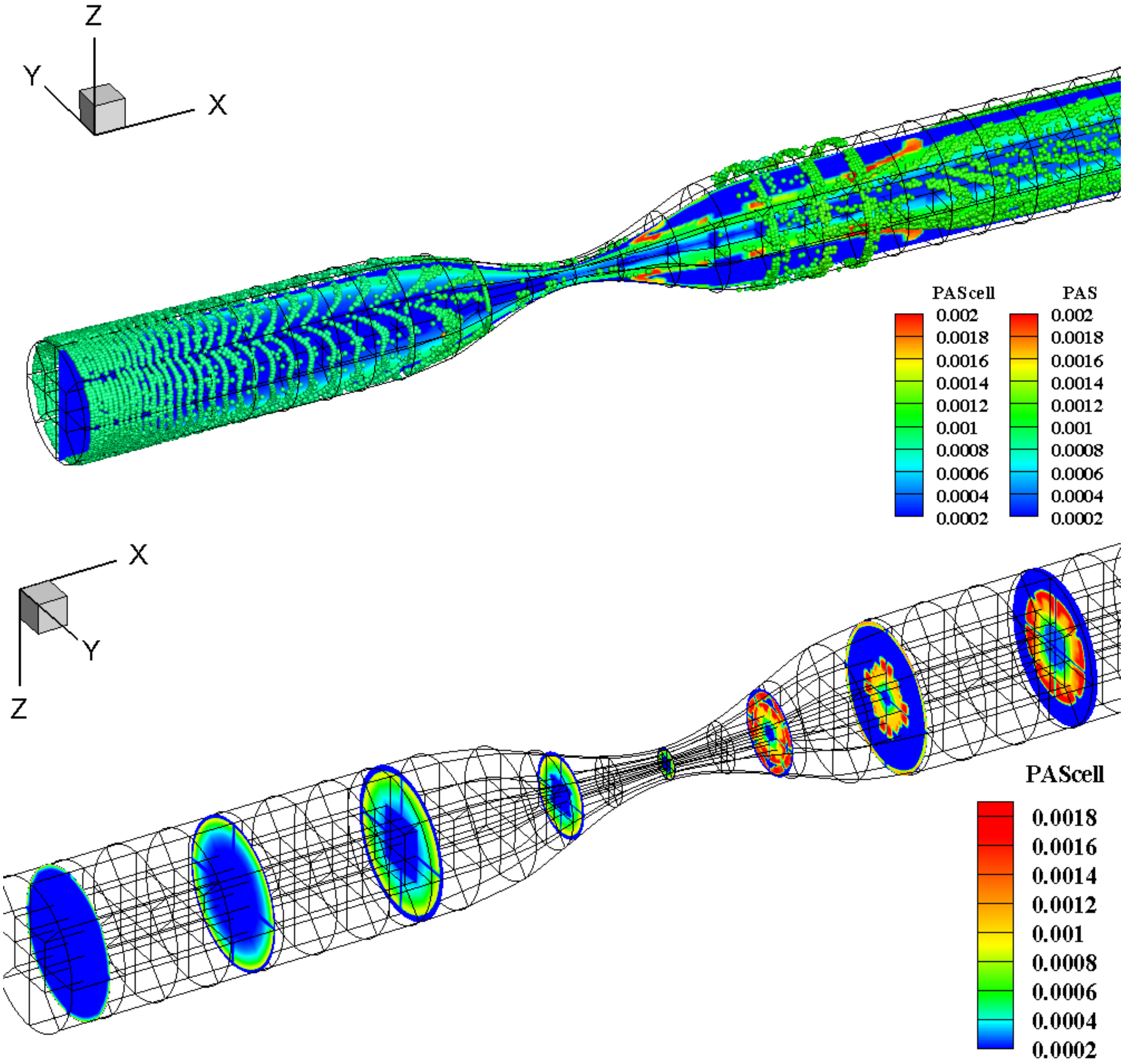

Figure 6.9 (Top) distribution of injected representative particles in the vessel along with contour plot of PAS field at Y=0 plane; both PAS^c and PAS^p values are plotted. (Bottom) distribution of platelet activation state (PAS) at different locations in axial direction. PAS values do not exceed 0.002 in the computational domain.

In addition to particle PAS values, to show the distribution of cell values of platelet activation state parameter (PAS) is plotted on X-Z planes (see Figure 6.8 for coordinates) at different Y locations: Y=0.2R, 0.4R, 0.6R, and 0.8R where R is the vessel nondimensional radius. Also, PAS contours are plotted at different X locations in Figure 6.9 (bottom). Shear-induced platelet activation occurs to greater extents in an annular region that becomes narrower as platelets navigate through the stenosed section. As seen in Figure 6.9 platelets are activated more in the poststenosis area (PAS=0.001-0.006), however, even values corresponding to this region are very small and can be neglected compared to the full activation state (PAS=1). Thus, as a concluding remark, the shear-mediated activation can be neglected in our simulations unless platelets are exposed to extremely high shear stresses for very long periods of time (> 10min).

6.4 Summary and Conclusion

The effect of shear stress is already taken into account in our model by using shear-dependent platelet adhesion rates and shear-dependent mass diffusivities for platelets and thrombin-related factors. But the shear-mediated platelet activation was not modeled. In this chapter, a useful Lagrangian model for quantifying the shear-induced platelet activation was presented. Platelet activation state parameter (PAS), which characterizes the shear-induced platelet activation, was introduced to our previously developed thrombosis model. As a first step, the implementation of the PAS model was verified for various static and dynamic shear conditions using the experimental (in-vitro) results of Sheriff et al. [88]. Then, once implemented in the GenIDLEST code, the model was applied to particles injected in stenosed tubes to examine the shear-induced platelet activation model in a typical stenosis with supraphysiological shear rates. It was shown that the contribution of shear stress to platelet activation is negligible (<0.1%) in physiological periods of time (<1 min). Therefore, shear-mediated activation can be neglected in our simulations unless platelets are exposed to high shear stresses for very long periods of time (> 10min). Simulation results presented in the next chapter are run without using the PAS model.

7 Preliminary work: Thrombus formation in left ventricular assist device (LVAD)

7.1 Introduction

Heart failure (HF) causes more than 300,000 deaths in the U.S. annually, which costs over $39 billion for the healthcare system [217]. In case the HF patients' condition is not improved by standard medical therapy or they are ineligible for heart transplant, they typically receive a left ventricle assist device (LVAD). LVAD technology has revolutionized the long-term assist device therapy as an alternative for heart transplantation. Over 25,000 people benefit from the use of LVADs and this number is predicted to grow exponentially with the aging population [218]. Often implantation of LVAD for patients with dilated cardiomyopathy (DCM) is followed by perioperative thrombosis. This is mainly caused by pathological hemodynamics and the remodeled geometry of the left ventricle. The schematic pictures of a normal heart and a heart with DCM are shown in Figure 7.1. The complex hemodynamics associated with LVAD surgery in infarcted left ventricle is not well understood and there is a critical need to elucidate the etiology of perioperative device-induced thrombosis. The objective of this chapter is to isolate the effect of LVAD on platelet activation and thrombosis, and identify the most susceptible regions in the native heart for device-induced thrombosis followed by LVAD implantation using the current thrombosis model.

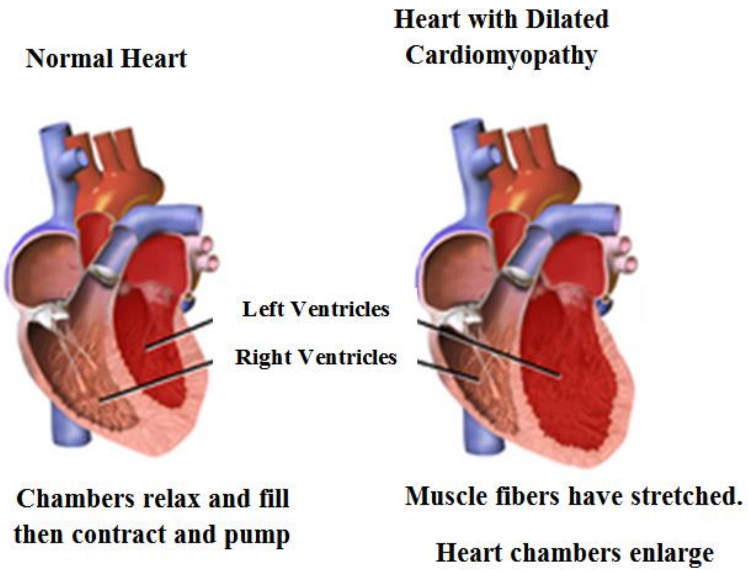

Figure 7.1 (Top) Normal left ventricle (LV) vs. LV with dilated cardiomyopathy (DCM); (bottom) schematic representation of heart with implanted LVAD. Images are reprinted from Blausen.com staff [219].

A left ventricular assist device consists of a continuous flow pump, two pipes, one for sucking the blood flow from the left ventricle (outflow cannula) and the other for routing the flow to the ascending aorta (inflow cannula), a controller, and four batteries as power sources (Figure 7.2a).

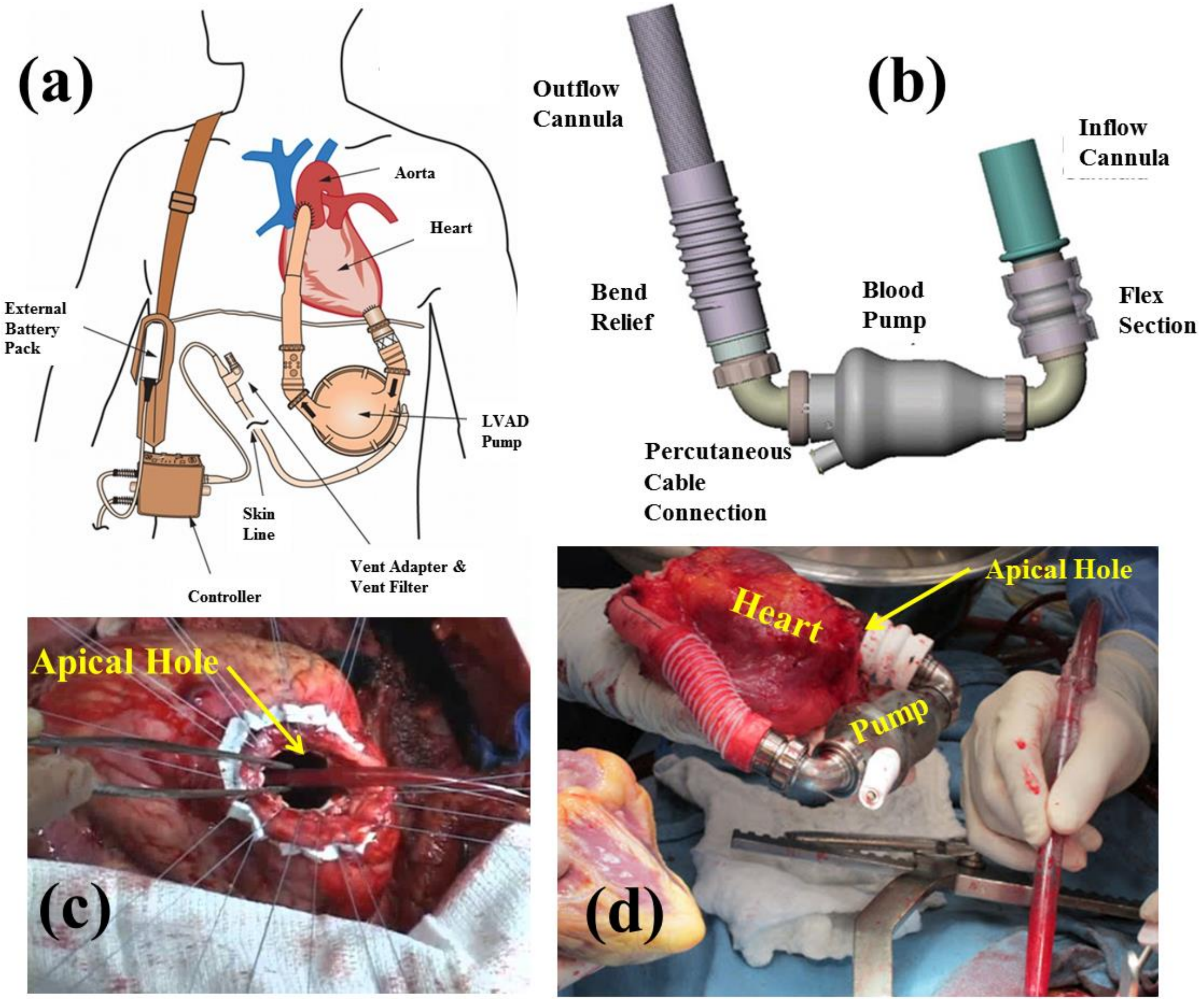

Figure 7.2 (a) Schematic picture of an implanted LVAD and its components. Image courtesy of St. Jude Medical, Inc. (b) The HeartMate axial rotary LVAD pump; the blood flow is sucked from the inflow cannula and routed to the aorta from outflow cannula. Image reprinted with permission from Thoratec Corporation (c) An apical hole created at the bottom of the left ventricle during LVAD implantation surgery. Picture reprinted from [220]. (d) Whole heart with an implanted LVAD; the location of LVAD pump and apical hole in the bottom of LV are indicated in the picture. Picture reprinted from [221].

Due to the malfunction of the damaged part of the left ventricle (i.e. apical aneurysm (AN)) the left ventricle would not be able to sufficiently pump the flow to the aorta with enough pressure. Consequently, to help the heart with pumping the high pressure flow an apical hole is created during the surgery (see Figure 7.2c) and the outflow cannula is inserted into the hole and stitched to the ventricle. The inflow cannula is also put into the aorta and stitched. The LVAD pump can be axial or centrifugal depending on patient-specific needs. An axial rotary pump is shown in Figure 7.2b. In this study, we focus on the flow circulating inside the left ventricle and do not model the blood flowing through the pump or aorta.

Several attempts have been made to test computational models for thrombogenesis at shear levels associated with LVADs. However, there is a lack of computational research specifically on perioperative device-induced thrombosis in HF patients that have undergone LVAD implantation. Seo et al. [3] used a coupled chemo-fluidic computational model to predict thrombin and fibrin generation and platelet density distribution in infarcted LVs with DCM. This high-fidelity model was tested for ventricles with large, medium and small apical aneurysm (AN) under pulsatile flow conditions. The model included both hemodynamics and biochemical reactions of coagulation. But constant parameters for generation rate of agonists were used. Navitsky et al. [161] introduced a thrombus susceptibility potential (TSP) metric based on wall shear rates and exposure times to improve a LVAD design under in-vivo conditions. Shear rates of 500 s^{-1} and 1000 s^{-1} were set as thresholds and cutoff values for initiation and inhibition of platelet deposition, respectively, based on data in [162]. This simplified model was used to investigate the flow inside the LVAD but no simulation was conducted using this model to investigate the effect of implantation of LVAD on hemodynamics inside the LV.

We hypothesize that the combination of the pulsatile flow through the mitral and aortic valves along with the continuous flow generated by the LVAD can lead to recirculation zones with non-physiological shear rates and regions with flow stasis that increase the risk of platelet activation and initiation of thrombus formation in the left ventricle with DCM. Our preliminary results support the mentioned hypothesis and will be presented in this chapter.

7.2 Methods

To perform the left ventricle simulations, first, an infarcted left ventricle is simulated. Then, a left ventricle with implanted assist device is modeled with physiologically relevant velocity profiles for the mitral inlet, and aortic and LVAD outlets. The MRI-based geometry of an infarcted ventricle with large apical aneurysm (AN) is given by Seo et al. [3]. Since the full three dimensional geometry of LV was not provided by Seo et al., the two dimensional geometry was used in our simulations. The geometry was extracted from graphs given in [3]. Figure 7.3a and b show the infarcted left ventricle with normal LV region, apical aneurysm (AN) region, and inlet and outlet boundaries at mitral valve, aortic valve, and assist device (LVAD) locations. To impose the proper profiles at mitral and aortic boundaries, experimental measurements of Bozkurt et al. [222] for an infarcted ventricle with dilated cardiomyopathy (DCM) are used (Figure 7.3c,d). For LVAD simulations a hole (with a diameter of 1.4 cm) is created at the bottom of the ventricle and flow rate profiles are imposed at one inlet (mitral) boundary and at two outlet (aortic and LVAD) boundaries [222]. Figure 7.3c shows the inlet and outlet velocity waveforms applied at mitral and aortic valves, respectively, for the infarcted LV without LVAD (see Appendix E for equations). Figure 7.3d shows the velocity waveforms for the infarcted LV with LVAD implanted at mitral, aorta, and LVAD boundaries. Reynolds number for LV without LVAD based on maximum velocity at mitral inlet (~13.65 cm.s^{-1}) and mitral valve diameter (1.5 cm) is 622 and for the LV with LVAD where maximum velocity at mitral inlet is 18.4 cm.s^{-1} is 838.

As seen in Figure 7.3a and b, the flow leaving the LV through aortic valve is equal for two cases. However, due to continuous flow going through LVAD mitral flow is higher for the case with LVAD.

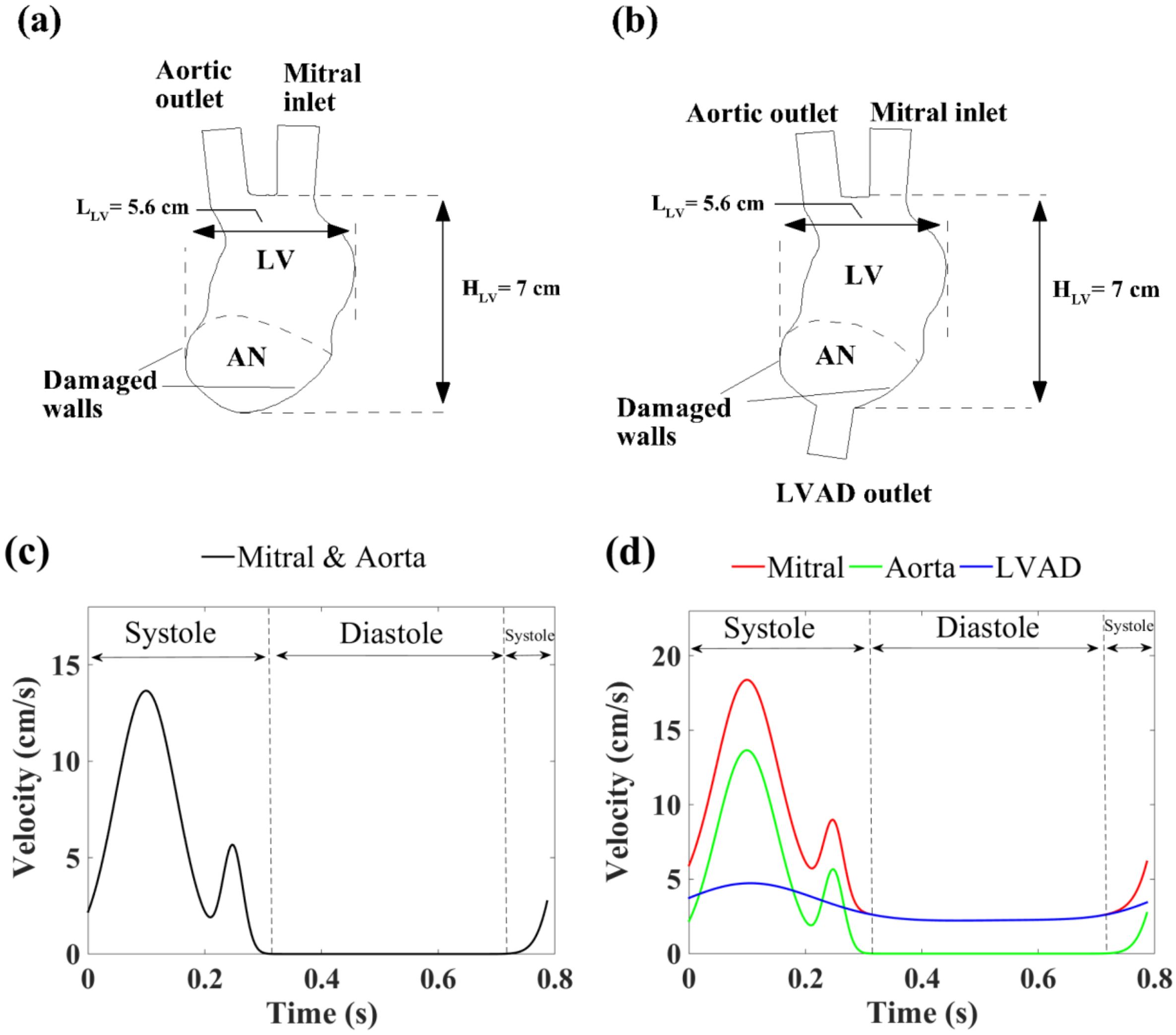

Figure 7.3. (a) Two dimensional geometry of infarcted LV without LVAD obtained from MRI images of Seo et al. [3] used in our simulations. (b) Geometry of infarcted LV with LVAD. (c) Velocity waveforms at mitral and aortic valves of infarcted LV without LVAD. (d) Velocity waveforms at mitral and aortic valves and LVAD outlet of LV with LVAD.

Inner wall surfaces were assumed to be coated with collagen which is known as a very adhesive substrate for platelets. The shear-dependent platelet adhesion rates (Eq. (5.1)) were used to account for the effect of wall shear rate on platelet deposition. Since, there is no experimental data available to set up the problem based on it, we assume arbitrary values for two variables that are present in Eq. (5.1); platelet adhesion rate baselines k_{rs_0}, k_{as_0}, $k_{aa_0}$and shear enhancement factor parameter λ. The parameter values were assumed to be $k_{rs_0} = 3.15 \times 10^{-6}$ m.s^{-1}, $k_{as_0} = k_{aa_0} = 3.92 \times 10^{-6}$ m.s^{-1}, and $\lambda = 1.6 \times 10^{-3}$ s. The flowing blood was assumed to be whole heparinized blood ([H] = 0.728 μM) with physiological levels of platelets and coagulation factors. This value was taken from the literature. Concentration of different constituents injected at the mitral valve inlet are given in Table 7.1.

Table 7.1 Whole blood properties and initial and inlet concentration of blood components used in LV simulations.

Platelets (PLT.mm^{-3})	252,000	[68]
Ratio of resting to activated platelets	20	[45]
ADP (μM)	0	[68]
TxA_2 (μM)	0	[68]
Prothrombin (μM)	1.1	[68]
Thrombin (U.ml^{-1})	0	[68]
Antithrombin (μM)	2.844	[68]
Heparin (μM)	0.728	[147]
Whole blood viscosity (Pa.s)	0.0035	[203]
Whole blood density (kg.m^{-3})	1064	[64]

7.3 Results

7.3.1 Flow characteristics

Unsteady hemodynamics in LV plays a major role in thrombosis; since platelet adhesion rates in our thrombosis model are wall shear-dependent and their role is directly manifested in the extent of platelet activation and deposition it is important to present results that demonstrate the unsteady flow dynamics in LV. Therefore, the concentration of platelets and distribution of platelet deposition are expected to strongly depend on flow dynamics. Here we present variation of velocity and vorticity fields during one representative cardiac cycle. Then, we will discuss the effect of these changes on platelet activation and thrombus formation.

Velocity contours

Velocity (vertical component) contours are plotted in Fig. 7.4 and Fig. 7.5 at different phases of the cycle. Six instants (t=0, t=0.1s, t=0.2s, t=0.25s, t=0.3s, t=0.7s) that correspond to extremum velocities in the applied waveforms are chosen to include in the contour plots.

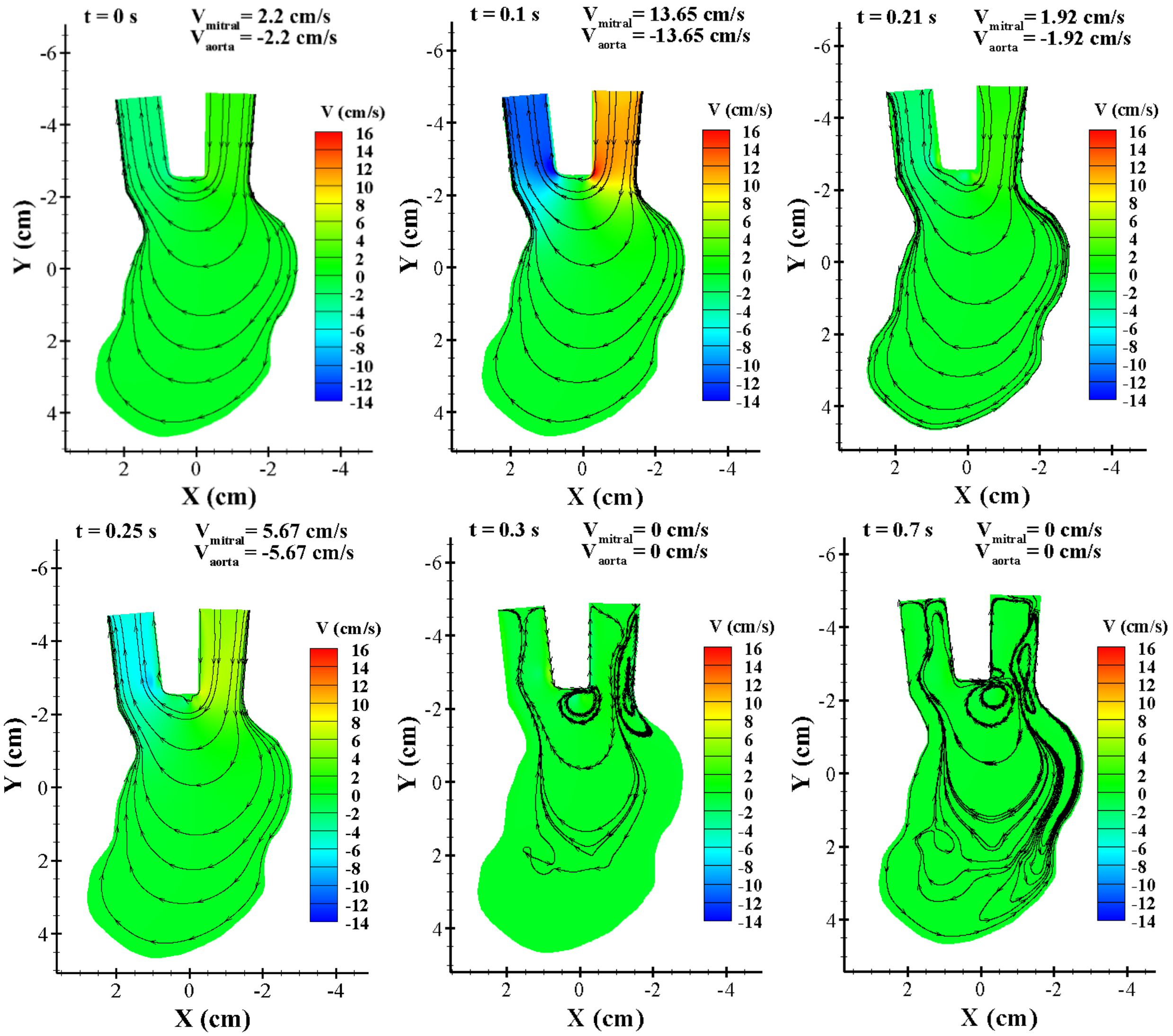

Figure 7.4 Velocity (vertical component) contours in the LV without assist device (LVAD) corresponding to t=0, t=0.1s, t=0.2s, t=0.25s, t=0.3s, and t=0.7s.

At t=0.1s, flow velocities at all boundaries reach their maximum values. At t=0.2s, flow rate reaches its local minimum, then increases to a local maximum at t=0.25s. Then, velocities reach their minimum values at t=0.3s and do not vary until t=0.7s. Velocity magnitudes at mitral valve, aorta, and LVAD boundaries with corresponding time are included in Figure 7.4 and Figure 7.5.

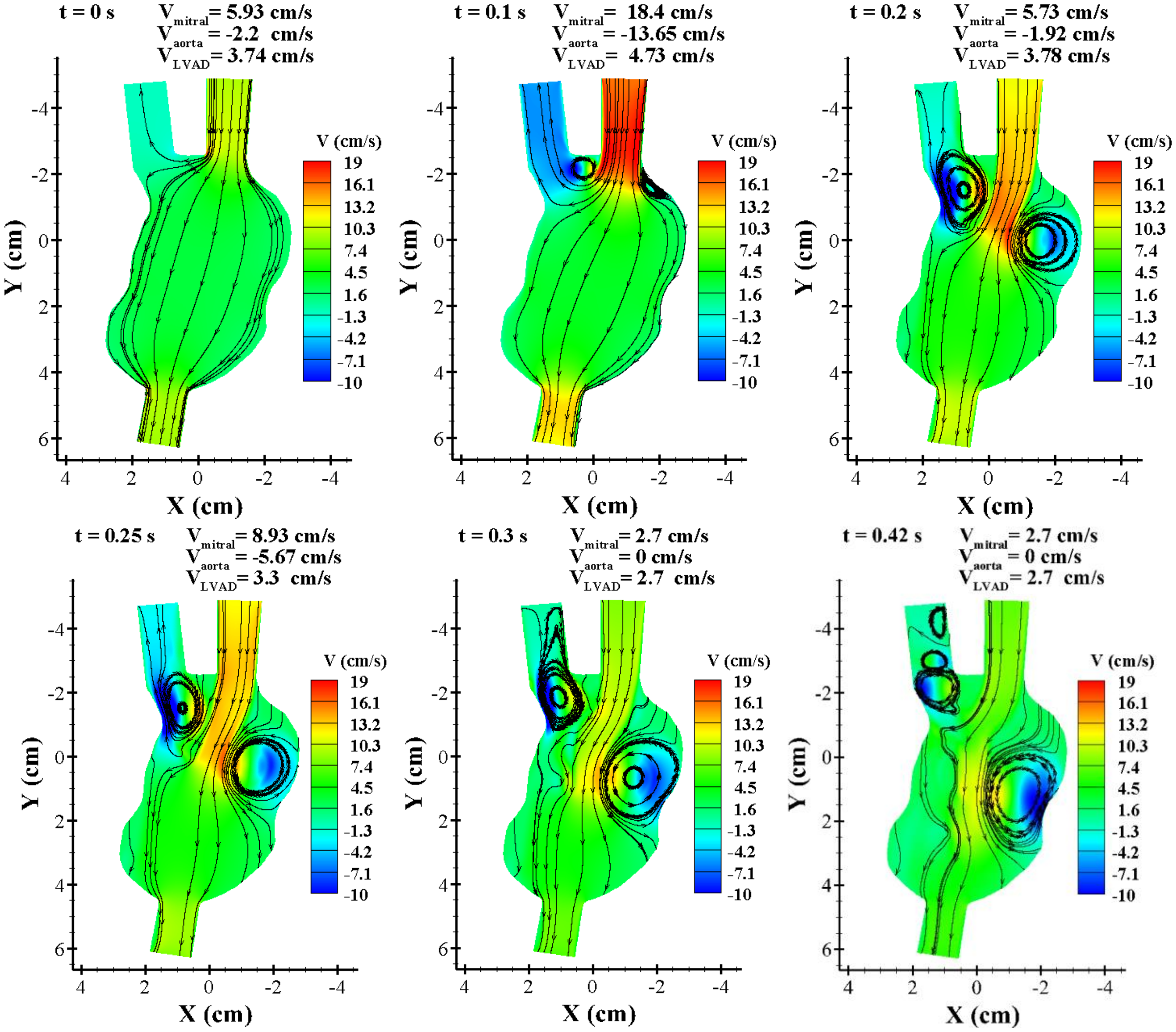
t = 0 s V_{mitral}= 5.93 cm/s V_{aorta} = -2.2 cm/s V_{LVAD}= 3.74 cm/s

t = 0.1 s V_{mitral}= 18.4 cm/s V_{aorta} = -13.65 cm/s V_{LVAD}= 4.73 cm/s

t = 0.2 s V_{mitral}= 5.73 cm/s V_{aorta} = -1.92 cm/s V_{LVAD}= 3.78 cm/s

t = 0.25 s V_{mitral}= 8.93 cm/s V_{aorta} = -5.67 cm/s V_{LVAD}= 3.3 cm/s

t = 0.3 s V_{mitral}= 2.7 cm/s V_{aorta} = 0 cm/s V_{LVAD}= 2.7 cm/s

t = 0.42 s V_{mitral}= 2.7 cm/s V_{aorta} = 0 cm/s V_{LVAD}= 2.7 cm/s

Figure 7.5 Velocity (vertical component) contours in the LV with assist device (LVAD) corresponding to t=0, t=0.1s, t=0.2s, t=0.25s, t=0.3s, and t=0.7s.

Comparison of the variation of velocity contours in LV without LVAD (see Figure 7.4) to those with LVAD (see Figure 7.5) reveals that the blood flow coming from the mitral valve (guided to the LVAD outlet) creates two mild to large recirculation regions one near the aortic valve in which flow circulates in clockwise direction and the other located between the mitral valve and AN (at x≈-2 cm) in which flow rotates in counterclockwise direction. Both of these vortices are generated at t=0.3s where flow rate is minimum at the mitral valve inlet boundary. Consequently, the cavity-like flow in the LV without LVAD is not present anymore when LVAD is connected to the apical hole. The first vortex (smaller one) is sucked from the aortic valve during a cycle, whereas the second vortex (larger one) moves towards LVAD during diastole phase. Since there are large recirculation areas in LV, vorticity contours are also presented to clearly show the different flow characteristics in a given LV with and without LVAD.

Vorticity contours

Vorticity for the instantaneous flow for LVs with and without LVAD are shown in Figure 7.6a and Figure 7.7 respectively. For the LV without LVAD, an overall clockwise circulating flow pattern (positive vorticity) and a thin layer with negative vorticity in the vicinity of all walls are observed (see Figure 7.6a). Our results are in agreement with numerical results of Seo et al. [3] for infarcted LVs with DCM (see Figure 7.6b).

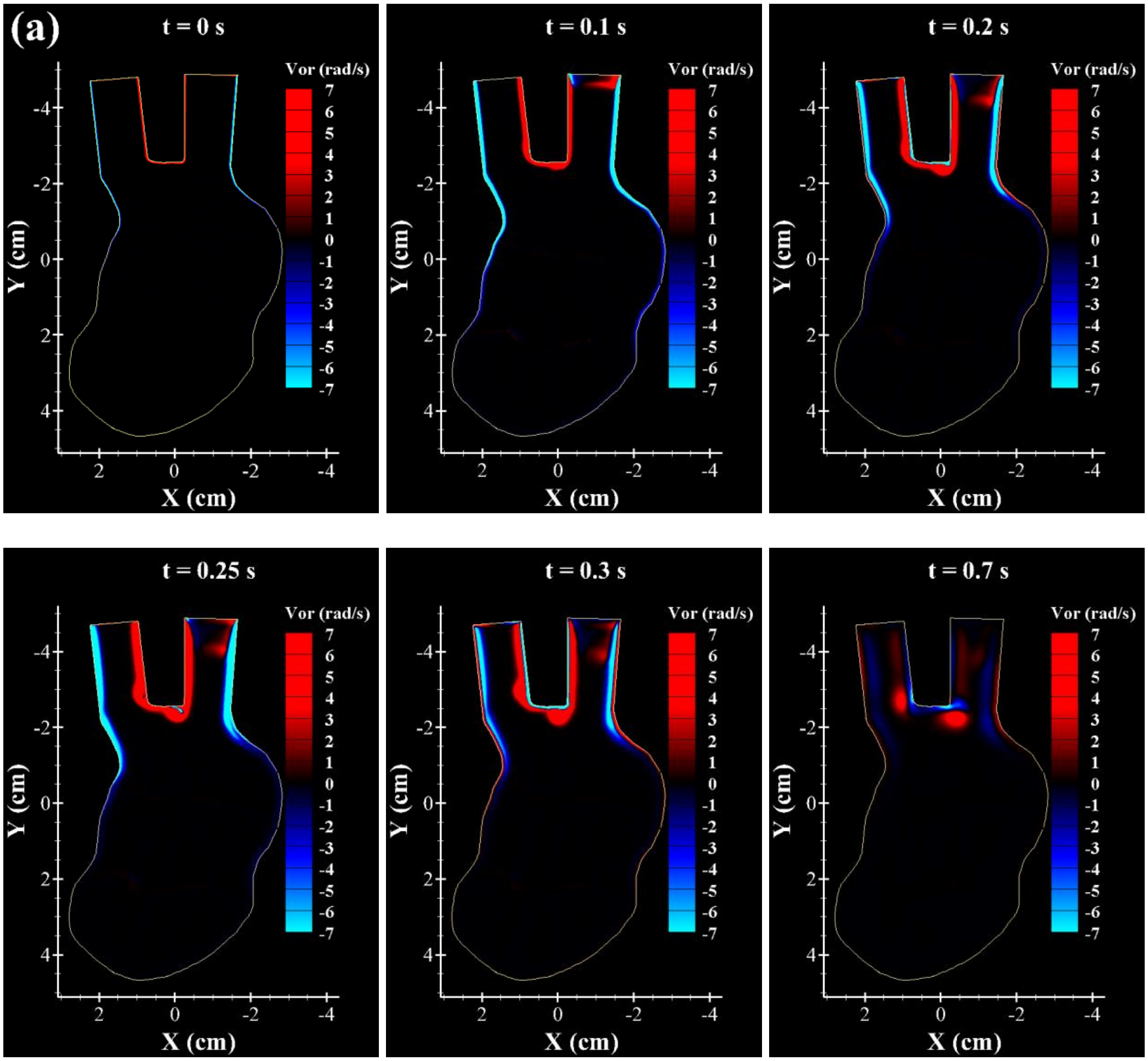

Results of Seo et al. (2016)

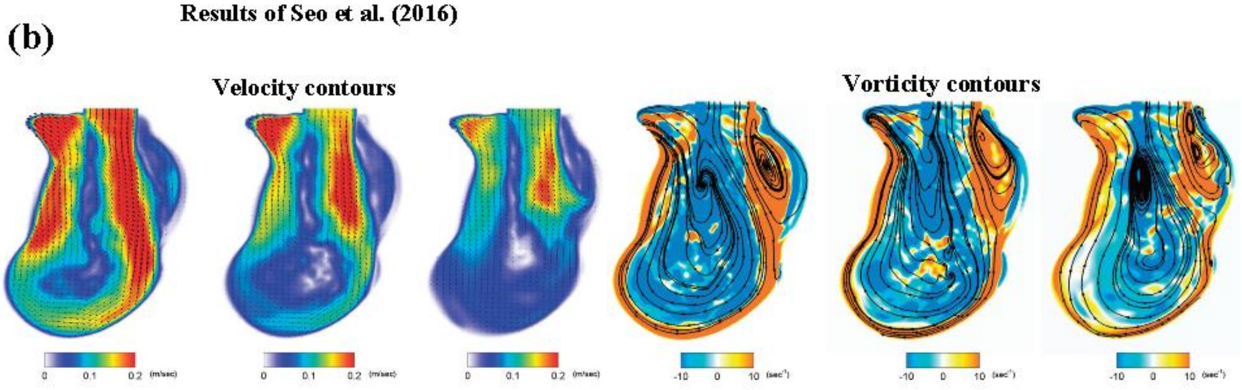

Figure 7.6 (a) Vorticity (normal to the plane component) contours in the LV without LVAD corresponding to t=0, t=0.1s, t=0.2s, t=0.25s, t=0.3s, and t=0.7s in our simulations. Negative vorticity indicates the clockwise

rotation and vice versa. (b) Time-averaged flow field and vorticity on the long-axis view cross-sectional plane for LVs with different AN sizes in the study of Seo et al. [3]. Note that due to different coordinates in our study and Seo's article, negative vorticity in Seo's results is equivalent to positive vorticity in our plots and vice versa. Image in Fig. 7.6(b) reprinted from with permission of Seo et al [3].

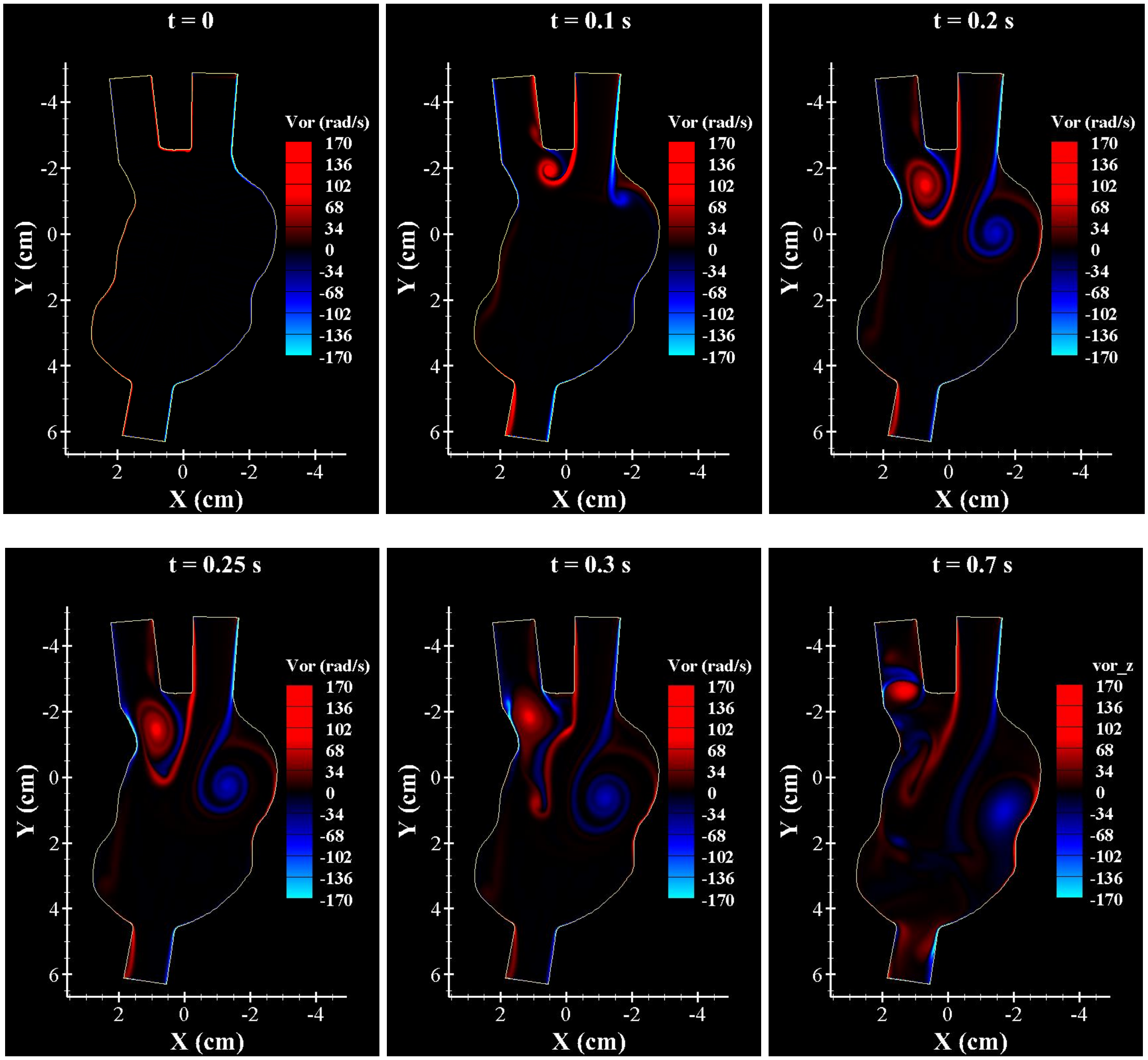

Figure 7.7 Vorticity (normal to the plane component) contours in the LV with LVAD corresponding to t=0, t=0.1s, t=0.2s, t=0.25s, t=0.3s, and t=0.7s. Negative vorticity indicates the counterclockwise rotation and vice versa. Vorticity magnitudes in the LV with assist device are one order of magnitude higher than the LV with no assist device (LVAD) implanted.

As indicated in Figure 7.7 (and Figure 7.5), the blood volume inside mitral inlet is washed out into the LV chamber. The sudden expansion into the LV cavity at the mitral value leads to generation of two vortices during systole phase (t=0.1s to t=0.3s): 1) vortices that rotate the flow in clockwise direction (see red vortices with positive values in Figure 7.7) and are sucked into the aorta; and 2) vortices with negative values that are generated because of flow separation at the dilated right-side wall (in vicinity of mitral inlet) of the LV. These vortices are damped in AN region and washed out to the LVAD outlet during diastole phase.

7.3.2 Platelet activation

Here we present the variation of distribution platelet activation and accumulated platelet deposition during one representative cardiac cycle.

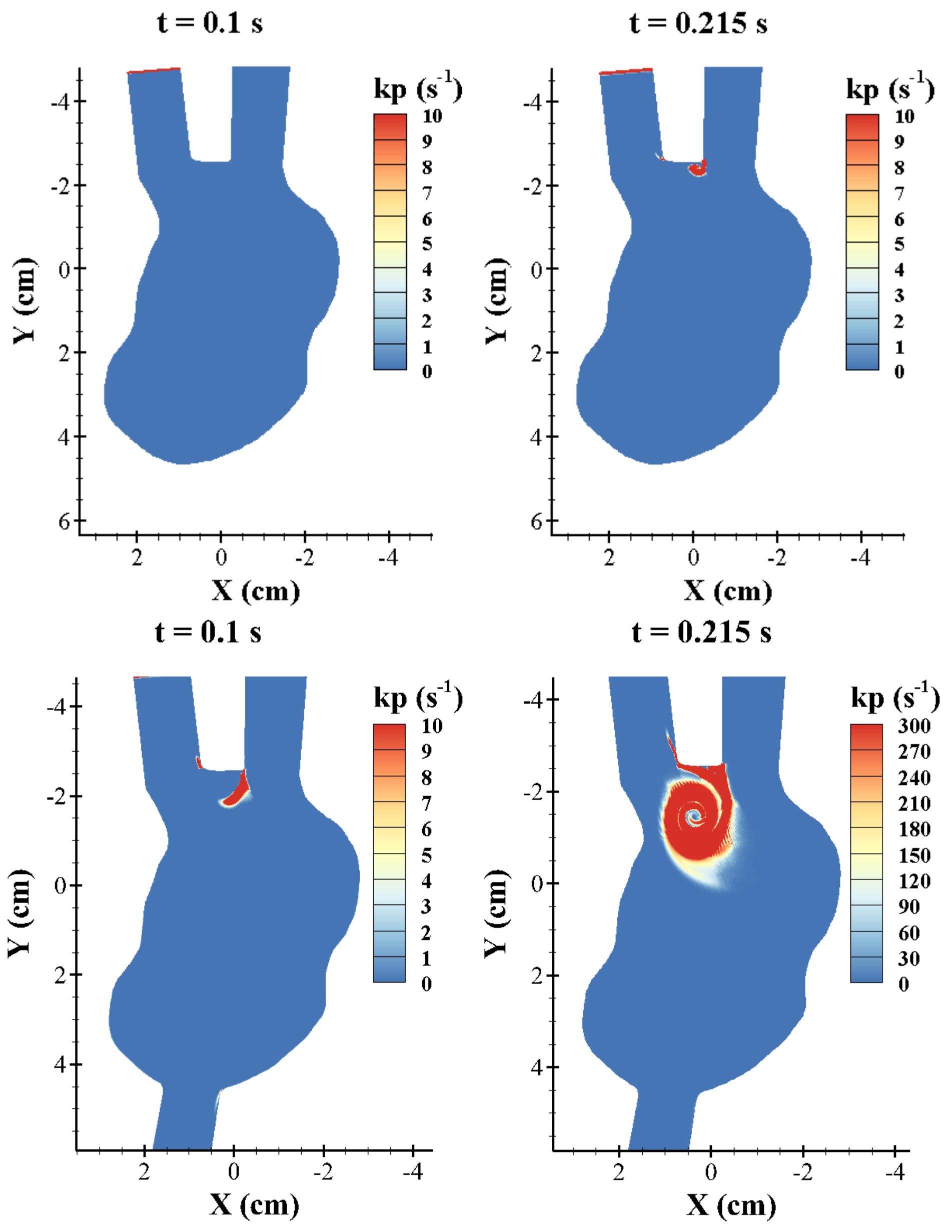

Figure 7.8 Platelet activation rate contours in LV without LVAD (top) and LV with LVAD (bottom) at t=0.1s (where the inlet flow rate at the mitral valve is maximum) and t=0.21s (where the flow rate is minimum during systole phase). Note that in the bottom left plot, scale maximum in the legend is changed from 10 to 300 due to extremely high activation rate values.

As seen in Figure 7.8, at t=0.21s in the LV without LVAD (top right) platelets get activated only in a small region near the bifurcation located between mitral and aortic valves. Comparing

Figure 7.6 and Figure 7.8 reveals that platelet activation rates are higher in locations with stronger coherent vortices and no activation occurs in other regions. We attribute the platelet activation to coherent vorticity generation in the LV. In the LV with LVAD since larger vortices are generated in regions with flow separation. Also, stronger vortices are generated in wall regions subjected to larger velocity gradients. Therefore, platelets are expected to get activated at much higher rates compared to LV without LVAD (k_{pa}^{max}=10 s^{-1}). Activation rates in the LV with assist device are one order of magnitude higher than the LV with no assist device. As seen in Figure 7.8 (bottom left) activation rates as high as 300 s^{-1} are observed between mitral and aortic valves. The same behavior is maintained during the whole cardiac cycle in both LVs with and without LVAD.

7.3.3 Thrombus formation

To show the effect of LVAD implantation on thrombus formation, results for platelet deposition are compared here for LV with and without LVAD implanted. Scatter plot of distribution of thrombus formation in the LV without LVAD and the LV with implanted LVAD are illustrated in Figure 7.9. Plots correspond to t=0.1s (where the inlet flow rate at the mitral valve is maximum) and t=0.21s (where the flow rate is minimum during systole phase). Symbol sizes in Figure 7.9 are based on the magnitude of platelet deposition; larger circles represent larger amounts of deposition (thrombus) and vice versa.

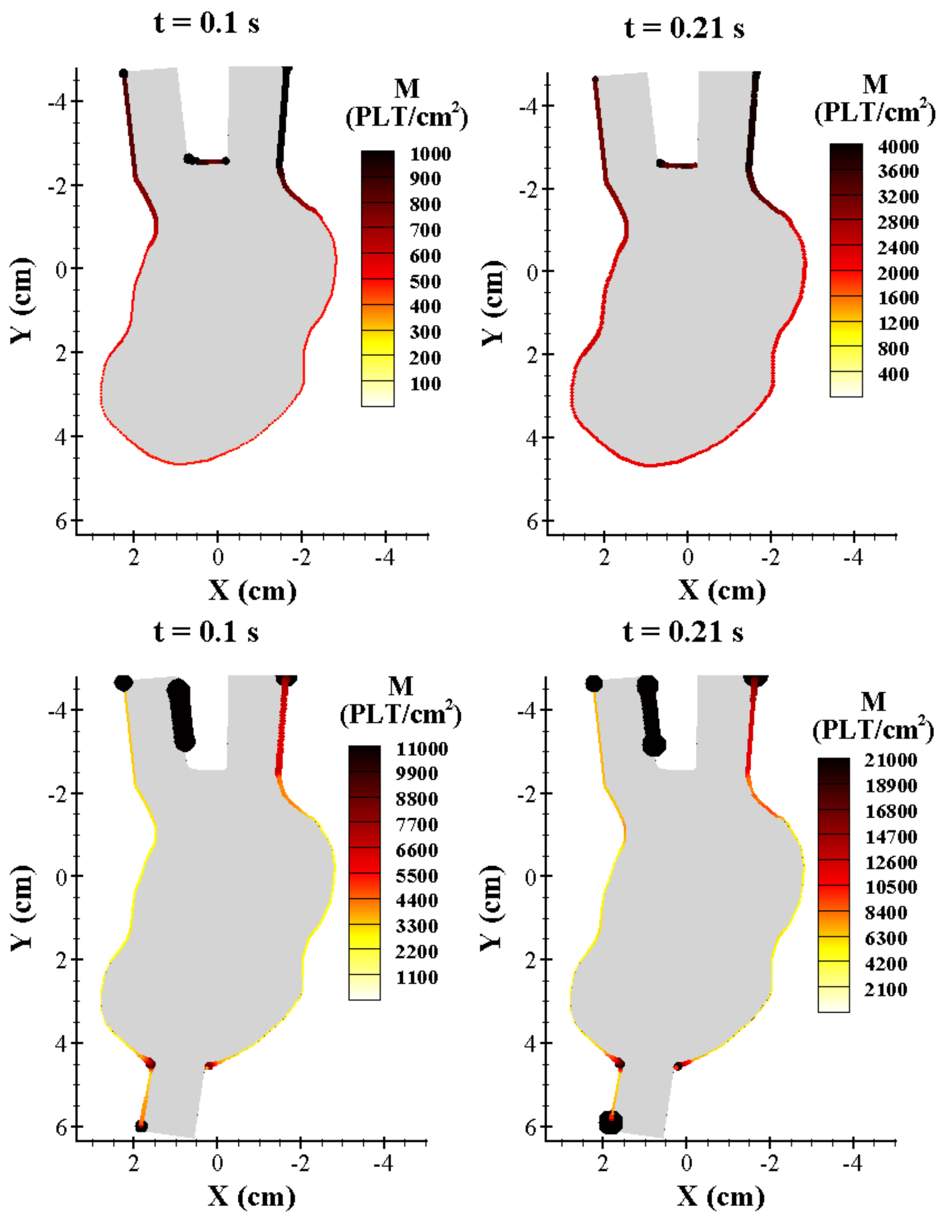

Figure 7.9 Scatter plot of distribution of thrombus formation in LV without LVAD (top) and LV with implanted LVAD (bottom) at t=0.1s (where the inlet flow rate at mitral valve reaches its maximum) and t=0.21s (where the flow rate is minimum during systole phase). Scatter sizes are based on the amount of platelet deposition. Large amount of deposition is observed for the LV with implanted LVAD in regions near the LVAD and aortic valve, whereas in the LV without LVAD deposition values are higher in the bifurcation located between mitral and aortic valves.

As seen in Figure 7.9, large amount of deposition is observed for the LV with implanted LVAD in regions near the LVAD and aortic valve, whereas in the LV without LVAD deposition values are higher in the bifurcation located between mitral and aortic valves. Also, thrombosis occurs to a greater extent in the LV with LVAD compared to the LV without LVAD. Peak values of platelet deposition are ~1000 PLT.cm^{-2} and 4000 PLT.cm^{-2} respectively at t=0.1s and t=0.21s in the LV without LVAD, whereas these values are ~11000 PLT.cm^{-2} and 21000 PLT.cm^{-2} for the LV with LVAD. However, as discussed earlier, locations of peak values are very different.

It has to be mentioned that although platelet activation rates are higher near the area between mitral and aortic valves, larger amounts of platelet deposition occur near the locations where LVAD is connected to the apical hole. As platelets get activated due to the unsteady flow field, specifically vortices that 1) travel from top of the LV to the bottom area and 2) travel into the aortic valve, they are transported towards these regions and deposit at walls with high shear rates. The different locations of platelet activation and platelet deposition were also observed in stenosed vessels (see Chapter 5, Section 5.3.5).

7.4 Summary and Conclusion

Thrombus formation and platelet activation were quantified in LVs with and without implanted LVAD and regions with larger amounts of platelet deposition were identified for each LV. It was shown that implantation of LVAD significantly changes the hemodynamics inside native LV. Vorticity magnitudes in the LV with assist device (~170 s^{-1}) are 1 order of magnitude higher than the LV without LVAD (~7 s^{-1}). As a result, distribution of platelet activation and deposition are different in the LV with LVAD. Activation rates in the LV with assist device are 1 order of magnitude higher ($k_{pa}^{max} \approx$300 s^{-1}) than the LV with no assist device ($k_{pa}^{max} \approx$10 s^{-1}). Thrombosis occurs to a greater extent in the LV with LVAD compared to the LV without

LVAD. Peak values of platelet deposition are ~1000 PLT.cm^{-2} and 4000 PLT.cm^{-2} respectively at t=0.1s and t=0.21s in the LV without LVAD, whereas these values are ~11000 PLT.cm^{-2} and 21000 PLT.cm^{-2} for the LV with LVAD. Also, the distribution of deposition was very different; large amount of deposition is observed for the LV with implanted LVAD in regions near the LVAD and aortic valve, whereas in the LV without LVAD deposition values are higher in the bifurcation located between mitral and aortic valves.

8 Conclusions

The main objective of this study was to develop a shear-dependent physiochemical model of thrombus formation and growth which is capable of predicting the rate of thrombus growth in stenosed vessels under different flow conditions. Sensitivity analysis was conducted to quantify the effect of three major coagulation factors (adenosine diphosphate, thromboxane A_2, and thrombin) as well as flow pulsatility on platelet activation and deposition. Also, the effect of mural thrombus geometry on thrombus growth rate was investigated using the ALE method in a wide range of vessel wall shear rates. Conclusions from the present work are summarized here as follows.

Stenosis degree and Reynolds number define the platelet adhesion rate

Our results reveal that the platelet adhesion in stenotic flow is a function of both stenosis severity and Reynolds number at the stenosis apex and cannot be defined solely by shear rate values at the vessel wall. To the best of our knowledge, this is the first model that attempts to generalize predictions to more than one experimental observation.

Effect of platelet activating agonists and flow pulsatility on thrombus formation

It was shown that ADP contributes substantially to platelet deposition and activation (~9% difference in deposition and 100% difference in activation were observed), whereas effects of thromboxane A_2 and thrombin on both deposition and activation are negligible. Also, it was shown that pulsatility can have considerable effect on thrombus formation, namely on the thrombus growth rate. The time-averaged rate of thrombus growth over 5 cycles for the pulsatile flow was shown to be approximately 1.5 times higher than an equivalent steady flow case. Our results show that pulsatility can lead to faster deposition and occlusion of stenosed vessels. This conclusion is in agreement with experimental findings in the literature.

Effect of mural thrombi geometry on thrombus growth rate

It was shown that thrombus growth rate can change considerably with growing thrombi. The model successfully predicts the nonlinear growth of thrombi in the stenosed area. Effect of enhanced shear activation and platelet aggregation is balanced by increased embolization due to higher drag forces exerted on platelet aggregates at high shear rates. Our results indicate that embolization occurs in supraphysiological wall shear rates (>20,000 s^{-1}). This finding matches with experimental observations in the literature. Also, it was shown that increase in Damkohler number increases the thrombus growth rate.

Implementation of a shear-induced platelet activation model

The effect of shear stress was already taken into account by using shear-dependent platelet adhesion rates and shear-dependent mass diffusivities for platelets and thrombin-related factors. However, to improve the model and take shear-mediated platelet activation, a useful Lagrangian model for quantifying the shear-induced platelet activation was presented in this chapter. Platelet activation state parameter (PAS), which characterizes the shear-induced platelet activation, was introduced to our previously developed thrombosis model. It was shown that the contribution of shear stress to platelet activation is negligible (<0.1%) in physiological periods of time (<1 min).

Effect of LVAD implantation on flow dynamics and thrombosis

It was shown that implantation of LVAD significantly changes the hemodynamics inside native LV. Vorticity magnitudes in the LV with assist device (~170 s^{-1}) are one order of magnitude higher than the LV without LVAD (~7 s^{-1}). As a result, distributions of platelet activation and deposition are different in the LV with LVAD. Activation rates in the LV with assist device are an order of magnitude higher (k_{pa}^{max} ≈300 s^{-1}) than the LV with no assist device (k_{pa}^{max} ≈10 s^{-1}). Thrombosis occurs to a greater extent in the LV with LVAD compared to the LV without LVAD. Peak values of platelet deposition are ~1000 PLT.cm^{-2} and 4000 PLT.cm^{-2} respectively at t=0.1s and t=0.21s in the LV without LVAD, whereas these values are ~11000 PLT.cm^{-2} and 21000 PLT.cm^{-2} for the LV with LVAD. Also, the distribution of deposition was very different; large amount of deposition is observed for the LV with implanted LVAD in regions near the LVAD and aortic valve, whereas in the LV without LVAD deposition values are higher in the bifurcation located between the mitral and aortic valves.

References

[1] S. P. Jackson, “The growing complexity of platelet aggregation,” *Blood*, vol. 109, no. 12, pp. 5087–5095, 2007.

[2] Z. M. Ruggeri, “Platelets in atherothrombosis,” *Nat. Med.*, vol. 8, no. 11, pp. 1227–1234, 2002.

[3] J. H. Seo, T. Abd, R. T. George, and R. Mittal, “A coupled chemo-fluidic computational model for thrombogenesis in infarcted left ventricles,” *Am. J. Physiol. Circ. Physiol.*, vol. 310, no. 11, pp. H1567–H1582, 2016.

[4] J. J. Sixma and P. G. Groot, “Regulation of platelet adhesion to the vessel wall,” *Ann. N. Y. Acad. Sci.*, vol. 714, no. 1, pp. 190–199, 1994.

[5] G. A. Skarja, R. L. Kinlough- Rathbone, D. W. Perry, F. D. Rubens, and J. L. Brash, “A cone- and- plate device for the investigation of platelet biomaterial interactions,” *J. Biomed. Mater. Res.*, vol. 34, no. 4, pp. 427–438, 1997.

[6] T. B. Tschopp, H. J. Weiss, and H. R. Baumgartner, “Decreased adhesion of platelets to subendothelium in von Willebrand’s disease,” *J. Lab. Clin. Med.*, vol. 83, no. 2, pp. 296–300, 1974.

[7] H. J. Weiss, “Flow-related platelet deposition on subendothelium,” *Thromb. Haemost.*, vol. 74, no. 1, pp. 117–122, 1995.

[8] P. A. Aarts, P. A. Bolhuis, K. S. Sakariassen, R. M. Heethaar, and J. J. Sixma, “Red blood cell size is important for adherence of blood platelets to artery,” *Blood*, vol. 62, no. 1, pp. 212–214, 1983.

[9] Y. Cadroy and S. R. Hanson, “Effects of red blood cell concentration on hemostasis and thrombus formation in a primate model,” *Blood*, vol. 75, no. 11, pp. 2185–2193, 1990.

[10] D. A. Reasor Jr, M. Mehrabadi, D. N. Ku, and C. K. Aidun, “Determination of critical parameters in platelet margination,” *Ann. Biomed. Eng.*, vol. 41, no. 2, pp. 238–249, 2013.

[11] B. S. Coller, J. H. Beer, L. E. Scudder, and M. H. Steinberg, “Collagen-platelet interactions: evidence for a direct interaction of collagen with platelet GPIa/IIa and an indirect interaction with platelet GPIIb/IIIa mediated by adhesive proteins,” *Blood*, vol. 74, no. 1, pp. 182–192, 1989.

[12] M. Gawaz, H. Langer, and A. E. May, “Platelets in inflammation and atherogenesis,” *J. Clin. Invest.*, vol. 115, no. 12, p. 3378, 2005.

[13] B. Nieswandt and S. P. Watson, “Platelet-collagen interaction: is GPVI the central receptor?,” *Blood*, vol. 102, no. 2, pp. 449–461, 2003.

[14] S. R. Patel, J. H. Hartwig, and J. E. Italiano Jr, “The biogenesis of platelets from megakaryocyte proplatelets,” *J. Clin. Invest.*, vol. 115, no. 12, p. 3348, 2005.

[15] H. J. Weiss, “von Willebrand Factor and Platelet Functiona,” *Ann. N. Y. Acad. Sci.*, vol. 614, no. 1, pp. 125–137, 1991.

[16] B. R. Bahnak, Q. Wu, L. Coulombel, Z. Assouline, D. Kerbiriou- Nabias, G. Piétu, L. Drouet, J. P. Caen, and D. Meyer, “Expression of von Willebrand factor in porcine vessels: heterogeneity at the level of von Willebrand factor mRNA,” *J. Cell. Physiol.*, vol. 138, no. 2, pp. 305–310, 1989.

[17] W. P. Houdijk, P. G. De Groot, P. F. Nievelstein, K. S. Sakariassen, and J. J. Sixma, “Subendothelial proteins and platelet adhesion. von Willebrand factor and fibronectin, not thrombospondin, are involved in platelet adhesion to extracellular matrix of human vascular endothelial cells,” *Arterioscler. Thromb. Vasc. Biol.*, vol. 6, no. 1, pp. 24–33, 1986.

[18] S. Beumer, M. J. IJsseldijk, P. G. de Groot, and J. J. Sixma, “Platelet adhesion to fibronectin in flow: dependence on surface concentration and shear rate, role of platelet membrane glycoproteins GP IIb/IIIa and VLA-5, and inhibition by heparin,” *Blood*, vol. 84, no. 11, pp. 3724–3733, 1994.

[19] D. Varga-Szabo, I. Pleines, and B. Nieswandt, “Cell adhesion mechanisms in platelets,” *Arterioscler. Thromb. Vasc. Biol.*, vol. 28, no. 3, pp. 403–412, 2008.

[20] D. A. Vorchheimer and R. Becker, “Platelets in atherothrombosis,” in *Mayo Clinic Proceedings*, 2006, vol. 81, no. 1, pp. 59–68.

[21] S. P. Jackson, W. S. Nesbitt, and S. Kulkarni, “Signaling events underlying thrombus formation,” *J. Thromb. Haemost.*, vol. 1, no. 7, pp. 1602–1612, 2003.

[22] Y. Huo and K. F. Ley, “Role of platelets in the development of atherosclerosis,” *Trends Cardiovasc. Med.*, vol. 14, no. 1, pp. 18–22, 2004.

[23] M. Frojmovic, T. Wong, and T. van de Ven, “Dynamic measurements of the platelet membrane glycoprotein IIb-IIIa receptor for fibrinogen by flow cytometry. I. Methodology, theory and results for two distinct activators,” *Biophys. J.*, vol. 59, no. 4, p. 815, 1991.

[24] J. L. Moake, N. A. Turner, N. A. Stathopoulos, L. Nolasco, and J. D. Hellums, “Shear-induced platelet aggregation can be mediated by vWF released from,” *Blood*, vol. 71, no. 5, pp. 1366–1374, 1988.

[25] R. N. Puri, R. W. Colman, and M. A. Liberman, “ADP-lnduced Platelet Activation,” *Crit. Rev. Biochem. Mol. Biol.*, vol. 32, no. 6, pp. 437–502, 1997.

[26] D. Woulfe, J. Yang, and L. Brass, “ADP and platelets: the end of the beginning,” *J. Clin. Invest.*, vol. 107, no. 12, p. 1503, 2001.

[27] D. J. Fitzgerald and G. A. FitzGerald, “Role of thrombin and thromboxane A2 in reocclusion following coronary thrombolysis with tissue-type plasminogen activator,” *Proc. Natl. Acad. Sci.*, vol. 86, no. 19, pp. 7585–7589, 1989.

[28] W. R. Wagner and J. A. Hubbell, “Local thrombin synthesis and fibrin formation in an in vitro thrombosis model result in platelet recruitment and thrombus stabilization on collagen in heparinized blood,” *J. Lab. Clin. Med.*, vol. 116, no. 5, pp. 636–650, 1990.

[29] H. K. Nieuwenhuis, J. W. N. Akkerman, W. P. M. Houdijk, and J. J. Sixma, “Human blood platelets showing no response to collagen fail to express surface glycoprotein Ia,” *Nature*, vol. 318, no. 6045, pp. 470–472, 1985.

[30] K. J. Clemetson and J. M. Clemetson, “Platelet receptor signalling,” *Hematol. J. Off. J. Eur. Haematol. Assoc.*, vol. 5, p. S159, 2004.

[31] P. Golino, L. M. Buja, J. H. Ashton, P. Kulkarni, A. Taylor, and J. T. Willerson, “Effect of thromboxane and serotonin receptor antagonists on intracoronary platelet deposition in dogs with experimentally stenosed coronary arteries,” *Circulation*, vol. 78, no. 3, pp. 701–711, 1988.

[32] C. G. Caro, J. M. Fitz-Gerald, and R. C. Schroter, “Atheroma and arterial wall shear observation, correlation and proposal of a shear dependent mass transfer mechanism for atherogenesis,” *Proc. R. Soc. London B Biol. Sci.*, vol. 177, no. 1046, pp. 109–133, 1971.

[33] J. M. Weiss and W. A. Smith, “Preconditioning applied to variable and constant density flows,” *AIAA J.*, vol. 33, no. 11, pp. 2050–2057, 1995.

[34] A. L. Fogelson and K. B. Neeves, “Fluid Mechanics of Blood Clot Formation,” *Annu. Rev. Fluid Mech.*, vol. 47, pp. 377–403, 2015.

[35] A. Alexander-Katz and R. R. Netz, “Dynamics and instabilities of collapsed polymers in

shear flow," *Macromolecules*, vol. 41, no. 9, pp. 3363–3374, 2008.

[36] S. M. Dopheide, M. J. Maxwell, and S. P. Jackson, "Shear-dependent tether formation during platelet translocation on von Willebrand factor," *Blood*, vol. 99, no. 1, pp. 159–167, 2002.

[37] K. Kawano, H. Yoshino, N. Aoki, H. Udagawa, A. Watanuki, Y. Hioki, Y. Hasumura, T. Yasumura, M. Homori, and M. Murata, "Shear- induced platelet aggregation increases in patients with proximal and severe coronary artery stenosis," *Clin. Cardiol.*, vol. 25, no. 4, pp. 154–160, 2002.

[38] S. Grüner, M. Prostredna, V. Schulte, T. Krieg, B. Eckes, C. Brakebusch, and B. Nieswandt, "Multiple integrin-ligand interactions synergize in shear-resistant platelet adhesion at sites of arterial injury in vivo," *Blood*, vol. 102, no. 12, pp. 4021–4027, 2003.

[39] A. M. Malek, S. L. Alper, and S. Izumo, "Hemodynamic shear stress and its role in atherosclerosis," *Jama*, vol. 282, no. 21, pp. 2035–2042, 1999.

[40] E. Sho, M. Sho, T. M. Singh, C. Xu, C. K. Zarins, and H. Masuda, "Blood flow decrease induces apoptosis of endothelial cells in previously dilated arteries resulting from chronic high blood flow," *Arterioscler. Thromb. Vasc. Biol.*, vol. 21, no. 7, pp. 1139–1145, 2001.

[41] P. W. Longest and C. Kleinstreuer, "Comparison of blood particle deposition models for non-parallel flow domains," *J. Biomech.*, vol. 36, no. 3, pp. 421–430, 2003.

[42] M. Li, "Microfluidic system for thrombosis under multiple shear rates and platelet therapies," 2013.

[43] M. Mehrabadi, L. D. C. Casa, C. K. Aidun, and D. N. Ku, "A Predictive Model of High Shear Thrombus Growth," *Ann. Biomed. Eng.*, pp. 1–12, 2016.

[44] E. F. Grabowski, P. Didisheim, J. C. Lewis, J. T. Franta, and J. Q. Stropp, "Platelet

adhesion to foreign surfaces under controlled conditions of whole blood flow: human vs rabbit, dog, calf, sheep, pig, macaque, and baboon," *ASAIO J.*, vol. 23, no. 1, pp. 141–149, 1977.

[45] A. C. Matzdorff, B. Kemkes-Matthes, R. Voss, and H. Pralle, "Comparison of β-thromboglobulin, flow cytometry, and platelet aggregometry to study platelet activation," *Pathophysiol. Haemost. Thromb.*, vol. 26, no. 2, pp. 98–106, 1996.

[46] T. Karino and H. L. Goldsmith, "Adhesion of human platelets to collagen on the walls distal to a tubular expansion," *Microvasc. Res.*, vol. 17, no. 3, pp. 238–262, 1979.

[47] L. Badimon and J. J. Badimón, "Mechanisms of arterial thrombosis in nonparallel streamlines: platelet thrombi grow on the apex of stenotic severely injured vessel wall. Experimental study in the pig model," *J. Clin. Invest.*, vol. 84, no. 4, p. 1134, 1989.

[48] W. Inauen, H. R. Baumgartner, T. Bombeli, A. Haeberli, and P. W. Straub, "Dose-and shear rate-dependent effects of heparin on thrombogenesis induced by rabbit aorta subendothelium exposed to flowing human blood," *Arterioscler. Thromb. Vasc. Biol.*, vol. 10, no. 4, pp. 607–615, 1990.

[49] A. Mailhac, J. J. Badimon, J. T. Fallon, A. Fernandez-Ortiz, B. Meyer, J. H. Chesebro, V. Fuster, and L. Badimon, "Effect of an eccentric severe stenosis on fibrin (ogen) deposition on severely damaged vessel wall in arterial thrombosis. Relative contribution of fibrin (ogen) and platelets," *Circulation*, vol. 90, no. 2, pp. 988–996, 1994.

[50] E. U. Saelman, H. K. Nieuwenhuis, K. M. Hese, P. G. de Groot, H. F. Heijnen, E. H. Sage, S. Williams, L. McKeown, H. R. Gralnick, and J. J. Sixma, "Platelet adhesion to collagen types I through VIII under conditions of stasis and flow is mediated by GPIa/IIa (alpha 2 beta 1-integrin)," *Blood*, vol. 83, no. 5, pp. 1244–1250, 1994.

[51] D. L. Bark, A. N. Para, and D. N. Ku, “Correlation of thrombosis growth rate to pathological wall shear rate during platelet accumulation,” *Biotechnol. Bioeng.*, vol. 109, no. 10, pp. 2642–2650, 2012.

[52] C. Escudero, M. Santos, J. Buján, M. Fuente, N. G. Honduvilla, E. Bañas, J. San Román, and F. J. Tendillo, “Optical aggregometry versus the PFA–100$^{\text{TM}}$: experimental studies in pigs treated with propofol,” *Platelets*, 2009.

[53] R. Lassila, J. J. Badimon, S. Vallabhajosula, and L. Badimon, “Dynamic monitoring of platelet deposition on severely damaged vessel wall in flowing blood. Effects of different stenoses on thrombus growth,” *Arterioscler. Thromb. Vasc. Biol.*, vol. 10, no. 2, pp. 306–315, 1990.

[54] C. Leuser, S. Schlottmann, R. Siekmann, M. Heidt, A. Moritz, and N. Bauer, “Use of the platelet function analyser PFA-100$^{\text{TM}}$ in juvenile pigs,” *Comp. Clin. Path.*, vol. 21, no. 5, pp. 761–767, 2011.

[55] J. Strony, A. Beaudoin, D. Brands, and B. Adelman, “Analysis of shear stress and hemodynamic factors in a model of coronary artery stenosis and thrombosis,” *Am. J. Physiol. Circ. Physiol.*, vol. 265, no. 5, pp. H1787–H1796, 1993.

[56] C. M. Doerschuk, G. P. Downey, D. E. Doherty, D. English, R. P. Gie, M. Ohgami, G. S. Worthen, P. M. Henson, and J. C. Hogg, “Leukocyte and platelet margination within microvasculature of rabbit lungs,” *J. Appl. Physiol.*, vol. 68, no. 5, pp. 1956–1961, 1990.

[57] H. Shankaran and S. Neelamegham, “Hydrodynamic forces applied on intercellular bonds, soluble molecules, and cell-surface receptors,” *Biophys. J.*, vol. 86, no. 1, pp. 576–588, 2004.

[58] H. Shankaran, P. Alexandridis, and S. Neelamegham, “Aspects of hydrodynamic shear

regulating shear-induced platelet activation and self-association of von Willebrand factor in suspension," *Blood*, vol. 101, no. 7, pp. 2637–2645, 2003.

[59] E. Westein, A. D. van der Meer, M. J. E. Kuijpers, J.-P. Frimat, A. van den Berg, and J. W. M. Heemskerk, "Atherosclerotic geometries exacerbate pathological thrombus formation poststenosis in a von Willebrand factor-dependent manner," *Proc. Natl. Acad. Sci.*, vol. 110, no. 4, pp. 1357–1362, 2013.

[60] V. T. Turitto and H. R. Baumgartner, "Platelet interaction with subendothelium in flowing rabbit blood: effect of blood shear rate," *Microvasc. Res.*, vol. 17, no. 1, pp. 38–54, 1979.

[61] J. E. Sadler, "Biochemistry and genetics of von Willebrand factor," *Annu. Rev. Biochem.*, vol. 67, no. 1, pp. 395–424, 1998.

[62] M. M. Frojmovic, R. F. Mooney, and T. Wong, "Dynamics of platelet glycoprotein IIb-IIIa receptor expression and fibrinogen binding. I. Quantal activation of platelet subpopulations varies with adenosine diphosphate concentration," *Biophys. J.*, vol. 67, no. 5, p. 2060, 1994.

[63] H. J. Weiss, *Platelets: pathophysiology and antiplatelet drug therapy*. AR Liss, 1982.

[64] B. J. Folie and L. V Mcintire, "Mathematical analysis of mural thrombogenesis. Concentration profiles of platelet-activating agents and effects of viscous shear flow," *Biophys. J.*, vol. 56, no. 6, pp. 1121–1141, 1989.

[65] R. L. Jones, N. H. Wilson, and C. G. Marr, "Thromboxane-like activity of prostanoids with aromatic substituents at C16 and C17," in *Chemistry, Biochemistry, and Pharmacological Activity of Prostanoids: Including the Proceedings of a Symposium on the Chemistry and Biochemistry of Prostanoids Held at The University of Salford, England, 10-14 July 1978*, 2013, p. 210.

[66] G. A. Adams and I. A. Feuerstein, “Maximum fluid concentrations of materials released from platelets at a surface,” *Am. J. Physiol. Circ. Physiol.*, vol. 244, no. 1, pp. H109–H114, 1983.

[67] A. L. Fogelson, “Continuum models of platelet aggregation: formulation and mechanical properties,” *SIAM J. Appl. Math.*, vol. 52, no. 4, pp. 1089–1110, 1992.

[68] E. N. Sorensen, G. W. Burgreen, W. R. Wagner, and J. F. Antaki, “Computational simulation of platelet deposition and activation: I. Model development and properties,” *Ann. Biomed. Eng.*, vol. 27, no. 4, pp. 436–448, 1999.

[69] N. Filipovic, M. Kojic, and A. Tsuda, “Modelling thrombosis using dissipative particle dynamics method,” *Philos. Trans. R. Soc. London A Math. Phys. Eng. Sci.*, vol. 366, no. 1879, pp. 3265–3279, 2008.

[70] A. R. L. Gear, “Platelet adhesion, shape change, and aggregation: rapid initiation and signal transduction events,” *Can. J. Physiol. Pharmacol.*, vol. 72, no. 3, pp. 285–294, 1994.

[71] J. Jesty, W. Yin, P. Perrotta, and D. Bluestein, “Platelet activation in a circulating flow loop: combined effects of shear stress and exposure time,” *Platelets*, 2009.

[72] K. S. Sakariassen, P. A. Holme, U. Ørvim, R. M. Barstad, N. O. Solum, and F. R. Brosstad, “Shear-induced platelet activation and platelet microparticle formation in native human blood,” *Thromb. Res.*, vol. 92, no. 6, pp. S33–S41, 1998.

[73] M. Nobili, J. Sheriff, U. Morbiducci, A. Redaelli, and D. Bluestein, “Platelet activation due to hemodynamic shear stresses: damage accumulation model and comparison to in vitro measurements,” *ASAIO J. (American Soc. Artif. Intern. Organs 1992),* vol. 54, no. 1, p. 64, 2008.

[74] P. A. Holme, U. Ørvim, M. J. A. G. Hamers, N. O. Solum, F. R. Brosstad, R. M. Barstad, and K. S. Sakariassen, “Shear-induced platelet activation and platelet microparticle formation at blood flow conditions as in arteries with a severe stenosis,” *Arterioscler. Thromb. Vasc. Biol.*, vol. 17, no. 4, pp. 646–653, 1997.

[75] M. J. Kunov, D. A. Steinman, and C. R. Ethier, “Particle volumetric residence time calculations in arterial geometries,” *J. Biomech. Eng.*, vol. 118, no. 2, pp. 158–164, 1996.

[76] M. Tambasco and D. A. Steinman, “On assessing the quality of particle tracking through computational fluid dynamic models,” *J. Biomech. Eng.*, vol. 124, no. 2, pp. 166–175, 2002.

[77] N. B. Purvis Jr and T. D. Giorgio, “The effects of elongational stress exposure on the activation and aggregation of blood platelets,” *Biorheology*, vol. 28, no. 5, pp. 355–367, 1991.

[78] S. C. Shadden and S. Hendabadi, “Potential fluid mechanic pathways of platelet activation,” *Biomech. Model. Mechanobiol.*, vol. 12, no. 3, pp. 467–474, 2013.

[79] M. R. Maxey and J. J. Riley, “Equation of motion for a small rigid sphere in a nonuniform flow,” *Phys. Fluids*, vol. 26, no. 4, pp. 883–889, 1983.

[80] J. Cao and S. E. Rittgers, “Particle motion within in vitro models of stenosed internal carotid and left anterior descending coronary arteries,” *Ann. Biomed. Eng.*, vol. 26, no. 2, pp. 190–199, 1998.

[81] J. D. Hellums, D. M. Peterson, N. A. Stathopoulos, J. L. Moake, and T. D. Giorgio, “Studies on the mechanisms of shear-induced platelet activation,” in *Cerebral ischemia and hemorheology*, Springer, 1987, pp. 80–89.

[82] P. D. Goodman, E. T. Barlow, P. M. Crapo, S. F. Mohammad, and K. A. Solen,

“Computational model of device-induced thrombosis and thromboembolism,” *Ann. Biomed. Eng.*, vol. 33, no. 6, pp. 780–797, 2005.

[83] J. D. Hellums, “1993 Whitaker Lecture: biorheology in thrombosis research,” *Ann. Biomed. Eng.*, vol. 22, no. 5, pp. 445–455, 1994.

[84] D. Bluestein, L. Niu, R. T. Schoephoerster, and M. K. Dewanjee, “Fluid mechanics of arterial stenosis: relationship to the development of mural thrombus,” *Ann. Biomed. Eng.*, vol. 25, no. 2, pp. 344–356, 1997.

[85] M. Tambasco and D. A. Steinman, “Path-dependent hemodynamics of the stenosed carotid bifurcation,” *Ann. Biomed. Eng.*, vol. 31, no. 9, pp. 1054–1065, 2003.

[86] M. Giersiepen, L. J. Wurzinger, R. Opitz, and H. Reul, “Estimation of shear stress-related blood damage in heart valve prostheses--in vitro comparison of 25 aortic valves,” *Int. J. Artif. Organs*, vol. 13, no. 5, pp. 300–306, 1990.

[87] J. S. Soares, J. Sheriff, and D. Bluestein, “A novel mathematical model of activation and sensitization of platelets subjected to dynamic stress histories,” *Biomech. Model. Mechanobiol.*, vol. 12, no. 6, pp. 1127–1141, 2013.

[88] J. Sheriff, J. S. Soares, M. Xenos, J. Jesty, and D. Bluestein, “Evaluation of shear-induced platelet activation models under constant and dynamic shear stress loading conditions relevant to devices,” *Ann. Biomed. Eng.*, vol. 41, no. 6, pp. 1279–1296, 2013.

[89] M. Grigioni, U. Morbiducci, G. D’Avenio, G. Di Benedetto, and C. Del Gaudio, “A novel formulation for blood trauma prediction by a modified power-law mathematical model,” *Biomech. Model. Mechanobiol.*, vol. 4, no. 4, pp. 249–260, 2005.

[90] M. Grigioni, C. Daniele, U. Morbiducci, G. D’Avenio, G. Di Benedetto, and V. Barbaro, “The Power- law Mathematical Model for Blood Damage Prediction: Analytical

Developments and Physical Inconsistencies," *Artif. Organs*, vol. 28, no. 5, pp. 467–475, 2004.

[91] C. H. Brown, L. B. Leverett, C. W. Lewis, C. P. Alfrey, and J. D. Hellums, "Morphological, biochemical, and functional changes in human platelets subjected to shear stress," *J Lab Clin Med*, vol. 86, no. 3, pp. 462–471, 1975.

[92] C. J. Jen and L. V McIntire, "Characteristics of shear-induced aggregation in whole blood," *J. Lab. Clin. Med.*, vol. 103, no. 1, pp. 115–124, 1984.

[93] M. W. Moritz, R. C. Reimers, R. K. Baker, S. P. Sutera, and J. H. Joist, "Role of cytoplasmic and releasable ADP in platelet aggregation induced by laminar shear stress," *J. Lab. Clin. Med.*, vol. 101, no. 4, pp. 537–544, 1983.

[94] Z. Elaïb, F. Adam, E. Berrou, J.-C. Bordet, N. Prévost, R. Bobe, M. Bryckaert, and J.-P. Rosa, "Full activation of mouse platelets requires an ADP secretion pathway regulated by SERCA3 ATPase-dependent calcium stores," *Blood*, p. blood-2015-10-678383, 2016.

[95] S. Kulkarni, S. M. Dopheide, C. L. Yap, C. Ravanat, M. Freund, P. Mangin, K. A. Heel, A. Street, I. S. Harper, and F. Lanza, "A revised model of platelet aggregation," *J. Clin. Invest.*, vol. 105, no. 6, p. 783, 2000.

[96] J. H. Ip, V. Fuster, D. Israel, L. Badimon, J. Badimon, and J. H. Chesebro, "The role of platelets, thrombin and hyperplasia in restenosis after coronary angioplasty," *J. Am. Coll. Cardiol.*, vol. 17, no. 6, pp. 77–88, 1991.

[97] S. M. Jung and M. Moroi, "Platelets interact with soluble and insoluble collagens through characteristically different reactions," *J. Biol. Chem.*, vol. 273, no. 24, pp. 14827–14837, 1998.

[98] D. M. Monroe, M. Hoffman, and H. R. Roberts, "Platelets and thrombin generation,"

Arterioscler. Thromb. Vasc. Biol., vol. 22, no. 9, pp. 1381–1389, 2002.

[99] G. J. Tangelder, D. W. Slaaf, H. C. Teirlinck, R. Alewijnse, and R. S. Reneman, "Localization within a thin optical section of fluorescent blood platelets flowing in a microvessel," *Microvasc. Res.*, vol. 23, no. 2, pp. 214–230, 1982.

[100] G. J. Tangelder, H. C. Teirlinck, D. W. Slaaf, and R. S. Reneman, "Distribution of blood platelets flowing in arterioles," *Am. J. Physiol. Circ. Physiol.*, vol. 248, no. 3, pp. H318–H323, 1985.

[101] A. R. Pries, D. Neuhaus, and P. Gaehtgens, "Blood viscosity in tube flow: dependence on diameter and hematocrit," *Am. J. Physiol. Circ. Physiol.*, vol. 263, no. 6, pp. H1770–H1778, 1992.

[102] V. Narsimhan, H. Zhao, and E. S. G. Shaqfeh, "Coarse-grained theory to predict the concentration distribution of red blood cells in wall-bounded Couette flow at zero Reynolds number," *Phys. Fluids*, vol. 25, no. 6, p. 61901, 2013.

[103] G. Bugliarello and J. W. Hayden, "Detailed characteristics of the flow of blood in vitro," *Trans. Soc. Rheol.*, vol. 7, no. 1, pp. 209–230, 1963.

[104] W. R. Wagner, *Biochemical and biophysical mechanisms of mural thrombosis on natural surfaces*. 1991.

[105] H. Hosseinzadegan and D. K. Tafti, "Validation of a Time Dependent Physio-Chemical Model for Thrombus Formation and Growth," in *ASME 2016 Fluids Engineering Division Summer Meeting collocated with the ASME 2016 Heat Transfer Summer Conference and the ASME 2016 14th International Conference on Nanochannels, Microchannels, and Minichannels*, 2016, p. V01AT04A007-V01AT04A007.

[106] P. A. M. M. Aarts, P. Steendijk, J. J. Sixma, and R. M. Heethaar, "Fluid shear as a

possible mechanism for platelet diffusivity in flowing blood," *J. Biomech.*, vol. 19, no. 10, pp. 799–805, 1986.

[107] K. H. Keller, "Effect of fluid shear on mass transport in flowing blood," in *Federation proceedings*, 1971, vol. 30, no. 5, pp. 1591–1599.

[108] V. T. Turitto and H. R. Baumgartner, "Platelet interaction with subendothelium in a perfusion system: physical role of red blood cells," *Microvasc. Res.*, vol. 9, no. 3, pp. 335–344, 1975.

[109] G. Antonini, G. Guiffant, D. Quemada, and A. M. Dosne, "Estimation of platelet diffusivity in flowing blood," *Biorheology*, vol. 15, no. 2, pp. 111–117, 1977.

[110] A. L. Zydney and C. K. Colton, "A concentration polarization model for the filtrate flux in cross-flow microfiltration of particulate suspensions," *Chem. Eng. Commun.*, vol. 47, no. 1–3, pp. 1–21, 1986.

[111] D. M. Wootton, C. P. Markou, S. R. Hanson, and D. N. Ku, "A mechanistic model of acute platelet accumulation in thrombogenic stenoses," *Ann. Biomed. Eng.*, vol. 29, no. 4, pp. 321–329, 2001.

[112] M. Mehrabadi, D. N. Ku, and C. K. Aidun, "A continuum model for platelet transport in flowing blood based on direct numerical simulations of cellular blood flow," *Ann. Biomed. Eng.*, vol. 43, no. 6, pp. 1410–1421, 2015.

[113] N. H. L. Wang and K. H. Keller, "Solute transport induced by erythrocyte motions in shear flow," *ASAIO J.*, vol. 25, no. 1, pp. 14–18, 1979.

[114] Y. I. Cho and K. R. Kensey, "Effects of the non-Newtonian viscosity of blood on flows in a diseased arterial vessel. Part 1: Steady flows," *Biorheology*, vol. 28, no. 3–4, pp. 241–262, 1991.

[115] F. Abraham, M. Behr, and M. Heinkenschloss, “Shape optimization in unsteady blood flow: A numerical study of non-Newtonian effects,” *Comput. Methods Biomech. Biomed. Engin.*, vol. 8, no. 3, pp. 201–212, 2005.

[116] S. Chien, “Shear dependence of effective cell volume as a determinant of blood viscosity,” *Science (80-.).*, vol. 168, no. 3934, pp. 977–979, 1970.

[117] F. N. Van de Vosse, J. De Hart, C. Van Oijen, D. Bessems, T. W. M. Gunther, A. Segal, B. Wolters, J. M. A. Stijnen, and F. P. T. Baaijens, “Finite-element-based computational methods for cardiovascular fluid-structure interaction,” *J. Eng. Math.*, vol. 47, no. 3–4, pp. 335–368, 2003.

[118] F. J. H. Gijsen, F. N. Van de Vosse, and J. D. Janssen, “Wall shear stress in backward-facing step flow of a red blood cell suspension,” *Biorheology*, vol. 35, no. 4, 5, pp. 263–279, 1998.

[119] T. G. Papaioannou and C. Stefanadis, “Vascular wall shear stress: basic principles and methods,” *Hell. J Cardiol*, vol. 46, no. 1, pp. 9–15, 2005.

[120] D. Quemada, “Rheology of concentrated disperse systems II. A model for non-newtonian shear viscosity in steady flows,” *Rheol. Acta*, vol. 17, no. 6, pp. 632–642, 1978.

[121] V. G. Levich, *Physicochemical hydrodynamics*. Prentice Hall, 1962.

[122] E. W. Merrill, “Rheology of blood,” *Physiol. Rev*, vol. 49, no. 4, pp. 863–888, 1969.

[123] F. Yilmaz and M. Y. Gundogdu, “A critical review on blood flow in large arteries; relevance to blood rheology, viscosity models, and physiologic conditions,” *Korea-Australia Rheol. J.*, vol. 20, no. 4, pp. 197–211, 2008.

[124] P. Neofytou and S. Tsangaris, “Flow effects of blood constitutive equations in 3D models of vascular anomalies,” *Int. J. Numer. methods fluids*, vol. 51, no. 5, pp. 489–510, 2006.

[125] R. B. Bird and P. J. Carreau, "A nonlinear viscoelastic model for polymer solutions and melts—I," *Chem. Eng. Sci.*, vol. 23, no. 5, pp. 427–434, 1968.

[126] B. M. Johnston, P. R. Johnston, S. Corney, and D. Kilpatrick, "Non-Newtonian blood flow in human right coronary arteries: steady state simulations," *J. Biomech.*, vol. 37, no. 5, pp. 709–720, 2004.

[127] K. Yasuda, "A Multi-Mode Viscosity Model and Its Applicability to Non-Newtonian Fluids," *J. Text. Eng.*, vol. 52, no. 4, pp. 171–173, 2006.

[128] P. Hanafizadeh, N. Mirkhani, M. R. Davoudi, M. Masouminia, and K. Sadeghy, "Non-Newtonian Blood Flow Simulation of Diastolic Phase in Bileaflet Mechanical Heart Valve Implanted in a Realistic Aortic Root Containing Coronary Arteries," *Artif. Organs*, vol. 40, no. 10, 2016.

[129] J. Jung, R. W. Lyczkowski, C. B. Panchal, and A. Hassanein, "Multiphase hemodynamic simulation of pulsatile flow in a coronary artery," *J. Biomech.*, vol. 39, no. 11, pp. 2064–2073, 2006.

[130] P. D. Ballyk, D. A. Steinman, and C. R. Ethier, "Simulation of non-Newtonian blood flow in an end-to-side anastomosis," *Biorheology*, vol. 31, no. 5, pp. 565–586, 1993.

[131] N. Casson, *A flow equation for pigment-oil suspensions of the printing ink type*. Pergamon press, 1959.

[132] Y. C. Fung and S. C. Cowin, "Biomechanics: mechanical properties of living tissues," *J. Appl. Mech.*, vol. 61, p. 1007, 1994.

[133] C. Picart, J.-M. Piau, H. Galliard, and P. Carpentier, "Human blood shear yield stress and its hematocrit dependence," *J. Rheol.*, vol. 42, no. 1, pp. 1–12, 1998.

[134] A. Valencia, A. Zarate, M. Galvez, and L. Badilla, "Non- Newtonian blood flow

dynamics in a right internal carotid artery with a saccular aneurysm," *Int. J. Numer. methods fluids*, vol. 50, no. 6, pp. 751–764, 2006.

[135] J. R. Buchanan, C. Kleinstreuer, S. Hyun, and G. A. Truskey, "Hemodynamics simulation and identification of susceptible sites of atherosclerotic lesion formation in a model abdominal aorta," *J. Biomech.,* vol. 36, no. 8, pp. 1185–1196, 2003.

[136] F. J. Walburn and D. J. Schneck, "A constitutive equation for whole human blood," *Biorheology,* vol. 13, no. 3, pp. 201–210, 1976.

[137] H. H. Lipowsky, S. Usami, and S. Chien, "In vivo measurements of hematocrit and apparent viscosity in the microvasculature of cat mesentery," *Microvasc Res*, vol. 19, pp. 297–319, 1980.

[138] H. H. Lipowsky, S. Kovalcheck, and B. W. Zweifach, "The distribution of blood rheological parameters in the microvasculature of cat mesentery," *Circ. Res.*, vol. 43, no. 5, pp. 738–749, 1978.

[139] S. W. Cho, S. W. Kim, M. H. Sung, K. C. Ro, and H. S. Ryou, "Fluid-structure interaction analysis on the effects of vessel material properties on blood flow characteristics in stenosed arteries under axial rotation," *Korea-Australia Rheol. J.*, vol. 23, no. 1, pp. 7–16, 2011.

[140] P. Siljander and R. Lassila, "Studies of Adhesion-Dependent Platelet Activation Distinct Roles for Different Participating Receptors Can Be Dissociated by Proteolysis of Collagen," *Arterioscler. Thromb. Vasc. Biol.*, vol. 19, no. 12, pp. 3033–3043, 1999.

[141] J. Rosing, J. L. Van Rijn, E. M. Bevers, G. Van Dieijen, P. Comfurius, and R. F. Zwaal, "The role of activated human platelets in prothrombin and factor X," *Blood*, vol. 65, no. 2, 1985.

[142] D. D. Wagner, M. Urban-Pickering, and V. J. Marder, “Von Willebrand protein binds to extracellular matrices independently of collagen,” *Proc. Natl. Acad. Sci.*, vol. 81, no. 2, pp. 471–475, 1984.

[143] J. A. Hubbell and L. V McIntire, “Platelet active concentration profiles near growing thrombi. A mathematical consideration,” *Biophys. J.*, vol. 50, no. 5, p. 937, 1986.

[144] J. A. Hubbell and L. V McIntire, “Visualization and analysis of mural thrombogenesis on collagen, polyurethane and nylon,” *Biomaterials*, vol. 7, no. 5, pp. 354–363, 1986.

[145] C. P. Markou, S. R. Hanson, J. M. Siegel, and D. N. Ku, “The role of high wall shear rate on thrombus formation in stenoses,” *ASME-PUBLICATIONS-BED*, vol. 26, p. 555, 1993.

[146] R. M. Barstad, H. E. Roald, Y. Cui, V. T. Turitto, and K. S. Sakariassen, “A perfusion chamber developed to investigate thrombus formation and shear profiles in flowing native human blood at the apex of well-defined stenoses,” *Arterioscler. Thromb. Vasc. Biol.*, vol. 14, no. 12, pp. 1984–1991, 1994.

[147] L. D. C. Casa and D. N. Ku, “High shear thrombus formation under pulsatile and steady flow,” *Cardiovasc. Eng. Technol.*, vol. 5, no. 2, pp. 154–163, 2014.

[148] M. Mehrabadi, L. D. C. Casa, C. K. Aidun, and D. N. Ku, “A predictive model of high shear thrombus growth,” *Ann. Biomed. Eng.*, vol. 44, no. 8, pp. 2339–2350, 2016.

[149] J. Folts, “An in vivo model of experimental arterial stenosis, intimal damage, and periodic thrombosis,” *Circulation*, vol. 83, no. 6 Suppl, p. IV3-14, 1991.

[150] A. Fernández-Ortiz, J. J. Badimon, E. Falk, V. Fuster, B. Meyer, A. Mailhac, D. Weng, P. K. Shah, and L. Badimon, “Characterization of the relative thrombogenicity of atherosclerotic plaque components: implications for consequences of plaque rupture,” *J. Am. Coll. Cardiol.*, vol. 23, no. 7, pp. 1562–1569, 1994.

[151] D. A. Dichek, "Control of Thrombosis on Synthetic Graft Surfaces-Gene Transfer Approach," *J. Vasc. Interv. Radiol.*, vol. 8, no. 4, pp. 707–709, 1997.

[152] W. Wang, T. G. Diacovo, J. Chen, J. B. Freund, and M. R. King, "Simulation of platelet, thrombus and erythrocyte hydrodynamic interactions in a 3D arteriole with in vivo comparison," *PLoS One*, vol. 8, no. 10, 2013.

[153] A. N. Para and D. N. Ku, "A low-volume, single pass in-vitro system of high shear thrombosis in a stenosis," *Thromb. Res.*, vol. 131, no. 5, pp. 418–424, 2013.

[154] P. D. Goodman, M. W. Hall, S. Sukavaneshvar, and K. A. Solen, "In vitro model for studying the effects of hemodynamics on device induced thromboembolism in human blood," *ASAIO J.*, vol. 46, no. 5, pp. 576–578, 2000.

[155] D. M. Wootton and D. N. Ku, "Fluid mechanics of vascular systems, diseases, and thrombosis," *Annu. Rev. Biomed. Eng.*, vol. 1, no. 1, pp. 299–329, 1999.

[156] D. N. Ku, D. P. Giddens, C. K. Zarins, and S. Glagov, "Pulsatile flow and atherosclerosis in the human carotid bifurcation. Positive correlation between plaque location and low oscillating shear stress," *Arterioscler. Thromb. Vasc. Biol.*, vol. 5, no. 3, pp. 293–302, 1985.

[157] Q. Liu, D. Mirc, and B. M. Fu, "Mechanical mechanisms of thrombosis in intact bent microvessels of rat mesentery," *J. Biomech.*, vol. 41, no. 12, pp. 2726–2734, 2008.

[158] D. L. Bark and D. N. Ku, "Platelet transport rates and binding kinetics at high shear over a thrombus," *Biophys. J.*, vol. 105, no. 2, pp. 502–511, 2013.

[159] W. S. Nesbitt, E. Westein, F. J. Tovar-Lopez, E. Tolouei, A. Mitchell, J. Fu, J. Carberry, A. Fouras, and S. P. Jackson, "A shear gradient–dependent platelet aggregation mechanism drives thrombus formation," *Nat. Med.*, vol. 15, no. 6, pp. 665–673, 2009.

[160] T. David, S. Thomas, and P. G. Walker, “Platelet deposition in stagnation point flow: an analytical and computational simulation,” *Med. Eng. Phys.*, vol. 23, no. 5, pp. 299–312, 2001.

[161] M. A. Navitsky, S. Deutsch, and K. B. Manning, “A thrombus susceptibility comparison of two pulsatile Penn State 50 cc left ventricular assist device designs,” *Ann. Biomed. Eng.*, vol. 41, no. 1, pp. 4–16, 2013.

[162] V. Balasubramanian and S. M. Slack, “The effect of fluid shear and co-adsorbed proteins on the stability of immobilized fibrinogen and subsequent platelet interactions,” *J. Biomater. Sci. Polym. Ed.*, vol. 13, no. 5, pp. 543–561, 2002.

[163] D. Bluestein, E. Rambod, and M. Gharib, “Vortex shedding as a mechanism for free emboli formation in mechanical heart valves,” *J. Biomech. Eng.*, vol. 122, no. 2, pp. 125–134, 2000.

[164] Y. Alemu and D. Bluestein, “Flow- induced Platelet Activation and Damage Accumulation in a Mechanical Heart Valve: Numerical Studies,” *Artif. Organs*, vol. 31, no. 9, pp. 677–688, 2007.

[165] M. Hedayat, H. Asgharzadeh, and I. Borazjani, “Platelet activation of mechanical versus bioprosthetic heart valves during systole,” *J. Biomech.*, 2017.

[166] J. L. Moake, N. A. Turner, N. A. Stathopoulos, L. H. Nolasco, and J. D. Hellums, “Involvement of large plasma von Willebrand factor (vWF) multimers and unusually large vWF forms derived from endothelial cells in shear stress-induced platelet aggregation,” *J. Clin. Invest.*, vol. 78, no. 6, p. 1456, 1986.

[167] B. Savage, F. Almus-Jacobs, and Z. M. Ruggeri, “Specific synergy of multiple substrate–receptor interactions in platelet thrombus formation under flow,” *Cell*, vol. 94, no. 5, pp.

657–666, 1998.

[168] Z. M. Ruggeri, J. N. Orje, R. Habermann, A. B. Federici, and A. J. Reininger, "Activation-independent platelet adhesion and aggregation under elevated shear stress," *Blood*, vol. 108, no. 6, pp. 1903–1910, 2006.

[169] I. V Pivkin, P. D. Richardson, and G. Karniadakis, "Blood flow velocity effects and role of activation delay time on growth and form of platelet thrombi," *Proc. Natl. Acad. Sci.*, vol. 103, no. 46, pp. 17164–17169, 2006.

[170] B. Vahidi and N. Fatouraee, "Large deforming buoyant embolus passing through a stenotic common carotid artery: A computational simulation," *J. Biomech.*, vol. 45, no. 7, pp. 1312–1322, 2012.

[171] Z. Xu, N. Chen, M. M. Kamocka, E. D. Rosen, and M. Alber, "A multiscale model of thrombus development," *J. R. Soc. Interface*, vol. 5, no. 24, pp. 705–722, 2008.

[172] Z. Xu, J. Lioi, J. Mu, M. M. Kamocka, X. Liu, D. Z. Chen, E. D. Rosen, and M. Alber, "A multiscale model of venous thrombus formation with surface-mediated control of blood coagulation cascade," *Biophys. J.*, vol. 98, no. 9, pp. 1723–1732, 2010.

[173] H. Kamada, Y. Imai, M. Nakamura, T. Ishikawa, and T. Yamaguchi, "Computational study on thrombus formation regulated by platelet glycoprotein and blood flow shear," *Microvasc. Res.*, vol. 89, pp. 95–106, 2013.

[174] H. Kamada, K. Tsubota, M. Nakamura, S. Wada, T. Ishikawa, and T. Yamaguchi, "A three- dimensional particle simulation of the formation and collapse of a primary thrombus," *Int. j. numer. method. biomed. eng.*, vol. 26, no. 3- 4, pp. 488–500, 2010.

[175] D. Mori, K. Yano, K. Tsubota, T. Ishikawa, S. Wada, and T. Yamaguchi, "Simulation of platelet adhesion and aggregation regulated by fibrinogen and von Willebrand factor,"

Thromb. Haemost., vol. 99, no. 1, pp. 108–115, 2008.

[176] A. Tosenberger, F. Ataullakhanov, N. Bessonov, M. Panteleev, A. Tokarev, and V. Volpert, “Modelling of thrombus growth in flow with a DPD-PDE method,” *J. Theor. Biol.*, vol. 337, pp. 30–41, 2013.

[177] A. L. Fogelson and R. D. Guy, “Immersed-boundary-type models of intravascular platelet aggregation,” *Comput. Methods Appl. Mech. Eng.*, vol. 197, no. 25, pp. 2087–2104, 2008.

[178] M. H. Flamm, T. V Colace, M. S. Chatterjee, H. Jing, S. Zhou, D. Jaeger, L. F. Brass, T. Sinno, and S. L. Diamond, “Multiscale prediction of patient-specific platelet function under flow,” *Blood*, vol. 120, no. 1, pp. 190–198, 2012.

[179] E. N. Sorensen, G. W. Burgreen, W. R. Wagner, and J. F. Antaki, “Computational simulation of platelet deposition and activation: II. Results for Poiseuille flow over collagen,” *Ann. Biomed. Eng.*, vol. 27, no. 4, pp. 449–458, 1999.

[180] A. Fogelson, H. Yu, and A. Kuharsky, “Computational modeling of blood clotting: coagulation and three-dimensional platelet aggregation,” in *Polymer and Cell Dynamics*, Springer, 2003, pp. 145–154.

[181] A. Alenitsyn, A. Kondratyev, I. Mikhailova, and I. Siddique, “Mathematical modeling of thrombus growth in mesenteric vessels,” *Math. Biosci.*, vol. 224, no. 1, pp. 29–34, 2010.

[182] D. L. Bark and D. N. Ku, “Wall shear over high degree stenoses pertinent to atherothrombosis,” *J. Biomech.*, vol. 43, no. 15, pp. 2970–2977, 2010.

[183] L. Crowl and A. L. Fogelson, “Analysis of mechanisms for platelet near-wall excess under arterial blood flow conditions,” *J. Fluid Mech.*, vol. 676, pp. 348–375, 2011.

[184] J. K. W. Chesnutt and H.-C. Han, “Platelet size and density affect shear-induced thrombus formation in tortuous arterioles,” *Phys. Biol.*, vol. 10, no. 5, p. 56003, 2013.

[185] J. K. W. Chesnutt and H.-C. Han, “Computational simulation of platelet interactions in the initiation of stent thrombosis due to stent malapposition,” *Phys. Biol.*, vol. 13, no. 1, p. 16001, 2016.

[186] D. Mukherjee, N. D. Jani, K. Selvaganesan, C. L. Weng, and S. C. Shadden, “Computational Assessment of the Relation Between Embolism Source and Embolus Distribution to the Circle of Willis for Improved Understanding of Stroke Etiology,” *J. Biomech. Eng.*, vol. 138, no. 8, p. 81008, 2016.

[187] R. Virchow, *Gesammelte abhandlungen zur wissenschaftlichen medicin*. Meidinger, 1856.

[188] N. K. C. Selvarasu, D. K. Tafti, and P. P. Vlachos, “Hydrodynamic effects of compliance mismatch in stented arteries,” *J. Biomech. Eng.*, vol. 133, no. 2, p. 21008, 2011.

[189] J. Aslan, A. Itakura, J. Gertz, and O. T. McCarty, “Platelet Shape Change and Spreading,” in *Platelets and Megakaryocytes*, vol. 788, J. M. Gibbins and M. P. Mahaut-Smith, Eds. Springer New York, 2012, pp. 91–100.

[190] E. U. M. Saelman, H. K. Nieuwenhuis, K. M. Hese, P. G. de Groot, H. F. G. Heijnen, and H. Sage, “Platelet Adhesion to Collagen Types I Through VI11 Under Conditions of Stasis and Flow Is Mediated by GPIa/IIa (a2Bl-Integrin),” 1994.

[191] N. Duraiswamy, J. M. Cesar, R. T. Schoephoerster, and J. E. Moore Jr, “Effects of stent geometry on local flow dynamics and resulting platelet deposition in an in vitro model,” *Biorheology*, vol. 45, no. 5, pp. 547–561, 2008.

[192] N. K. C. Selvarasu and D. K. Tafti, “Effects of elastic modulus change in helical tubes under the influence of dynamic changes in curvature and torsion,” *J. Biomech. Eng.*, vol. 136, no. 8, p. 81001, 2014.

[193] A. G. van der Giessen, J. J. Wentzel, F. N. van de Vosse, A. F. van der Steen, P. J. de

Feyter, and F. J. Gijsen, “Plaque and Shear Stress Distribution in Human Coronary Bifurcations: a Multi-Slice Computed Tomography Study,” in *ASME 2007 Summer Bioengineering Conference*, 2007, pp. 477–478.

[194] F. J. H. Gijsen, J. J. Wentzel, A. Thury, B. Lamers, J. C. H. Schuurbiers, P. W. Serruys, and A. F. Van der Steen, “A new imaging technique to study 3-D plaque and shear stress distribution in human coronary artery bifurcations in vivo,” *J. Biomech.*, vol. 40, no. 11, pp. 2349–2357, 2007.

[195] N. Maalej and J. D. Folts, “Increased shear stress overcomes the antithrombotic platelet inhibitory effect of aspirin in stenosed dog coronary arteries,” *Circulation*, vol. 93, no. 6, pp. 1201–1205, 1996.

[196] T. V Colace and S. L. Diamond, “Direct observation of von Willebrand factor elongation and fiber formation on collagen during acute whole blood exposure to pathological flow,” *Arterioscler. Thromb. Vasc. Biol.*, vol. 33, no. 1, pp. 105–113, 2013.

[197] J. O. Taylor, L. Yang, S. Deutsch, and K. B. Manning, “Development of a platelet adhesion transport equation for a computational thrombosis model,” *J. Biomech.*, vol. 50, pp. 114–120, 2017.

[198] J. O. Taylor, R. S. Meyer, S. Deutsch, and K. B. Manning, “Development of a computational model for macroscopic predictions of device-induced thrombosis,” *Biomech. Model. Mechanobiol.*, vol. 15, no. 6, pp. 1713–1731, 2016.

[199] N. K. C. Selvarasu and D. K. Tafti, “Investigation of the effects of dynamic change in curvature and torsion on pulsatile flow in a helical tube,” *J. Biomech. Eng.*, vol. 134, no. 7, p. 71005, 2012.

[200] E. N. Sorensen, “Computational simulation of platelet transport, activation, and

deposition," University of Pittsburgh, 2002.

[201] A. Lévêque, *Les Lois de la transmission de chaleur par convection, par André Lévêque*. Dunod, 1928.

[202] M. J. Griffith, "Kinetics of the heparin-enhanced antithrombin III/thrombin reaction. Evidence for a template model for the mechanism of action of heparin," *J. Biol. Chem.*, vol. 257, no. 13, pp. 7360–7365, 1982.

[203] H. L. Goldsmith and V. T. Turitto, "Rheological aspects of thrombosis and haemostasis: basic principles and applications. ICTH-Report-Subcommittee on Rheology of the International Committee on Thrombosis and Haemostasis," *Thromb. Haemost.*, vol. 55, no. 3, pp. 415–435, 1986.

[204] J. Rosing, J. L. Van Rijn, E. M. Bevers, G. van Dieijen, P. Comfurius, and R. F. Zwaal, "The role of activated human platelets in prothrombin and factor X activation," *Blood*, vol. 65, no. 2, pp. 319–332, 1985.

[205] M. Li, D. N. Ku, and C. R. Forest, "Microfluidic system for simultaneous optical measurement of platelet aggregation at multiple shear rates in whole blood," *Lab Chip*, vol. 12, no. 7, pp. 1355–1362, 2012.

[206] M. Mehrabadi, D. N. Ku, and C. K. Aidun, "Effects of shear rate, confinement, and particle parameters on margination in blood flow," *Phys. Rev. E*, vol. 93, no. 2, p. 23109, 2016.

[207] V. Govindarajan, V. Rakesh, J. Reifman, and A. Y. Mitrophanov, "Computational Study of Thrombus Formation and Clotting Factor Effects under Venous Flow Conditions," *Biophys. J.*, vol. 110, no. 8, pp. 1869–1885, 2016.

[208] T. V Colace, R. W. Muthard, and S. L. Diamond, "Thrombus growth and embolism on

tissue factor-bearing collagen surfaces under flow role of thrombin with and without fibrin," *Arterioscler. Thromb. Vasc. Biol.*, vol. 32, no. 6, pp. 1466–1476, 2012.

[209] L. D. C. Casa, D. H. Deaton, and D. N. Ku, "Role of high shear rate in thrombosis," *J. Vasc. Surg.*, vol. 61, no. 4, pp. 1068–1080, 2015.

[210] H. Hosseinzadegan and D. K. Tafti, "Prediction of Thrombus Growth: Effect of Stenosis and Reynolds Number," *Cardiovasc. Eng. Technol.*, pp. 1–18, 2017.

[211] P. Gopalakrishnan and D. K. Tafti, "A parallel boundary fitted dynamic mesh solver for applications to flapping flight," *Comput. Fluids*, vol. 38, no. 8, pp. 1592–1607, 2009.

[212] J. A. Oliver, D. M. Monroe, H. R. Roberts, and M. Hoffman, "Thrombin activates factor XI on activated platelets in the absence of factor XII," *Arterioscler. Thromb. Vasc. Biol.*, vol. 19, no. 1, pp. 170–177, 1999.

[213] D. M. Monroe, H. R. Roberts, and M. Hoffman, "Platelet procoagulant complex assembly in a tissue factor- initiated system," *Br. J. Haematol.*, vol. 88, no. 2, pp. 364–371, 1994.

[214] J. M. Ramstack, L. Zuckerman, and L. F. Mockros, "Shear-induced activation of platelets," *J. Biomech.*, vol. 12, no. 2, pp. 113–125, 1979.

[215] D. Bluestein, W. Yin, K. Affeld, and J. Jesty, "Flow-induced platelet activation in a mechanical heart valve," *J. Heart Valve Dis.*, vol. 13, no. 3, pp. 501–508, 2004.

[216] P. L. Blackshear Jr, F. D. Dorman, and J. H. Steinbach, "Some mechanical effects that influence hemolysis." LWW, 1965.

[217] D. Mozaffarian, E. J. Benjamin, A. S. Go, D. K. Arnett, M. J. Blaha, M. Cushman, S. R. Das, S. de Ferranti, J.-P. Després, and H. J. Fullerton, "Heart disease and stroke statistics—2016 update," *Circulation*, vol. 133, no. 4, pp. e38–e360, 2016.

[218] M. R. Mehra, G. C. Stewart, and P. A. Uber, "The vexing problem of thrombosis in long-

term mechanical circulatory support." Elsevier, 2014.

[219] Blausen.com, "Medical gallery of Blausen Medical 2014," *Wikiversity Journal of Medicine*, 2014. [Online]. Available: https://en.wikiversity.org/wiki/WikiJournal_of_Medicine/Medical_gallery_of_Blausen_Medical_2014.

[220] A. Blitz, "Heartmate II LVAD Implantation. Arie Blitz, MD," 2011. [Online]. Available: https://youtu.be/I4r5_3uS0Nc.

[221] A. Clegg, "Heart with LVAD," 2011.

[222] S. Bozkurt, F. N. van de Vosse, and M. C. M. Rutten, "Enhancement of arterial pressure pulsatility by controlling continuous-flow left ventricular assist device flow rate in mock circulatory system," *J. Med. Biol. Eng.*, vol. 36, no. 3, pp. 308–315, 2016.

Appendices

Appendix A

In GenIDLEST, species concentrations y_i in implemented (flux and source) equations are nondimensional ($\frac{kg\ species}{kg\ fluid}$). Here we present the nondimensionalized form of equations 3.13-3.18 that are used in our code:

A.1. Flux of resting platelets

In Sorensen et al.[179]:

$$j_r(x,t)(\frac{PLT}{cm^2.s}) = -S(x,t).k_{rs}.[RP]$$

where k_{rs} is in $\frac{cm}{s}$ and $[RP]$ has unit of $\frac{PLT}{ml}$ or $\frac{PLT}{cm^3}$

$[RP]$ conversion:

$$y_{RP}\left(\frac{kg}{kg}\right) = \frac{mplt\left(\frac{kg}{PLT}\right) \times [RP]\left(\frac{PLT}{cm^3}\right)}{\rho_{ref}(\frac{kg}{m^3}) \times 10^{-6}(\frac{m^3}{cm^3})} \quad \rightarrow \quad [RP]\left(\frac{PLT}{cm^3}\right) = \frac{10^{-6} \times \rho_{ref} \times y_{RP}}{mplt}$$

where $mplt$ is the mass of a single platelet in kg.

k_{rs} conversion:

For k_{rs} the dimensional value is used in the code. But it is converted to $\frac{m}{s}$ from $\frac{cm}{s}$

$$k_{rs}\left(\frac{m}{s}\right) = 10^{-2}(\frac{m}{cm}) \times k_{rs}(\frac{cm}{s})$$

$$k_{rs}\left(\frac{cm}{s}\right) = 10^{2}(\frac{cm}{m}) \times k_{rs}(\frac{m}{s})$$

$S(x,t)$ is nondimensional (%).

The dimensional flux would be as follows:

$$j_r(x,t)\left(\frac{PLT}{cm^2.s}\right) = -S(x,t) \times k_{rs}\left(\frac{m}{s}\right) \times \frac{10^{-4}\left(\frac{m^2}{cm^2}\right) \times \rho_{ref}\left(\frac{kg}{m^3}\right) \times y_{RP}}{mplt\left(\frac{kg}{PLT}\right)}$$

$$j_r(x,t)\left(\frac{PLT}{m^2.s}\right) = -S(x,t) \times k_{rs}\left(\frac{m}{s}\right) \times \frac{10^{-4}\left(\frac{m^2}{cm^2}\right) \times 10^4\left(\frac{cm^2}{m^2}\right) \times \rho_{ref}\left(\frac{kg}{m^3}\right) \times y_{RP}}{mplt\left(\frac{kg}{PLT}\right)}$$

$$j_r(x,t)\left(\frac{kg}{m^2.s}\right) = -S(x,t) \times k_{rs}\left(\frac{m}{s}\right) \times \frac{\rho_{ref}\left(\frac{kg}{m^3}\right) \times y_{RP}}{mplt\left(\frac{kg}{PLT}\right)} \times mplt\left(\frac{kg}{PLT}\right)$$

The flux should be divided by $\frac{\rho_{ref}.D_{ref}}{L_{ref}}$. Therefore in our framework the nondimensional flux is

$$j^*_{RP} = j_r\left(\frac{kg}{m^2.s}\right) \times \frac{L_{ref}}{\rho_{ref}.D_{ref}}$$

$$= \ -S(x,t) \times k_{rs}\left(\frac{m}{s}\right) \times (\rho_{ref}\left(\frac{kg}{m^3}\right) \times y_{RP}) \times (\frac{L_{ref}(m)}{\rho_{ref}\left(\frac{kg}{m^3}\right) \times D_{ref}\left(\frac{m^2}{s}\right)})$$

$$= -S(x,t) \times k_{rs}\left(\frac{m}{s}\right) \times \frac{y_{RP} \times L_{ref}(m)}{D_{ref}\left(\frac{m^2}{s}\right)}$$

A.2. Flux of activated platelets

Similarly:

$$j^*_{AP} = -\left(S(x,t) \times k_{as}\left(\frac{m}{s}\right) + \left(\frac{Mas(x,t)}{M_\infty}\right) \times k_{aa}\left(\frac{m}{s}\right)\right) \times \frac{y_{AP} \times L_{ref}(m)}{D_{ref}\left(\frac{m^2}{s}\right)}$$

A.3. Flux of ADP

In Sorensen et al. [179]:

$$j_{ADP}(x,t)\left(\frac{nmol}{cm^2.s}\right) = \lambda_{ADP}.(\theta.S(x,t).k_{rs}.[RP] + k_{pa}.M_r(x,t))$$

where k_{rs} is in $\frac{cm}{s}$ and $[RP]$ has unit of $\frac{PLT}{ml}$ or $\frac{PLT}{cm^3}$. k_{pa} is in $\frac{1}{s}$, and λ_{ADP} is in $\frac{nmol}{PLT}$. Also $M_r(x,t)$ has the unit of $\frac{PLT}{cm^2}$.

$S(x,t)$ is nondimensional, M_r is not nondimensionalized as well as k_{rs}, k_{pa} and λ_{ADP}. However again unit of k_{rs} is converted to $\frac{m}{s}$ from $\frac{cm}{s}$.

Therefore:

$$j_{ADP}(x,t)\left(\frac{nmol}{cm^2.s}\right) = \lambda_{ADP}\left(\frac{nmol}{PLT}\right).(\theta.S(x,t).10^2 \times k_{rs}\left(\frac{m}{s}\right).[RP]\left(\frac{PLT}{cm^3}\right) + k_{pa}\left(\frac{1}{s}\right).M_r(x,t)\left(\frac{PLT}{cm^2}\right))$$

Recall:

$$y_{RP}\left(\frac{kg}{kg}\right) = \frac{mplt\left(\frac{kg}{PLT}\right)\times[RP]\left(\frac{PLT}{cm^3}\right)}{\rho_{ref}(\frac{kg}{m^3})\times 10^{-6}(\frac{m^3}{cm^3})} \quad \rightarrow \quad [RP]\left(\frac{PLT}{cm^3}\right) = \frac{10^{-6}\times\rho_{ref}\times y_{RP}}{mplt}$$

Plugging $[RP]$ in the flux equation gives

$$j_{ADP}(x,t)\left(\frac{nmol}{cm^2.s}\right) = \lambda_{ADP}\left(\frac{nmol}{PLT}\right).\left(\theta.S(x,t).10^2\times k_{rs}\left(\frac{m}{s}\right).\frac{10^{-6}\left(\frac{m^3}{cm^3}\right)\times\rho_{ref}\left(\frac{kg}{m^3}\right)\times y_{RP}}{mplt\left(\frac{kg}{PLT}\right)} + k_{pa}\left(\frac{1}{s}\right).M_r(x,t)\left(\frac{PLT}{cm^2}\right)\right)$$

In SI units:

$$j_{ADP}(x,t)\left(\frac{kg}{m^2.s}\right) = \lambda_{ADP}\left(\frac{nmol}{PLT}\right).\left(\theta.S(x,t).10^2\times k_{rs}\left(\frac{m}{s}\right).\frac{10^{-6}\left(\frac{m^3}{cm^3}\right)\times\rho_{ref}\left(\frac{kg}{m^3}\right)\times y_{RP}}{mplt\left(\frac{kg}{PLT}\right)} + k_{pa}\left(\frac{1}{s}\right).M_r(x,t)\left(\frac{PLT}{cm^2}\right)\right)\times ADPmw\left(\frac{kg}{mol}\right)\times 10^{-9}\left(\frac{mol}{nmol}\right)\times 10^4\left(\frac{cm^2}{m^2}\right)$$

Dividing this by $\frac{\rho_{ref}.D_{ref}}{L_{ref}}$ gives:

$$j^*_{ADP}(x,t) = \lambda_{ADP}\left(\frac{nmol}{PLT}\right).\left(\theta.S(x,t).10^2 \times k_{rs}\left(\frac{m}{s}\right).\frac{10^{-6}\left(\frac{m^3}{cm^3}\right)\times \rho_{ref}\left(\frac{kg}{m^3}\right)\times y_{RP}}{mplt\left(\frac{kg}{PLT}\right)} + k_{pa}\left(\frac{1}{s}\right).M_r(x,t)\left(\frac{PLT}{cm^2}\right)\right)\times mw_{ADP}\left(\frac{kg}{mol}\right)\times 10^{-9}\left(\frac{mol}{nmol}\right)\times 10^4\left(\frac{cm^2}{m^2}\right) \times \frac{L_{ref}}{\rho_{ref}D_{ref}}$$

A.4. Flux of TxA$_2$ (Thromboxane A$_2$)

In Sorensen et al. [179]:

$$j_{TxA2}(x,t)\left(\frac{nmol}{cm^2.s}\right) = M_{at}(x,t)\left(\frac{PLT}{cm^2}\right).s_{p,j}\left(\frac{nmol}{PLT.s}\right)$$

In SI units:

$$j_{TxA2}(x,t)\left(\frac{kg}{m^2.s}\right) = M_{at}(x,t)\left(\frac{PLT}{cm^2}\right).s_{p,j}\left(\frac{nmol}{PLT.s}\right)\times \mathrm{mw}_{TxA2}\left(\frac{kg}{mol}\right)\times 10^{-9}\left(\frac{mol}{nmol}\right) \times 10^4\left(\frac{cm^2}{m^2}\right)$$

Dividing this by $\frac{\rho_{ref}.D_{ref}}{L_{ref}}$ gives:

$$j^*_{TxA2}(x,t) = M_{at}(x,t)\left(\frac{PLT}{cm^2}\right).s_{p,j}\left(\frac{nmol}{PLT.s}\right)\times \mathrm{mw}_{TxA2}\left(\frac{kg}{mol}\right)\times 10^{-9}\left(\frac{mol}{nmol}\right)\times 10^4\left(\frac{cm^2}{m^2}\right) \times \frac{L_{ref}}{\rho_{ref}D_{ref}}$$

A.5. Flux of Prothrombin

In Sorensen et al. [179]:

$$j_{pt}(x,t)\left(\frac{nmol}{cm^2.s}\right) =$$

$$-\beta\left(\frac{nmol}{U}\right).\left(M_{at}\left(\frac{PLT}{cm^2}\right).\phi_{at}\left(\frac{U}{PLT.s.\frac{nmol}{cm^3}}\right) + M_r(x,t)\left(\frac{PLT}{cm^2}\right).\phi_{rt}\left(\frac{U}{PLT.s.\frac{nmol}{cm^3}}\right)\right).[PT]\left(\frac{nmol}{cm^3}\right)$$

$$y_{PT}\left(\frac{kg}{kg}\right) = \frac{mw_{PT}\left(\frac{kg}{mol}\right)\times[RP]\left(\frac{nmol}{cm^3}\right)\times 10^{-9}\left(\frac{mol}{nmol}\right)}{\rho_{ref}\left(\frac{kg}{m^3}\right)\times 10^{-6}\left(\frac{m^3}{cm^3}\right)}$$

$$\rightarrow \quad [RP]\left(\frac{nmol}{cm^3}\right) = \frac{10^{-6}\left(\frac{m^3}{cm^3}\right)\times\rho_{ref}\left(\frac{kg}{m^3}\right)\times y_{PT}\left(\frac{kg}{kg}\right)}{mw_{PT}\left(\frac{kg}{mol}\right)\times 10^{-9}\left(\frac{mol}{nmol}\right)}$$

$$j_{pt}(x,t)\left(\frac{nmol}{cm^2.s}\right) =$$

$$-\beta\left(\frac{nmol}{U}\right).\left(M_{at}\left(\frac{PLT}{cm^2}\right).\phi_{at}\left(\frac{U}{PLT.s.\frac{nmol}{cm^3}}\right) + M_r(x,t)\left(\frac{PLT}{cm^2}\right).\phi_{rt}\left(\frac{U}{PLT.s.\frac{nmol}{cm^3}}\right)\right) \times \frac{10^{-6}\left(\frac{m^3}{cm^3}\right)\times\rho_{ref}\left(\frac{kg}{m^3}\right)\times y_{PT}\left(\frac{kg}{kg}\right)}{mw_{PT}\left(\frac{kg}{mol}\right)\times 10^{-9}\left(\frac{mol}{nmol}\right)}$$

In SI units:

$$j_{pt}(x,t)\left(\frac{kg}{m^2.s}\right) =$$

$$-\beta\left(\frac{nmol}{U}\right).\left(M_{at}\left(\frac{PLT}{cm^2}\right).\phi_{at}\left(\frac{U}{PLT.s.\frac{nmol}{cm^3}}\right)+M_r(x,t)\left(\frac{PLT}{cm^2}\right).\phi_{rt}\left(\frac{U}{PLT.s.\frac{nmol}{cm^3}}\right)\right)$$
$$\times\frac{10^{-6}\left(\frac{m^3}{cm^3}\right)\times\rho_{ref}\left(\frac{kg}{m^3}\right)\times y_{PT}\left(\frac{kg}{kg}\right)}{mw_{PT}\left(\frac{kg}{mol}\right)\times 10^{-9}\left(\frac{mol}{nmol}\right)}\times mw_{PT}\left(\frac{kg}{mol}\right)\times 10^{-9}\left(\frac{mol}{nmol}\right)$$
$$\times 10^{4}\left(\frac{cm^2}{m^2}\right)$$

$$=-\beta\left(\frac{nmol}{U}\right).\left(M_{at}\left(\frac{PLT}{cm^2}\right).\phi_{at}\left(\frac{U}{PLT.s.\frac{nmol}{cm^3}}\right)+M_r(x,t)\left(\frac{PLT}{cm^2}\right).\phi_{rt}\left(\frac{U}{PLT.s.\frac{nmol}{cm^3}}\right)\right)$$
$$\times 10^{-6}\left(\frac{m^3}{cm^3}\right)\times\rho_{ref}\left(\frac{kg}{m^3}\right)\times y_{PT}\left(\frac{kg}{kg}\right)\times 10^{4}\left(\frac{cm^2}{m^2}\right)$$

Dividing this by $\frac{\rho_{ref}.D_{ref}}{L_{ref}}$ yields:

$$j_{pt}^{*}(x,t)=-\beta\left(\frac{nmol}{U}\right).\left(M_{at}\left(\frac{PLT}{cm^2}\right).\phi_{at}\left(\frac{U}{PLT.s.\frac{nmol}{cm^3}}\right)\right.$$
$$\left.+M_r(x,t)\left(\frac{PLT}{cm^2}\right).\phi_{rt}\left(\frac{U}{PLT.s.\frac{nmol}{cm^3}}\right)\right)\times 10^{-6}\left(\frac{m^3}{cm^3}\right)\times\rho_{ref}\left(\frac{kg}{m^3}\right)\times y_{PT}\left(\frac{kg}{kg}\right)$$
$$\times 10^{4}\left(\frac{cm^2}{m^2}\right)\times\frac{L_{ref}}{\rho_{ref}D_{ref}}$$

A.6. Flux of Thrombin

Similarly:

$$j_{t}^{*}(x,t)=\beta\left(\frac{nmol}{U}\right).\left(M_{at}\left(\frac{PLT}{cm^2}\right).\phi_{at}\left(\frac{U}{PLT.s.\frac{nmol}{cm^3}}\right)+M_r(x,t)\left(\frac{PLT}{cm^2}\right).\phi_{rt}\left(\frac{U}{PLT.s.\frac{nmol}{cm^3}}\right)\right)$$
$$\times 10^{-6}\left(\frac{m^3}{cm^3}\right)\times\rho_{ref}\left(\frac{kg}{m^3}\right)\times y_{PT}\left(\frac{kg}{kg}\right)\times 10^{4}\left(\frac{cm^2}{m^2}\right)\times\frac{L_{ref}}{\rho_{ref}D_{ref}}\times\frac{mw_{T}\left(\frac{kg}{mol}\right)}{mw_{PT}\left(\frac{kg}{mol}\right)}$$

A.7. Flux of ATIII

Zero flux is defined for ATIII.

Appendix B

Using the original best-fit values introduced by Sorensen et al. [179], the axial distribution of platelet deposition was found to be much less shear-dependent than experimental results of Badimon and Badimon [47] for stenosis degrees of 35, and 55 %. Also it was observed that for 80% stenosis, not only did the results not match, but the deposition was found to be inversely correlated to local wall shear rate especially for high flow conditions (i.e. 40 and 60 ml/min); we attribute this to low concentration of platelets near the wall. Therefore, an augmented adhesion rate of platelets was employed to make the platelet-wall reaction mechanism dominant near the apex. Following an approach similar to that of David et al. [160] the new adhesion rates of platelets k_i (i.e. k_{rs}, k_{as}, and k_{aa}) are defined as linear functions of local wall shear rate (Eq. 3.21).

Note that the model is calibrated in two steps. First, the best-fit values are obtained for λ which augments the effect of wall shear rate to match the axial distribution of deposition; in the second step, k_{i_0} is calibrated in order to reach the experimental values of total deposition in the stenosis. In the first step the only interest is the distribution of platelet deposition and magnitude of k_{i_0} does not affect the distribution. This is because in the flux terms for platelets, concentrations are multiplied by k_{i_0} which is not a function of axial position (see Eqs. 3.13 and 3.14). Therefore, the deposition values in all five segments will be scaled up or down by the same factor. This was confirmed by trying two different sets of k_{i_0} using the same λ values to assure that the results are affected only by altering the enhancement factor.

Shear enhancement factor λ as a function of stenosis degree and Reynolds number

A 5th order polynomial function is obtained for shear enhancement factor with the general form:

$$\begin{aligned}\lambda(r,s) = {} & c_1 r^2 s^3 + c_2 r^3 s^2 + c_3 r^4 s + c_4 r^5 + c_5 r s^3 + c_6 r^2 s^2 + c_7 r^3 s + c_8 r^4 + c_9 s^3 \\ & + c_{10} r s^2 + c_{11} r^2 s + c_{12} r^3 + c_{13} s^2 + c_{14} r s + c_{15} r^2 + c_{16} s + c_{17} r + c_{18}\end{aligned} \tag{B.1}$$

where coefficients $c_1 - c_{18}$ are given in Table B.1., r is the Reynolds number based on the diameter and mean velocity at the apex and s is the stenosis degree (%).

Platelet adhesion rates base values as functions of stenosis degree and Reynolds number

We fit surfaces to the obtained values of k_{rs_0}, k_{as_0}, and k_{aa_0} (in m.s^{-1}) to obtain a general function of stenosis degree and local Re at the apex of the stenosis as follows:

$$\begin{aligned}k_{i_0}(r,s) = {} & c_1 r^2 s^3 + c_2 r^3 s^2 + c_3 r^4 s + c_4 r^5 + c_5 r s^3 + c_6 r^2 s^2 + c_7 r^3 s + c_8 r^4 + c_9 s^3 \\ & + c_{10} r s^2 + c_{11} r^2 s + c_{12} r^3 + c_{13} s^2 + c_{14} r s + c_{15} r^2 + c_{16} s + c_{17} r + c_{18}\end{aligned} \tag{B.2}$$

where $c_1 - c_{18}$ are constants given in Table B.1.

Figure B.1. Surface fit for best-fit values of shear enhancement factor λ

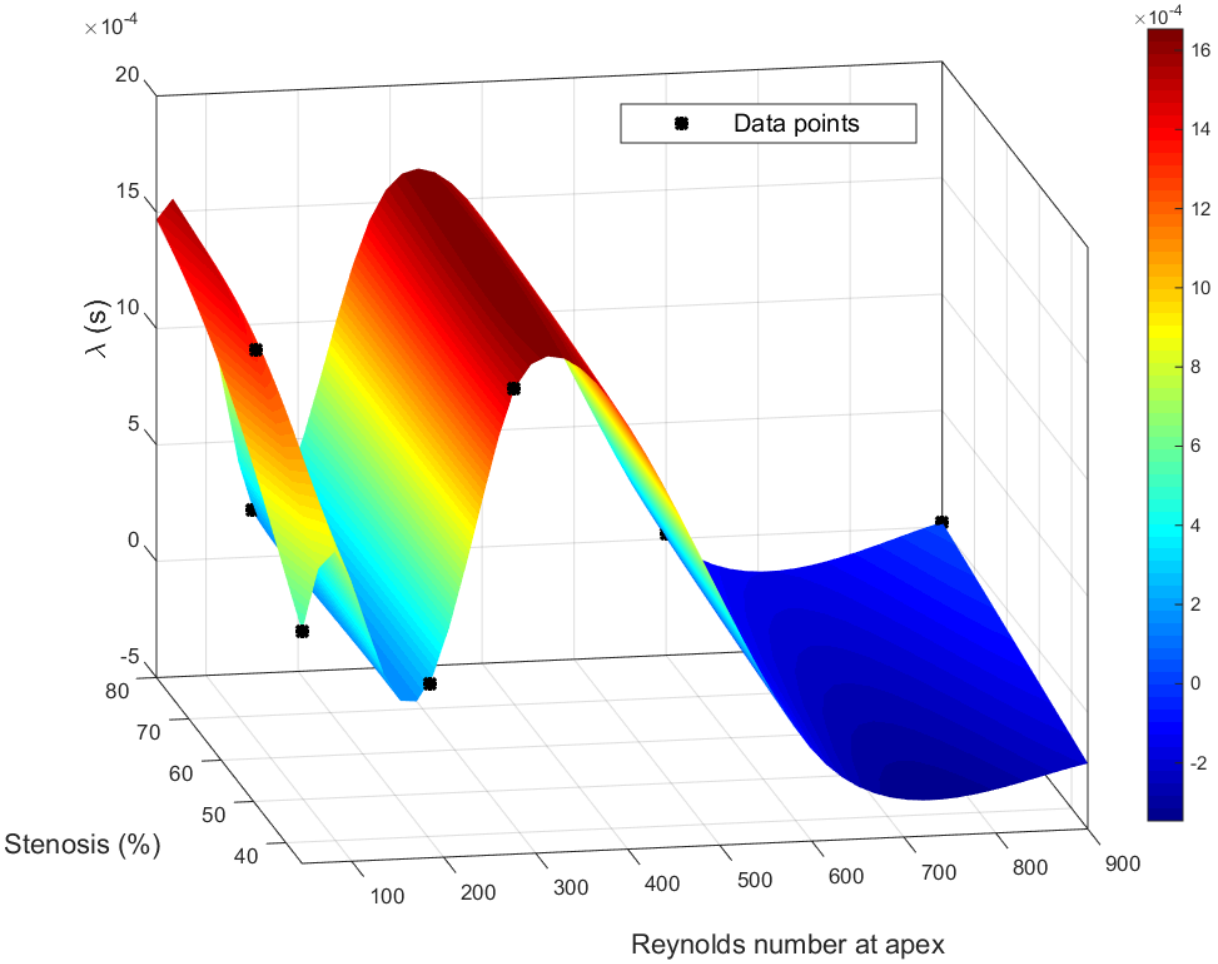

Figure B.1 shows the corresponding surface fit to λ best-fit values. It is observed that the shear enhancement factor is not a function of stenosis degree for Re>150. For lower Re numbers, λ increases with stenosis percentage. This trend implies that for low Re flow, augmentation of platelet adhesion (outflux) terms due to high shear near the apex is needed to reflect higher deposition values in this region. In other words, the platelet-surface reaction mechanisms are predominant in low Re flow.

Table B.1. Coefficient values of polynomial equation for best-fit values of λ(Eq. 3.21) and k_{i_0}(Eq.3. 22)

λ	c_1	c_2	c_3	c_4	c_5	c_6
Re < 277	-1.48×10^{-13}	-2×10^{-13}	-3.7×10^{-14}	-2.6×10^{-14}	4.744×10^{-11}	1.08×10^{-10}
	c_7	c_8	c_9	c_{10}	c_{11}	c_{12}
	4.6×10^{-11}	1.46×10^{-11}	-2.234×10^{-9}	-1.6×10^{-8}	-1.5×10^{-8}	-2.536×10^{-9}
	c_{13}	c_{14}	c_{15}	c_{16}	c_{17}	c_{18}
	3.95×10^{-7}	1.466×10^{-6}	1.27×10^{-7}	5.96×10^{-7}	7.626×10^{-6}	-1.071×10^{-3}
Re ≥ 277	c_1	c_2	c_3	c_4	c_5	c_6
	3.237×10^{-15}	-3×10^{-16}	-2.4×10^{-16}	5.09×10^{-17}	-4.616×10^{-12}	-4.6×10^{-13}
	c_7	c_8	c_9	c_{10}	c_{11}	c_{12}
	6.6×10^{-13}	-2.7×10^{-13}	1.62×10^{-9}	1.09×10^{-9}	-5.9×10^{-10}	4.845×10^{-10}
	c_{13}	c_{14}	c_{15}	c_{16}	c_{17}	c_{18}
	-4.2×10^{-7}	1.82×10^{-7}	-3.7×10^{-7}	-8.106×10^{-6}	1.23×10^{-4}	-1.29×10^{-2}
k_{rs_0}	c_1	c_2	c_3	c_4	c_5	c_6
Re < 277	1.32×10^{-14}	1.71×10^{-14}	1.081×10^{-15}	1.094×10^{-15}	-3.807×10^{-12}	-9.665×10^{-12}
	c_7	c_8	c_9	c_{10}	c_{11}	c_{12}
	-2.324×10^{-12}	-5.1×10^{-13}	1.31×10^{-10}	1.453×10^{-9}	9.53×10^{-10}	5.03×10^{-11}
	c_{13}	c_{14}	c_{15}	c_{16}	c_{17}	c_{18}
	-2.79×10^{-8}	-1.087×10^{-7}	4.8×10^{-9}	-7.784×10^{-7}	-1.473×10^{-6}	2.685×10^{-4}

	c_1	c_2	c_3	c_4	c_5	c_6
$\mathrm{Re} \geq 277$	-4.5×10^{-16}	-1.23×10^{-17}	1.2×10^{-17}	-7.8×10^{-19}	6.17×10^{-13}	1.23×10^{-13}
	c_7	c_8	c_9	c_{10}	c_{11}	c_{12}
	-3.2×10^{-14}	4.966×10^{-15}	-2×10^{-10}	-1.5×10^{-10}	2.65×10^{-11}	-9.355×10^{-12}
	c_{13}	c_{14}	c_{15}	c_{16}	c_{17}	c_{18}
	4.8×10^{-8}	-6.5×10^{-9}	7.4×10^{-9}	-8.513×10^{-7}	-2.293×10^{-6}	2.815×10^{-4}

k_{as_0} , k_{aa_0}	c_1	c_2	c_3	c_4	c_5	c_6
$\mathrm{Re} < 277$	1.647×10^{-14}	2.13×10^{-14}	1.344×10^{-15}	1.367×10^{-15}	-4.733×10^{-12}	-1.202×10^{-11}
	c_7	c_8	c_9	c_{10}	c_{11}	c_{12}
	-2.889×10^{-12}	-6.39×10^{-13}	1.634×10^{-10}	1.806×10^{-9}	1.185×10^{-9}	6.249×10^{-11}
	c_{13}	c_{14}	c_{15}	c_{16}	c_{17}	c_{18}
	-3.469×10^{-8}	-1.351×10^{-7}	5.968×10^{-9}	-9.677×10^{-7}	-1.831×10^{-6}	3.338×10^{-4}

	c_1	c_2	c_3	c_4	c_5	c_6
$\mathrm{Re} \geq 277$	-5.59×10^{-16}	-1.53×10^{-17}	1.493×10^{-17}	-9.745×10^{-19}	7.667×10^{-13}	1.527×10^{-13}
	c_7	c_8	c_9	c_{10}	c_{11}	c_{12}
	-4.03×10^{-14}	6.174×10^{-15}	-2.54×10^{-10}	-1.875×10^{-10}	3.3×10^{-11}	-1.163×10^{-11}
	c_{13}	c_{14}	c_{15}	c_{16}	c_{17}	c_{18}
	5.968×10^{-8}	-8.081×10^{-9}	9.2×10^{-9}	-1.058×10^{-6}	-2.851×10^{-6}	3.5×10^{-4}

Appendix C

In the pulsatile case of Casa and Ku [147], the mean wall shear rate within a cycle was 3800 s^{-1} to be consistent with the steady case. 62 beats occur per minute and each cycle is 1.02 second (T=1.02s). The frequency of pulsatility was 0.97 Hz and the blood perfusion continued for 4 min. Due to slight differences in different cycles in the experiments and also in order to have a periodic profile as a function of time to use in our calculations, a curve was fitted to the experimental data. A curve fit was done using a sum-of-sine profile in MATLAB® (MATLAB 8.4, The Mathworks Inc., Natick, MA, 2014) for 0-1 s. The fitted curve equation reads as follows:

$$V(t) = a_1 \sin(b_1 t + c_1) + a_2 \sin(b_2 t + c_2) + a_3 \sin(b_3 t + c_3) + a_4 \sin(b_4 t + c_4) + a_5 \sin(b_5 t + c_5) \tag{C.1}$$

where $V(t)$ is the inlet velocity (in $\mathrm{mm.s^{-1}}$) and $a_1 - a_5$, $b_1 - b_5$, and $c_1 - c_5$ are constants given in Table C.1.

Table C.1. Constants used in Eq. C.1. for the pulsatile flow case of Casa and Ku [147].

a_1	2.523	b_1	1.234	c_1	-0.5972
a_2	0.977	b_2	6.39	c_2	-0.4166
a_3	5.058	b_3	2.534	c_3	0.2988
a_4	10.88	b_4	3.361	c_4	5.118
a_5	14.54	b_5	3.205	c_5	2.254

Appendix D

PAS model code

The MATLAB code used to calculate the platelet activation state parameter (PAS) was implemented as follows:

```
close all
clear all
clc
% Shear Stress = 70 dynes/cm2
% Frequency = 3.13 Hz
dt=0.001;
tau = @(x)[1400*x.*(x>=0&x<=0.05)+(-
1400*x+140).*(x>0.05&x<=0.1)+0.*(x>0.1&x<=0.32)];
x=linspace(0,0.32,321);
time = 0:dt:240;
period = 0.32;
Tau = tau(mod(time,period));
% figure(1); plot(time,Tau);
C1 = 1.3e-4;
C2 = 0;
a = 1.0293;
b = 0.7249;
t = 0;
PAS =0;
for i = 2:(240/dt) + 1
    t(i) = t(i-1) + dt;
    PAS(i) = PAS(i-1) + C1 * b * t(i)^(b-1) * Tau(i)^a * (t(i)-t(i-1)) + C2 *
a * Tau(i)^(a-1) * t(i)^b * (Tau(i)-Tau(i-1));
end
figure(2);
plot(t/60,PAS);
```

The Euler explicit method was used to integrate shear stress over exposure time. Note that shear stresses in the equations are not in SI and have unit of dynes.cm^{-2}.

Appendix E

The MATLAB code used for plotting the velocity profiles at mitral, aortic, and LVAD boundaries in simulations of LV with LVAD [222] is given below. LVAD and aortic profiles are taken from the study of Bozkurt et al. [222] and the mitral velocity profile is simply the summation of these two.

```
%Velocity profiles at Mitral, Aortic, and LVAD boundaries in LV with LVAD
a1=16.09;b1=0.09931;c1=0.07345;
a2=-164.8;b2=0.8885;c2=0.014;
a3=5.971;b3=1.035;c3=0.02316;
a4=178.2;b4=0.888;c4=0.01741;
a5=6.415;b5=0.248;c5=0.0245;
aa1=3.376;bb1=0.09976;cc1=0.166;
aa2=0.0;bb2=-9.059;cc2=7.015e-4;
aa3=-67.12;bb3=0.8807;cc3=0.1481;
aa4=70.04;bb4=0.8822;cc4=0.148;
aa5=2.731;bb5=0.8126;cc5=1.519;
aa6=1.368e7;bb6=6.053;cc6=1.117;
figure(1)
    plot(0:0.002:0.73,(8.4882e-1)*(a1*exp(-(((0:0.002:0.73)-b1)/c1).^2)...
        +a2*exp(-(((0:0.002:0.73)-b2)/c2).^2)...
        +a3*exp(-(((0:0.002:0.73)-b3)/c3).^2)...
        +a4*exp(-(((0:0.002:0.73)-b4)/c4).^2)...
        +a5*exp(-(((0:0.002:0.73)-b5)/c5).^2))...
        ,'black','LineWidth',1);
    hold on
    plot(0:0.002:0.73,(8.4882e-1)*(aa1*exp(-(((0:0.002:0.73)-bb1)/cc1).^2)...
        +aa2*exp(-(((0:0.002:0.73)-bb2)/cc2).^2)...
        +aa3*exp(-(((0:0.002:0.73)-bb3)/cc3).^2)...
        +aa4*exp(-(((0:0.002:0.73)-bb4)/cc4).^2)...
        +aa5*exp(-(((0:0.002:0.73)-bb5)/cc5).^2)...
        +aa6*exp(-(((0:0.002:0.73)-bb6)/cc6).^2))...
        ,'green','LineWidth',1);
    hold on
    plot(0:0.002:0.73,(8.4882e-1)*(a1*exp(-(((0:0.002:0.73)-b1)/c1).^2)...
        +a2*exp(-(((0:0.002:0.73)-b2)/c2).^2)...
        +a3*exp(-(((0:0.002:0.73)-b3)/c3).^2)...
        +a4*exp(-(((0:0.002:0.73)-b4)/c4).^2)...
        +a5*exp(-(((0:0.002:0.73)-b5)/c5).^2))+(8.4882e-1)*(aa1*exp(-
(((0:0.002:0.73)-bb1)/cc1).^2)...
        +aa2*exp(-(((0:0.002:0.73)-bb2)/cc2).^2)...
        +aa3*exp(-(((0:0.002:0.73)-bb3)/cc3).^2)...
        +aa4*exp(-(((0:0.002:0.73)-bb4)/cc4).^2)...
        +aa5*exp(-(((0:0.002:0.73)-bb5)/cc5).^2)...
        +aa6*exp(-(((0:0.002:0.73)-bb6)/cc6).^2))...
        ,'red','LineWidth',1);
    ylabel('Velocity (cm/s)');
    xlabel('Time (s)');
    legend('Aorta','LVAD','Mitral');
```